DOE-ER-0313/71
ORNL/SPR-2022/2416
Distribution
Categories
UC-423, -424

FUSION MATERIALS
SEMIANNUAL PROGRESS REPORT
FOR THE PERIOD ENDING

December 31, 2021

Prepared for
DOE Office of Fusion Energy Sciences
(AT 60 20 10 0)

DATE PUBLISHED: March 2022

Prepared by
OAK RIDGE NATIONAL LABORATORY
Oak Ridge, Tennessee 37831
Managed by
UT-Battelle, LLC
For the
U.S. DEPARTMENT OF ENERGY

FOREWORD

This is the seventy-first in a series of semiannual technical progress reports on fusion materials science activity supported by the Fusion Energy Sciences Program of the U.S. Department of Energy. It covers the period ending December 31, 2021. This report focuses on research addressing the effects on materials properties and performance of exposure to the neutronic, thermal and chemical environments anticipated in the chambers of fusion experiments and energy systems. This research is a major element of the national effort to establish the materials knowledge base for an economically and environmentally attractive fusion energy source. Research activities on issues related to the interaction of materials with plasmas are reported separately.

The results reported are the products of a national effort involving a number of national laboratories and universities. A large fraction of this work, particularly in relation to fission reactor irradiations, is carried out collaboratively with partners in Japan, Russia, and the European Union. The purpose of this series of reports is to provide a working technical record for the use of program participants, and to provide a means of communicating the efforts of fusion materials scientists to the broader fusion community, both nationally and worldwide.

This report has been compiled by Stephanie Melton, Oak Ridge National Laboratory. Her efforts, and the efforts of the many persons who made technical contributions, are gratefully acknowledged.

Daniel Clark
Research Division
Office of Fusion Energy Sciences

TABLE OF CONTENTS

TABLE OF CONTENTS

TABLE OF CONTENTS

TABLE OF CONTENTS

1. FERRITIC/MARTENSITIC STEEL DEVELOPMENT

1.1 PERFORMANCE EVALUATION OF MODIFIED 3Cr-3WVTa BAINITIC STEELS—Y. Yamamoto (Oak Ridge National Laboratory)

OBJECTIVE

This work aims to evaluate the advantages in the mechanical performance of newly proposed, modified 3Cr-3WVTa bainitic steels developed at ORNL. The proposed steel was designed to eliminate the need for post-weld heat treatment (PWHT), as well as providing improved mechanical properties of both base metal and weldments compared to those of existing commercial bainitic steels or ferritic-martensitic (F-M) steels. The target applications are high-temperature structural components in fusion reactors, such as helium-cooled vacuum vessels operating up to 450°C and blanket support structures operating up to 550°C.

SUMMARY

Process optimization of the compositionally modified 3Cr-3WVTa-base bainitic ferritic steel (Mod. 3Cr-3WVTa steel) has been conducted targeting property improvement (e.g., tensile strength, impact toughness, etc.) through refinement of the prior austenite grain size (PAGS) during normalization process. Re-normalization at 1,000°C, applied to Mod. 3Cr-3WVTa steel formerly processed and normalized at 1,100°C, resulted in refining the average PAGS from 187 to 97 μm, which was due to newly formed PAGs from bainitic ferrite in the heating process like recrystallization. A cyclic heat-treatment with re-normalization at 1,000°C for three times also resulted in additional PAG refinement (97 → 81 μm), although the effect was limited. On the other hand, the Mod. 3Cr-3WVTa steel with newly processed and normalized at 1,000°C revealed further PAG refinement to 41 ± 6 μm. It was found that the PAG refinement of Mod. 3Cr-3WVTa steel through re-normalization process led to the improvement of creep-rupture performance compared to the same material with the larger PAG.

PROGRESS AND STATUS

A compositionally modified 3Cr-3WVTa bainitic ferritic steel (Mod. 3Cr-3WVTa steel, ID: MLC02T) has been proposed which contains higher Mn and lower C than the original 3Cr-3WVTa steel to expect maintaining high hardenability and reducing the as-normalized hardness, targeting a reduced property inhomogeneity across the weldment in as-welded (no PWHT) condition. The nominal compositions of the original and modified steels are summarized in Table 1. A new heat of Mod. 3Cr-3WVTa steel was produced through vacuum-induction-melted processed which was homogenized at 1200°C, followed by hot-rolling and normalization at 1100°C, and then applied tempering at 700°C. The creep-rupture performance and impact toughness evaluations across the weldments (with/without PWHT), as well as those of the base metal, were comprehensively conducted to date. Because of the improved impact toughness in the as-welded (and the as-normalized) condition combining with the better cross-weld creep performance than those of the original steel, the Mod. 3Cr-3WVTa steel is considered to have achieved the target characteristics of the improved mechanical performance without PWHT.

Table 1. Nominal composition of 3Cr-3WVTa base bainitic steels (balanced Fe)

Name	Alloy composition, wt.%	Remarks
MLC02T	3Cr-3W-0.2V-0.16Si-2.0Mn-0.1Ta-0.05C	Modified (newly proposed)
Original	3Cr-3W-0.2V-0.16Si-0.4Mn-0.1Ta-0.1C	Require PWHT, proposed in 1990's[1]

Now the project targets to comprehensively evaluate the mechanical properties of Mod. 3Cr-3WVTa steel without applying tempering process. The present material consisted of fully bainitic ferritic structure with the prior austenite grain size (PAGS) of 187 ± 7 μm, which was considered relatively coarse and might have negatively impacted on some mechanical properties such as tensile properties, impact toughness, etc. Because of this consideration, the PAG refinement has been attempted though lower-temperature normalization process. Figure 1 represents as-normalized microstructures of Mod. 3Cr-3WVTa steel with various heat-treatments, and Table 2 summarizes the measured PAGS as well as the planned (and

competed) property evaluation. By comparing with the Mod. 3Cr-3WVTa steel formerly processed and normalized at 1,100°C (1a), re-normalization at 1,000°C for 30 min (1b) resulted in refining the PAG with the size of 97 ± 5 μm, which was due to newly formed PAGs from bainitic ferrite in the heating process like recrystallization. A cyclic heat-treatment with re-normalization at 1,000°C for three times was also applied to expect additional PAG refinement, although the effect was limited (97 → 81 μm). This result suggests that a further grain refinement is not expected through cycle heat-treatment. On the other hand, the material newly processed and normalized at 1,000°C revealed further PAG refinement to 41 ± 6 μm. This significant reduction of PAGS was hypothetically due to the conditions of the material prior to the normalization: the hot-rolled material consisted of fine and complicated microstructure due to the deformation and phase transformation during cooling to room temperature, which assisted increasing the austenite grain nucleation frequency. The normalized materials with three different PAG are to be subjected to mechanical property evaluation to investigate the performance response the Mod. 3Cr-3WVTa steel from the PAG variation.

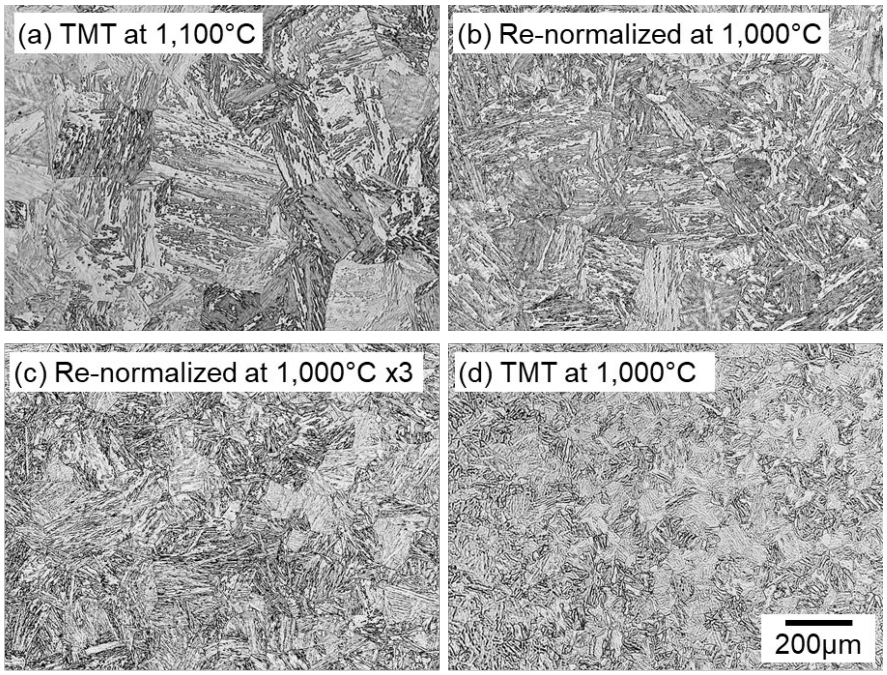

Figure 1. Optical micrographs of Mod. 3Cr-3WVTa steels after hot-rolling and normalization; (a) thermo-mechanically treated (TMT) at 1,100°C, (b) re-normalized at 1,000°C, and (c) newly processed at 1,000°C.

Table 2. Summary of applied processes, prior austenite grain size (PAGS), and planned/completed property evaluations of Mod. 3Cr-3WVTa steel to date

Thermomechanical process	PAGS, μm	Property evaluation	Remarks
(a): Hot-roll and normalization at 1,100°C for 30min	187 ± 7	Creep, Charpy (including weldment)	Mostly completed
(b): (a) + re-normalization at 1,000°C for 30min	97 ± 5	Long-term aging → Tensile, Charpy	In progress
(c): (a) + re-normalization at 1,000°C for 30min x3	81 ± 5	Creep, Charpy	In progress
(d): Hot-roll and normalization at 1,000°C for 30min	41 ± 6	Creep, Charpy (including weldment)	To be conducted

Creep-rupture performance evaluation of the Mod. 3Cr-3WVTa steel processed and normalized at 1,100°C + tempering at 700°C (N+T) has been mostly completed. Figure 2a represents Larson-Miller Parameter

plot of the base metal and the cross-weld specimens of the Mod. 3Cr-3WVTa steel tested at 500 and 550°C, together with those of the original 3Cr-3WVTa steel, showing better cross-weld creep-rupture performance of the Mod. 3Cr-3WVTa steel without PWHT than those of the original steel weldment with PWHT. Two creep-rupture tests are currently in progress, including the base metal at 550°C and 230MPa and the cross-weld specimen at 550°C and 170MPa (> 9,500h and > 11,000h, respectively, as of 1/31/2022). In addition to the N+T specimens, creep-rupture tests of the "re-normalized" samples ("as-normalized" and "normalized + tempered") at 550°C and 295MPa were also initiated to evaluate the effect of re-normalization and PAG refinement on creep-rupture performance. Figure 2b shows the comparison of creep-rupture curves of the N+T specimen (ruptured at 2,857h) with those of the re-normalized specimens tested for more than 4,000h (tests in progress). The re-normalized specimens exhibited significantly improved creep-deformation resistance with nearly 7 and 3 times smaller minimum creep rates in the as-normalized and normalized + tempered specimens, respectively, than that of the N+T specimen. The obtained results were opposite from the expectation when considered the refined PAG size in the re-normalized specimens, so that the improvement mechanism is not clear. The detailed microstructure characterization is planned to investigate the mechanism, after completing the creep-rupture testing.

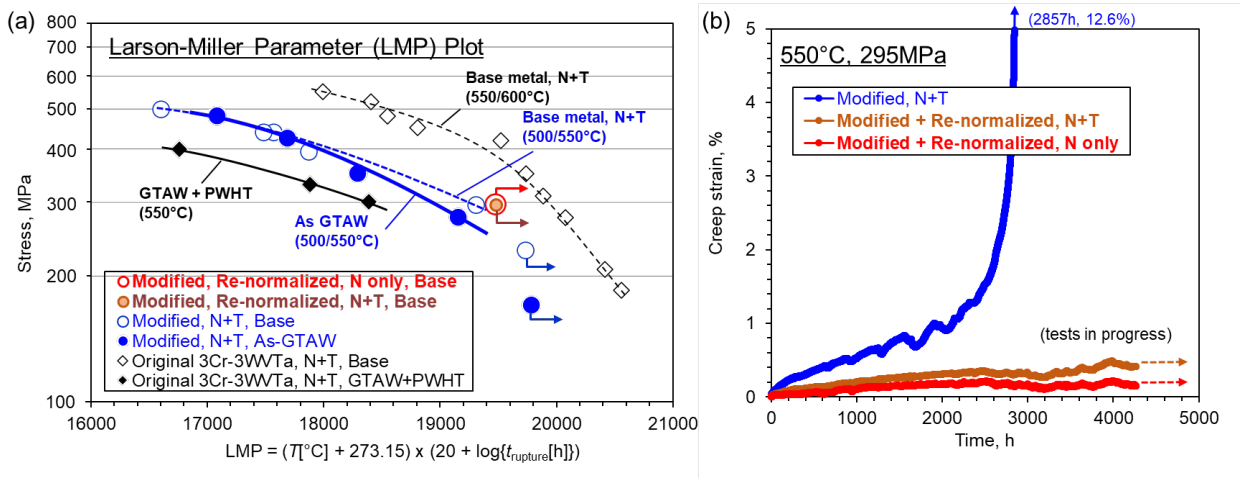

Figure 2. (a) Larson-Miller Parameter (LMP) plot of Mod. 3Cr-3WVTa steel base and weldments compared with those of the original steel, and (b) creep-rupture curves of Mod. 3Cr-3WVTa steel before and after re-normalization at 1,000°C.

Future Plans

In addition to on-going creep-rupture performance evaluation of the re-normalized specimens, three different property evaluations are scheduled: (1) a comprehensive creep-rupture performance evaluation of the Mod. 3Cr-3WVTa steel processed at 1,000°C, including both the base metal and the cross-weld specimen, (2) a measurement of the ductile-brittle transition temperature of the same material through Charpy impact toughness tests, and (3) tensile and impact toughness property evaluation of the re-normalized specimens after long-term aging at 500°C targeting up to 10,000h. For the first and second evaluation, the specimen machining is currently in progress. For the third evaluation, the aging has already been initiated in Dec. 2021.

References

[1] R.L. Klueh et al., Int. J. Pressure Vessels and Piping, 84 (2007) 29-36.

1.2 NANOPRECIPITATE STABILITY UNDER ELEVATED TEMPERATURE AND IRRADIATION IN A NOVEL ADDITIVELY MANUFACTURED STEEL—T.M.K. Green, K.G. Field (University of Michigan)

OBJECTIVE

This project aims to study the dynamic evolution of nanoprecipitates and helium present in an irradiated 9Cr steel that was fabricated via additive manufacturing (AM).

SUMMARY

A novel alloy designated as ANA2 (Additive-manufactured Nanostructured Alloy, Composition #2) was developed using computational thermodynamics to create an ultra-fine dispersion of MX precipitates through composition optimization for the laser blown powder AM process. As previously reported [1], unirradiated ANA2 contains two types of (V,Cr)N precipitates, (i) globular (V,Cr)N precipitates are located on grain boundaries with an average size and number density of 15.1±3.5nm and 6.1×10^{20} m^{-3} and (ii) fine platelet (V,Cr)N precipitates are located intragranular in the matrix with a size of 5.8±1.2 nm and a number density of 2.5×10^{22} m^{-3}. The platelets are normal to the {001} planes of the matrix. The (V,Cr)N platelets provide an estimated sink strength of 9×10^{14} m^{-2} [2]. These high-density precipitate populations then provide an ideal testbed to evaluate the role of helium on precipitate stability in high sink strength ferritic-martensitic steels not fabricated using more costly oxide dispersion strengthened (ODS)-based fabrication routes. To evaluate the role of helium under irradiation, ANA2 has been undergoing a systematic ion beam irradiation campaign that varies dose, dose rate, temperature, and helium implantation rate. Preliminary observations have been made as to the stability and evolution of the (V,Cr)N precipitates in the absence of helium to date.

PROGRESS AND STATUS

To study the separate effects of temperature and irradiation on the evolution of (V,Cr)N precipitates, two series of controlled single ion beam irradiation experiments were performed for a total of five irradiations (Table 1). The temperature series (irradiations 1.1A, 1.1B, and 1.1C) achieved a nominal damage of 50 dpa with a dose rate of 10^{-4} dpa/s at three different irradiation temperatures (400, 500, and 300°C). The dose rate series (irradiations 1.2A and 1.2B) achieved a nominal damage of 50 dpa with an irradiation temperature of 400°C at two different dose rates (10^{-3} and 5×10^{-4} dpa/s). Preliminary analysis is shown for irradiations 1.1A and 1.1B.

Table 1. Irradiation parameters for the completed temperature and dose rate series

Parameters	Temperature Series			Dose Rate Series	
	Irradiation 1.1A	**Irradiation 1.1B**	**Irradiation 1.1C**	**Irradiation 1.2A**	**Irradiation 1.2B**
Ions	9 MeV Fe^{3+}	9 MeV Fe^{3+}	9 MeV Fe^{3+}	9 MeV Fe^{3+}	9 MeV Fe^{3+}
Total displacements per atom (dpa)	50	50	50	50	50
Dose rate (dpa/s)	10^{-4}	10^{-4}	10^{-4}	10^{-3}	5×10^{-4}
Temperature (°C)	400	500	300	400	400

STEM images of ANA2 after irradiation 1.1A (400°C, 50dpa, 10^{-4} dpa/s) and irradiation 1.1B (500°C, 50dpa, 10^{-4} dpa/s) with corresponding chemical composition maps taken with electron energy dispersive

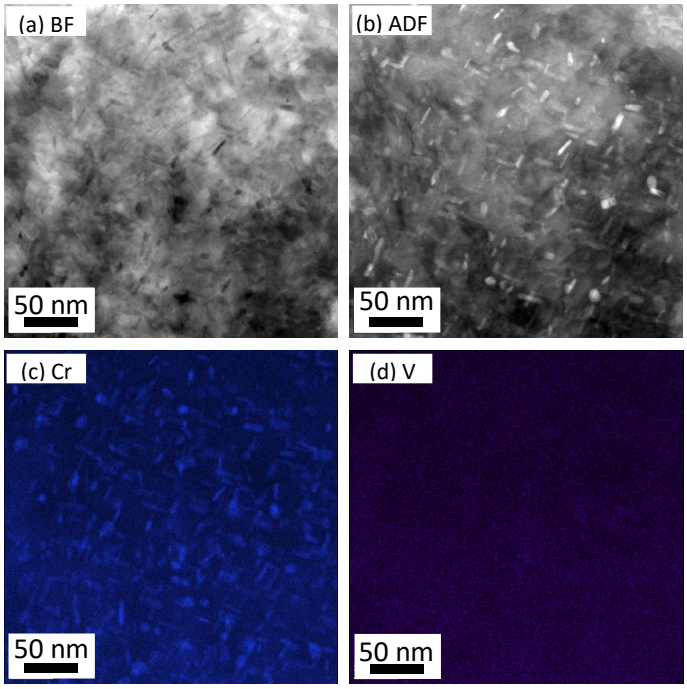

Figure 1. (a) STEM BF, (b) STEM annular dark field (ADF), (c) elemental map of Cr, and an (d) elemental map of V taken from a depth taken at a depth of 1100-1300 nm after irradiation at 400°C

spectroscopy (EDS) are shown in Figures 1 and 2, respectively. Platelet MX precipitates with similar morphology as those observed in the unirradiated specimens are present after irradiation at 400°C but are no longer enriched in V. After irradiation at 500°C the original (V,Cr)N precipitates completely dissolved, but small globular precipitates and large (e.g., >10-20 nm) elongated precipitates enriched in Ta and W are observed throughout the damage profile. No cavities were found in either condition. This initial results suggest that even in the absence of helium under irradiation, that the (V,Cr)N precipitates are unstable with their overall response being sensitive to the irradiation temperature, most likely due to the balance between back diffusion and ballistic dissolution of Cr and V atoms under irradiation. On-going work includes evaluating the precipitate response from irradiations 1.1C and 1.2A&B to better define the overall temperature response and evaluate the dose rate response. These irradiations will then provide the foundational understanding on the role of back diffusion and ballistic dissolution of the (V,Cr)N precipitates before introducing additional complexities through dual-beam irradiations that will introduce helium under irradiation.

Future Work

It is hypothesized that irradiation at 400°C induced the back diffusion of V into the matrix from the original (V,Cr)N precipitates whereas irradiation at 500°C induced the complete dissolution of the (V,Cr)N precipitates in ANA2 at the nominal dose. Irradiation and temperature at 500°C both played roles in the formation of new precipitates containing Ta, W, Ni, and Si.

Work is ongoing to optimize sample preparation to create TEM lamellae free from FIB-induced damage. Once the process is complete, further analysis of all five completed irradiated ANA2 conditions will be

accomplished, including STEM-EDS mapping, high resolution TEM, and through-focus TEM cavity analysis. The interplay of the MX precipitates and helium will be studied with dual beam irradiations.

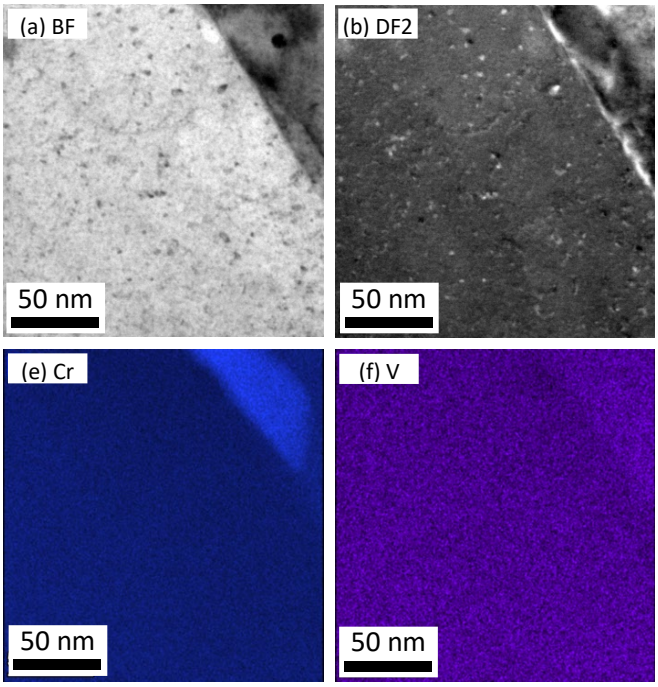

Figure 2. (a) STEM BF, (b) STEM dark field (DF2), (c) elemental map of Cr, and an (d) elemental map of V taken at a depth of 1,100-1,300 nm after irradiation at 500°C.

Acknowledgements

Research and development efforts associated with synthesis of ANA2 using additive manufacturing was supported by the Laboratory Directed Research and Development Program of Oak Ridge National Laboratory (ORNL) and the U.S. Department of Energy (DOE), Office of Nuclear Energy (NE), Advanced Fuels Campaign, under Contract No. DE-AC05-00OR22725 with UT-Battelle, LLC. Samples from these efforts were procured, irradiated, and characterized as part of an FES sponsored Early Career Award (DE-SC0021138).

References

[1] Parish, Chad, Kato, Yutai, and Melton, Stephanie. 2021. "Fusion Materials Semiannual Progress Report for the Period Ending December 31, 2020". United States. https://doi.org/10.2172/1783295. https://www.osti.gov/servlets/purl/1783295.

[2] W. Zhong, N. Sridharan, D. Isheim, K.G. Field, Y. Yang, K. Terrani, L. Tan, Microstructures and mechanical properties of a modified 9Cr ferritic-martensitic steel in the as-built condition after additive manufacturing, Journal of Nuclear Materials. 545 (2021). https://doi.org/10.1016/j.jnucmat.2020.152742.

1.3 MICROHARDNESS MEASUREMENT UPDATES FOR SELECTED SSJ3 SPECIMENS IN F8B1/2, F11B3, RB15J, AND RB19J CAPSULES—X. Chen, J. Reed, C. On, J.W. Geringer, Y. Katoh (Oak Ridge National Laboratory)

The extended abstract presents updates of hot cell microhardness measurements on selected SSJ3 tensile specimens in F8B1/2, F11B3, RB15J, and RB19J capsules

Vickers microhardness measurements were performed on selected SSJ3 tensile specimens in F8B1/2, F11B3, RB15J, and RB19J capsules. Measurements were made on the left and right tab regions of each tensile specimen (Figure 1). The hardness tester used was Mitutoyo HV-120B located in cell #4 of the irradiated materials examination and testing facility at Oak Ridge National Laboratory. All tests were performed with 1 kg force and 15 sec dwell time. For each measurement result, the indentation image was checked to make sure the indentation is of sufficient quality for the hardness measurements. The measurement results are summarized in Table 1. Except for specimens A2 and 094, all other specimens showed reasonably small standard deviation in hardness measurements (≤5% of the average hardness values), meaning that the irradiation temperatures probably were uniform for those specimens.

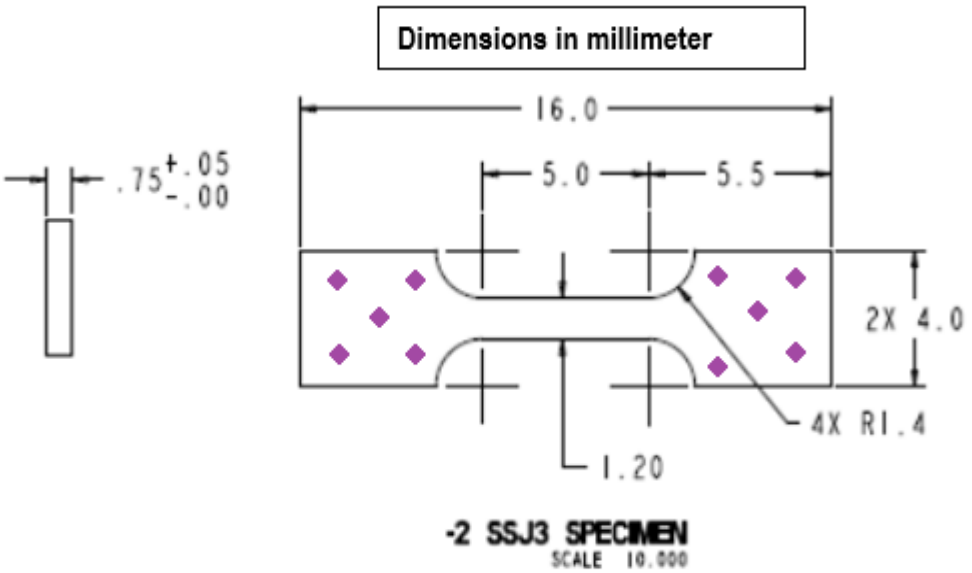

Figure 1. Schematic for indentation made on SSJ3 tensile specimens.

Table 1. Summary of microhardness measurement results for selected SSJ3 tensile specimens in F8B1/2, F11B3, RB15J, and RB19J

Capsule ID	Specimen ID	Hardness measurements (HV)										Avg. HV	Std. Dev. HV
		Left tab					Right tab						
		1	2	3	4	5	1	2	3	4	5		
F8B1/2	A2	243.6	259.0	254.2	253.7	304.7	317.6	314.3	303.5	319.6	337.0	290.7	34.2
F11B3	091	351.2	331.2	420.9	366.3	358.2	365.4	378.9	455.2	386.8	427.0	384.1	38.7
	092	345.1	351.2	361.4	370.4	385.0	355.0	346.6	354.3	367.1	382.3	361.8	14.1
	093	443.0	389.4	390.3	364.6	405.2	377.2	386.8	391.3	375.4	392.2	391.5	21.2
	094	336.2	372.1	373.7	387.7	366.3	401.4	394.9	410.0	379.7	389.4	381.1	20.9
	191	372.1	396.7	390.3	409.0	390.3	398.6	396.7	434.4	404.2	398.6	399.1	15.9
	192	372.1	359.8	359.8	378.9	359.8	367.1	377.2	396.7	359.8	356.6	368.8	12.6
	193	376.3	359.0	364.6	349.6	335.5	345.8	355.8	391.3	369.6	342.1	359.0	17.0
	194	335.5	360.6	357.4	346.6	354.3	355.0	347.3	355.0	390.3	345.8	354.8	14.4
	2791	451.8	459.8	410.0	418.9	378.9	404.2	403.3	422.9	439.7	439.7	422.9	25.0
	2792	475.2	478.8	491.3	445.2	466.8	439.7	413.9	417.9	469.2	432.3	453.0	26.9
	2793	414.9	376.3	399.5	422.9	425.0	406.2	403.3	429.1	424.0	401.4	410.3	16.2
	2794	359.8	355.0	367.9	377.2	363.8	351.9	344.3	374.6	373.7	367.1	363.5	10.7
RB15J	OVAh	289.7	274.8	269.5	281.3	288.6	278.0	290.3	288.0	284.6	296.2	284.1	8.1
	OVAp	300.4	281.3	283.5	284.6	295.6	289.7	293.2	284.6	288.6	284.1	288.6	6.2
	OWAa	284.1	284.1	281.3	283.5	293.2	281.8	278.0	276.9	282.4	289.7	283.5	4.9
	OWAf	281.8	289.2	289.2	289.2	290.3	290.3	291.5	282.9	286.3	296.2	288.7	4.2
RB19J	SV6E	286.3	293.2	284.1	285.2	254.6	280.2	287.4	293.8	285.7	287.4	283.8	11.0
	SV6F	249.0	264.9	277.5	266.9	270.6	286.3	271.1	282.4	291.5	254.2	271.4	13.5
	SV6G	267.5	240.1	255.1	237.0	245.4	280.2	265.9	274.2	248.1	265.4	257.9	14.9
	TV66	300.4	298.6	301.0	306.0	309.1	298.6	298.6	307.2	307.9	306.0	303.3	4.3
	TV67	292.1	298.0	293.2	298.6	298.6	295.6	300.4	293.2	296.2	301.0	296.7	3.1
	TV68	289.2	309.1	298.0	310.4	298.0	302.3	292.7	296.8	296.2	304.7	299.7	6.8

1.4 DEUTERIUM RETENTION COMPARISON FOR HIGH AND LOW CARBON FUSION BLANKET STRUCTURAL MATERIALS—W. Zhong, L. Tan, Y. Katoh (Oak Ridge National Laboratory)

OBJECTIVE

The objective of this work is to investigate the carbon effects on the thermal retention and desorption properties in ferritic martensitic steels. The carbon composition plays a significant role in precipitation behaviors in FM steels, and these precipitates serve trapping sites for hydrogen, and alter hydrogen retention properties. In this work, two castable nanostructured alloys (CNAs) that have different carbon compositions were selected and compared for their hydrogen retention and desorption properties.

SUMMARY

Two representative CNAs that have different carbon compositions were selected for investigating the carbon effects on the hydrogen retention and desorption properties; they are high carbon content alloy CNA8 (Fe-8.7Cr-1.0W-0.5Mn-0.14Si-0.09Ta-0.14Ti-0.05V-0.1C) and low carbon content alloy CNA9 (Fe-8.7Cr-1.0W-0.5Mn-0.14Si-0.09Ta-0.14Ti-0.05V-0.05C). These two alloys have similar grain structures but different precipitates. These two alloys were exposed to 1 atmosphere deuterium gas at 450℃, followed by the thermal desorption and in-situ deuterium flux measurement up to 900℃ with the heating ramping rate of 0.5℃/s. CNA8 and CNA9 have similar desorption peaks. CNA8 shows slightly higher retention than CNA9, and both alloys have comparable retention to other CNAs alloys.

PROGRESS AND STATUS

Electron backscatter diffraction (EBSD) was performed on CNA8 and CNA9, and they show similar tempered – martensite grain structures as shown in the Figure 1. Due to the different carbon composition, the precipitates are different in two alloys. Scanning electron microscopy, transmission electron microscopy and energy dispersive spectroscopy were used to investigate the precipitates. Both $Cr_{23}C_6$ and MC (M=Ti and Ta primarily) precipitates were observed in CNA8, as shown in Figure 2a/b. $Cr_{23}C_6$ precipitates (marked with blue arrows) have elongated morphology with higher number density, and the MC precipitates (marked with yellow arrows) have spherical morphology. In comparison, only spherical MC precipitates were observed in CNA9.

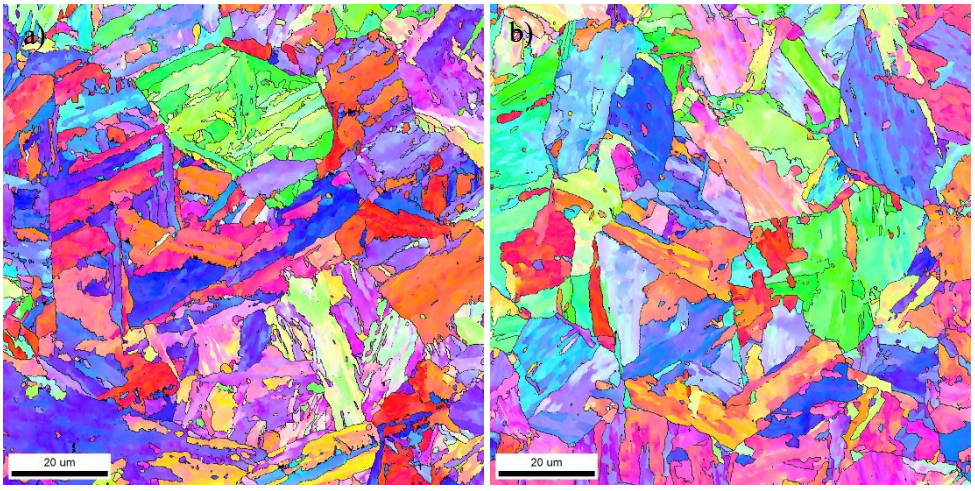

Figure 1. Inverse pole figure of a) CNA8 and b) CNA9, showing the similar grain structure of the two alloys.

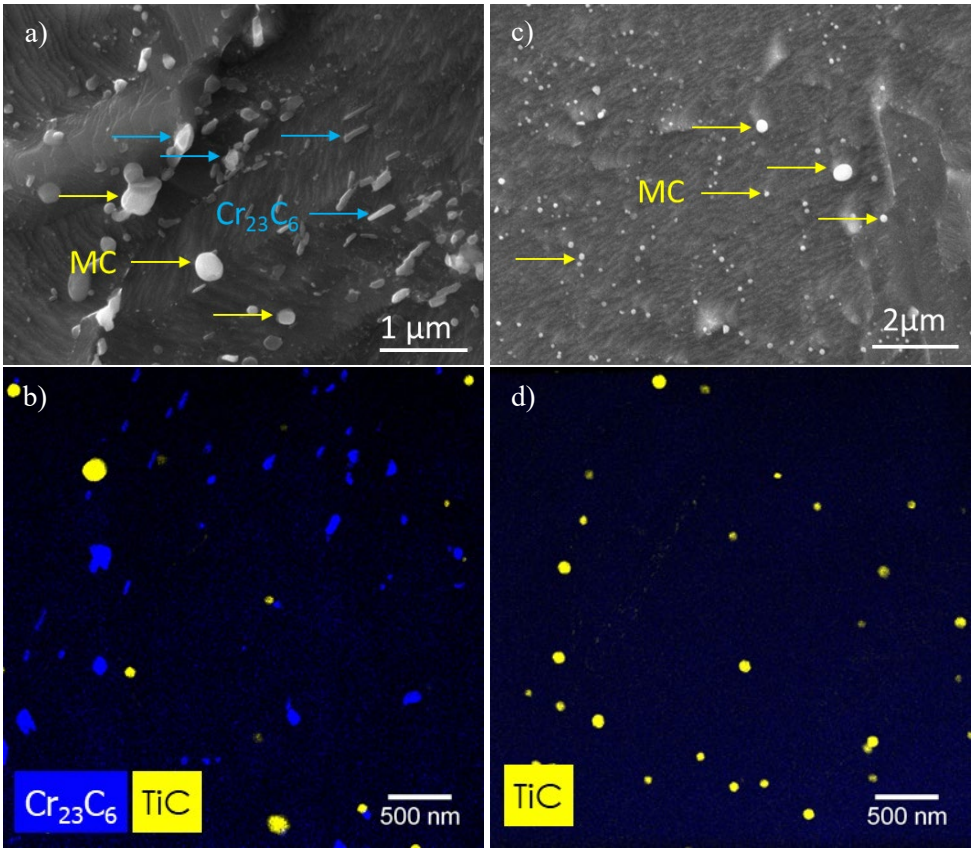

Figure 2. Precipitates distribution in a,b) CNA8 and c,d) CNA9. Both $Cr_{23}C_6$ and MC precipitates were observed in CNA8, while only MC precipitates were observed in CNA9.

The thermal desorption measurement was performed after the exposure to deuterium gas. Figure 3 shows the desorption rate as a function of temperature. CNA8 and CNA9 show similar desorption peaks, indicating similar hydrogen trapping strength in both alloys. The total retention in both alloys is also comparable to other CNAs in Ref. [1].

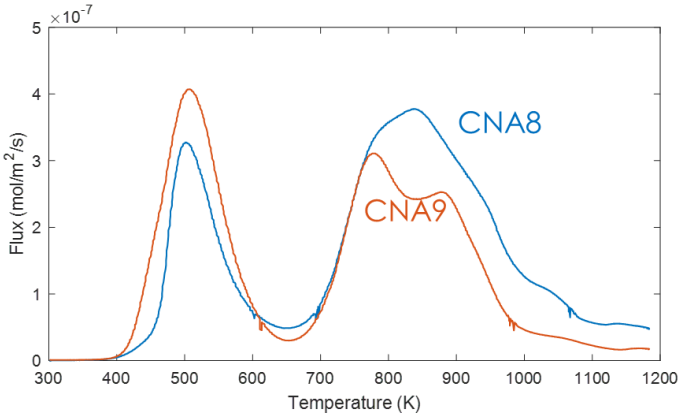

Figure 3. Thermal desorption as a function of temperature in CNA8 and CNA9.

Future Work

Irradiation effects on the thermal retention and desorption properties of representative fusion blanket structural materials are to be investigated.

References

[1] Chen, Ze, Xunxiang Hu, Minyou Ye, and Brian D. Wirth. "Deuterium transport and retention properties of representative fusion blanket structural materials." Journal of Nuclear Materials 549 (2021): 152904.

2. ODS AND NANOCOMPOSITED ALLOY DEVELOPMENT

2.1 ODS FeCrAl PRODUCTION USING ADDITIVE MANUFACTURING WITH IN SITU OXIDATION—T. Austin, S. J. Zinkle (University of Tennessee), N. Sridharan (Lincoln Electric)

OBJECTIVE

The objective of this task is to investigate the feasibility of producing oxide dispersion strengthened (ODS) ferritic steel alloy parts using laser-based directed energy deposition (DED) additive manufacturing (AM) in an oxygen-rich environment as an alternative to the conventional mechanical alloying and powder metallurgy manufacturing processes. This reduces the fabrication difficulty of these high-performance parts while allowing for increasingly geometrically complex ODS alloy components to be produced.

SUMMARY

The Fe – 12Cr – 6Al – 2Mo – 0.18Y (wt%) alloy powder was consolidated using a DED AM process in an oxygen-rich environment using varied build parameters. Using DED AM would allow for the production of ODS steel without extensive mechanical alloying (MA), hot isostatic pressing (HIPing), and metalworking. The specimens were characterized using optical microscopy, scanning electron microscopy (SEM), transmission electron microscopy (TEM), atom probe tomography (APT), inductively coupled plasma optical emission spectroscopy (ICP-OES), combustion analysis via inert gas fusion (IGF), and microhardness testing. These characterization processes allowed for the microstructure, chemical composition, and physical properties of each sample to be examined. The results indicate that nanoscale precipitation was achieved using *in situ* oxidation during fabrication. Further analysis of the specimens suggested that precipitation may not have been completed during the AM process. Specimens with the largest oxygen retention from manufacturing underwent a heat-treatment (HT, all HT specimens have undergone the same HT and carry a '_HT' at the end of the specimen name) and were further characterized using TEM and APT. An appreciable amount of precipitation was present and comparable to conventional alloys.

PROGRESS AND STATUS

The 20 mm x 20 mm x 20-30 mm (height) specimen cubes were built using a pneumatically conveyed powder, DED AM system built by DM3D Technology with gas atomized metal powder (Fe – 12Cr – 6Al – 2Mo – 0.18Y wt%) provided by ATI Powder Metals in an oxygen rich environment. Oxygen was provided during powder consolidation by maintaining the build chamber under ambient air conditions or by adding oxygen into the welding gas streams. Figure 1 shows a schematic of both experimental setups. Further discussion of the varied operating parameters and is discussed in previous reports [1-3].

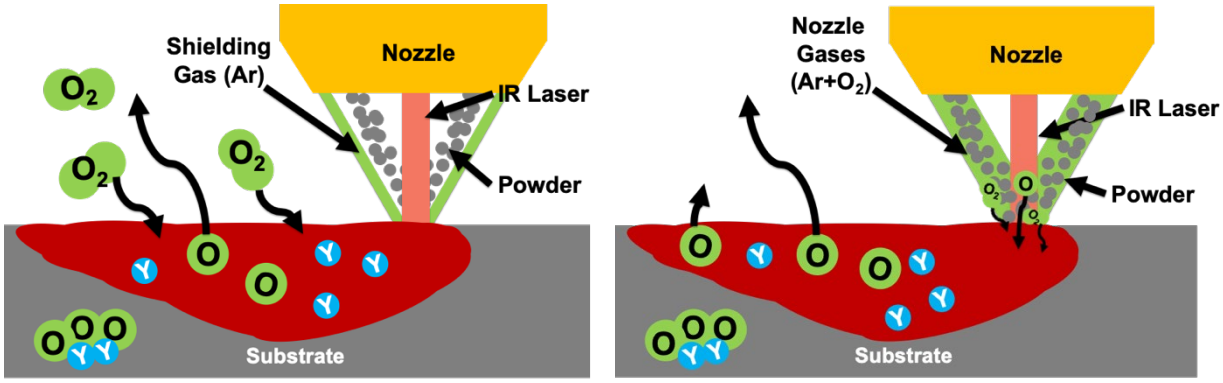

Figure 1. Schematic of DED AM process using *in situ* oxidation: consolidation under air (left), and under Ar with Ar-O_2 blended gas stream (right).

The TEM samples were prepared from each specimen using conventional focused ion beam (FIB) lift-out techniques [5] and delivered to Oak Ridge National Laboratory's (ORNL's) Center for Nanophase Materials Sciences (CNMS) for more thorough characterization. Under CNMS Proposal #2021-A-00697, samples from each specimen were examined using TEM (shown in Figure 2 below). These experiments showed that sporadic precipitation was present across the range of operating parameters. Surprisingly, the specimens that showed precipitation were not necessarily those that had the best oxygen retention during fabrication (see composition results for all specimens in the most recent previous report) [3]. Ar_10O_2_5 and Ar10O_2_1 had oxygen concentrations of 0.0254 wt% and 0.0075 wt%, respectively. Meanwhile, the specimen with the most oxygen retained had 0.0670 wt% (Ar_10O_2_4), roughly half of conventionally fabricated alloys [4].

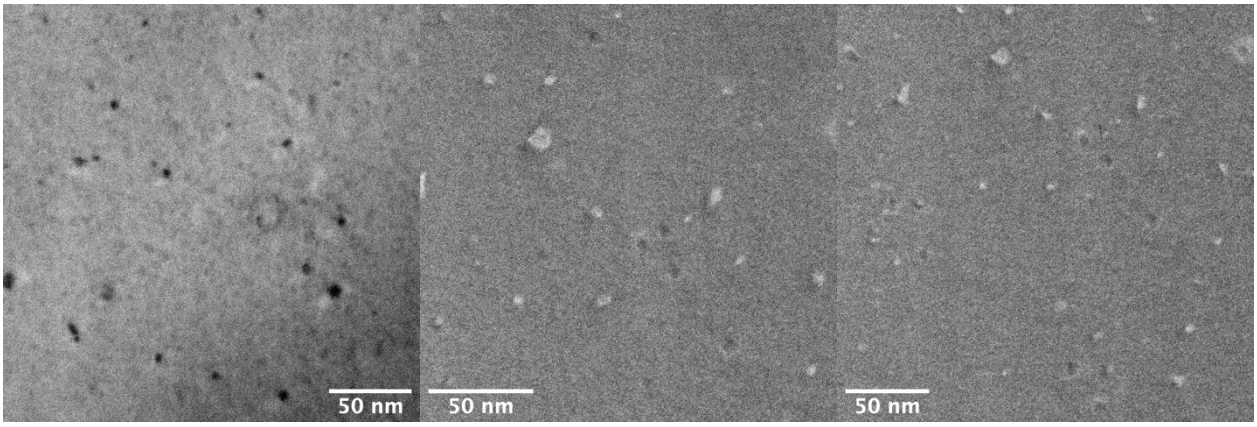

Figure 2. BF and HAADF TEM images of nanoscale precipitation in Ar10O_2_5 (left) and Ar10O_2_1 (right), respectively.

Further, the agglomeration present in select specimens appeared to be less than that required to consume all the oxygen available from the compositional analysis. To examine if precipitation was incomplete, samples from specimens with the largest amount of oxygen retained during manufacturing were sectioned and a HT was applied. The precipitation literature for ODS-FeCrAl suggests that precipitation could complete in as little as 15 minutes at 200°C [4]. To ensure complete precipitation we settled on a one-hour HT at 600°C. After HT, new TEM lamellae were prepared and examined for comparison with their non-HT'd counterparts. A significant improvement in the uniformity of precipitation was apparent and is shown in Figure 3 below. Precipitation went from a sporadic dispersion with local densities on the order of 4.5e21

per cubic meter to a more uniform dispersion with a density on the order of 1e22 per cubic meter. Meanwhile, the average diameter remained small (6.5 nm v. 6.2 nm, respectively) as desired.

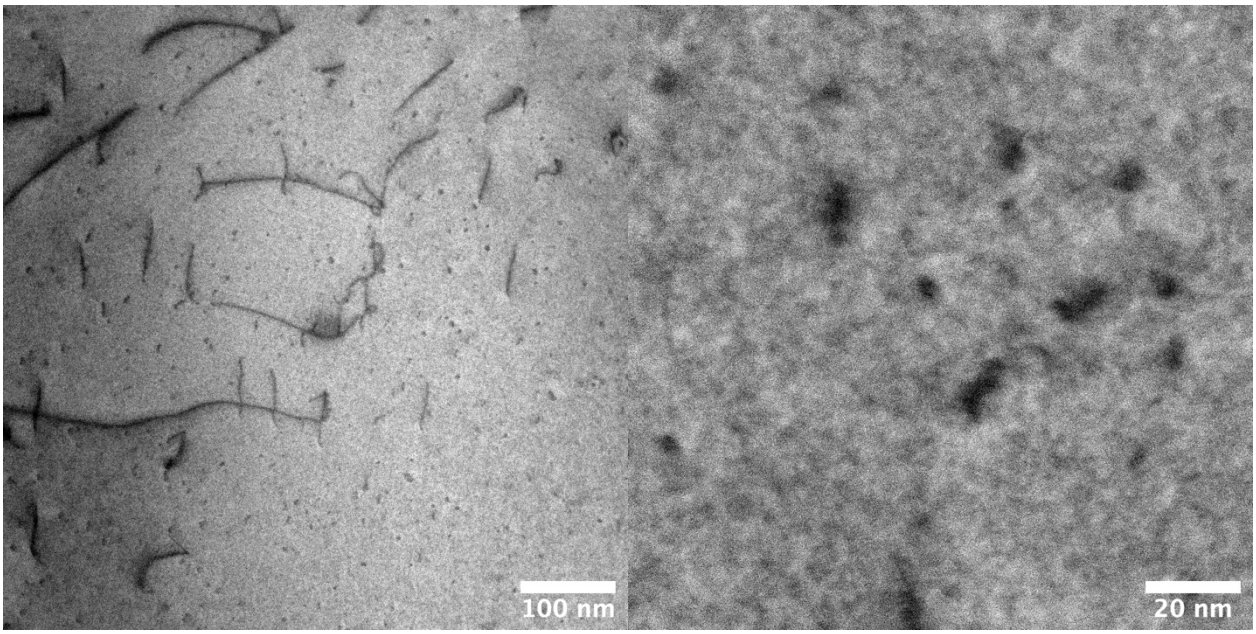

Figure 3. BF images of Ar10O_2_3 with increased precipitation post-HT.

To further examine the kinds of precipitates present within the AM produced specimens, APT lift-out needles were prepared, also at CNMS. Due to the moderate density of precipitates, finding precipitates in APT samples was difficult. One of the found precipitates is pictured below. Unexpectedly, there was a significant increase in phosphorus present near the precipitate. The as-received powder did not contain appreciable amounts of phosphorus. However, the substrate used to build the specimens contained phosphorus as shown in Table 1 below. Considering the diffusivity of phosphorus in BCC steel and the propensity of phosphorus to diffuse to interfaces, the segregation of phosphorus at the yttrium rich oxide clusters is understandable [6, 7]. During the HT phosphorus would have sufficient mobility to diffuse approximately 130 nm while the precipitates are only 30 nm apart on average. Further experimentation will utilize additional care when choosing substrates.

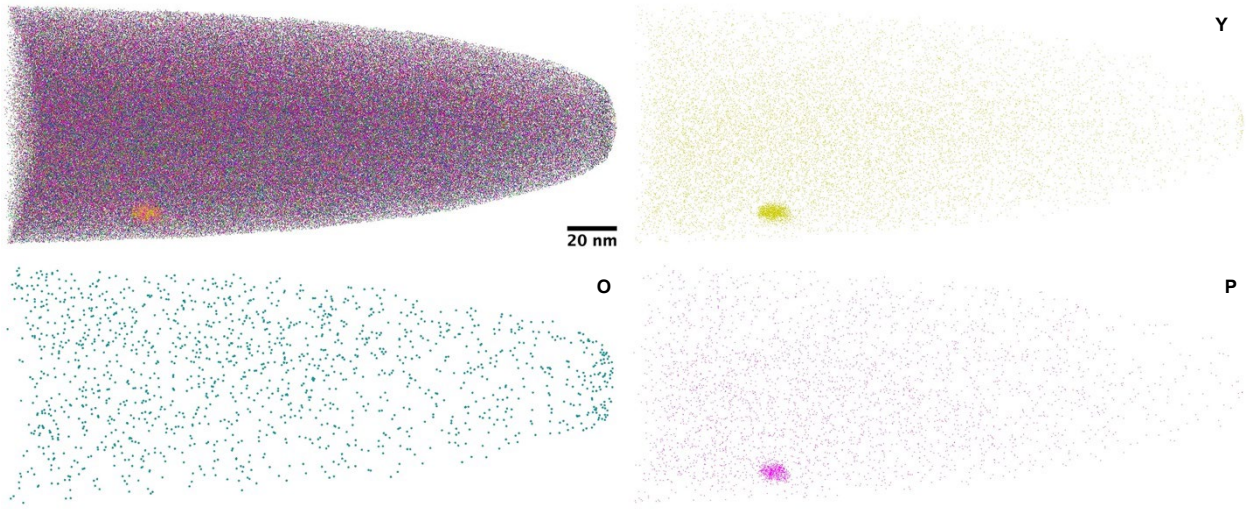

Figure 4. APT needle of Ar10O2_3 showing a nanoscale yttrium-rich precipitate surrounded by a phosphorus shell.

Table 1. Chemical Analysis of As-Received Powder and Build Substrate

	Sample	As-Received Powder	Substrate
Constituent [wt%]	Al	6.09	0.03
	Cr	12.14	2.24
	Fe	79.57	95.66
	Mo	2	0.89
	Y	0.18	<0.01
	C	0.003	0.12
	O	0.0107	0.0012
	N	0.0004	0.0097
	P	--	0.01
	Si	--	0.21
	Cu	--	0.15
	Mn	--	0.51
	Nb	--	0.01
	Ni	--	0.12
	Co	--	0.01
	Sn	--	0.01
	S	--	0.008

Finally, microhardness measurements were performed on each specimen. These results were compared with the literature for non-ODS FeCrAl to evaluate the improvement in the material properties of ODS FeCrAl produced using DED AM with *in situ* oxidation. The results can be seen in Figure 5 below. On average, the hardness of the specimens created in this study ranged from 220 to 235 Vickers hardness. Non-ODS FeCrAl generally has a hardness value ranging from 170 to 200 Vickers hardness [8]. Therefore, a noticeable improvement in the hardness was achieved in the AM ODS FeCrAl samples compared to the literature values for non-ODS FeCrAl. Some of the variability in the hardness values of our specimens can be attributed to the cracking phenomenon and pores discussed in previous reports [1, 2].

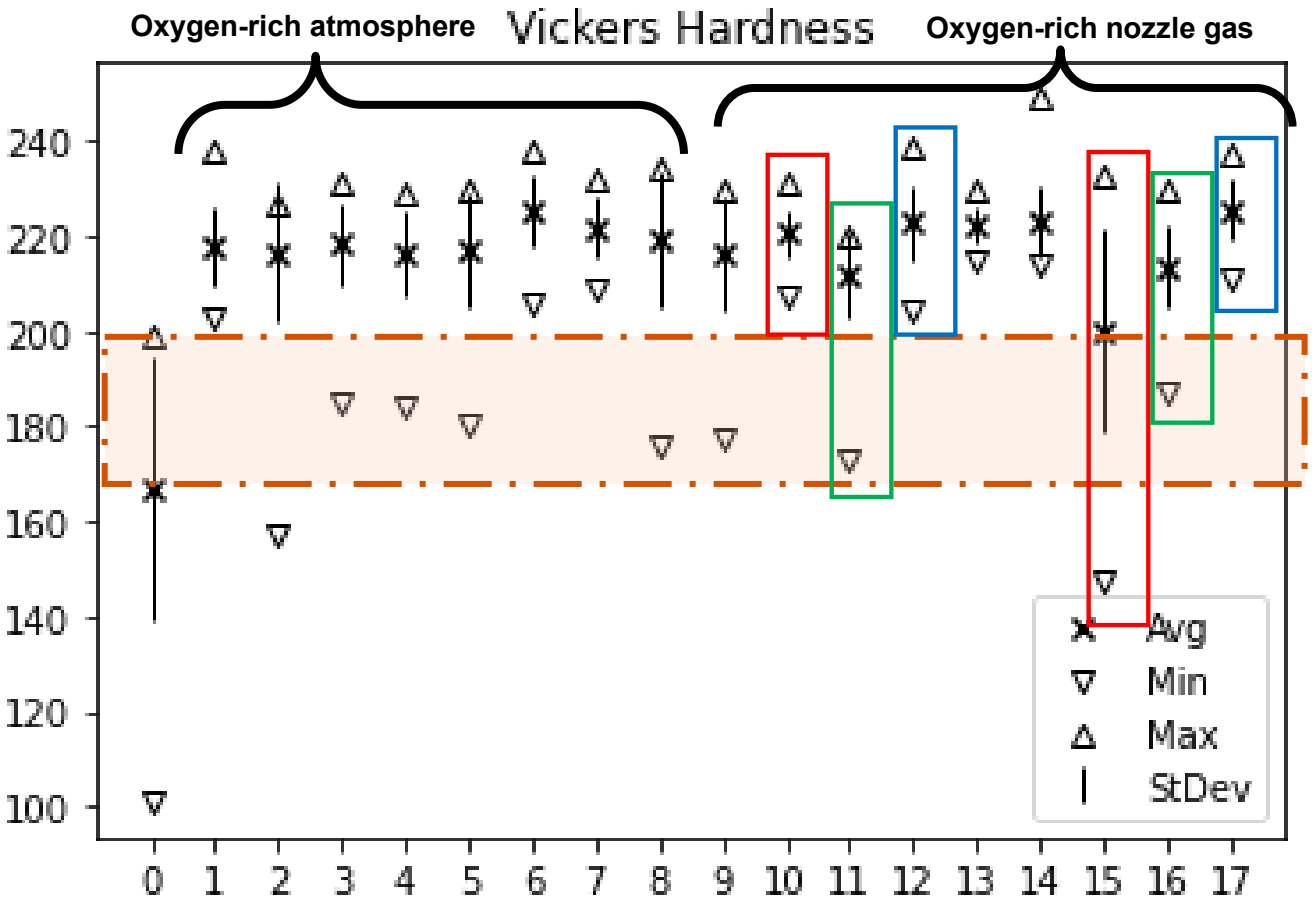

Figure 5. Hardness measurements of the as-built and post-HT'd specimens (outlined in red, green and blue) compared to non-ODS FeCrAl (outlined in orange) [8].

0 = As Received Powder

1 = 350WP

2 = 350WC

3 = 400WP

4 = 400WC

5 = 350WPHT

6 = 350WCHT

7 = 400WPHT

8 = 400WCHT

9 = Ar10O2_1

10 = Ar10O2_2

11 = Ar10O2_3

12 = Ar10O2_4

13 = Ar10O2_5

14 = Ar10O2_6

15 = Ar10O2_2_HT

16 = Ar10O2_3_HT

17 = Ar10O2_4_HT

Future Plans

In the next round of experimentation, a focus will be made on further improving the build quality of the specimens by additional refinement of the operating parameters [2]. Additionally, potential changes to the alloy composition will be evaluated to further refine the precipitate size and reduce the amount of agglomeration shown in previous reports [1,3]. Lastly, thorough mechanical testing in addition to the characterization techniques mentioned above will be performed on the new samples to give a more comprehensive comparison between the new samples and previous builds.

Acknowledgements

We thank Brian Jordan and Dennis Brown for their assistance in planning/performing modifications to the AM system and completing production of the specimens characterized above. A portion of this research was conducted at the Center for Nanophase Materials Sciences, which is a DOE Office of Science User Facility. We thank Ray Unocic, Jonathan Poplawsky, and James Burns for their assistance with the work performed at ORNL's Center for Nanophase Materials Sciences.

References

[1] T. Austin, S.J. Zinkle, N. Sridharan. "ODS FeCrAl Production Using Additive Manufacturing with *In Situ* Oxidation", Fusion Materials Semiannual Progress Report for period ending June 30, 2019, DOE/ER-0313/66 (2019), p. 133-139.

[2] T. Austin, S.J. Zinkle, N. Sridharan. "ODS FeCrAl Production Using Additive Manufacturing with *In Situ* Oxidation", Fusion Materials Semiannual Progress Report for period ending Dec. 31, 2019, DOE/ER-0313/67 (2019), p. 109-114.

[3] T. Austin, S.J. Zinkle, N. Sridharan. "ODS FeCrAl Production Using Additive Manufacturing with *In Situ* Oxidation", Fusion Materials Semiannual Progress Report for period ending Dec. 31, 2020, DOE/ER-0313/69 (2020), p. 163-169.

[4] C.P. Massey, S.N. Dryepondt, P.D. Edmondson, M.G. Frith, K.C. Littrell, A. Kini, B. Gault, K.A. Terrani, S.J. Zinkle, "Multiscale investigations of nanoprecipitate nucleation, growth, and coarsening in annealed low-Cr oxide dispersion strengthened FeCrAl powder.", Acta Materialia, 166 (2019), p. 1-17.

[5] M.K. Miller, K.F. Russell, "Atom probe specimen preparation with a dual beam SEM/FIB miller.", 107(9) (2007) 761-766.

[6] M. Militzer, J. Wieting, "Comments on the grain boundary segregation and diffusion of phosphorus in a 12%CrMoV-steel.", Scripta Metallurgica et Materialia, 28 (1993), p. 1043-1046.

[7] J.A. Hudson, S.G. Druce, G. Gage, M. Wall. "Thermal Ageing Effects in Structural Steels.", Theoretical and Applied Fracture Mechanics, 10 (1988), p. 123-133.

[8] K.G. Field, M.A. Snead, Y. Yamamoto, K.A. Terrani., "Handbook on the Material properties of FeCrAl Alloys for Nuclear Power Production Applications.", ORNL/SPR-2018/905 Rev. 1. (2018).

2.2 PRELIMINARY PROGRESS IN COLD SPRAY OF GARS ODS STEEL POWDER ON A FERRITIC MARTENSITIC STEEL SUBSTRATE—D. Zhang, K. A. Ross, J. T. Darsell, L. Li, D. J. Edwards, W. Setyawan (Pacific Northwest National Laboratory)

OBJECTIVE

The objective of this work is to explore an alternative route of fabricating an oxide dispersion strengthened (ODS) steel plate, including the potential of plating such an ODS plate onto a substrate of reduced activation ferritic martensitic (RAFM) steel. As a first-round trial, cold spray was used to successfully deposit ODS steel powder onto ferritic martensitic steel (P92) plate coupons. A larger-size plate will be deposited and undergoes a subsequent thermo-mechanical processing to further improve the interface quality and characteristics of dispersed oxide particles.

SUMMARY

Cold spray was used to successfully deposit ODS steel powder onto ferritic martensitic steel (P92) plate coupons. The feedstock ODS steel powder was provided by collaborators at Ames Laboratory, made with their unique gas atomization reaction synthesis (GARS). The GARS ODS steel powder had the nominal composition of 14YWT (14Cr-0.4Ti-3W-0.35Y-0.1O, wt.%). Meanwhile the powder (mainly spherical) was not ball milled, hence it can be cold sprayed. P92 steel plate was used as a surrogate for RAFM steel, having a nominal composition of 9Cr-2W-0.5Si-0.5Mn-0.4Mo-0.3Ni-0.2V-0.1C, wt.%. A state-of-the-art cold spray system was used with helium carrier gas and robust processing parameters to ensure good deposition quality.

PROGRESS AND STATUS

Introduction

The conventional fabrication route [1] of ODS steel plate involves production of powder by gas atomization, ball milling, powder vacuum canning, hot isostatic pressing, hot cross rolling, cold rolling, with annealing steps often required in-between rolling steps. This route is time consuming, expensive, hard to scale up, and extremely delicate as cracks can develop and the plate can “bend out of shape” during the laborious rolling process. Based on the realistic consideration that conventional route is not capable of producing tons of ODS steel for fusion energy application, some researchers [1] proposed to “plate” a mm-level thickness of ODS steel onto RAFM steel, with the idea that the ODS steel plating would be a critical top layer to handle expected extreme temperature and radiation dose in a fusion environment. This means that on top of the laborious plate fabrication process, additional bonding step (e.g., diffusion bonding) is required to make ODS steel plating. Therefore, it would be highly desirable to directly deposit an ODS steel layer onto a RAFM steel without the abovementioned laborious steps. Unfortunately, melt-based additive methods won’t be suitable as dispersed particles tend to agglomerate in molten metals. Cold spray is a solid-state based method that could offer a potential solution. Yet effective cold spray would require the feedstock powder to be mainly spherical for aerodynamic purposes. Namely, the flaky ball milled ODS steel powder won’t work well with cold spray.

The GARS method produces spherical precursor ODS steel powder with an outer shell of Cr-rich oxide, whereas the nano-oxide forming species, i.e., Y and Ti, are at the powder interior in the form of Fe-intermetallics. Upon heating and consolidation (e.g. hot isostatic pressing), oxygen atoms diffuse into the powder interior to react with Y/Ti, forming Y-Ti-O nano-oxides [2]. Therefore, GARS ODS steel powder offers the geometrical (i.e., spherical) and compositional (i.e., Y/Ti/O species all contained in the powder) requirements for cold spray deposition.

Experimental Procedure

Figure 1(a) shows a cross-section overview in scanning electron microscope (SEM) of the GARS ODS steel powder provided by Ames Laboratory. The powder size ranges between 45 μm and 108 μm. Figure 1(b) is a medium magnification SEM image of several powder particles, showing the grain substructure inside. Figure 1(c) is a high magnification image inside one powder particle, showing bright spots mainly decorating the grain boundaries. Energy dispersive X-ray spectroscopy (EDS) mapping in Figure 1(d) reveals that these bright spots correspond to Y signals, namely these are Fe-Y intermetallic particles.

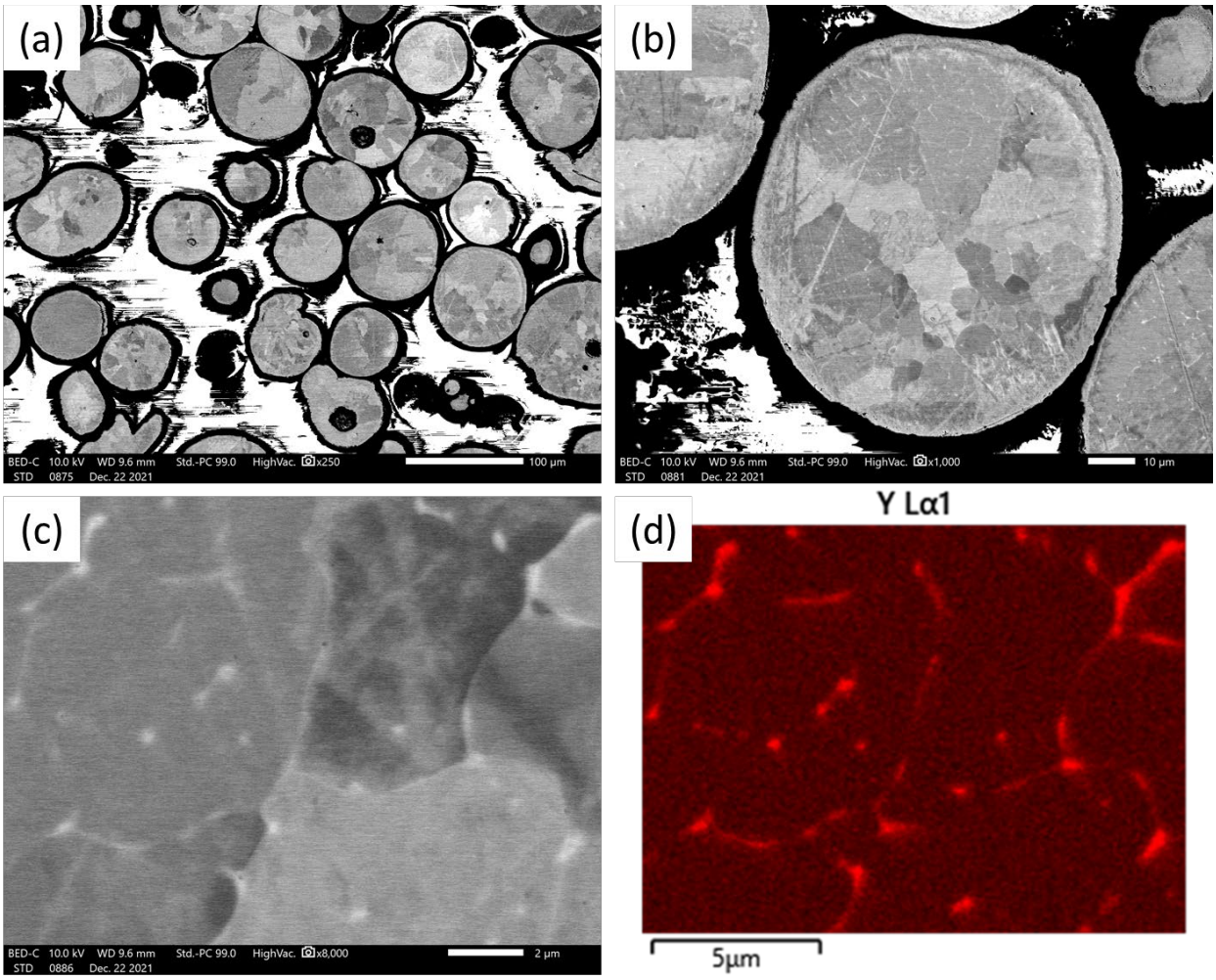

Figure 1. (a) Cross-section SEM overview of the GARS ODS steel powder. (b) Grain substructure inside powder particles. (c) Bright spots decorating the grain boundaries. (d) EDS map showing bright spots are Fe-Y intermetallic particles.

The GARS ODS steel powder was sieved to several tighter size ranges, with the 75-90 μm range yielding 555 g powder that was sufficient for cold spray trials. Smaller size ranges yielded insufficient powder for the powder feeder. Therefore, three size ranges, namely 45-53 μm, 53-63 μm, and 63-75 μm were blended back together, yielding 481 g powder that met the threshold of the powder feeder. In this way, two size ranges, namely 45-75 μm and 75-90 μm, were cold sprayed to investigate the effectiveness of cold spray in depositing powder with varying sizes. If successful, the two size ranges can also be blended to utilize most of the GARS powder for larger scale cold spray.

Preliminary Results and Future Work

For this first-round study, small pieces of P92 plate, i.e., one inch by one inch, were used as substrates. The substrates had an as-machined surface which could be beneficial for bonding at the cold spray interface. Based on prior experience with steels and Ni alloys, a set of robust cold spray parameters were chosen to ensure effective deposition and preserve limited GARS powder. For example, helium carrier gas was used at 600 psi, with the gas temperature at 650 °C. It is noted that 650 °C would still be considered "cold" for ODS steel powder since such a temperature wouldn't alter the powder microstructure. For each powder size range, 2 coupons were deposited, with representative coupon images shown in Figure 2. In addition, since there was more 75-90 μm powder to utilize, a third coupon was deposited with a slightly lower gas pressure (400 psi) to test the cold spray quality with reduced gas consumption.

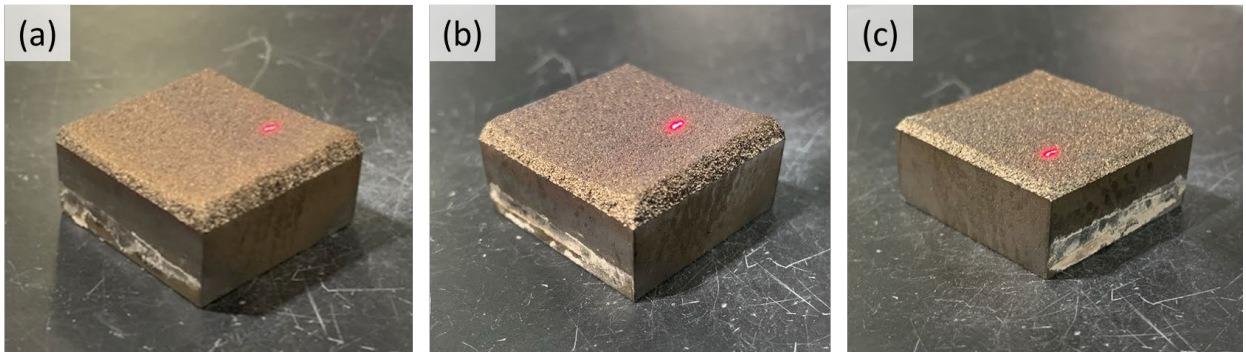

Figure 2. (a) Representative cold spray deposited coupon with 45-75 μm powder. 8.0 g powder was deposited, with an average thickness of 1.45 mm. (b) Representative cold spray deposited coupon with 75-90 μm powder. 8.6 g powder was deposited, with an average thickness of 1.65 mm. (c) Cold spray deposited coupon with 75-90 μm powder using a lower helium gas pressure (400 psi). 5.14 g powder was deposited, with an average thickness of 1.07 mm.

Future work includes adhesion testing between the deposit and substrate, characterization of the sprayed (hence deformed) GARS powder and interface quality, and potential heat treatment to form Y-Ti-O particles. In addition, larger plate(s) will be deposited with 45-75 μm and 75-90 μm powders blended, followed by subsequent thermo-mechanical processing to further improve the interface quality and characteristics of dispersed oxide particles.

Acknowledgements

This research is funded by the U.S. Department of Energy Office of Fusion Energy Sciences under contract DE-AC05-76RL01830. We are grateful to cold spray technical support provided by Daniel Graff, Gary Neuenschwander, and Eric Loeffler.

References

[1] M. Rieth, M. Dürrschnabel, S. Bonk, G. Pintsuk, G. Aiello, J. Henry, Y. de Carlan, B.E. Ghidersa, H. Neuberger, J. Rey, C. Zeile, N. De Wispelaere, E. Simondon, J. Hoffmann, Impact of materials technology on the breeding blanket design – Recent progress and case studies in materials technology, Fusion Engineering and Design 166 (2021) 112275.

[2] J. Rieken, Gas atomized precursor alloy powder for oxide dispersion strengthened ferritic stainless steel, Ames Laboratory (AMES), Ames, IA (United States), 2011, p. 362.

3. CERAMIC COMPOSITE STRUCTURAL MATERIAL DEVELOPMENT

3.1 CHARACTERIZATION OF ATOMIC-SCALE DEFECTS IN NEUTRON IRRADIATED SILICON CARBIDE—T. Koyanagi, Y. Katoh (Oak Ridge National Laboratory), X. Hu (Sichuan University), D. Sprouster (Stony Brook University)

OBJECTIVE

The objective of this study is to provide experimental information on atomic-scale defects in irradiated SiC to allow better modeling of the microstructural response in a fusion nuclear environment.

SUMMARY

The characterization of atomic-scale defects in SiC, including Frenkel pairs, antisites, and small defect clusters, is the key to understanding the dynamic self-stabilizing mechanisms in certain ceramic compounds under irradiation. Although the configurations and energetics of such defects have been studied in theoretical simulations, experimental validation of the results has been limited.

We used two techniques for the characterization of microstructures: positron annihilation spectroscopy and high-energy x-ray diffraction (XRD). Based on the systematic investigation, we present experimental evidence showing how disorder of Si and C atoms developed under neutron irradiation.

PROGRESS AND STATUS

In our previous studies, modern characterization techniques including positron annihilation spectroscopy [1] and high-energy XRD [2,3] were employed to study atomistic defects of neutron-irradiated, high-purity SiC. It is possible to integrate the findings for an in-depth understanding of microstructural evolution in irradiated SiC.

Positron lifetime spectroscopy [1] and XRD pair distribution function analysis [3] were employed for the same-irradiation conditions (i.e., the specimens were in same irradiation vehicle), as shown in Figure 1a and Figure 1b, respectively. Irradiation temperatures ranged from 380 to 790°C where self-interstitial clusters, atomistic vacancy defects, and antisite defects are present [4]. The positron lifetimes presented correspond to the long lifetime based on two components fitting where the long lifetimes result from positron trapping in the vacancy-type defects in neutral and/or negative charge states [1]. With the limited effects of irradiation temperature, the long positron lifetime tended to increase with increasing neutron damage (Figure 1a). The results indicated the growth of atomic scale vacancy clusters based on the interpretation of the lifetime according to the theoretical values [5]. Similarly, the growth of atomistic defects was indicated by the pair distribution function analysis. Figure 1b shows the Si and C atomic displacement parameters as a function of neutron damage [3]. The atomic displacement parameter captures diminished x-ray intensity from atom displacements from their mean positions in a crystal structure and is affected by lattice defects. The continuous increase of lattice defects in both Si and C sub-lattice sites are indicated in Figure 1b.

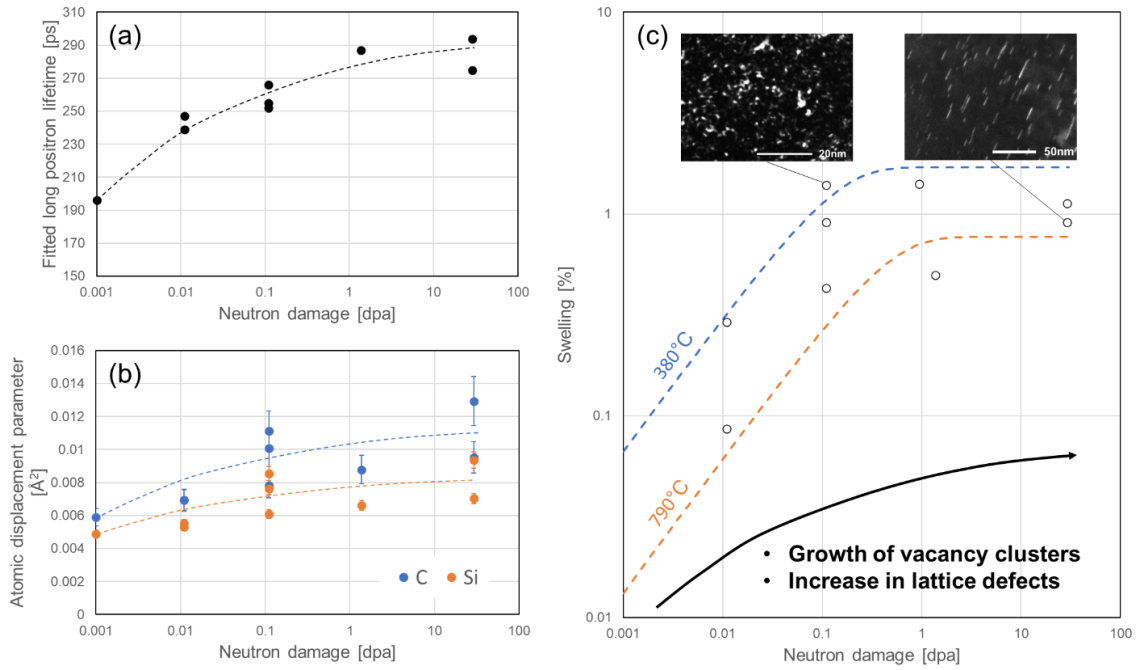

Figure 1. (a) Positron lifetime [1], (b) XRD atomic displacement parameter of Si and C atoms [3], and (c) swelling [6] and microstructural evolution [6,7] of polycrystalline chemical vapor-deposited β-SiC neutron irradiated at 380–790°C. The blue and orange dotted lines show the swelling behavior modeled by Katoh et al. [8]. The dotted lines in (a) and (b) indicate the data trends. The black arrow in (c) explains the growth of vacancy clusters and increase in lattice defects based on (a) and (b), even after the saturation of swelling at ~1 dpa.

The microstructural evolution of SiC irradiated at 380–790°C is summarized in Figure 1c. Previously, swelling evaluations [6,8] and conventional transmission electron microscopy observations [6,7] found the swelling saturation at ~1 dpa, and small interstitial clusters grew into dislocation loops. The positron annihilation spectroscopy and XRD analyses revealed that atomistic defects, including lattice defects, and small vacancy clusters also tended to grow, regardless of the swelling saturation. These findings of the atomistic defect growth are valuable for validating the atomistic modeling of radiation damage in SiC. Additionally, the growth of vacancy defects stimulates future studies on potential onset neutron doses of void swelling in SiC at relatively low temperatures and on trapping He and H in vacancy defects at different neutron doses relevant to fusion reactor applications [9].

Future Plans

Other characterization techniques including Raman spectroscopy will be applied to SiC specimens irradiated with same irradiation conditions to obtain a complete picture of material degradation behavior under harsh irradiation environments.

REFERENCES

[1] X. Hu, T. Koyanagi, Y. Katoh, B.D. Wirth, Positron annihilation spectroscopy investigation of vacancy defects in neutron-irradiated 3C-SiC, Phys. Rev. B. 95 (2017). doi:10.1103/PhysRevB.95.104103.

[2] D.J. Sprouster, T. Koyanagi, E. Dooryhee, S.K. Ghose, Y. Katoh, L.E. Ecker, Microstructural evolution of neutron irradiated 3C-SiC, Scr. Mater. 137 (2017) 132–136. doi:10.1016/j.scriptamat.2017.02.030.

[3] D.J. Sprouster, L.L. Snead, E. Dooryhee, S.K. Ghose, T. Koyanagi, Y. Katoh, Pair distribution function analysis of neutron-irradiated silicon carbide, J. Nucl. Mater. 527 (2019) 151798. doi:10.1016/j.jnucmat.2019.151798.

[4] L.L. Snead, T. Nozawa, Y. Katoh, T.S. Byun, S. Kondo, D.A. Petti, Handbook of SiC properties for fuel performance modeling, J. Nucl. Mater. 371 (2007) 329–377. doi:10.1016/j.jnucmat.2007.05.016.
[5] J. Wiktor, X. Kerbiriou, G. Jomard, S. Esnouf, M.F. Barthe, M. Bertolus, Positron annihilation spectroscopy investigation of vacancy clusters in silicon carbide: Combining experiments and electronic structure calculations, Phys. Rev. B - Condens. Matter Mater. Phys. 89 (2014). doi:10.1103/PhysRevB.89.155203.
[6] T. Koyanagi, Y. Katoh, K. Ozawa, K. Shimoda, T. Hinoki, L.L. Snead, Neutron-irradiation creep of silicon carbide materials beyond the initial transient, J. Nucl. Mater. 478 (2016) 97–111. doi:10.1016/j.jnucmat.2016.06.006.
[7] T. Koyanagi, M.J. Lance, Y. Katoh, Quantification of irradiation defects in beta-silicon carbide using Raman spectroscopy, Scr. Mater. 125 (2016) 58–62. doi:10.1016/j.scriptamat.2016.08.004.
[8] Y. Katoh, T. Koyanagi, J.L. McDuffee, L.L. Snead, K. Yueh, Dimensional stability and anisotropy of SiC and SiC-based composites in transition swelling regime, J. Nucl. Mater. 499 (2018) 471–479. doi:10.1016/j.jnucmat.2017.12.009.
[9] X. Hu, T. Koyanagi, J. Zhao, T. Yamamoto, Y. Katoh, Microstructural evolution of 3C-SiC exposed to simultaneous neutron irradiation and helium implantation, J. Nucl. Mater. 509 (2018) 366–376. doi:10.1016/j.jnucmat.2018.07.007.

3.2 X-RAY CHARACTERIZATION METHODS FOR BERYLLIDE-BASED MATERIALS FOR MULTIPLIER APPLICATIONS—D. Bhardwaj, D.J. Sprouster, J. R. Trelewicz, L.L. Snead (Stony Brook University)

OBJECTIVE

Stony Brook University in partnership with KIT has begun to support the characterization and development of neutron multipliers. The SBU is aiding in the non-destructive characterization of a range of beryllides (Be_x-Ti, Be_x-Cr, Be_x-Zr as example), including both baseline and irradiated specimens. Central to this program is the study of the fundamental structure and properties of the beryllides and the impact of phase and multi-phase structure on phenomenon such as oxidation and irradiation performance. The core of the research work will include computational thermodynamics (modeling) and elevated temperature x-ray scattering, thermophysical properties in the radiological laboratory at Stony Brook University. Of critical importance will be the cataloguing of beryllide phases, many of which are not currently known in the literature.

SUMMARY

Current international leadership in solid breeder blanket concepts, including their underlying materials development, is held between the European and Japanese national programs. The primary solid breeder concept, the Helium-Cooled Pebble-Bed design, operates in the range of 300-520°C with major materials systems being tungsten as first wall, Eurofer-97 structure, Li_4SiO_4 breeder, and $Be_{12}Ti$ multiplier. Beryllium rich intermetallic, such as $Be_{12}Ti$, offer reduced tritium retention. While beryllides appear to be very attractive for solid breeder blanket applications, the specific choice of titanium beryllide needs to be based on microstructural and irradiation performance data. The radiation tolerance and survivability of beryllides in fusion environments, are currently under investigation in the EURO Fusion program. In this report, we describe our recent x-ray characterization efforts applied to a first set of baselines Beryllide specimens supplied by the EURO Fusion program.

PROGRESS AND STATUS

Introduction

The crystallographic structure of three beryllide specimens supplied by KIT were characterized with XRD. The specimens included monoliths of $CrBe_{12}$, $TiBe_{12}$ fabricated via vacuum hot pressing (VHP) and $TiBe_{12}$ pebbles mounted on carbon tape. The XRD patterns were collected using a recently purchased Bruker D8-Advance X-Ray diffractometer at SBU. The XRD patterns were collected in Reflection Geometry mode (Bragg-Brentano). A Nickel filter prior to the detector optics was used to filter K_β emission lines. The XRD patterns were recorded with a two-theta range of 10-110^o with a time/step to be 2s, at a step size of 0.01^o. After the data collection the XRD patterns are analyzed in EVA and MATCH3! for phase identification.

Experimental Procedure

The XRD patterns for the monolithic (a) $CrBe_{12}$ and (b) $TiBe_{12}$, and (c) pebble $TiBe_{12}$ are shown in Figure 1. Optical images of the different samples are shown in the insets of each panel of Figure 1 for reference. The anticipated tetragonal phase for $CrBe_{12}$ and $TiBe_{12}$ (I4/mmm) is clearly observable in all XRD patterns, with no hexagonal-close packed reflections for unreacted Be, Ti, or body-centered cubic reflections for Cr. Furthermore, no reflections from any hexagonally close packed BeO are observable for any of the measured specimens. The tetragonal structure in the monolithic and pebble samples show single beryllide

phases, confirm the phase purity of each specimen. It is noted that an amorphous background is observable in each specimen attributable to the sample holders (for monolithic samples in Figure 1 (a) and (b)), and carbon mounting tape (pebble specimen Figure 1 (c)). The complexity in the structure of these given beryllides will be further studied by refining the XRD pattern to determine the lattice parameters.

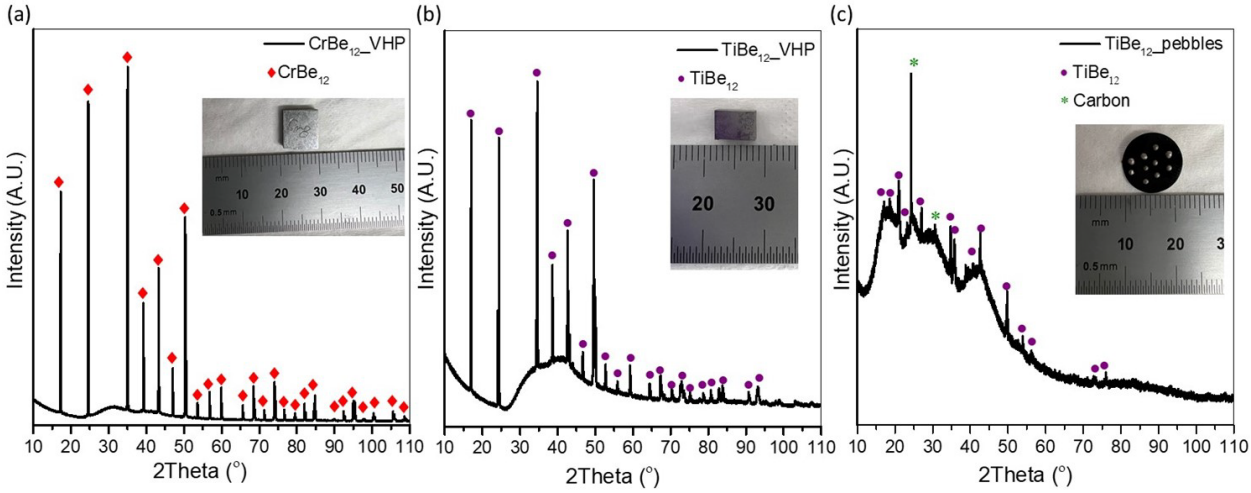

Figure1. XRD pattern for (a) CrBe12, (b) TiBe12_VHP and (c) TiBe12_pebbles.

Results

These beryllide samples have been prepared and measured as pre-irradiation examination for an upcoming MITR irradiation to take place in March of 2022 for one cycle at nominal temperatures of 500 and 725°C. Post-irradiation examination will take place towards the end of the fiscal year.

Acknowledgement

The work was funded under Grant DE-SC0018332 to the Research Foundation at State University of New York, Stony Brook by the US Department of Energy Office of Fusion Energy Sciences.

4. PLASMA-FACING AND HIGH HEAT FLUX MATERIALS AND COMPONENT TESTING

4.1 PROPERTIES AND CHARACTERIZATION OF THE 2ND GENERATION OF Cu-Cr-Nb-Zr ALLOYS FOR FUSION ENERGY APPLICATIONS—Y. Yang (Oak Ridge National Laboratory), L. Wang, S. J. Zinkle (University of Tennessee), Lance Snead (Stony Brook University)

OBJECTIVE

This study aims at developing high creep strength and high thermal conductivity Cu-Cr-Nb-Zr alloys with reduced Nb contents for long pulse fusion high heat flux structures, through an accelerated approach of computational thermodynamics guided alloy design.

SUMMARY

Work performed during the reporting period (07/01/2021-12/31/2021) is to characterize the precipitates in the newly designed 2nd generation of Cu-Cr-Nb-Zr alloys and establish the correlation between these precipitate characteristics and the improvement of creep properties.

PROGRESS AND STATUS

In previous work [1,2], we have successfully developed the 1st generation of Cu-Cr-Nb-Zr (CCNZ) alloys. The currently developed 2nd generation of Cu-Cr-Nb-Zr alloys, compared to the 1st generation, have the following advantages: 1) mitigated crack initiation and propagation at grain boundary (GB) due to less clustered laves_Cr_2Nb precipitates at GB; 2) reduced activity in fusion applications due to the reduced Nb content; 3) longer creep rupture life, especially for the higher applied stress levels. During the reporting period, a detailed microstructural characterization has been performed to understand beneficial roles of precipitates on property enhancement.

The SEM BSE image in Figure 1a shows the microstructure the 2nd generation CCNZ alloy before creep tests and the distribution of micron-scale precipitates. The grain size is about 33±1.5 mm. Micron and sub-micron scale Laves_Cr_2Nb and Cr precipitates were observed at GB, which are primarily formed during solidification. The TEM image and EDS maps in Figure 1b-e show the distribution of nano-scale precipitates in the Matrix. There are primarily two types of nano-scale precipitates: Cr precipitates have a spherical morphology with a mean diameter about 5.5±1.0 nm and a number density of 1.62×10^{22} m^{-3}; and Cu_5Zr precipitates have a lenticular morphology with a mean length about 11.7±1.1 nm and a number density of 4.35×10^{21} m^{-3}. The presence of GB micron-scale Laves_Cr_2Nb and Cr precipitates and matrix nanoscale Cr and Cu_5Zr precipitates is consistent with thermodynamic calculation.

The coarsening of precipitate coarsening was analyzed on the tab section of the creep-ruptured specimen. The mean diameter of Cr and length of Cu_5Zr are plotted in Figure 2 as a function of time, together with their TEM image and EDS map. Both types of precipitates are coarsening resistant. The mean diameter of Cr and length of Cu_5Zr precipitates after 600 h aging at 500°C are ~17 nm and ~40 nm, respectively. These high number-density and coarsening resistant precipitates can potentially impede the dislocation movement and mitigate dislocation creep.

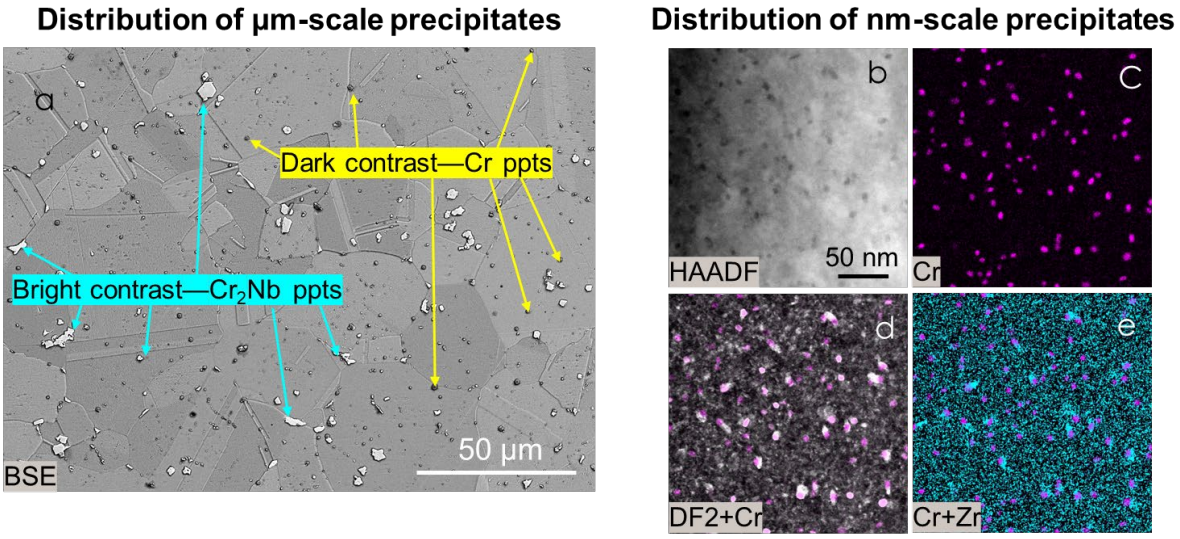

Figure 1. Microstructure of the 2nd CCNZ alloy before creep test. a) A SEM/BSE image showing grain size and distribution of micron-scale GB precipitates; b) TEM and EDS maps showing the distribution of nanoscale matrix precipitates.

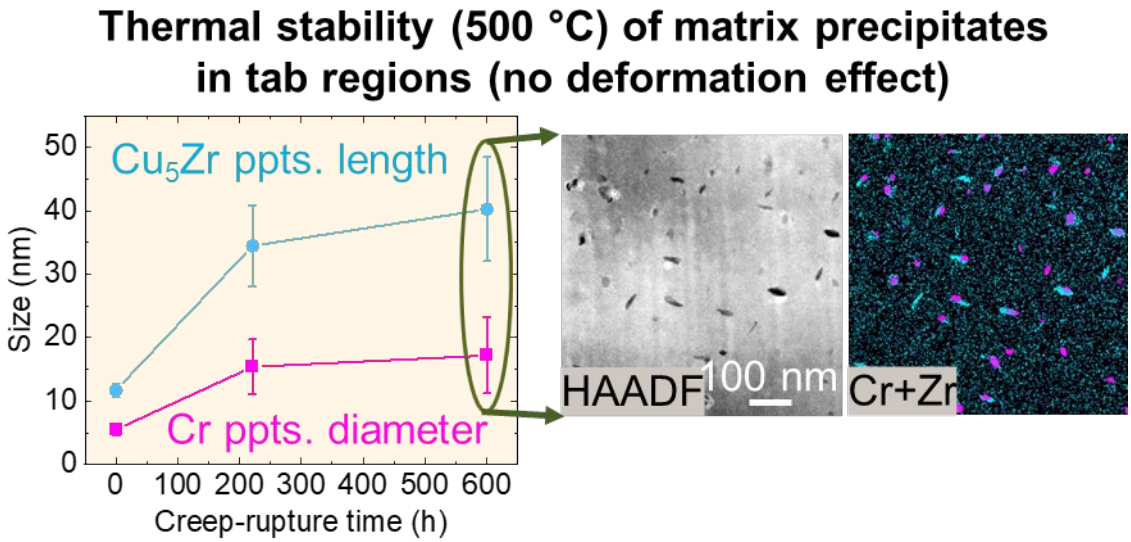

Figure 2. Size of matrix nanoscale Cr and Cu_5Zr precipitates as a function of aging time and TEM image/EDS map showing precipitates after 600h aging.

The creep property is also beneficial from the micron-scale GB Laves_Cr_2Nb and Cr precipitates. Figure 3 shows that GB laves_Cr_2Nb precipitates can blunt the crack propagation. It is also noticeable that some Zr is also dissolved in the Laves_Cr_2Nb precipitates.

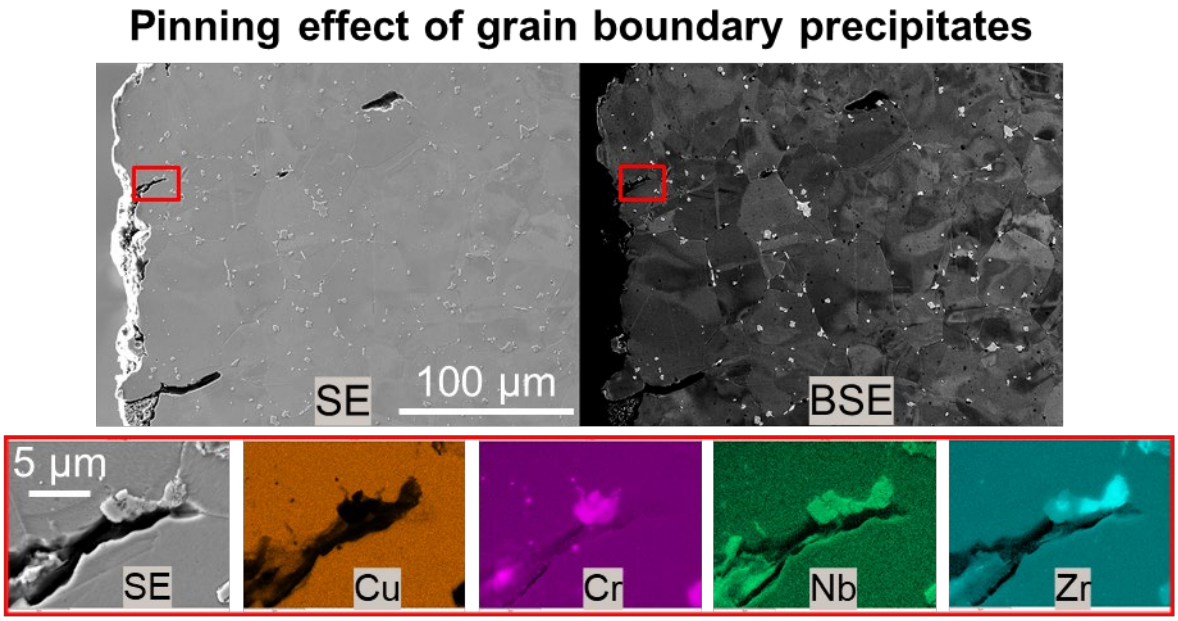

Figure 3. Pinning effect of grain boundary precipitates in mitigating crack propagation.

To summarize, the improved creep property in the 2nd gen CCNZ alloy is due to the formation of bi-model precipitates: micron-scale GB Laves_Cr_2Nb and nano-scale matrix Cr and Cu_5Zr precipitates. The GB precipitates can efficiently pin the grain boundary and blunt the crack propagation, and the matric precipitates can help mitigate dislocation creep.

References

[1.] Yang, Y., Wang, L., Snead, L., & Zinkle, S. J. (2018). Development of novel Cu-Cr-Nb-Zr alloys with the aid of computational thermodynamics. Materials & Design, 156, 370-380.

[2.] Wang, L., Zheng, C., Kombaiah, B., Tan, L., Sprouster, D. J., Snead, L. L., ... & Yang, Y. (2020). Contrasting roles of Laves_Cr2Nb precipitates on the creep properties of novel CuCrNbZr alloys. Materials Science and Engineering: A, 779, 139110.

4.2 ON THE ROLE OF ANNEALING ON MICROSTRUCTURE AND MECHANICAL PROPERTIES OF 90 to 97W TUNGSTEN HEAVY ALLOYS—M.E. Alam, G.R. Odette (University of California Santa Barbara)

OBJECTIVE

This research explore the effect of high-temperature annealing on the microstructure and mechanical properties of 90 to 97W tungsten heavy alloys (WHAs) for fusion divertor application.

SUMMARY

The commercially available liquid-phase sintered 90, 92.5, 95, and 97 wt.% tungsten heavy alloys (WHA) show remarkable room temperature (RT) maximum load fracture toughness (K_{Jm} ≈ 69 to 107 MPa√m, depending on W content) compared to pure W (≈ 8 ± 4 MPa√m). However, these alloys are to be used as divertor in fusion reactors at a temperature ≈ 1300 ºC due to various limiting factors. Therefore, these four WHAs are annealed at 1300 ºC for 24 h in a vacuum. Microstructural observation on prior and post-annealed samples reveal no to very minimal changes in W-particle size, texture, ductile phase (DP) area fractions, DP ligament thickness, or DP constituent's chemistry. The Vickers microhardness (HV) reduces up to 16% with increasing W content after annealing. The 1300 ºC/24 h anneal does not significantly change the RT tensile properties for all WHAs except for the 95 and 97W WHAs where ductility doubles. RT fracture toughness on the precracked 3PB reveals an increase in toughness for annealed WHAs (up to 42% for 97W WHA). The damage mode also shifts from microcrack process-zone dilatational toughening mechanism to W-DP decohesion dominated toughening mechanism.

PROGRESS AND STATUS

Introduction

The tungsten heavy alloys (WHAs), a class of bi-phase metallic composites, are typically composed of tungsten (W) powder consolidated by liquid-phase sintering (LPS) with relatively lower melting point ductile phase (DP) metals like Ni, Fe, Cu, and Co; and well known for their good room to high-temperature tensile strength and ductility [1–4]. In addition to use in very high temperatures environments, like rocket nozzles, main applications of WHA include use in ordnance, such as kinetic energy penetrators, counterbalances and flywheels, where high mass densities are necessary [1,3,5]. The WHAs are recently being considered as potential structural plasma-facing materials for fusion reactor divertor applications [6–13]. For example, Neu et al. [8,9] reported the use of 97W-2Ni-1Fe WHAs as divertor tiles for the mid-size tokamak ASDEX Upgrade facilities that experienced cyclic plasma heat flux up to 20MW/m^2 and surface temperature up to 2200 ºC and found a lower cracking tendency for WHAs compared to pure W. However, for a variety of reasons, for example, W-recrystallization or fuzz formation, the maximum service temperatures for divertors are likely to ≈ 1300 ºC [8,9,14–19]. Exposing DP or WHA at a higher temperature for a longer time might change the microstructure and eventually affect the mechanical properties. Therefore, in this study, we have annealed four as-received WHAs at 1300 ºC for 24 h to understand annealing effect on microstructure and mechanical properties, which were not studied well previously.

Detail microstructural observation reveals very little change in W-particle size, contiguity, DP phase compositions, area percentage, or DP thickness for pre-and post-annealed conditions. Vickers microhardness (HV) reduces after annealing, especially for higher W content WHAs. The RT tensile results show unaffected 0.2% yield strength for all WHA's and ductility for 90 and 92.5 W WHA; however, 95 and 97W nearly double their respective ductility after annealing, while maintaining similar tensile strengths. The hardening exponent is also reduced. The RT maximum load fracture toughness, K_{Jm}, increased after annealing for all the WHAs except 92.5W WHA. Surface damage mode profile also changes from W-microcleavage formation, arrest, and blunting for the as-received condition to W-DP decohesion dominated mechanism.

Experimental Procedure

Details of materials acquisition, specimen fabrication, microstructural observation, pre cracking and mechanical testing procedures can be found elsewhere [6,20]. Briefly, four commercially available 90, 92.5, 95, and 97 wt.% W, balanced with DP phase (Ni/Fe = 7/3 ratio), (dubbed as 90W, 92.5W, 95W and 97W, respectively) WHAs were acquired from Mi-Tech Metals, Indianapolis, IN, USA as a liquid phase sintered plates. Basic microstructural characterization involves optical, scanning electron microscopy (SEM), energy dispersive spectroscopy (EDS) and electron backscatter diffraction (EBSD) on the pre-and post-annealed conditions. W-particles size, W-W contiguity, chemical composition of DP, DP area fraction, ligament thickness (t), thickness to W-particle (t/W), and local fracture modes are observed using mentioned characterization tools and imageJ64 software. We have evaluated Vicker's microhardness (HV), RT tensile, and fracture toughness for the mechanical characterizations on the annealed WHAs. Again, detailed characterization procedures are reported in [6,20].

Results

Microstructure

Figure 1 shows the SEM micrographs of the polished and etched 90-97W WHAs before (Figure 1a-d) and after (Figure 1e-h) annealing; the microstructural observation results are also summarized in Table 1. In all cases, W-particles are roughly spheroidal, surrounded by an interconnected honeycomb web structure of DP. The EDS point scan reveals W particles are nearly 100% pure, irrespective of alloy compositions or annealing conditions. The size of the W-particles also did not change before and after annealing and, are ≈ 17 ± 7 μm for 90W, increases with increasing W% content in the WHAs to ≈ 38 ± 15 μm for 97W (Table 1 and Figure 1). The DP area % also remains the same prior- and post-annealed conditions considering standard deviation (Table 1). The EDS's multiple point scans on the ductile phase reveal that the DP remains Ni-rich after annealing with a nominal average composition of ≈ 52% Ni, 31% W and 17% Fe from the prior-anneal 50%Ni, 32%W and 18%W condition. However, these variations are statistically insignificant (Table 2 and Figure 2). The W-W contiguity increases for higher W-containing WHA's; however, that remains unchanged after annealing for the respective WHA alloys except for 97W annealed condition that reduces from 0.582 to 0.477 (≈ 18%). No DP ligament thickness (t) variations were observed irrespective of WHA alloys or annealing conditions. As expected, the t/W ratio or DP/W area fraction reduces with increasing W content in the WHA as W particle size increases. However, in both cases, this ratio does not change after annealing for the respective WHAs. The EBSD was also used on selective WHA's (90W and 97W) to observe the texture formation after annealing. The inverse pole figure (IPF) map shown in Figure 3 for annealed 90W and 97W shows that the randomly oriented W particles are embedded in very coarse-grained NiWFe DP. No high misorientation angles (>15º) were observed in W-particles at the scanned area for both annealed WHAs. However, some speckles are observed in the W or DP phases, which might be generated due to the polishing effect. The DP grains are very coarse and ≈ 165 x 165 μm area shows only ≈ two different continuous color grades with incomplete shape (Figure 3c for 90W and Figure 3f for 97W). A similar observation has been observed on as-received 90W and 97W, performed at PNNL [21]. In general, 1300 ºC/24 h annealing has little to no effect on any aspect of the observed microstructures on the various as-received WHA plates.

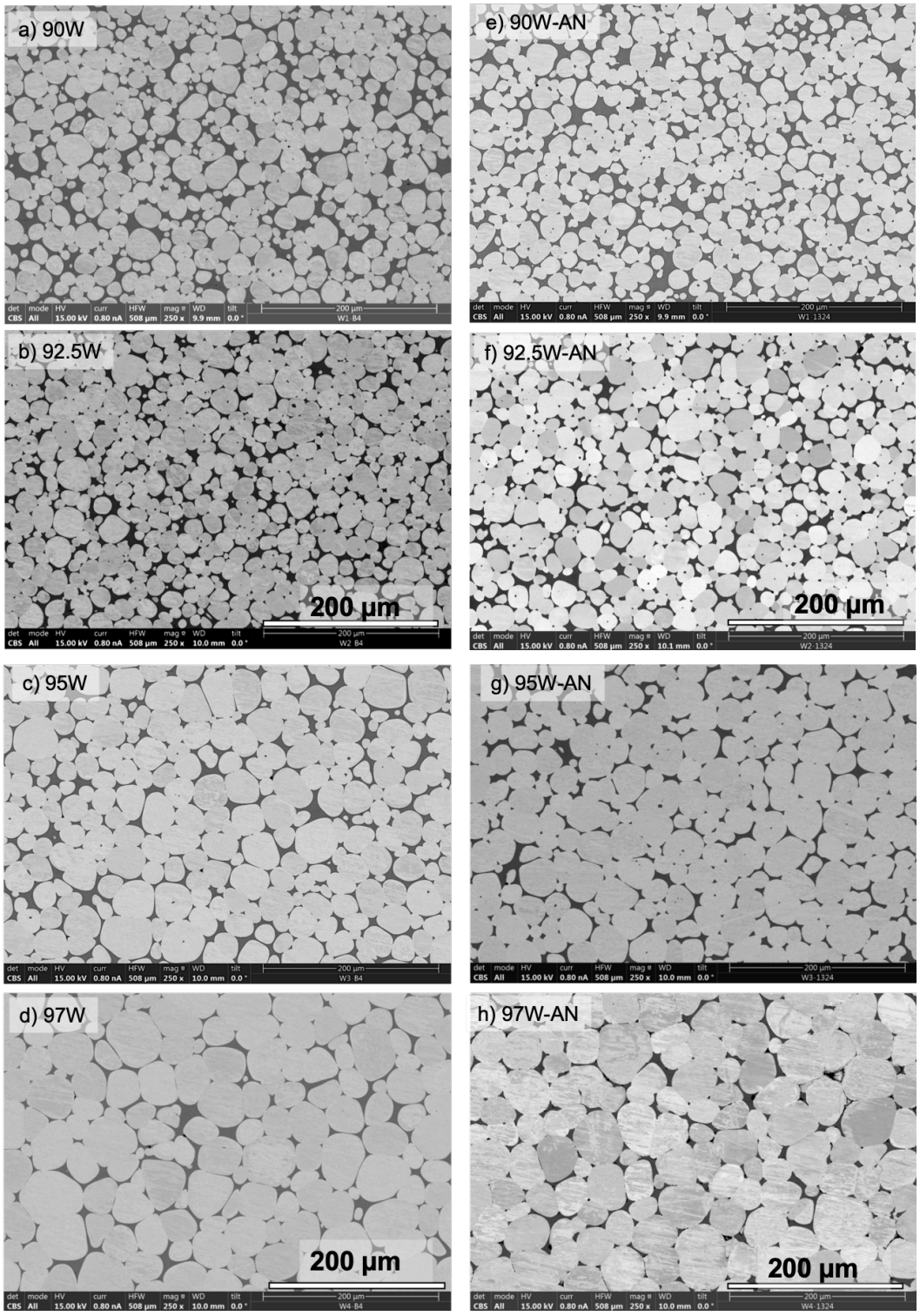

Figure 1. Low magnification SEM images of 90 to 97W WHAs before (a-d, left column) and after (e-h, right column) 1300 ºC/24 h annealing. Scale is 200 µm for all cases.

Table 1. The W-particle size, DP area %, W-W contiguity, DP thickness, t/W and DP/W for the as-received and 1300 ºC/24 h annealed WHA's

WHAs	Condition	W-particles, μm	DP area, %	W-W contiguity, C_w	DP thickness, t, μm	t/W μm/μm	DP/W area
90W	As-received	17 ± 7	16.1 ± 3.8	0.285	5.9 ± 5.4	0.35	0.22
	Annealed	17 ± 6	18.6 ± 0.8	0.302	5.7 ± 4.7	0.33	0.22
92.5W	As-received	18 ± 7	11.8 ± 2.2	0.402	4.0 ±. 3.7	0.22	0.12
	Annealed	19 ± 7	11.0 ± 0.8	0.408	5.7 ± 6.4	0.3	0.19
95W	As-received	26 ± 11	10.7 ± 1.3	0.426	5.1 ± 4.1	0.20	0.13
	Annealed	28 ± 11	9.3 ± 0.8	0.405	4.2 ± 3.3	0.15	0.09
97W	As-received	38 ± 15	6.4 ± 1.5	0.582	4.5 ± 5.0	0.12	0.07
	Annealed	38 ± 14	5.7 ± 0.1	0.477	5.3 ± 4.0	0.14	0.06

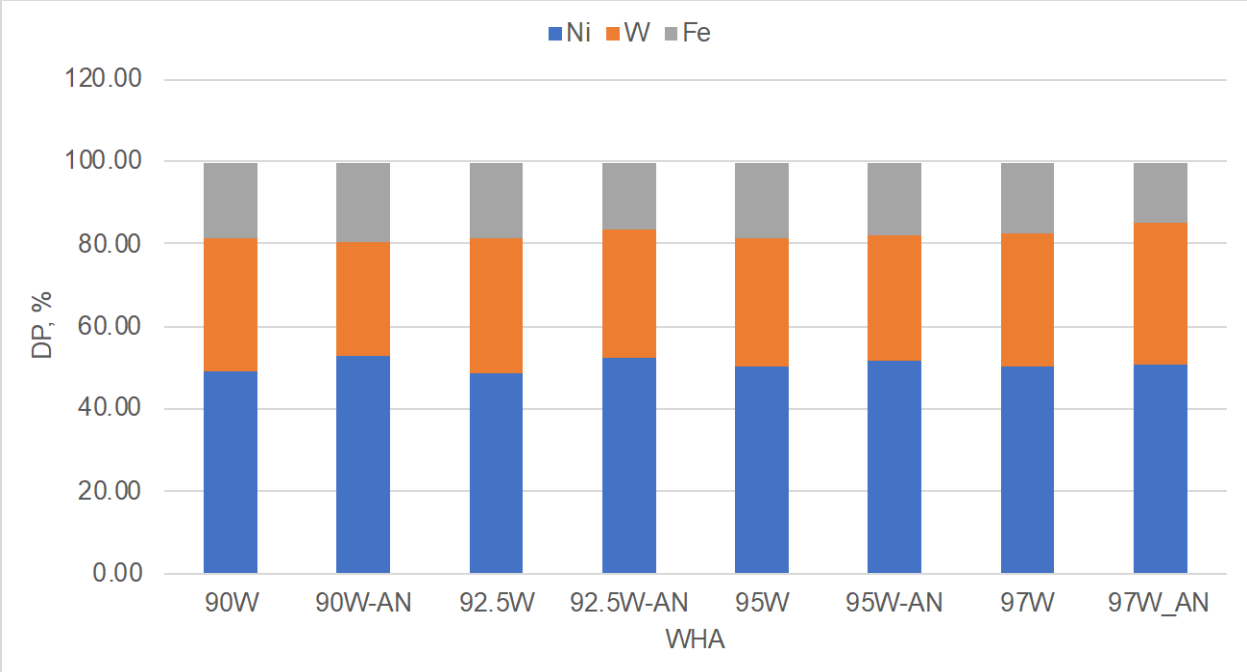

Figure 2. EDS point scan showing DP constituents (i.e., Ni, W and Fe wt.%) as a function of WHA alloy compositions and annealing conditions.

Table 2. EDS point scan results for DP composition variations as a function of WHA alloy contents and annealing conditions

WHAs	Condition	Ni, wt. %	W, wt. %	Fe, wt. %
90W	As-received	49.3 ± 0.4	32. 0 ± 0.4	18.7 ± 0.2
	Annealed	52.7 ± 0.9	27.6 ± 1.1	19.7 ± 0.5
92.5W	As-received	48.7 ± 0.7	32.9 ± 1.2	18.4 ± 0.6
	Annealed	52.4 ± 0.2	31.2 ± 0.3	16.4 ± 0.3
95W	As-received	50.2 ± 0.7	31.5 ± 0.9	18.3 ± 0.3
	Annealed	51.9 ± 1.2	30.2 ± 1.4	17.9 ± 0.5
97W	As-received	50.3 ± 0.6	32.3 ±0.7	17.4 ± 0.3
	Annealed	50.8 ± 0.5	34.33 ± 1.5	14.9 ± 1.5

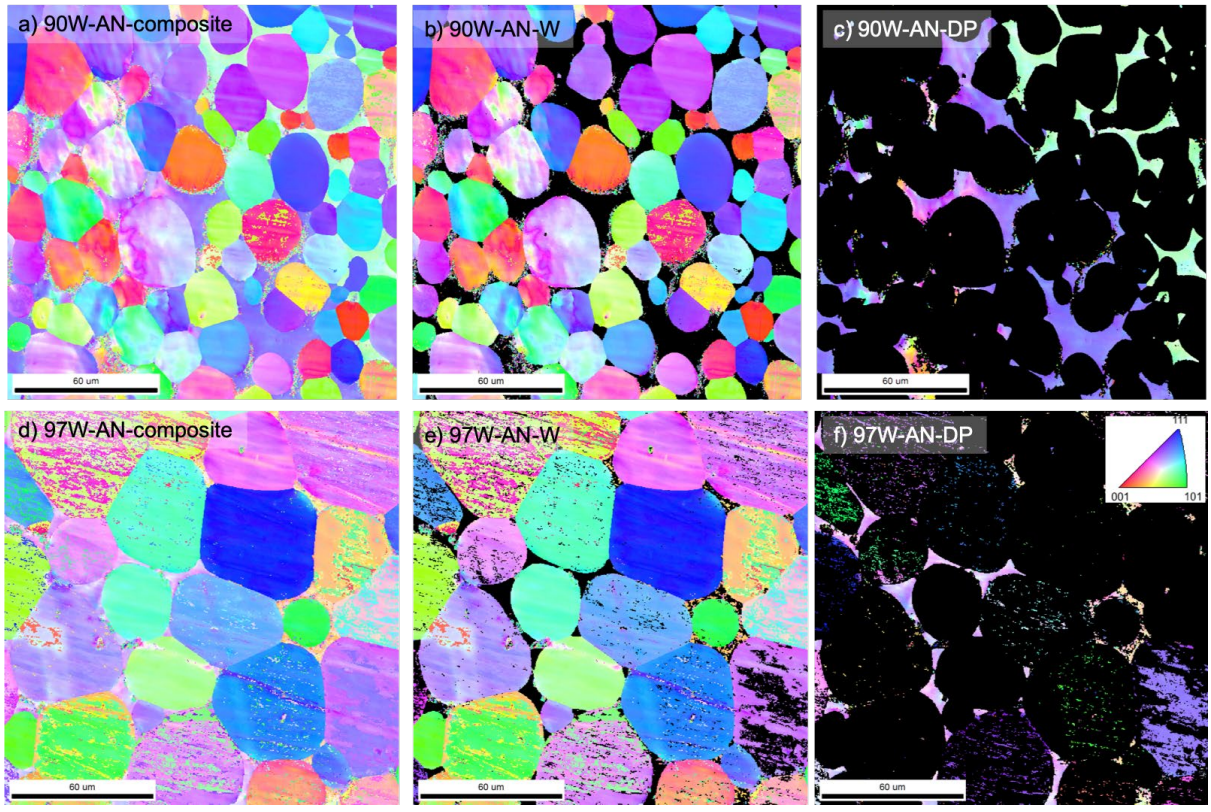

Figure 3. EBSD IPF map showing the random texture orientation for W and DP for 90W (a-c), and 97W (d-f) annealed conditions. Here, left column: composite, middle column: W, and right column: DP in both cases.

RT Microhardness and tensile tests

Room temperature Vicker's microhardness (H_v) measurements for the as-received and annealed WHA's are shown in Table 3 and Figure 4a. As-received results are also reported previously in [22]. While the average microhardness increases with increasing W from 321 ± 8 kg_f/mm^2 for 90W to 344 ± 9 kg_f/mm^2 for 97W for as-received conditions, the hardening trend is somewhat downward for annealed conditions from 326 ± 9 kg_f/mm^2 for 90W to 289 ± 18 kg_f/mm^2 for 97W annealed WHAs. In general, high-temperature annealing is expected to soften the WHA composites, which it does for all up to 16% for 97W, except for 90W, which remains unchanged. The diverting trend of hardening after annealing with increased W is not yet fully understood. However, nanoindentation will be performed in future on each individual W and DP phases for all alloys and annealed conditions to understand these constituents' effects on the hardness or even on strength and toughness.

Table 3. RT Vickers microhardness (HV), and tensile properties of WHA's

WHAs	Conditions	$HV_{0.5}$ Kg_f/mm^2	σ_y, MPa	σ_u, MPa	ε_u, %	ε_t, %
90W	As-received	321 ± 8	621 ± 29	891 ± 35	18 ± 4	21 ± 7
	Annealed	326 ± 9	588 ± 12	809 ± 11	17.3 ± 1.0	22.5 ± 2.9
92.5W	As-received	334 ± 8	616 ± 44	886 ± 12	13.5 ± 2.2	16 ± 4
	Annealed	302 ± 13	603 ± 4	796 ± 17	14.1 ± 2.2	17.0 ± 3.2
95W	As-received	349 ± 7	600 ± 15	818 ± 10	7.3 ± 1	8 ± 1
	Annealed	279 ± 23	588 ± 9	774 ± 12	13.1 ± 1.9	15.5 ± 0.3
97W	As-received	344 ± 9	594 ± 27	701 ± 67	3.4 ± 1	4 ± 1
	Annealed	289 ± 18	572 ± 14	707 ± 10	7.5 ± 0.9	8.8 ± 1.0

Figure 4b shows the representative RT engineering stress-strain (σ–ε) curves for all the 90 - 97W pre- and post-annealed WHAs. The corresponding tensile data are shown in Figure 4c for 0.2% yield (σ_y), and ultimate tensile strengths (σ_u); and Figure 4d for total elongation (ε_t). The engineering σ–ε curves look generally similar for the WHA's except the higher W% WHAs that systematically fail early. Further, curves are less strain-hardened for the annealed condition (Figure 4b). Both Table 3 and Figure 4c show that the 1300 ºC/24 h annealing did not affect on σ_y (≈ 600 MPa with a softening of ≤ 5%), which are essentially the same for all the alloys. On the contrary, σ_u decreases for the respective WHA alloys up to 10%, except for 97W, after annealing, which might be due to lower strain hardening exponent. However, annealed σ_u is nearly similar for up to 95W (≈ 800 MPa), and then drops to ≈ 700 MPa for 97W (Table 3). Total elongation does not vary significantly for the respective WHAs for up to 92.5W after annealing but increases to ≈ 2x for the 95W and 97W. In all cases, annealed results are more consistent with lower standard deviation, which implies that annealing might help to homogenize the microstructure.

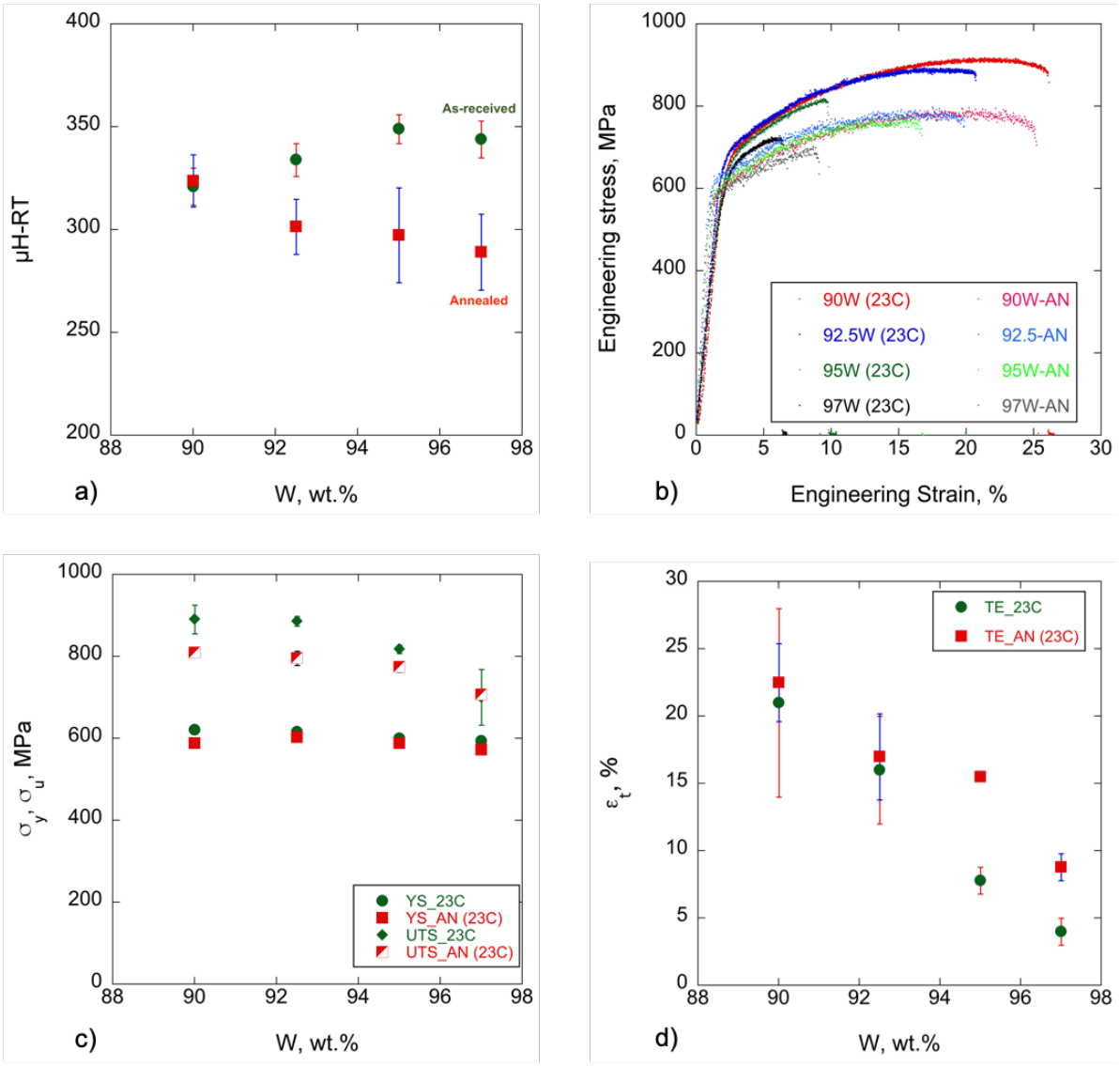

Figure 4. a) Vicker's microhardness values for as-received (green circles) and annealed (red squares) WHA's; b) RT engineering σ–ε curves; c) 0.2% yield (σ_y) and ultimate tensile (σ_u) strengths; d) total elongations (ε_t) for as-received (green circles), and annealed (red squares) WHAs, respectively.

Room temperature (RT) fracture toughness

The RT fracture toughness tests on the various WHAs are conducted on fatigue pre-cracked 3PB bars. The nominal dimension of these bend bars is 16 x 3.3 x 1.65 mm (length x width x thickness), and are precracked to a/W ≈ 0.4 to 0.5 using load ratio R ≈ 0.1. The normalized load-displacement (P_n-d) curves for all the annealed specimens are shown in Figure 5. The load normalization is performed by $P_n = 0.25*P/(1-a/W)^2$ and described in [22]. The representative P-d curves for all the WHA alloys at both conditions are plotted in Figure 6a; their corresponding K_{Jm} values are plotted in Figure 6b, as well as tabulated in Table 4. As reported previously [22], all of the as-received WHAs from 90 to 97WR specimens show very stable crack growth. The RT maximum load fracture toughness, K_{Jm} for as-received condition is nearly the same up to 95W (≈ 100 ± 15 MPa√m), in spite of contiguity increase (Tables 1 and 5). The as-received 97W shows relatively smaller K_{Jm} with an average ≈ 69 ± 12 MPa√m. The 1300 ºC/ 24 h annealed improves the fracture toughness in all cases up to 42% (for 97W), except for 92.5 WHA which shows negligible improvement

(Table 5). Note, though the normalized load for as-received WHAs is higher for the respective alloys, the maximum load displacement is higher for the annealed specimens, making them tougher (Figure 6a). Moreover, the standard deviation for the annealed specimens is reduced compared to as-received conditions, which are also reflected by the annealed P-d curves shown in Figure 5. Again, this suggests that annealing helps to homogenize the microstructure. The K_{Jm} for the annealed specimens is ≈ 12 to 16x higher than typical monolithic W toughness (K_{Ic} ≈ 8 ± 4 MPa√m). Though these results are within the ASTM E1921 validity limit (≈ 120 to 132 MPa√m) for the specimen dimension given by $K_{Jlim} = \{Eb_o\sigma_y/30(1-\upsilon^2)\}^{0.5}$, where b_o is the unbroken ligament (here 1.65 to 2.00 mm), and σ_y is the yield stress at test temperature (≈ 600 MPa at 23 ºC); however, size effect has been observed for larger WHA specimens, especially for 97W. Therefore, larger specimens will be annealed and tested in the future.

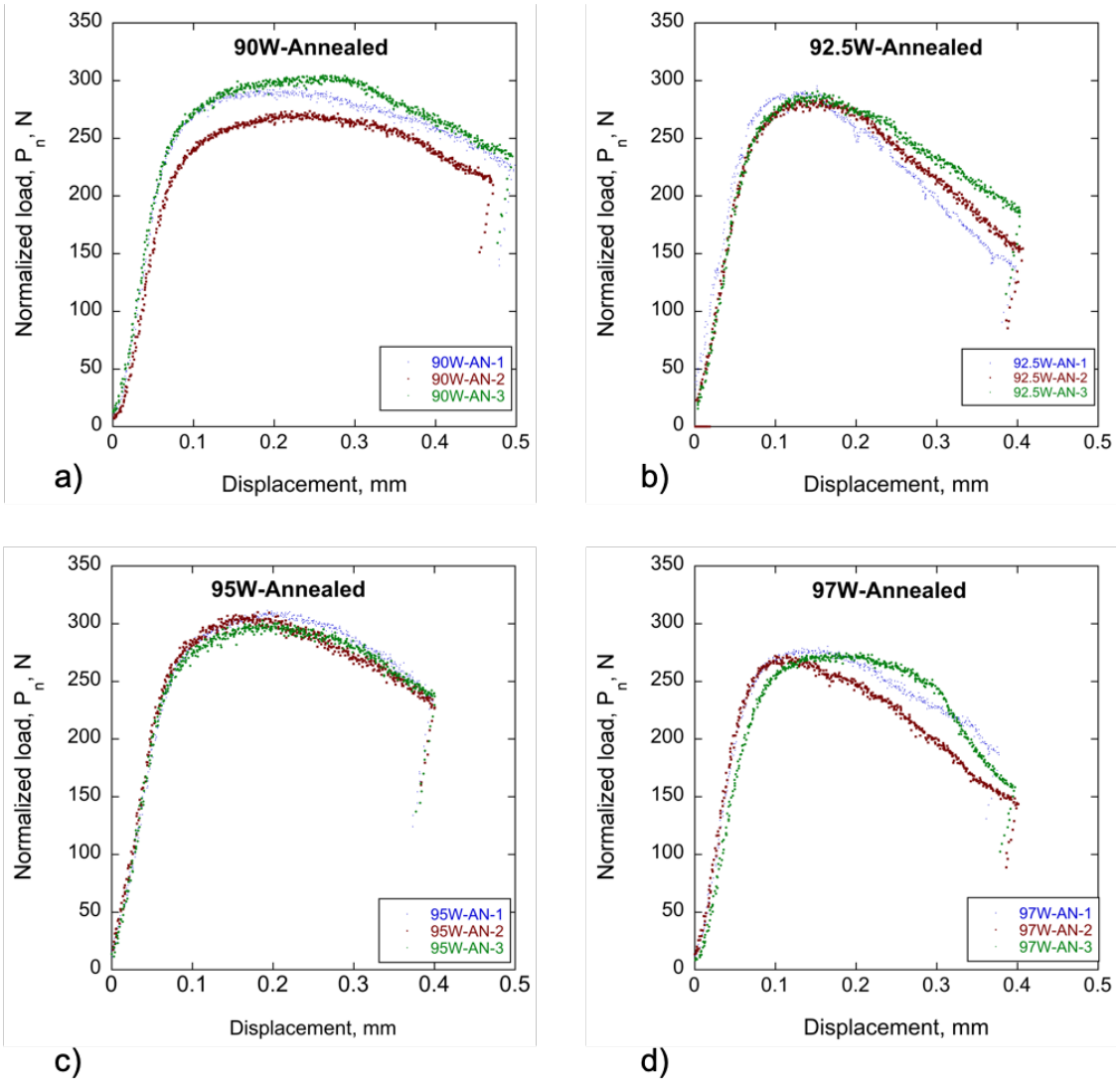

Figure 5. Normalized RT load-displacement (P_n-d) curves for annealed WHAs: a) 90W; b) 92.5W; c) 95W; and d) 97W, respectively

Table 4. RT maximum load fracture toughness (K_{Jm}) of as-received [22] and annealed WHAs

Condition/Alloys	90W	92.5W	95W	97W
As-received	97 ± 18	96 ± 12	107 ± 14	69 ± 12
Annealed	127 ± 11	100 ± 7	117 ± 2	98 ± 17

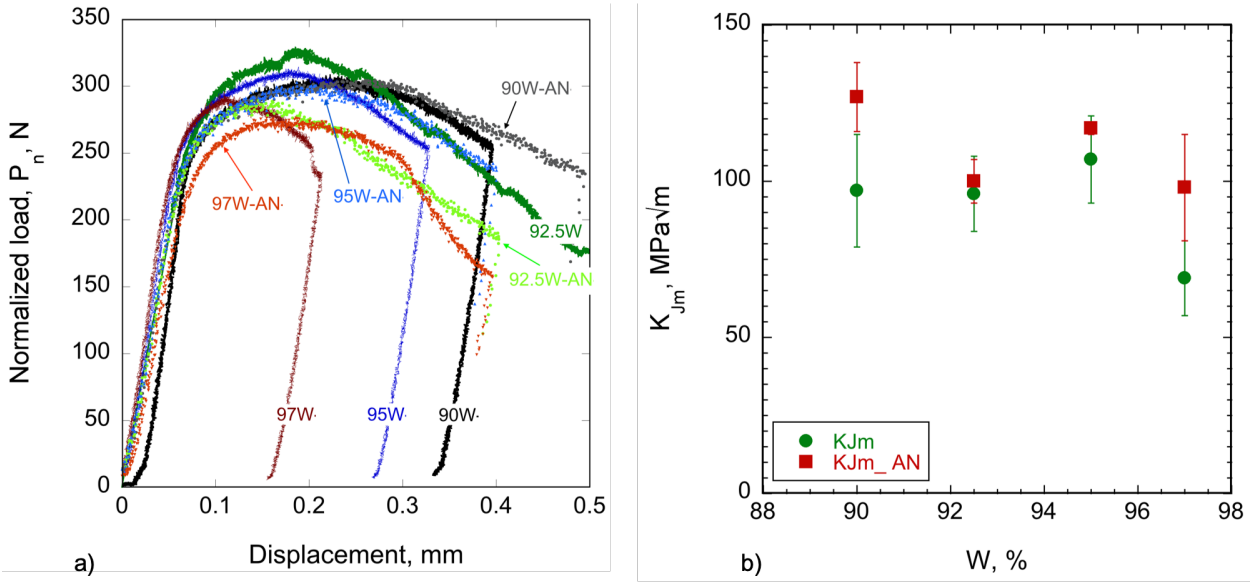

Figure 6. a) Normalized RT load-displacement (P_n-d) curves for as-received and annealed WHAs; and b) corresponding average maximum load fracture toughness, K_{Jm} in MPa√m.

Damage mechanism for tensile specimens

Figure 7 shows the side surface SEM micrographs for the RT tensile tested WHAs for as received and annealed conditions. The lower magnification SEM images for the as-received 90W to 97W WHAs are shown in Figure 7a-d, whereas for annealed 90W to 97W WHAs are shown in Figure 7e-h. Relatively higher magnification SEM images for the respective alloys are shown in Figure 7i-l for as-received and in Figure 7m-p for annealed conditions. It can be seen from the lower magnification SEM images for as-received WHAs (Figure 7a-d) that the number of side-surface cracks or damaged area reduce with increasing W% in the WHA alloys. The qualitative crack density is also reduced away from the fracture tip for the same specimen. Corresponding high magnification SEM images show that the W-particles are deformed, micro cleaved, arrested, and blunted by the DP phases for the lower W% WHAs (i.e., 90W and 92.5W, Figure 7i,j). These cracks become much sharper with increasing W contents that interconnect to span several particles before failure without troubling neighbouring particles, especially for as received 95/97W WHAs (Figure 7k,l), responsible for their lower ductility. For the as-received conditions, the DP effectively holds, carries, and transfers the load to W-particles; hence, they deform simultaneously before failure. Details tensile test damage development for as-received WHAs can be found in Reference [22].

In contrast to as-received WHAs, all the annealed WHAs, including 97W, show well-distributed damage development throughout the gage length (Figure 7e-h). High magnification side surface SEM micrographs for annealed tensile specimens also revealed that the damage mechanism had been changed (Figure 7m-p). The 1300 ºC/24 h annealing might help homogenize the composite microstructure and soften the lower melting point (MP ≈ 1500 ºC) DP compared to high MP (≈ 3410 ºC) W particles. Therefore, only the DP phase all over the gage length has been deformed, whereas W particles remain relatively undeformed.

Global DP deformations, especially for 95W and 97W WHAs, help to improve overall ductility for annealed WHA compared to their as-received counterpart. However, individual phase properties before and after annealing need to be confirmed, which will be estimated by nanoindentation in the future.

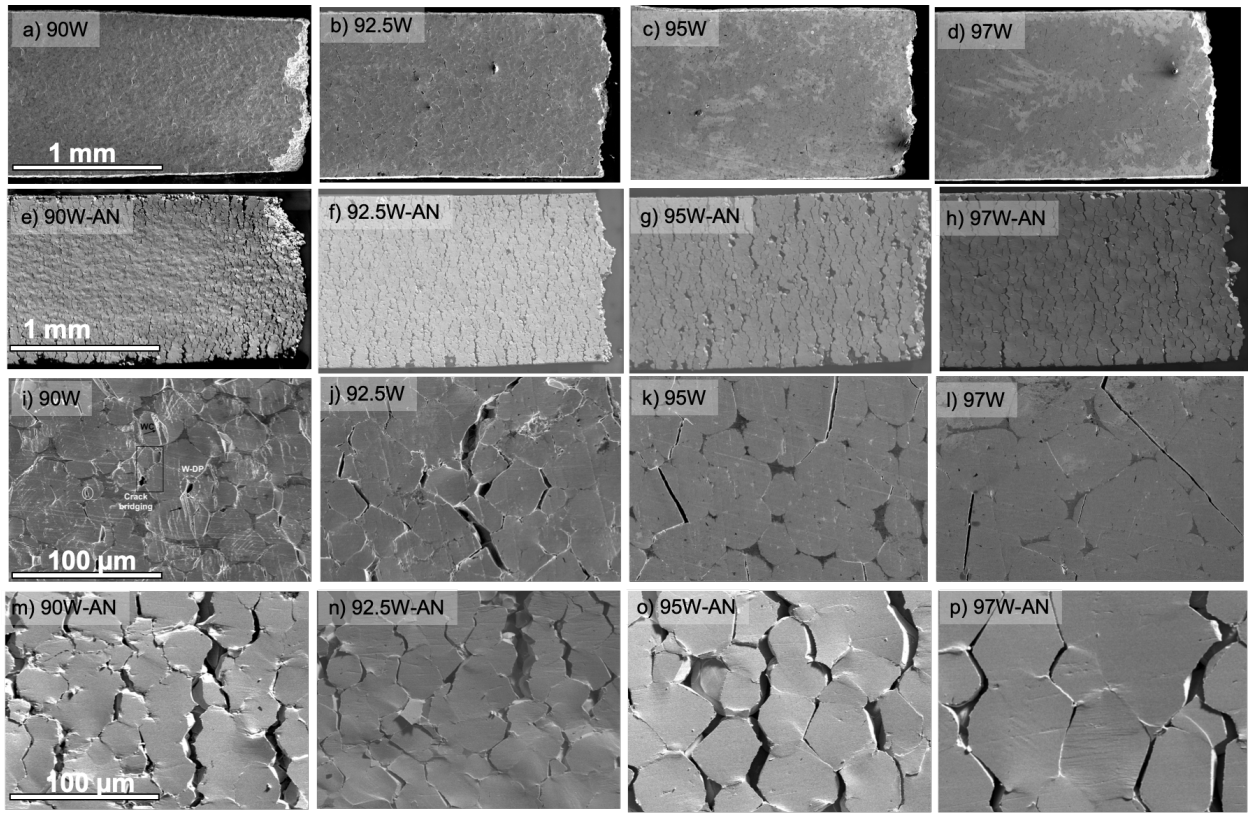

Figure 7. SEM micrographs on the side surface tensile specimens for a-d) as-received, and e-h) 1300 ºC/24 h annealed WHA's for 90W, 92.5W, 95W and 97W, respectively. Higher magnification SEM images for respective WHAs are shown in (i-l) as-received and (m-p) annealed conditions. Scale bars for the respective rows are shown in the first column.

The SEM micrographs on the fractured face of the broken RT tensile as-received and annealed WHA specimens are shown in Figure 8 that manifests all well-known four local failure modes, namely: W-W interparticle fracture (WW), W cleavage (WC), W-NiWFe interfacial debonding (WD), and NiWFe ductile phase rupture (DR). However, as evident from the side surface observations, fractured face also shows a relatively higher number of WC for the as-received condition, whereas more DP is observed for the annealed condition for the respective WHA alloy.

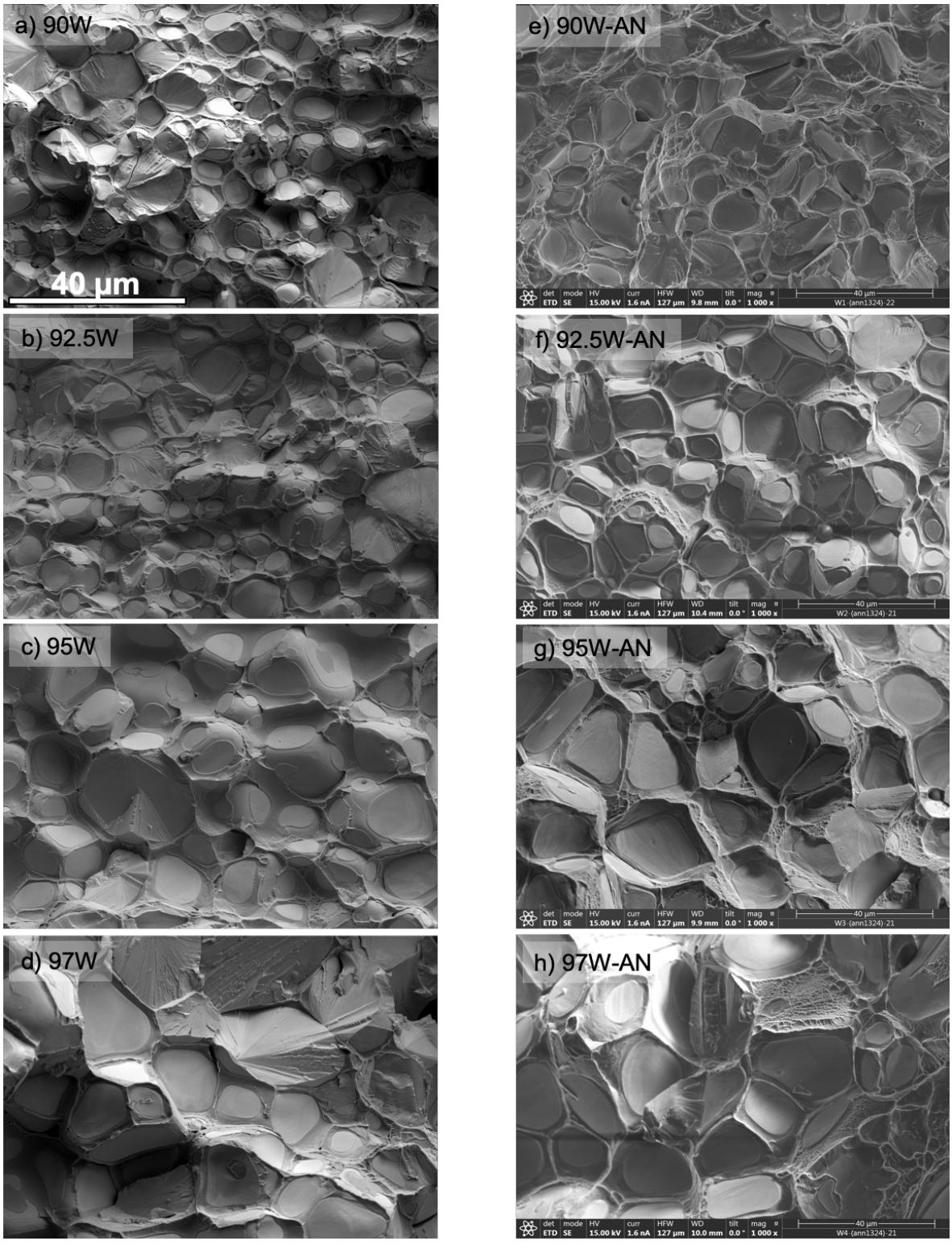

Figure 8. SEM micrographs on the fractured face for tensile specimens for: a-d) as-received, and e-h) 1300 ºC/24 h annealed WHA's for 90W, 92.5W, 95W, and 97W, respectively.

Damage mechanism for fracture toughness specimens

Side surface observations for all the RT as-received toughness specimens show large numbers of particle-sized WC blunted microcracks in the process-zone with decreased density from lower to higher content WHAs (Figure 9a-d, and Reference [22]). Some W-DP interfacial debonding (WD) and WW interface fracture events are also observed (Figure 10a,b). The WC microcracks might have initiated at small pores in the as-received WHAs. The NiWFe DP and blunt arrest the microcracks under increased loading. A few microcracks are linked up to 2 to 3 particle diameters, especially in the 97W WHA due to low DP (Figure 10b). Like in the tensile tests, cleaved and unbroken W particles are also deformed along the principal stress direction. The strain in W particles normal to the loading direction, including the blunted microcracks, is again higher in the 90W WHA compared to that in 97W WHA. Nevertheless, in general, all of these events develop a new ductile-phase toughening mechanism that involves process zone microcrack formation, arrest, blunting, and bridging by DP, as opposed to the classical macrocrack bridging and deflection toughening. Detailed damage mechanism for the RT as-received WHAs can be found in Reference [22].

The side surface damage profile for fracture toughness annealed specimens shows similar events like the tensile damage mechanism for annealed WHA (Figure 9e-h). Opposite to the as-received damage profile, the 1300 ºC/24 h annealed WHAs show a well distributed plastic process, nearly equal in the area (or volume), irrespective of WHA alloys, though the density of damage is lower for higher W content annealed WHAs due to larger particle size. High magnification SEM images on the side surface annealed 90W and 97W WHA shown in Figure 10c and d, respectively, reveal the shifting of damage mechanism to ductile phase deformation and decohesion dominated mechanism from process-zone W-particles microcracking, arrest, and blunting mechanism for as-received WHAs.

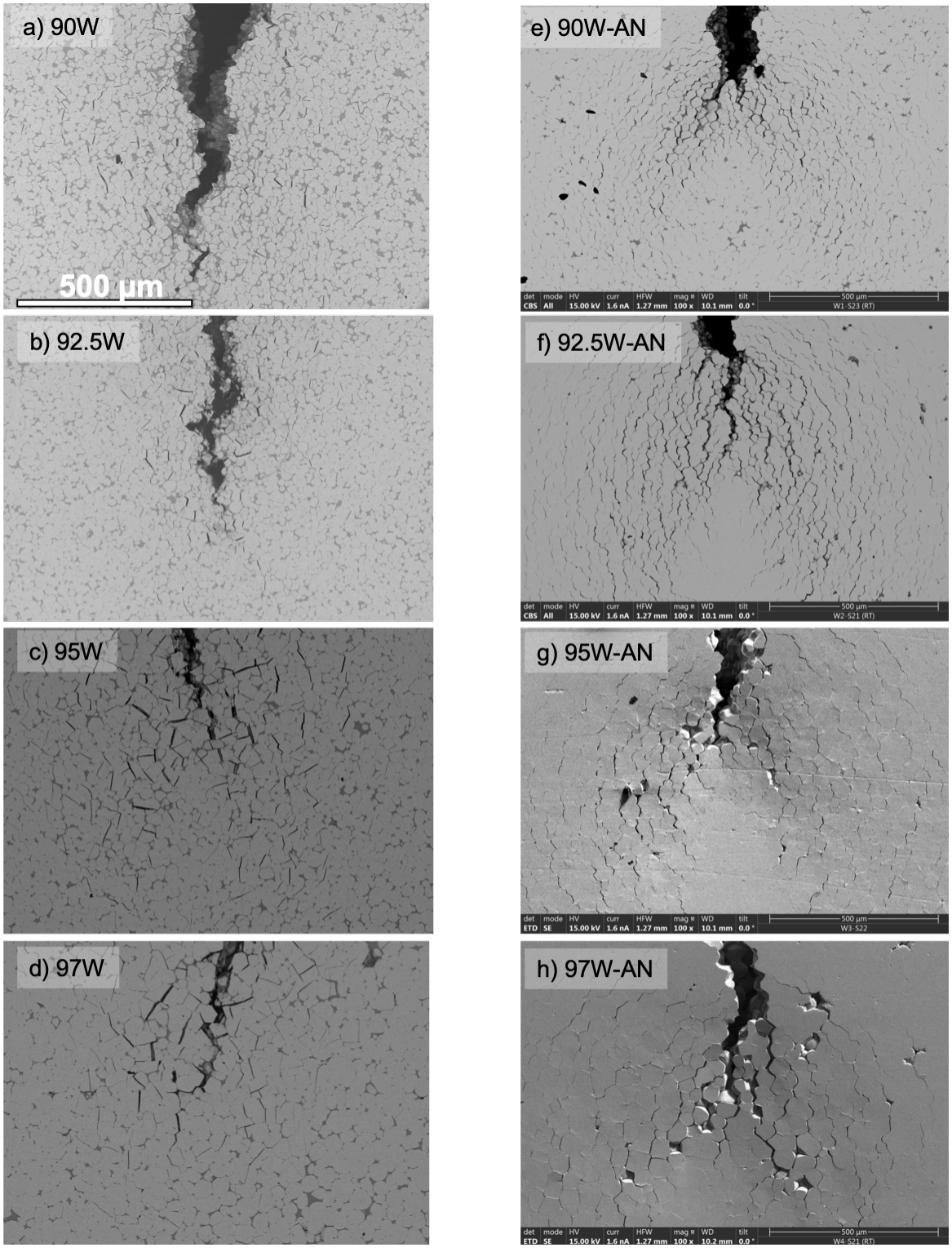

Figure 9. Low magnification, side surface SEM micrographs for the fracture toughness WHAs specimens: a-d) as-received; e-h) 1300 ºC/24 h annealed condition. Scale: 500 µm.

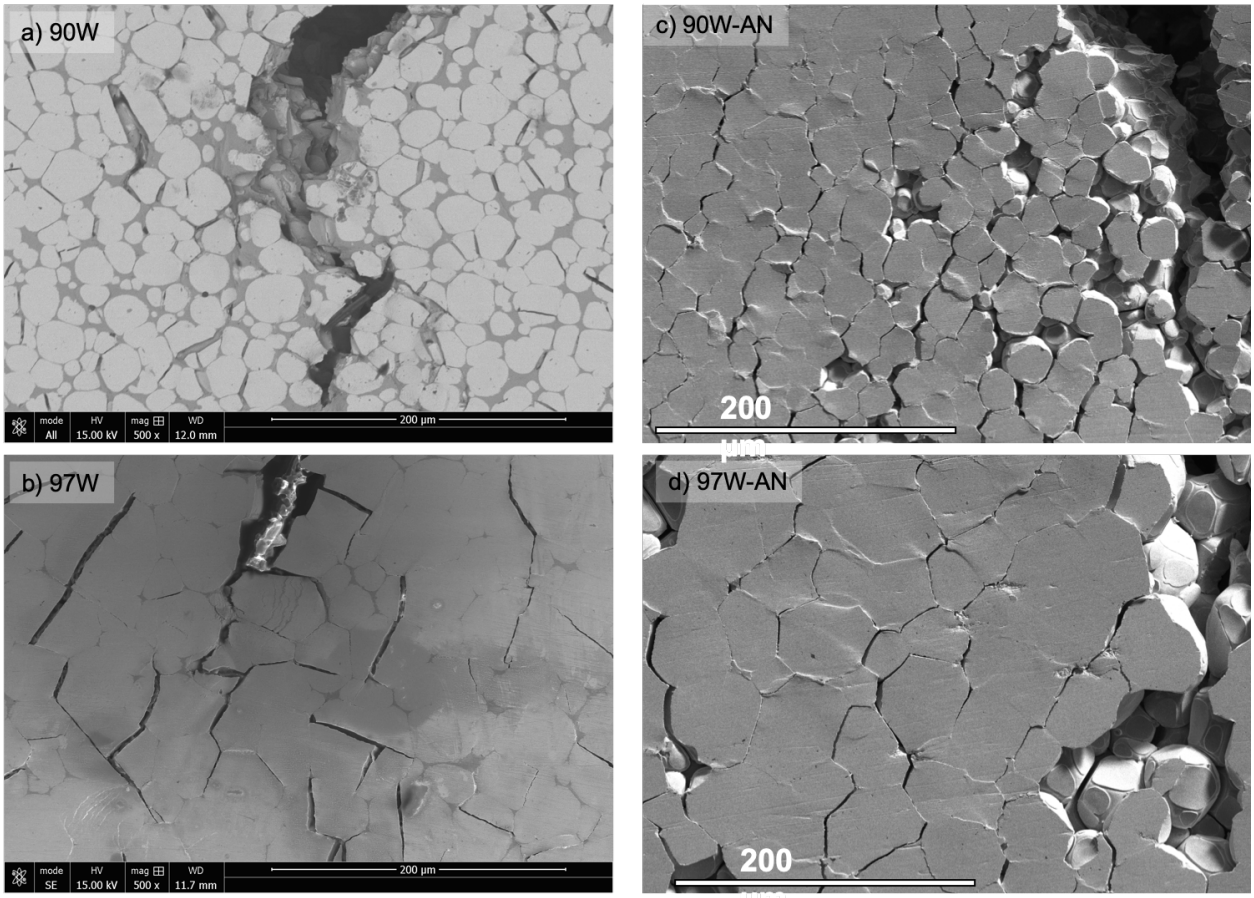

Figure 10. High magnification, side surface SEM micrographs for the fracture toughness WHAs specimens: a-b) as-received 90W and 97W; c-d) 1300 ºC/24 h annealed 90W, and 97W, respectively. Scale: 200 µm.

Figure 11 shows the high magnification SEM images probed on the fractured face of toughness bend bars, both for as-received (Figure 11a-b for 90W and 97W, respectively), and annealed (Figure 11c-d for 90W and 97W, respectively) conditions. All four local fracture modes (i.e. WW, WC, WR and DR) in all cases were measured by line intercept method (LIM) that are shown in Table 5 and plotted in Figure 12. The variation of local fracture modes for the respective alloys before and after annealing seems negligible, though qualitatively, the presence of DR seems higher for the respective annealed WHAs (Figure 11).

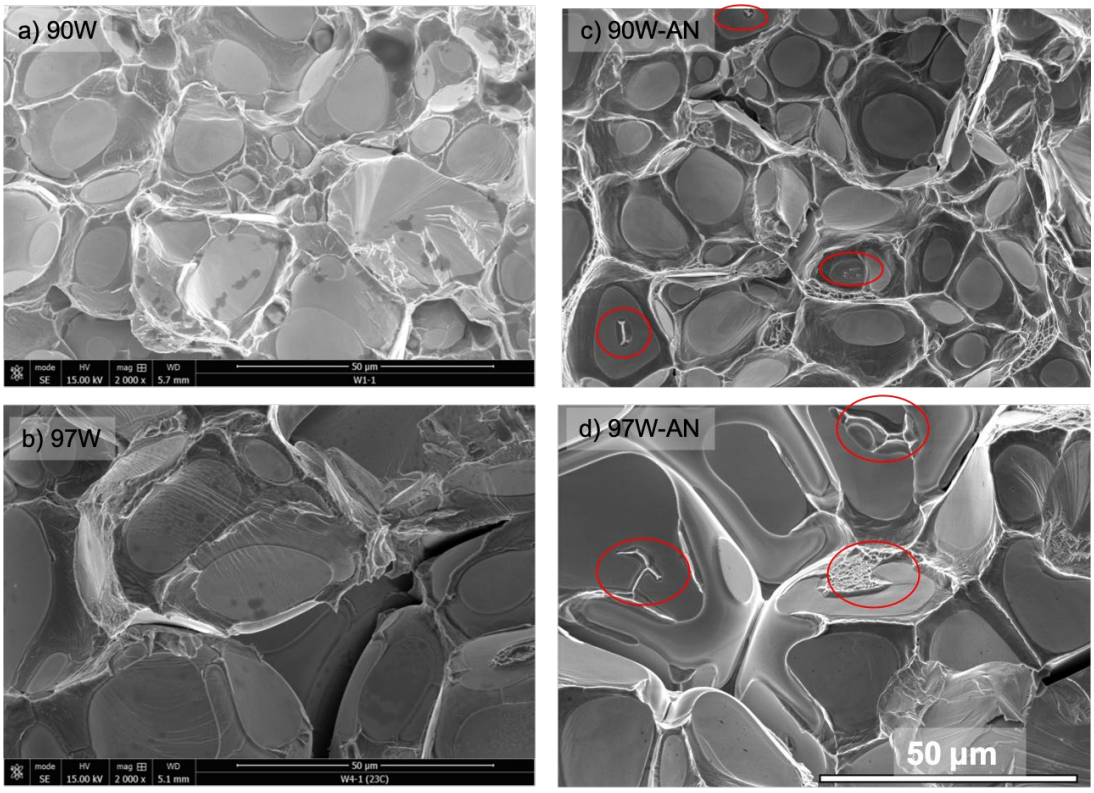

Figure 11. High magnification SEM micrographs on fractured face for the fracture toughness WHAs specimens: a-b) as-received 90W and 97W; c-d) 1300 ºC/24 h annealed 90W, and 97W, respectively. Scale: 50 µm.

Table 5. The percentage of local fracture features from toughness fractographs of WNiFe

WHAs	Condition	WW	WC	WD	DR
90W	As-received	31.7	12.0	44.1	12.2
	Annealed	35.4	8.8	45.7	10.1
92.5W	As-received	37.1	10.9	40.5	11.5
	Annealed	47.8	7.7	37.2	7.3
95W	As-received	42.6	13.5	32.8	11.1
	Annealed	45.2	13.7	33.5	7.6
97W	As-received	67.2	17.6	10.8	4.4
	Annealed	56.2	22.5	16.9	4.4

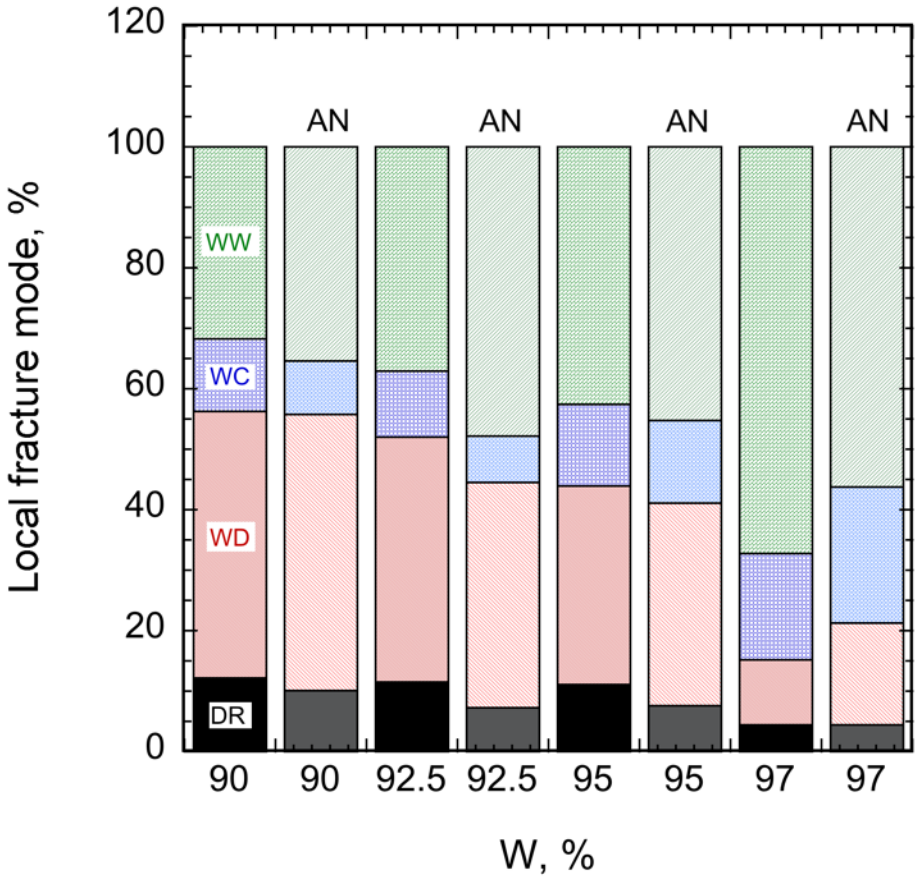

Figure 12. Local fracture modes for all the as-received and annealed 90 to 97 W WHAs.

Conclusion

Annealing performed on four different WHAs from 90W to 97W reveals that 1300ºC/24h annealing has minimum effect on microstructure when compared with the as-received condition. After annealing, the microhardness reduces for higher W content WHAs (16% for 97W). However, tensile strength almost remains the same for all alloys at both conditions, though the uniform and total elongation doubles for 95W and 97W. After annealing, RT fracture toughness for all alloys also improves up to 42% (for 97W), except 92.5W WHA, which remains almost the same. Damage development mechanisms, both for RT tensile and fracture toughness specimens, also shift from process-zone W-particles microcrack formation, and dilatational toughening for the as-received condition to DP decohesion-based mechanism for annealed WHAs.

Future Work

Nanoindentation will be probed on each of the individual phases for all alloys and conditions to understand their effect on strength and toughness.

Size effect has been observed for the small baseline specimens for as-received condition, especially for 97W WHA. However, the size effect is minimal for 3x large specimens. Therefore, 3x large specimens will be annealed at the same 1300 ºC/24h condition.

High temperature tests of fracture toughness and subcritical crack growth rates will be initiated.

Acknowledgments

We like to acknowledge the support provided by U.S. Department of Energy (DOE) through the Office of Fusion Energy Sciences PNNL under contract DE-AC05-76RL01830 and UCSB DOE-Fusion 8-442520-22419-3. The U.S. National Science Foundation supported California Nanoscience Institute provided facilities critical the success of this research.

References

[1] Y. Şahin, Recent progress in processing of tungsten heavy alloys, J. Powder Technol. 2014 (2014) 1–22.

[2] K. Hu, X. Li, X. Ai, S. Qu, Y. Li, Fabrication, characterization, and mechanical properties of 93W-4.9Ni-2.1Fe/95W-2.8Ni-1.2Fe/95W-2.8Ni-1.2Fe-1Al2O3 heavy alloy composites, Mater. Sci. Eng. A. 636 (2015) 452–458.

[3] X. Gong, J. Fan, F. Ding, Tensile mechanical properties and fracture behavior of tungsten heavy alloys at 25-1100 °C, Mater. Sci. Eng. A. 646 (2015) 315–321.

[4] U.R. Kiran, A. Panchal, M. Sankaranarayana, G.V.S.N. Rao, T.K. Nandy, Effect of alloying addition and microstructural parameters on mechanical properties of 93% tungsten heavy alloys, Mater. Sci. Eng. A. 640 (2015) 82–90.

[5] W.D. Cai, Y. L, R.J. Dowding, F.A. Mohamed, E.J. Lavernia, A review of tungsten-based alloys as kinetic energy penetrator materials, Rev. Part. Mater. 3 (1995) 71–131.

[6] C. Henager Jr, W. Setyawan, T. Roosendaal, N. Overman, B. Borlaug, E. Stevens, K. Wagner, R. Kurtz, G.R. Odette, B. Nguyen, K. Cunningham, Ductile-phase toughened tungsten for plasma-facing materials in fusion reactors, Int. J. Powder Metall. 53 (2017) 53–69.

[7] M. Scapin, Mechanical characterization and modeling of the heavy tungsten alloy IT180, Int. J. Refract. Met. Hard Mater. 50 (2015) 258–268.

[8] R. Neu, H. Maier, M. Balden, S. Elgeti, H. Gietl, H. Greuner, A. Herrmann, A. Houben, V. Rohde, B. Sieglin, I. Zammuto, Investigations on tungsten heavy alloys for use as plasma facing material, Fusion Eng. Des. 124 (2017) 450–454.

[9] R. Neu, H. Maier, M. Balden, R. Dux, S. Elgeti, H. Gietl, H. Greuner, A. Herrmann, T. Höschen, M. Li, V. Rohde, D. Ruprecht, B. Sieglin, I. Zammuto, Results on the use of tungsten heavy alloys in the divertor of ASDEX Upgrade, J. Nucl. Mater. 511 (2018) 567–573.

[10] H. Sattar, S. Jielin, H. Ran, M. Imran, W. Ding, P. Das Gupta, H. Ding, Impact of microstructural properties on hardness of tungsten heavy alloy evaluated by stand-off LIBS after PSI plasma irradiation, J. Nucl. Mater. 540 (2020) 152389.

[11] Q. An, A. Elshafiey, L. Huang, D.A. Hammer, M. Hassani, Plasma and X-ray radiation-induced damage mechanisms in a tungsten heavy alloy, J. Nucl. Mater. 539 (2020) 152325.

[12] G.R. Odette, M.E. Alam, K. Cunningham, Ductile-Phase Toughened Tungsten for Plasma Facing Materials, DOE-UCSB-ER54275, United States, 2019.

[13] T. Laas, K. Laas, J. Paju, J. Priimets, S. Tõkke, B. Väli, V. Shirokova, M. Antonov, V.A. Gribkov, E. V. Demina, V.N. Pimenov, M. Paduch, R. Matulka, M. Akel, Behaviour of tungsten alloy with iron and nickel under repeated high temperature plasma pulses, Fusion Eng. Des. 151 (2020).

[14] W.D. Klopp, W.R. Witzke, Mechanical properties and recrystallization behavior of electron-beam-melted tungsten compared with arc-melted tungsten, 1966.

[15] J. V. Haag IV, D.J. Edwards, C.H. Henager, W. Setyawan, J. Wang, M. Murayama, Characterization of Ductile Phase Toughening Mechanisms in a Hot-Rolled Tungsten Heavy Alloy, Acta Mater. 204 (2020) 116523.

[16] K. Tsuchida, T. Miyazawa, A. Hasegawa, S. Nogami, M. Fukuda, Recrystallization behavior of hot-rolled pure tungsten and its alloy plates during high-temperature annealing, Nucl. Mater. Energy. 15 (2018) 158–163.

[17] A. Alfonso, D. Juul Jensen, G.N. Luo, W. Pantleon, Thermal stability of a highly-deformed warm-rolled tungsten plate in the temperature range 1100-1250 °c, Fusion Eng. Des. 98–99 (2015) 1924–1928.

[18] G.M. Wright, D. Brunner, M.J. Baldwin, K. Bystrov, R.P. Doerner, B. Labombard, B. Lipschultz, G. De Temmerman, J.L. Terry, D.G. Whyte, K.B. Woller, Comparison of tungsten nano-tendrils grown in Alcator C-Mod and linear plasma devices, J. Nucl. Mater. 438 (2013) S84–S89.
[19] D. Dasgupta, D. Maroudas, B.D. Wirth, Prediction of temperature range for the onset of fuzz formation in helium-plasma-implanted tungsten, Surf. Sci. 698 (2020) 121614.
[20] M.E. Alam, G.R. Odette, C.H. Henager, W. Setyawan, Fracture Toughness of Rolled 90WNiFe Tungsten Heavy Metal Alloy, Fusion React. Mater. Progr. Semiannu. Prog. Rep. DOE0313/67 (2019) 52–65.
[21] J. Wang, D. Collins, N.R. Overman, W. Setyawan, Tensile Testing and Microstructural characterization of Ductile Phase Toughened W-NiFe Alloys, Fusion React. Mater. Progr. Semiannu. Prog. Rep. DOE0313/68 (2020) 102–120.
[22] M.E. Alam, G.R. Odette, On the remarkable fracture toughness of 90 to 97W-NiFe alloys revealing powerful new ductile phase toughening mechanisms, Acta Mater. 186 (2020) 324–340.

4.3 UPDATE ON THE INFLUENCE OF SPECIMEN SIZE AND GEOMETRY ON THE FRACTURE TOUGHNESS OF TUNGSTEN HEAVY METAL ALLOYS—M.E. Alam, G.R. Odette (University of California, Santa Barbara)

OBJECTIVE

This study aims to assess the effect of specimen size and geometry on the room temperature fracture toughness of tungsten heavy metal alloys for future fusion divertor application.

SUMMARY

We previously showed that commercial tungsten (W)-based heavy metal alloy (WHA) composites containing 90 to 97 wt.% W, reinforced with 3 to 10 wt.% NiFe ductile phase (DP), have room temperature (RT) maximum load elastic-plastic fracture toughness (K_{Jc}) values of ≈ 70 to 110 MPa√m, which are far higher than for monolithic W (≈ 8 MPa√m). In all cases, fracture took place by stable ductile crack tearing. However, these results are based on very small (16 x 3.3 x 1.65 mm) bend bar tests, which naturally raises the issue of size effects on the measured K_{Jc}. Here, we experimentally assess size and geometry effects on the K_{Jc} of WHA. Since the fracture processes are somewhat similar, we analyze the WHA results in terms of validity criteria that have been developed for cleavage and ductile tearing R-curve fracture of steels. Specifically, we examine the relation between K_{Jc} and a dimensionless elastic-plastic zone confinement deformation criteria $M = \sigma_o b_o/J_c$. Here σ_o is the flow stress, J_c is the measured J at maximum load (assumed to approximately coincide with crack extension) and b_o is the unbroken ligament dimension. Tests on bend specimens from 3 to 8 times larger than original small bend bar suggest that the M required for size independence of K_{Jc} is ≈ 200. However, the DP fraction also plays a role, and there are additional effects of compact tension versus bend bar specimen geometries, likely related compliance effects of post-initiation crack stability under load control.

BACKGROUND

Tungsten's (W) remarkable combination of high melting temperature, strength, thermal conductivity, and low sputtering rates make it the leading candidate for the plasma-facing fusion reactor components [1–4]. Unfortunately, intrinsically high brittle to ductile transition temperatures, coupled with low toughness and tensile ductility, which are further degraded neutron irradiation, may limit the use of monolithic W as a structural material for fusion applications [1–8]. Fortunately, the introduction of small amounts of a ductile phase (DP) can increase the toughness of brittle matrix materials [9–12], like W heavy alloys (WHA). Such ductile phase toughening (DPT), in the WHA studied here, was provided by embedding brittle W-particles in a honeycomb of a Ni-Fe-W ductile solid solution phase [13–29].

The advantages and open questions about WHA related to fusion service are described elsewhere [17,30–35]; and WHA fabrication routes and basic properties are the subjects of extensive literature [18–20,27,36,37]. The dominant limiting structural property for W and W-alloys is often low fracture toughness [3,7,8,38]. Fracture toughness is likely to be especially important for fusion divertor applications, with high and cyclic thermal loads, often resulting in the formation of many sharp surface cracks in W [1,2,39,40]. However, only a few papers in the literature report pre-cracked fracture toughness K_{Jc} data on WHAs [26,30,32].

Classical ductile phase toughening systems are primarily due to bridging a macrocrack's wake, propagating in a brittle matrix, and crack arrest-re-nucleation-deflection mechanisms [9,11]. However, in the case of the WNiFe WHA, toughening is dominated by *microcrack* arrest, blunting, and bridging in a fully ductilized crack tip plastic process zone [30]. Plastic and process zone deformation, including the embedded W particles, and dilatational effects of microcrack blunting, dissipate large amounts of energy. Further, the process-zone dilatation extensively shields (lowers) the crack tip stress fields, suppressing further fracture processes.

These mechanisms lead to the ductilization of the entire W-NiFe biphasic microstructure resulting in large crack tip opening displacement (CTOD) ductility, and the corresponding development of large classical plasticity zones. The microscopic damage in the process zone involves W cleavage (WC), W particle-particle boundary fracture (WW), ductile phase rupture (DP), and W-DP decohesion (WD) [30]. Ductile rupture (DR) of the DP ligaments surrounding arrested microcracks and decohered W-particle associated voids results in the various forms of damage coalescence. Thus, on a meso-macro scale, the RT fracture of the W-NiFe WHA resembles either: a) intergranular fracture (WW); b) quasi cleavage (WC) or; c) coalescence of the decohered microvoids (WD). Note, however, in WHA, the plastic microcrack blunting shielding is far more effective than that provided by elastic microcracks in brittle matrix systems [41–43].

Given the similarities of the fracture processes, it follows that the deformation limits that define self-similar small-scale yielding (SSY) fields and other validity criteria in steels may, with appropriate modification, be applicable to the WHA. The SSY stress fields peak at 3-5 times the σ_y (depending on the strain hardening) at a distance of ≈ 2 CTOD ahead of a blunting crack [44]. In steels, cleavage occurs when the local fields greater than critical stress encompass a critical volume of material in front of the crack tip [45–47]. Note that this local fracture process can also describe the weakest link (Weibull) statistics [44,47]. An alternative view is that ductile crack extension (tearing) of the macrocrack occurs when the arrested blunted microcrack coalesces by crack tip strain-controlled rupture of the DP ligaments. Crack propagation in WHA involves a varying combination of these fracture modes.

In our previous study [30], we measured K_{Jc} in four 90 to 97W-NiFe WHAs from RT down to liquid nitrogen temperature (-196 °C), using fatigue pre-cracked bend bars, generally following ASTM E1921 test standards [48]. The WHA alloys were shown to have much higher RT toughness (≈ 9x to 13x) and much lower brittle to ductile transition temperatures (BDTT -150 ºC for 90W to -25 ºC for 97W) compared to monolithic W (typically, several hundred °C) [5,30,49].

However, these results were based on tests using small bend bar specimens (thickness B ≈ 1.65 mm, ligament b_o = 1.65 - 2 mm, width W = 2B; span S = 4W) [30]. While, due to the high yield strength and elastic moduli of the WHA, the tests were nominally consistent with the ASTM E-1921 criteria for avoiding constraint loss effects, the small specimen dimensions naturally raise the questions about size effects [46,47,50,51].

Size and geometry effects in steels for cleavage fracture arise from: a) triaxial constraint loss beyond a small-scale yielding (SSY) deformation limit, which lowers the high blunting crack tip stress fields; and b) weakest link statistical effects in highly stressed near tip volumes, associated with differences the crack front length. Singly, and in combination, these mechanisms result in a decrease in the average measured cleavage K_{Jc} with increasing cracked body size. Ductile tearing fracture is also affected by lower stress triaxiality at small specimen size beyond SSY deformation limits. And, in the limit, ductile fracture may occur at net section stress limits for massive crack tearing and specimen hinging [44]. Here we probe the effect of specimen size on the measured K_{Jc} by testing specimens that are 3, 6, and 8 times (3x, 6x and 8x) larger than the small (1x) bend bars. We test a compact tension (CT) with a B that is ≈ 5.5x that of the 1x bend bar.

Various criteria are used to specify the SSY deformation limits in steels. The most relevant is the ASTM Standard E1921 ASTM Master Curve Standard Practice "T_o" for determining the K_{Ic} and K_{Jc} fracture toughness of steels in the cleavage transition. ASTM E1921 specifies a deformation limit for determining the master curve 100 MPa$\sqrt{m}$ reference temperature T_o as

$$K_{Jlim} = \sqrt{[b_o \sigma_y E'/30]}$$
$$E' = E/[1-\nu^2]$$

Here, σ_y is the yield stress, E is the elastic modulus, and ν is Poisson's ratio. However, the deformation limit actually should be expressed in terms of the elastic-plastic J-integral at fracture (J_{lim}), as
$J_{lim} = b_o \sigma_o / M$.

Thus, E', which is ≈ 232 GPa for steels versus the average of 432 GPa for 90- to 97W WHA, has no effect on the deformation limit. The E1921 M for steels is 30, but accounting for differences in the E' between steels and WHAs, the equivalent ASTM E-1921 for WHA deformation limit is $30E'_{WHA}/E_{steel} \approx 56$. However, the E-1921 deformation limit for steels is known to be far too permissive, and M from 100 to 200 is more required to completely avoid constraint loss in bend bars.

The report is organized as follows under the PROGRESS AND STATUS section. Following an Experimental Procedure Section, the Results Section summarizes the effects of the specimen size on: the load-displacement curves and the corresponding maximum load plastic K_{Jp}, elastic K_{Ic} and total K_{Jm} values as a function of $\sigma_o b_o/J_t$, (here, $J_t = J_{Jm} = J_p + J_e$), for WHA with various DP contents. We also describe the crack propagation modes, fracture surface damage statistics, side surface deformation, and micro-cracking observations. A Discussion Section summarizes specimen size and geometry effects for WHA. We also assess the effect of ductile phase fractions.

PROGRESS AND STATUS

Experimental Procedure

Materials

Four commercial (Mi-Tech Metals, Indianapolis, IN, USA) liquid-phase sintered (LPS) WHA were received in the form of 100 mm x 100 mm x 14 mm plates. These WHA plates contained 90, 92.5, 95, and 97W (wt. %) with a DP balance of an initial 70% Ni and 30% Fe. The DP is nominally enriched with W during the liquid phase sintering to an fcc solid solution composition of ≈ 50% Ni, 30% W, and 20% Fe (wt.%) for the W-NiFe WHAs. The NiWFe phase forms a semi-continuous thin-walled honeycomb web structure surrounding the much larger volume fraction of W-particles.

Characterization

The WHA specimens were fabricated by electrical discharge machining (EDM), ground with 220 to 2000 grit sandpaper to remove EDM damage and residual surface stresses, selectively polished down with 0.5μ-diamond paste, and finally etched in a 30% hydrogen peroxide solution for 10 min to facilitate microstructural characterization. Scanning electron microscopy (SEM) with energy dispersive spectroscopy (EDS) was used to image the W particles and the surrounding ductile phase, and to identify their respective compositions. The W particle size distribution was determined by sampling ~ 500 individual grains using 'ImageJ64' software. The W particle size increases from 17 ± 7 μm for 90W to 38 ± 15 μm for 97W [30]. The DP area fraction, which decreases from ≈ 16 ± 4% for 90W to ≈ 6 ± 2% for 97W, was measured by converting the SEM BSE micrographs into binary black-white images and measuring the associated DP area portion, whereas the DP ligament thickness (≈ 5 ± 5 μm for all WHAs) was measured by line-intercept method (LIM) [30].

Room temperature fracture toughness tests were conducted on three-point bend (3PB) bars with length, width and thickness of: small 1x ≈ 16 x 3.33 x 1.67 mm, medium = 3x, large = 6x and extra-large = 8x dimensions. The specimens were fatigue pre-cracked to nominal crack length (a)-to width (W) ratio, (a/W) ≈ 0.40 to 0.5 at a maximum ΔK_I =18 MPa$\sqrt{m}$ and a load ratio, R = 0.1. The specimens were heat-tinted at 400 ºC for 1 to 5 mins, depending on specimen thickness. The 3PB tests with a span S/W ratio of ≈ 4 were carried out on an MTS 810 servo-hydraulic universal testing machine. The modified 0.35-CT (length x width x thickness ≈ 20 x 19 x 9 mm) specimens were fabricated from the tested 6x large 95W 3PB bars halves to ensure maximum utilization of materials. The CT specimens were also fatigue pre-cracked to an a/W ≈ 0.45 following the similar pre-cracking procedures to 3PB bars. The detailed CT geometry, tested for this study, can be found elsewhere [52].

The load (P) and load point displacements (d) were measured and the K_{Jm} are defined at the P_m based on the ASTM E1921 standard practice method of estimating the J-integral elastic-plastic contributions $J_m = J_e$

+ J_p, as $K_{Jm} = \sqrt{\{J_m E/(1-\nu^2)\}}$; $J_e = K_e^2(1-\nu^2)/E$; and $J_p = 2A_P/Bb_o$ [48]. Here, E is the elastic modulus (≈ 390 - 405 GPa, increasing with W) and ν is Poisson's ratio (≈ 0.28), B is specimen thickness, b_o is initial unbroken ligament, and A_p is plastic area [44,48,53]. It is also of interest to compare normalized P_n-d_n curves by dividing P by the plane strain limit load P_o, and d by the span (S) of the bend specimen. Here, for the 3PB bar: limit load $P_o = 1.455Bb_o^2\sigma_o/S$, and for CT specimens: $P_o = 1.455\eta Bb_o\sigma_o$ for plane strain conditions, where σ_o = flow stress, and $\eta = \sqrt{[(2a/b_o)^2+(4a/b_o)+2]} – (2a/b_o+1)$ for CT [44]. When the fracture is dominated by well-contained crack tip stress and strain fields (in the limit SSY), $P_n = P/P_o$ is < 1, and decreases with the $\sqrt{a}$ in the elastic regime.

To facilitate *in-situ* optical observation of the crack tip region, the fracture specimen sides were sanded with a sequence of 2000 grit SiC followed by 9μ, 3μ, and 1μ diamond lapping paper. The fracture tests were carried out at a 0.04mm/min crosshead speed. The pre-crack and post-test crack lengths were also measured after the specimens were broken in LN_2 to ensure no further ductile crack extension had occurred. Three to seven specimens were tested for each condition.

The SEM was used to observe the side and fracture surfaces of the broken specimens. Four local fracture modes, namely: W-W interparticle fracture (WW), W-cleavage (WC), W-DP interfacial debonding (WD), and DP ruptures (DR) were measured using a line-intercept method (LIM) [19,30]. Additional details about the characterization techniques can be found elsewhere [30].

Results

Here we summarize the results from the fracture tests including a) normalized P_n-d_n data; and b) $K_{Jc/Ic}$ data as a function of WHA alloy composition and size. Note, the normalized P_n-d_n curves are for facilitating inter-comparisons of the effect of specimen size and DP content, as well as to signal crack-dominated fracture, and are not used to calculate toughness values.

Figure 1 shows typical P_n-d_n curves for the various W contents and specimen sizes from 1x to 8x. Corresponding $K_{Jc/Ic}$ results are plotted in Figure 2 and summarized in Table 1, including those previously reported for the 1x small specimens [30]. Note, not all possible combinations of W contents and specimen size were tested. The P_n-d_n curves in Figure 1a for 1x specimens manifest stable ductile tearing for all the W contents [30]. The P_n curves for 90W to 95W 1x specimens are similar that averaged K_{Jm} ≈ 100 ± 15 MPa$\sqrt{m}$. However, 97W specimen experienced much lower d_n at P_{max}, corresponding to a much lower plastic J_p and these are reflected in their K_{Jm} values (≈ 69 ± 12 MPa$\sqrt{m}$) plotted in Figure 2a. The P_n at the initial deviation from the elastic loading line ranged from 0.662 to 0.717 averaging 0.692 ± 0.025 (Table 2). The corresponding normalized maximum P_n ranged from 0.808 to 0.885, averaging 0. 848 ± 0.038. Notably, these K_{Jm} toughness is still ≈ 9 - 13x higher than that for typical monolithic W of K_{Ic} ≈ 8 ± 4 MPa$\sqrt{m}$.

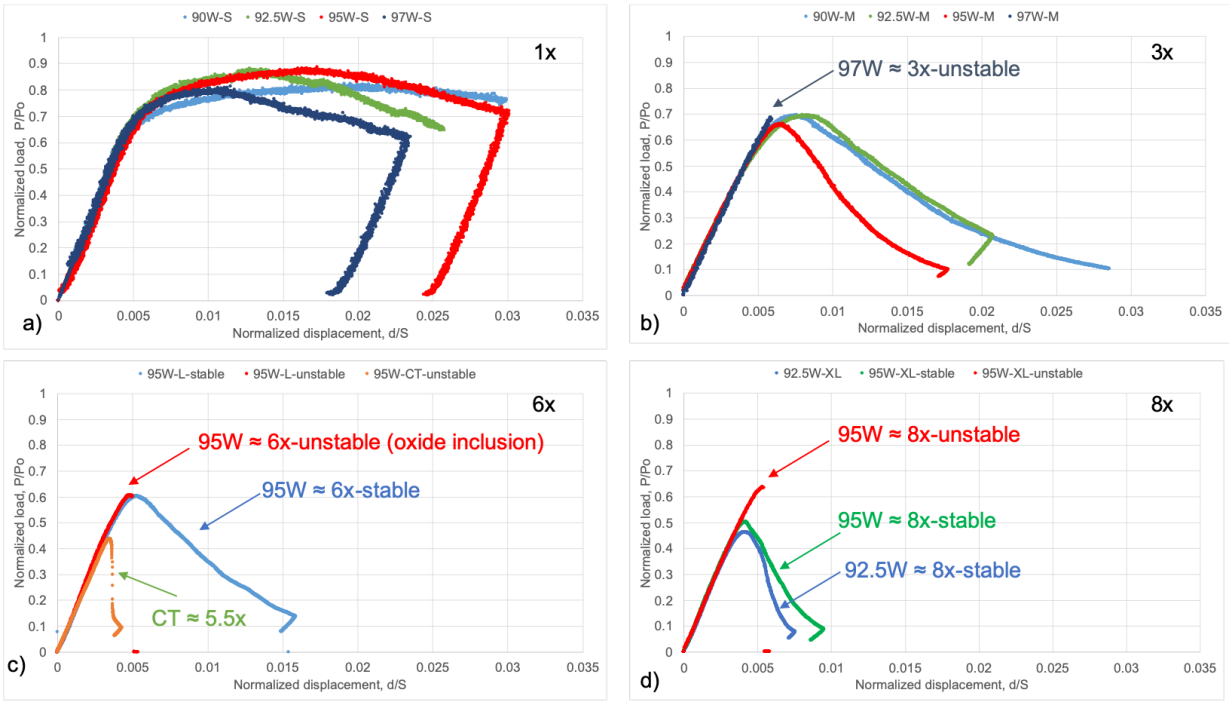

Figure 1. The normalized load-displacement (P_n-d_n) curves for 3PB bars at RT test for a) small, 1x; b) medium, 3x; c) large, 6x; and d) extra-large, 8x specimens, respectively. Note, 0.35-CT (≈ 5.5x) 95W also plotted in Figure 1c.

The normalized P_n-d_n curves for 3x larger specimens are shown in Figure 1b. All the 3x specimens show stable crack growth up to 95W. The K_{Jm} slightly decreases with increasing W (92 ± 6 MPa√m for 90W and 75 ± 4 MPa√m for 95W), while at 97W, the fracture is elastic with an average K_{Ic} ≈ 38 ± 4 MPa√m (Table 1 and Figure 2b). Note, again the K_{Ic} of 3x 97W is still higher by a factor of 4.5 than the monolithic W (8 ± 4 MPa√m). The K_{Jm} differences between 1x and 3x specimens appear to be larger at 95W; however, this is primarily the result of the large deviations of the 1x specimen K_{Jm}, which are due to local microstructural inhomogeneity initiation sites (Figure 3). Note, even though the specimens are characterized from the same plate, the DP area % varies from 13 % to 22 % for the 90W and that for 5 to 9% for the 97W WHA plate (Figure 3). In general, the P_n at the initial deviation for the 3x specimens from the elastic loading line ranged from 0.606 to 0.679 averaging 0.647 ± 0.034. The corresponding normalized maximum P_n ranged from 0.659 to 0.695, averaging 0.683 ± 0.017, which are lower than the 1x specimens.

Table 1. The RT K_{Jm}/K_{Ic}, DP area %, and crack propagation mode as a function of specimen size for the W-NiFe WHAs

WHA alloy/ specimen size*	DP %	K_{Ic}, MPa√m	K_{Jm}, MPa√m	Crack propagation mode
90W_1x	16.8	36 ± 4	97 ± 18	stable
92.5W_1x	12.2	39 ± 4	96 ± 12	stable
95W_1x	11.1	42 ± 6	107 ± 14	stable
97W_1x	6.5	36 ± 5	69 ± 12	stable
90W_3x	15.7	52 ± 2	92 ± 6	stable
92.5W_3x	12.5	50 ± 3	84 + 11	stable
95W_3x	9.3	49 ± 1	75 ± 4	stable
97W_3x	5.3	38 ± 4	-	unstable
95W_6x	8.1	59 ± 1	89 ± 9	stable
95W_6x	6.3	59 ± 1	76 ± 5	unstable (oxide)
95W-5.5x-CT	7.2	49 ± 5	63 ± 8	unstable
92.5W_8x	9.3	55 ± 3	81 ± 7	stable
95W_8x	9.0	60	82	stable
95W_8x	7.6	60	78	unstable

*Small, 1x: B= 1.67 mm; medium, 3x: B = 5 mm; large, 3x: B= 10 mm; extra-large, 8x: B= 12.7 mm. W= 2B; Span = 4W; total length = 4.5W.

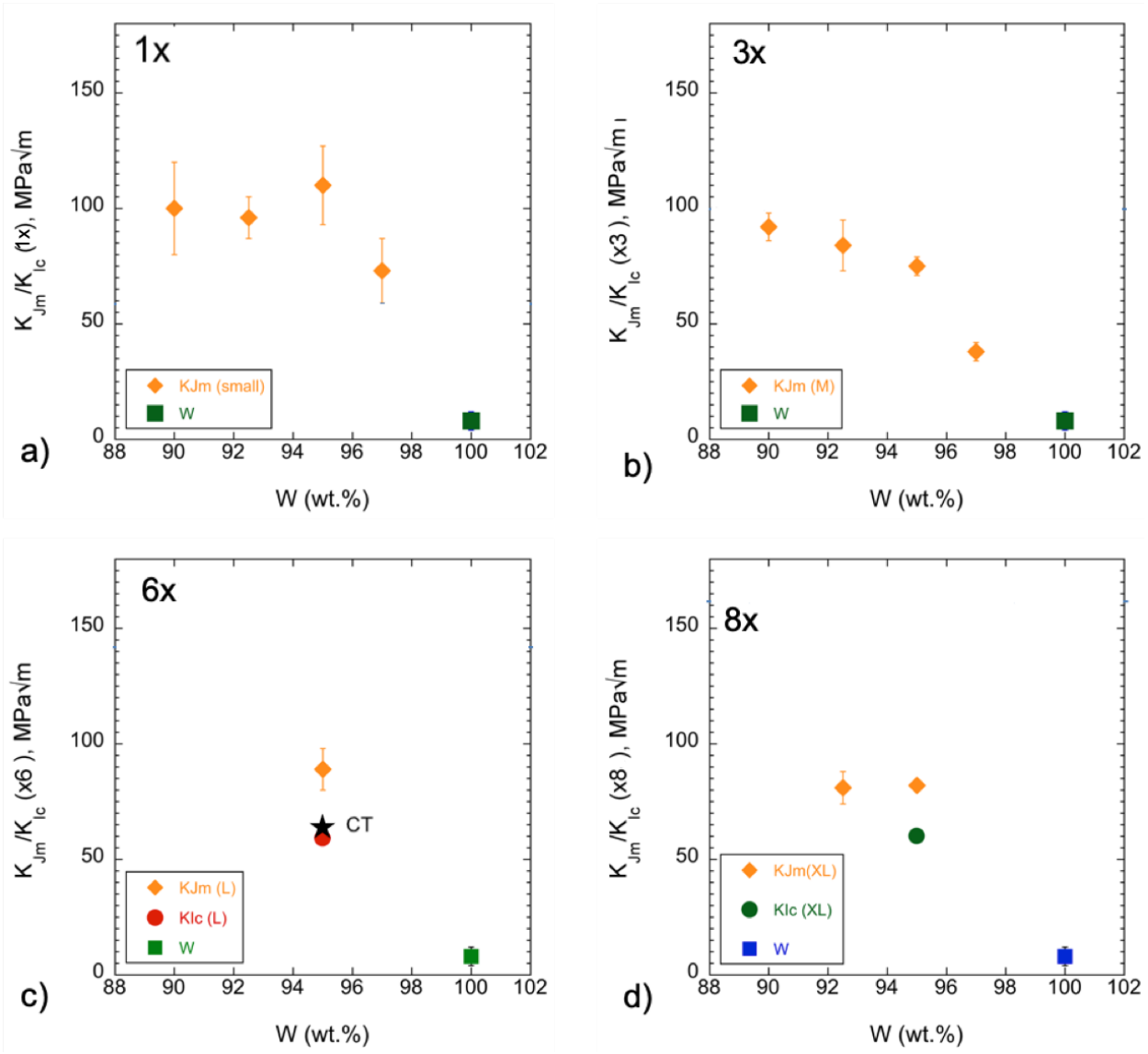

Figure 2. The RT fracture toughness (K_{Jm} or K_{Ic}, in MPa√m) as a function of specimen size for the: a) small, 1x; b) medium, 3x; c) large, 6x and d) extra-large, 8x specimens, respectively. Note, K_{Jm} for the 0.35-CT (≈ 5.5x thick) is also plotted in Figure 2c.

We have further selectively tested 6x (only for 95W) and 8x specimens (for 92.5 and 95W), and their normalized P_n-d_n curves are shown in Figure 1c and 1d, respectively. Out of four RT tests for 6x 95W, only two 6x (B ≈ 10 mm) specimens show ductile tearing, while the other two fractured unstably (Figure 1c). However, in the case of unstable fracture for the 6x 95W, very large oxide inclusions (~1 mm x 0.7 mm) near the pre-crack tip were found and are likely the cause of the unstable elastic crack propagation [52]. The average K_{Jm} for stable 6x 95W is ≈ 89 ± 9 MPa√m, and the oxide-inclusion unstable specimens is ≈ 76 ± 3 MPa√m, considering small plastic yielding before fracture with an elastic K_{Ic} ≈ 59 ± 1 MPa√m (Table 1). Despite the elastic fracture observed in these two specimens, all four specimens show reasonably similar fracture toughness averaging ≈ 82 ± 9 MPa√m (considering the plastic portion of the oxide-inclusion specimens), that falls within the standard deviation range between the 1x and 3x 95W K_{Jm} (Table 1). Here, the average P_n at yield and maximum are ≈ 0.590 ± 0.006, and 0.606 ± 002, respectively, which are much lower than the 1x or 3x specimens' respective values (Table 2).

Table 2. The yield point deviation and maximum values of P_n (= P/P_o) and d/S as a function of specimen sizes, alloys and geometry

WHA/Size	P/Po at yield point	d/S at yield point	P/Po at max	d/S at max	Δ(P/Po)
90W-1x	0.662	0.005	0.824	0.0195	0.162
92.5W-1x	0.707	0.005	0.876	0.0129	0.169
95W-1x	0.717	0.006	0.885	0.0172	0.168
97W-1x	0.682	0.005	0.808	112	0.126
Average	**0.692**	**0.005**	**0.848**	**28.012**	**0.156**
Stdev	**0.025**	**0.001**	**0.038**	**55.992**	**0.020**
90W-3x	0.67	0.00586	0.695	0.00758	0.025
92.5W-3x	0.606	0.0054	0.694	0.0084	0.088
95W-3x	0.633	0.0055	0.659	0.0065	0.026
97W-3x	0.679	0.0059	0.679	0.0059	0
Average	**0.647**	**0.006**	**0.682**	**0.007**	**0.035**
Stdev	**0.034**	**0.000**	**0.017**	**0.001**	**0.037**
95W-6x-stable	0.585	0.0044	0.605	0.005	0.02
95W-6x-unstable	0.594	0.0046	0.608	0.0048	0.014
Average	**0.5895**	**0.0045**	**0.6065**	**0.0049**	**0.017**
Stdev	**0.0064**	**0.0001**	**0.0021**	**0.0001**	**0.0042**
95W-5.5x-CT	0.433	0.0035	0.435	0.0035	0.002
92.5W-8x	0.441	0.0033	0.462	0.004	0.021
95W-8x-stable	0.478	0.0036	0.489	0.0044	0.011
95W-8x-unstable	0.604	0.0048	0.634	0.0054	0.03
Average	**0.5077**	**0.0039**	**0.5283**	**0.0046**	**0.0207**
Stdev	**0.0855**	**0.0008**	**0.0925**	**0.0007**	**0.0095**

Modified 0.35-CT (≈ 5.5x) specimens were fabricated from the tested 6x 95W WHA 3PB bars halves to ensure maximum utilization of materials. Four CT specimens were tested at RT, and all of them show unstable crack propagation after reaching the maximum load. The representative P_n-d_n curve for 0.35-CT (≈ 5.5x) 95W specimens is shown in Figure 1c and toughness values are summarized and plotted in Table 1 and Figure 2c, respectively. The average K_{Jm} or K_{Ic} for 95W CT, which has almost similar thickness ≈ 5.5x to the 6x 3PB 95W, is lower than the other 95W specimens tested in 3PB bend fixture, and can be correlated with the yield or maximum P_n, which is again, much lower for the CT specimens than the 3PB specimens for the same alloy or thickness (Table 2). This can be likely be related to the compliance effects of post-initiation crack stability under load control.

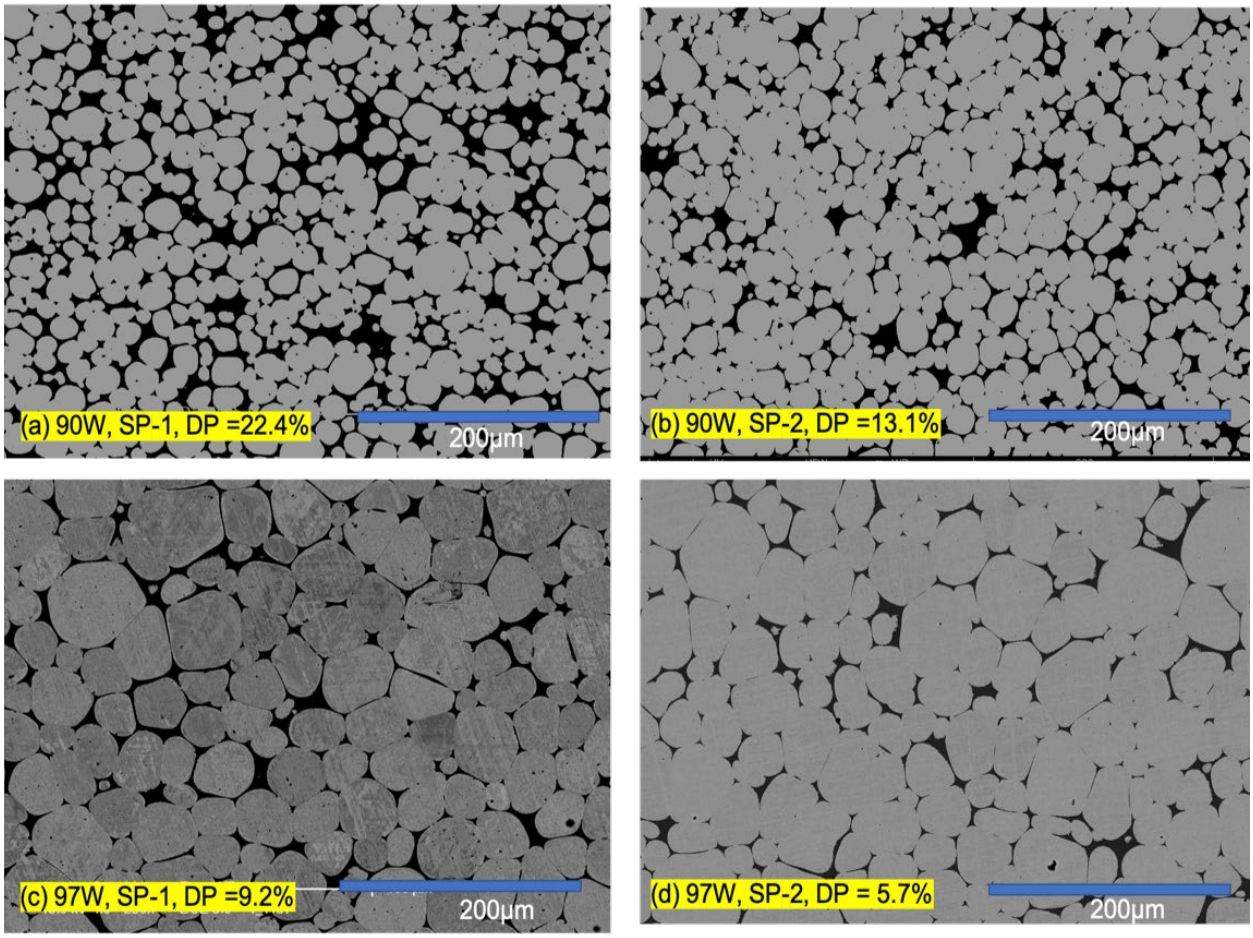

Figure 3. Backscattered SEM images showing local microstructural variations prepared from two different specimens of the same plate for: a,b) 90W, and c,d) 97W-NiFe alloys, respectively.

Only two 8x specimens from each of the 92.5W and 95W WHA were tested at RT. Representative P_n-d_n curves are shown in Figure 1d. Both the 92.5W 8x specimens showed stable crack growth with similar K_{Jm} (≈ 81 ± 7 MPa√m) to 3x (84 MPa√m) and slightly lower than the 1x 92.5W (96 MPa√m, Table 1). However, for two of the 8x 95W tested specimens, one of them failed elastically, while the other experienced stable DT crack growth (Figure 1d). The K_{Jm} for stable 8x 95W is 82 MPa√m, whereas that is 78 MPa√m for unstable one, considering the slightly yielding part prior to unstable propagation (Table 1 and Figure 2d). In both cases, the elastic portion of the toughness is 60 MPa√m, which is ≈ 7.5 x higher than the monolithic W (Table 1). The P_o at yield point deviation and max are 0.508 ± 0.085 and 0.528 ± 0.093, respectively, which are the lowest compared to any of the smaller size specimens (Figure 1 and Table 2).

Further tests on the 90W, with 8x specimens and 97W for 6x and 8x specimens have not been conducted since they are likely to undergo stable crack growth and elastic fracture, respectively. Note, the larger specimens tested at room temperature meet an alternative J_{mc}-based size criterion for tests on the 90W to 97W alloys, as discussed later in the discussion section.

Discussion

The ASTM E1921 is one of the widely used standard practices to specify the deformation limit for determining the size effect and the master curve 100 MPa√m reference temperature T_o as

$K_{Jlim} = \sqrt{[b_o\sigma_y E'/30]}$
$E' = E/[1-\nu^2]$

Here, σ_y is the yield stress, E is the elastic modulus, and ν is Poisson's ratio.

The ASTM E1921 testing validity limit of K_{Jlim} using M = 30 for all the WHAs (90 to 97W) and sizes (1x to 8x) ranged from 120 to 336 MPa$\sqrt{m}$, which is larger than any of the measured K_{Jm} values. In that regard, K_{Jm} values are valid, even for the 1x specimens. However, the deformation limit should be expressed in terms of the elastic-plastic J-integral at fracture (J_{lim}), as

$J_{lim} = J_t = b_o\sigma_o/M$. Here, σ_o is flow stress.

W1921 M for steels is 30, which is believed to be far too permissive. Also, considering the differences of elastic modulus (E ≈ 200 vs. 400 GPa), Poisson's ratio (ν: 0.3 vs. 0.28), and the structures (single-phase vs. bi-phase) between steels and WHAs, the M values should be reassessed for WHAs. Therefore, we have plotted the K_{Ic}, K_{Jp} and K_{Jm} values vs $M = b_o\sigma_o/J_{lim}$ in Figure 4 as a function of alloy, specimen size and geometry. The average M for 1x specimen is 85 ± 28, and that goes up with increasing specimen size, to ≈ 728 ± 19 for the 8x specimens. The M value, therefore, should be ≈ 200 to avoid constrain loss in bend bars. The K_{Jlim} limit for 1x to 8x specimens using M = 200 ranged from 46 to 130 MPa$\sqrt{m}$. In both cases, measured K_{Jm} for 1x specimens are higher than the K_{Jlim} values.

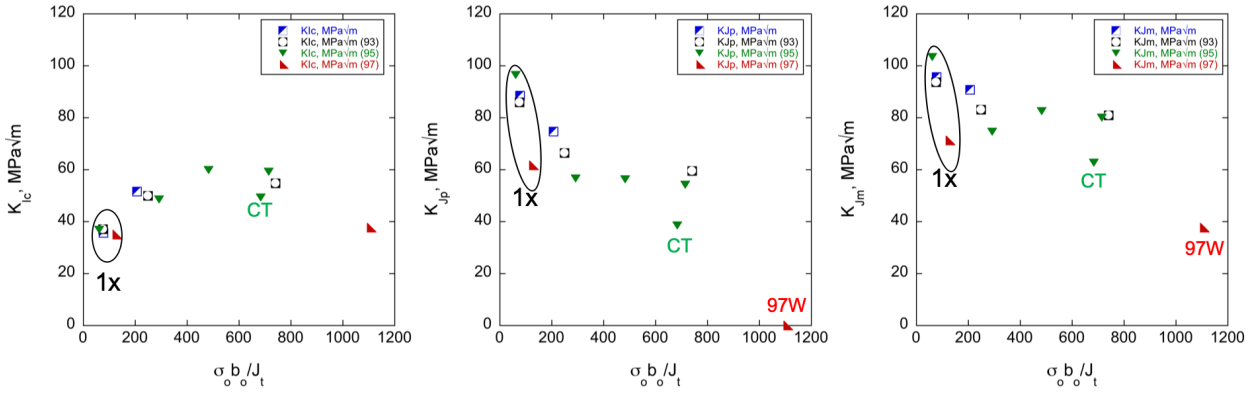

Figure 4. The K_{Ic}, K_{Jp} and K_{Jm} values vs $M = b_o\sigma_o/J_{lim}$ are plotted in a); b); and c), respectively.

The average K_{Ic} values (≈ 36 ± 1 MPa$\sqrt{m}$) for 1x specimens is much smaller than the larger specimens (52 ± 7 MPa$\sqrt{m}$), whereas the K_{Jp} shows the opposite trend (83 ± 15 for 1x, and 61 ± 8 MPa$\sqrt{m}$ for larger 3PB bars). Note, 3x or larger specimens has minimal size effects on toughness (Table 1, Figures 2,4), except for the 3x 97W 3PB and 5.5x 95W CT specimens that shows unstable crack propagation. C

With a few exceptions, the 1x, 3x, 6x, and 8x specimens show similar side surface damage profiles. For all the stable crack growth events, the W-particles are cleaved remotely, arrested, and blunted by the DP in the process zone [30]. Then the arrested and blunted multiple coplanar W-microcracks are bridged by DP ligament that shifts the classical ductile phase toughening (DPT) mechanism from macrocrack bridging and deflection to process zone microcrack arrest, blunting and bridging. Under these conditions, large-scale bridging effects and arrest mechanisms stabilize the microcracks against propagation, in part due to the small dimensions of the W-particles and the corresponding initial microcracks. Moreover, the W particles that are surrounded by DP plastically deform under high stresses in the principal stress directions prior to fracture. The most beneficial consequence of this combination of micromechanisms is the large dissipation of plastic energy, partly due to the dilatational strains from the blunting microcracks that also shield the crack tip fields that significantly reduce the local stress concentrations. Thus, the process zone deformation

leading to crack growth resembles, in some ways, classical microvoid nucleation (microcrack initiation), growth (microcrack blunting and opening), and coalesce (microcrack linking and unstable growth).

However, more WC linkage occurs in the larger versus the smaller specimens, and earlier linkage increases with higher W up to 95W. In contrast, there is no distributed process-zone microcracking in the 3x 97W, two of four 6x 95W, and one of elastically fractured 8x 95W specimens. A large number of more proximate co-planar microcracks almost immediately link to form a single macro crack that is unstably propagates by elastic fracture, analogous to low-temperature test for 1x specimens [30]. Note, for the two elastically fractured 6x 95W WHA, very large oxide inclusions (~1 mm x 0.7 mm) near the pre-crack tip were found in both of these brittle specimens, and are likely the cause of the unstable elastic crack propagation.

The normalized P_n-d_n curves show that even for ductile tearing, both the maximum load and displacement reduce with increasing specimen sizes and W%, contributing to lower toughness (Tables 1, 2 and Figures 1,2, 5a). As a result of the requisite 3-dimensional flow geometry of the NiWFe honeycomb web surrounding a large volume fraction of harder W particles, deformation results in a highly triaxial stress state in the DP and large W-NiWFe interface stresses, which produces small pores or microcracks. With increasing size, the triaxial stress level is even higher; plus the lower DP% for higher W% WHA, especially for 97W, might be enough to reach or exceed the critical stress level needed for unstable crack propagation. However, plastic rupture of the linked microcrack bridging ligaments still contributes to a higher WHA fracture toughness compared to monolithic W. Due to the specimen to specimen or plate to plate DP% variations, we have measured DP% of the tested specimens, and the results are tabulated in Table 1 and also plotted in Figure 5b. The result shows the average RT K_{Jm} varies with the DP area fraction at a rate of ≈ 2.1 MPa√m/% DP; and that elastic fracture occurs only at an DP area fraction < 10%, except 1x specimens (Table 1).

All the 0.35-CT (≈ 5.5x) 95W specimens experience unstable crack propagation after reaching the maximum load and show relatively smaller K_{Ic}, K_{Jp} and K_{Jm} values compared to the 3PB tested 95W specimens with ≈ similar thickness (6x). The unstable CT vs stable 3PB 95W is mainly due to the compliance effects of post-initiation crack stability under load control. Only limited process-zone microcracking was observed, and the overall plastic process zone is much smaller than for the ductile tearing 95W.

Conclusion

The effect of various specimen sizes on the room temperature fracture toughness for the WNiFe WHA has been conducted. The key results and conclusions can be summarized as follows:

- The RT fracture toughness for 1x (thickness, B = 1.65 mm) specimens of 90 to 95W WHA alloys averages K_{Jm} ≈ 100 ± 15 MPa√m, decreasing to 69 ± 12 MPa√m at 97W, and is 9 – 13x higher than that of monolithic W (typical K_{Ic} ≈ 8 ± 4 MPa√m). Though these measured K_{Jm} values are lower than the ASTM E-1921 testing validity limit of K_{Jlim} ($\sqrt{(b_o\sigma_y E'/30)}$ ≈ 120 MPa√m, however, the size of the 1x specimen might raise the question, and therefore, 3 to 8x larger specimens were tested.
- The K_{Jm} slightly decreases with increasing size and W up to 95W (92 ± 6 MPa√m for 90W and 79 ± 7 MPa√m for 95W). However, 3x 97W (K_{Ic} ≈ 38 ± 4 MPa√m) and two 6x, one 8x 95W (K_{Ic} ≈ 60 ± 1 MPa√m), and all 5.5x 95W CT specimens fractured elastically, at K_{Ic} ≈ 5 to 8 times higher than for monolithic W.
- With few exceptions, extensive stable crack growth occurs in all the 1x to 8x specimen that tests at RT. While there are multiple toughening mechanisms, the dominant effects of the DP is plasticizing the crack tip process zone, including deformation of the normally brittle W particles, and dilatational energy dissipation and shielding, both due to stable arrested microcrack blunting.

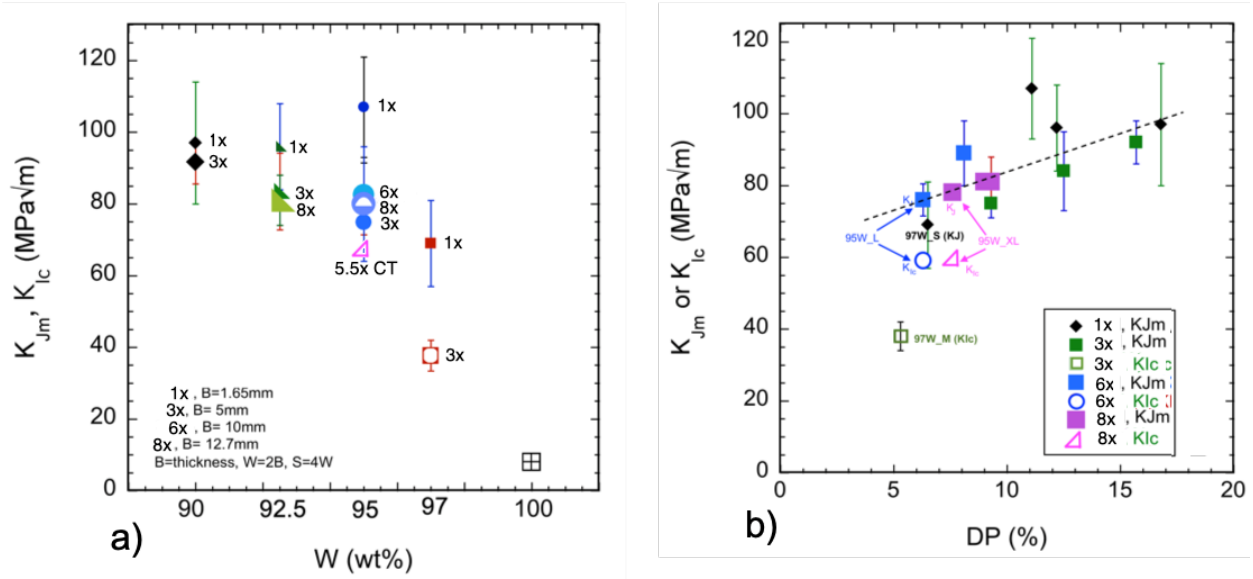

Figure 5. a) The RT K_{Jm} or K_{Ic} values; and b) the effect of DP area % on RT toughness for WHAs.

- Even at 97W, the WHA is fully ductilized for RT 1x fracture specimens. However, while K_{Ic} remains high in this case, the ductile tearing in 97W specimens gives way to elastic fracture in 3x specimens.
- Ductile tearing persists in WHA with up to 95W for up to 8x specimens.
- Size effects may emerge at even larger sizes, especially those linked to statistical weakest link effects.
- An exception to these general trends was two 95W WHA that contained massive brittle oxide inclusions at the precrack, along with lower DP area fractions and weakly bonded W-DP interfaces, that fractured elastically, but still at a high K_{Ic}.
- Except for 1x specimens, ≈ 10% NiWFe DP area fraction is required for stable crack propagation at RT for larger specimens, irrespective of alloy compositions.
- Considering higher elastic modulus of W compared to Fe, microcrack toughening mechanism for WHA bi-phase materials, we propose a dimensionless elastic plastic zone confinement deformation criteria, $M= b_o\sigma_o/J_{lim}$ for the WHA should be ≈ 200 to avoid any cleavage fracture.

Acknowledgment

We acknowledge the support provided by U.S. Department of Energy through the Office of Fusion Energy Sciences (8-442520-22419-3).

References

[1] M. Rieth, S.L. Dudarev, S.M. Gonzalez De Vicente et al, Recent progress in research on tungsten materials for nuclear fusion applications in Europe, J. Nucl. Mater. 432 (2013) 482–500.

[2] P. Norajitra, R. Giniyatulin, W. Krauss, V. Kuznetsov, I. Mazul, I. Ovchinnikov, J. Reiser, M. Rieth, V. Widak, Current status of He-cooled divertor development for DEMO, Fusion Eng. Des. 84 (2009) 1429–1433.

[3] V. Philipps, Tungsten as material for plasma-facing components in fusion devices, J. Nucl. Mater. 415 (2011) S2–S9.

[4] J. Davis, V. Barabash, A. Makhankov, L. Plöchl, K. Slattery, Assessment of tungsten for use in the ITER plasma facing components, J. Nucl. Mater. 258–263 (1998) 308–312.

[5] E. Gaganidze, A. Chauhan, H.C. Schneider, D. Terentyev, G. Borghmans, J. Aktaa, Fracture-mechanical properties of neutron irradiated ITER specification tungsten, J. Nucl. Mater. 547 (2021) 152761.

[6] C. Henager Jr, W. Setyawan, T. Roosendaal, N. Overman, B. Borlaug, E. Stevens, K. Wagner, R. Kurtz, G.R. Odette, B. Nguyen, K. Cunningham, Ductile-phase toughened tungsten for plasma-facing materials in fusion reactors, Int. J. Powder Metall. 53 (2017) 53–69.
[7] J. Reiser, J. Hoffmann, U. Jäntsch, M. Klimenkov, S. Bonk, C. Bonnekoh, M. Rieth, A. Hoffmann, T. Mrotzek, Ductilisation of tungsten (W): On the shift of the brittle-to-ductile transition (BDT) to lower temperatures through cold rolling, Int. J. Refract. Met. Hard Mater. 54 (2016) 351–369.
[8] B. Gludovatz, S. Wurster, A. Hoffmann, R. Pippan, Fracture toughness of polycrystalline tungsten alloys, Int. J. Refract. Met. Hard Mater. 28 (2010) 674–678.
[9] K.T. Venkateswara Rao, G.R. Odette, R.O. Ritchie, Ductile-reinforcement toughening in γ-TiAl intermetallic-matrix composites: Effects on fracture toughness and fatigue-crack propagation resistance, Acta Metall. Mater. 42 (1994) 893–911.
[10] G.R. Odette, B.L. Chao, J.W. Sheckherd, G.E. Lucas, Ductile phase toughening mechanisms in a TiAl-TiNb laminate composite, Acta Metall. Mater. 40 (1992) 2381–2389.
[11] M.G. Mendiratta, J.J. Lewandowski, D.M. Dimiduk, Strength and ductile-phase toughening in the two-phase Nb/Nb5Si3 alloys, Metall. Trans. A. 22 (1991) 1573–1583.
[12] L.S. Sigl, P.A. Mataga, B.J. Dalgleish, R.M. McMeeking, A.G. Evans, On the toughness of brittle materials reinforced with a ductile phase, Acta Metall. 36 (1988) 945–953.
[13] D. V. Edmonds, P.N. Jones, Interfacial embrittlement in liquid-phase sintered tungsten heavy alloys, Metall. Trans. A. 10 (1979) 289–295.
[14] B.C. Muddle, Interphase boundary precipitation in liquid phase sintered W-Ni-Fe and W-Ni-Cu alloys, Metall. Trans. A. 15 (1984) 1089–1098.
[15] A. Mondal, D. Agrawal, A. Upadhyaya, Microwave Sintering of Refractory Metals/ alloys: W, Mo, Re, W-Cu, W-Ni-Cu and W-Ni-Fe Alloys, J. Microw. Power Electromagn. Energy. 44 (2010) 28–44.
[16] Z.A. Hamid, S.F. Moustafa, W.M. Daoush, F.A. Mouez, M. Hassan, Fabrication and characterization of tungsten heavy alloys using chemical reduction and mechanical alloying methods, Open J. Appl. Sci. 03 (2013) 15–27.
[17] M. Scapin, Mechanical characterization and modeling of the heavy tungsten alloy IT180, Int. J. Refract. Met. Hard Mater. 50 (2015) 258–268.
[18] X. Gong, J. Fan, F. Ding, Tensile mechanical properties and fracture behavior of tungsten heavy alloys at 25-1100 °C, Mater. Sci. Eng. A. 646 (2015) 315–321.
[19] K. Hu, X. Li, X. Ai, S. Qu, Y. Li, Fabrication, characterization, and mechanical properties of 93W-4.9Ni-2.1Fe/95W-2.8Ni-1.2Fe/95W-2.8Ni-1.2Fe-1Al2O3 heavy alloy composites, Mater. Sci. Eng. A. 636 (2015) 452–458.
[20] U.R. Kiran, A. Panchal, M. Sankaranarayana, G.V.S.N. Rao, T.K. Nandy, Effect of alloying addition and microstructural parameters on mechanical properties of 93% tungsten heavy alloys, Mater. Sci. Eng. A. 640 (2015) 82–90.
[21] M.B. Shongwe, S. Diouf, M.O. Durowoju, P.A. Olubambi, M.M. Ramakokovhu, B.A. Obadele, A comparative study of spark plasma sintering and hybrid spark plasma sintering of 93W-4.9Ni-2.1Fe heavy alloy, Int. J. Refract. Met. Hard Mater. 55 (2016) 16–23.
[22] R. German, J. Hanafee, S. DiGiallonardo, Toughness variation with test temperature and cooling rate for liquid phase sintered W-3.5Ni-1.5Fe, Metall. Trans. A. 15 (1984) 121–128.
[23] K.S. Churn, R.M. German, Fracture behavior of W-Ni-Fe heavy alloys, Metall. Trans. A, Phys. Metall. Mater. Sci. 15 A (1984) 331–338.
[24] D. V Edmonds, Structure/property relationships in sintering heavy alloys, Refract. Met. Hard Mater. 10 (1991) 15–26.
[25] R.M. German, A. Bose, S.S. Mani, Sintering time and atmosphere influences on the microstructure and mechanical properties of tungsten heavy alloys, Metall. Trans. A. 23 (1992) 211–219.
[26] K.M.O. Zamora, J.G. Sevillano, M.F. Perez, Fracture toughness of W heavy metal alloys, Mater. Sci. Eng. A. 157 (1992) 151–160.
[27] A. Upadhyaya, Processing strategy for consolidating tungsten heavy alloys for ordnance applications, Mater. Chem. Phys. 67 (2001) 101–110.

[28] Z.H. Zhang, F.C. Wang, S.K. Li, L. Wang, Deformation characteristics of the 93W-4.9Ni-2.1Fe tungsten heavy alloy deformed by hydrostatic extrusion, Mater. Sci. Eng. A. 435–436 (2006) 632–637.
[29] S. Islam, X. Qu, X. He, Investigation of composition and microstructure effect on fracture behaviour of tungsten heavy alloys, Powder Metall. 50 (2007) 11–13.
[30] M.E. Alam, G.R. Odette, On the remarkable fracture toughness of 90 to 97W-NiFe alloys revealing powerful new ductile phase toughening mechanisms, Acta Mater. 186 (2020) 324–340.
[31] G.R. Odette, M.E. Alam, K. Cunningham, Ductile-Phase Toughened Tungsten for Plasma Facing Materials, DOE-UCSB-ER54275, United States, 2019.
[32] M.E. Alam, J. Wang, C.H. Henager, W. Setyawan, G.R. Odette, The effect of hot rolling on the strength and fracture toughness of 90W–7Ni3Fe tungsten heavy metal alloys, Mater. Sci. Eng. A. 824 (2021) 141738.
[33] R. Neu, H. Maier, M. Balden, R. Dux, S. Elgeti, H. Gietl, H. Greuner, A. Herrmann, T. Höschen, M. Li, V. Rohde, D. Ruprecht, B. Sieglin, I. Zammuto, Results on the use of tungsten heavy alloys in the divertor of ASDEX Upgrade, J. Nucl. Mater. 511 (2018) 567–573.
[34] Q. An, A. Elshafiey, L. Huang, D.A. Hammer, M. Hassani, Plasma and X-ray radiation-induced damage mechanisms in a tungsten heavy alloy, J. Nucl. Mater. 539 (2020) 152325.
[35] T. Laas, K. Laas, J. Paju, J. Priimets, S. Tõkke, B. Väli, V. Shirokova, M. Antonov, V.A. Gribkov, E. V. Demina, V.N. Pimenov, M. Paduch, R. Matulka, M. Akel, Behaviour of tungsten alloy with iron and nickel under repeated high temperature plasma pulses, Fusion Eng. Des. 151 (2020).
[36] Y. Şahin, Recent progress in processing of tungsten heavy alloys, J. Powder Technol. 2014 (2014) 1–22.
[37] W.D. Cai, Y. L, R.J. Dowding, F.A. Mohamed, E.J. Lavernia, A review of tungsten-based alloys as kinetic energy penetrator materials, Rev. Part. Mater. 3 (1995) 71–131.
[38] A.A.N. Németh, J. Reiser, D.E.J. Armstrong, M. Rieth, The nature of the brittle-to-ductile transition of ultra fine grained tungsten (W) foil, Int. J. Refract. Met. Hard Mater. 50 (2015) 9–15.
[39] J.H. You, Design feasibility study of a divertor component reinforced with fibrous metal matrix composite laminate, J. Nucl. Mater. 336 (2005) 97–109.
[40] J. Riesch, Y. Han, J. Almanstötter, J.W. Coenen, T. Höschen, B. Jasper, P. Zhao, C. Linsmeier, R. Neu, Development of tungsten fibre-reinforced tungsten composites towards their use in DEMO - Potassium doped tungsten wire, Phys. Scr. T167 (2016) 14006.
[41] A.G. Evans, R.M. Cannon, Toughening of brittle solids by martensitic transformations, Acta Metall. 34 (1986) 761–800.
[42] J.W. Hutchinson, Non-linear fracture mechanics, Tech. Univ. of Denmark, 1979.
[43] M. Rühle, A.G. Evans, R.M. McMeeking, P.G. Charalambides, J.W. Hutchinson, Microcrack toughening in alumina/zirconia, Acta Metall. 35 (1987) 2701–2710.
[44] T.L. Anderson, Fracture Mechanics: Fundamentals and Applications, 3rd ed., Taylor & Francis Group, FL, USA, 2005.
[45] G.R. Odette, H.J. Rathbun, M. Hribernik, T. Yamamoto, M. He, P. Spätig, A Multiscale Approach to Measuring and Modeling Cleavage Fracture Toughness in Structural Steels, in: V. Ghetta, D. Gorse, D. Mazière, V. Pontikis (Eds.), Mater. Issues Gener. IV Syst., Springer Netherlands, Dordrecht, 2008: pp. 203–226.
[46] H.J. Rathbun, G.R. Odette, M.Y. He, T. Yamamoto, Influence of statistical and constraint loss size effects on cleavage fracture toughness in the transition–A model based analysis, Eng. Fract. Mech. 73 (2006) 2723–2747.
[47] H.J. Rathbun, G.R. Odette, T. Yamamoto, G.E. Lucas, Influence of statistical and constraint loss size effects on cleavage fracture toughness in the transition—A single variable experiment and database, Eng. Fract. Mech. 73 (2006) 134–1158.
[48] ASTM E1921-20, Standard Test Method for Determination of Reference Temperature , To , for Ferritic Steels in the Transition Range, in: Annu. B. ASTM Stand., ASTM International, 100 Barr Harbor Drive, PO Box C700, West Conshohocken, PA 19428-2959, United States, 2020: pp. 1–25.

[49] G.R. Odette, E. Stergar, D. Gragg, K. Fields, J. Heathcote, C.H. Henager, R. J. Kurt, W-Alloy and Composite Fracture test Method Development and Initial Exploration of Ductile Phase Toughening, Usion React. Mater. Progr. Semiannu. Prog. Rep. DOE0313/52 (2012) 89–102.
[50] T. Anderson, R. Dodds, Specimen Size Requirements for Fracture Toughness Testing in the Transition Region, J. Test. Eval. 19 (1991) 123–134.
[51] Kim Wallin, The Size Effect in KIC Results, Eng. Fract. Mech. 22 (1985) 149–163.
[52] M.E. Alam, G.R. Odette, On the effect of specimen size, geometry and ductile phase content on the fracture toughness of tungsten heavy metal alloys, DOE Fusion React. Mater. Progr. Semiannu. Prog. Rep. DOE0313/66 (2019) 45–52.
[53] J.R. Davis, Properties and Selection: Nonferrous Alloys and Special-Purpose Materials, 10th ed., ASM Handbook, ASM, Metal Park, Ohio, 1993.

4.4 TRANSPORT PROPERTY EVALUATION OF NEUTRON IRRADIATED TUNGSTEN MATERIALS FROM THE PHENIX AND SHINE CAMPAIGNS—J. R. Echols, L. M. Garrison, Y. Katoh (Oak Ridge National Laboratory)

OBJECTIVE

The goal of the PHENIX and TITAN collaborations is to expand the database on neutron irradiation effects in tungsten materials. This task evaluates the effects of neutron dose, Re and Os content, thermal neutron shielding, and temperature on the thermal transport in single and poly-crystalline tungsten.

SUMMARY

Thermal diffusivity measurements have been performed at the Oak Ridge National Laboratory (ORNL) on neutron irradiated tungsten from capsules both with and without thermal neutron shielding. These measurements are compared with new analysis on electrical resistivity data to develop a model to predict thermal diffusivity for tungsten with an arbitrary percentage of Re/Os transmutation. This comparison reveals that Os segregation plays a large role in preventing thermal diffusivity degradation in neutron-irradiated tungsten.

PROGRESS AND STATUS

The TITAN and PHENIX programs, together, have neutron irradiated thousands of tungsten and tungsten alloy samples in the High Flux Isotope Reactor (HFIR) at ORNL. These samples were irradiated at a variety of fluences (0.02-20 $x10^{25}$ n/m^2, E>0.1MeV) and temperatures (100-1000°C). Associated doses in dpa are in the range of 0.02-4.5dpa. The PHENIX campaign utilized a Gd shield to reduce thermal neutron fluence (greatly reducing transmutation), while the TITAN campaign exposed samples to the full HFIR neutron spectrum. Tabs of tested tensile specimens from both campaigns have undergone thermal diffusivity testing at ORNL. These samples present a unique opportunity to greatly expand the thermal conductivity database of neutron irradiated tungsten, while investigating the effects of irradiation dose, temperature, and spectrum.

Table 1 shows all specimens of single-crystalline tungsten (SCW) which have been thermal diffusivity tested thus far in this work. For the shielded capsules, Re and Os calculations are taken from HFIR's isotopic calculations. The Re and Os calculations for the unshielded capsules are taken from the FISPACT values reported in [1], assuming self-shielding.

Electron transport properties are expected to drive most thermal transport in tungsten for fusion reactors. Therefore, electrical resistivity work previously performed on samples in the PHENIX campaign makes for an important comparative check to ensure this assumption holds after irradiation. Full experimental details from this resistivity work can be found in previous reports [2, 3]. Both SCW and polycrystalline tungsten (PCW) were evaluated for this work.

Diffusivity measurements were conducted on a Netzsch LFA467 HT, which utilizes a flash method of thermal diffusivity measurement. Tensile samples which had previously been evaluated were thinly coated with a graphene spray to reduce reflectivity, then fitted to a custom fixture within the device, and finally placed under vacuum. A brief laser pulse (order 0.1ms) heated one side of the tab while the temperature on the other side is monitored to determine the rate of heat transfer through the material. An example curve is shown in Figure 2. For each sample, five measurements were taken at each testing temperature. Tests began at room temperature, after which the device heated the material and take additional measurements at 50°C increments up to the irradiation temperature (minus a safety margin). Measurements were then taken in 100°C intervals back to room temperature to ensure that radiation damage had not been annealed out by exceeding the maximum radiation temperature (which would exhibit as an increase in diffusivity).

Table 1. Sample ID, irradiation temperature, dose, shielded state, and calculated Re and Os content for all tested samples

Sample ID	*Irradiation Temp (°C)*	*Dose (dpa)*	*Notes*	*Initial Re (%at)*	*Final Re (%at)*	*Final Os (%at)*
Norad	20	0	Shielded	0	0	0
UE03	480	0.237	Shielded	0	0.16	0.00
UE0G	830	0.744	Shielded	0	0.52	0.02
UE0L	930	0.614	Shielded	0	0.39	0.01
1W07	430	0.560	Unshielded	0	3.70	0.71
1W18	710	0.440	Unshielded	0	3.00	0.48
1W27	800	0.570	Unshielded	0	3.70	0.73
1W14	800	0.015	Unshielded	0	0.13	0.01
1W19	770	1.800	Unshielded	0	7.10	4.70
1W52	690	0.110	Unshielded	0	0.85	0.05
1W15	90	0.004	Unshielded	0	0.03	0.00
1W25	90	0.020	Unshielded	0	0.16	0.01
1W31	800	2.900	Unshielded	0	7.40	8.70

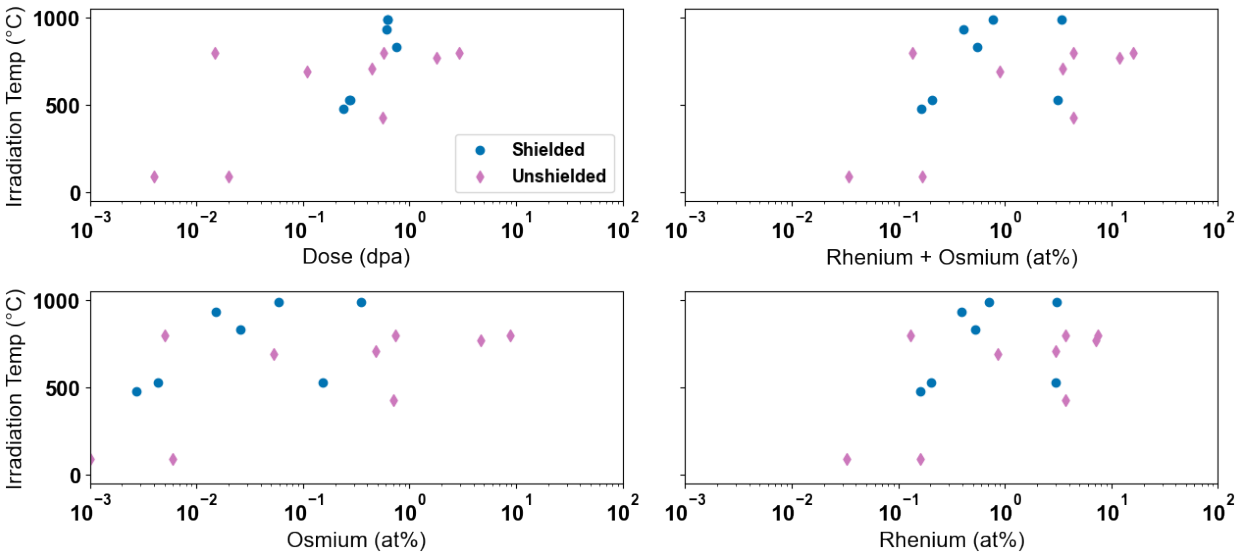

Figure 1. Visualizations of irradiation temperatures, dose, and transmutation for tested and planned samples.

Example diffusivity curves from example unirradiated, irradiated shielded, and irradiated unshielded samples are shown in Figure 2. The Re values (for these high irradiation temperatures) can be seen to clearly be more correlated to diffusivity changes than pure dose. This is easily observed by comparing the unshielded sample and shielded sample with 0.85 %(at) Re, which have almost identical diffusivity curves, despite total dose differences greater than 700%.

From the work of Tanno et al [4] we have modelled the resistivity of the W-Re-Os system using Matthiessen's rule. This rule states that the total resistivity (ρ) of a crystalline metallic system can be

represented by the sum of the lattice resistivity (ρ_0) and the resistivity of imperfections (impurity atoms, voids, vacancies, grain boundaries, etc.). For impurities with similar atomic masses, this expression can be written (with *A* representing an impurity coefficient and *x* representing the atomic percent of an impurity):

$$\rho = \rho_0 + \sum_{i=0}^{n} A_i\left(\frac{x_i}{100}\right)\left(\frac{1-x_i}{100}\right)$$

Tanno et al reported impurity coefficients (*A*) of 145 for Re and 640 for Osmium, which are used to model the resistivity as a function of impurity content in solid solution. This model is shown, at room temperature, alongside resistivity data from the literature [4, 5] and our data in Figure 3. The model is reasonably consistent with this real-world data.

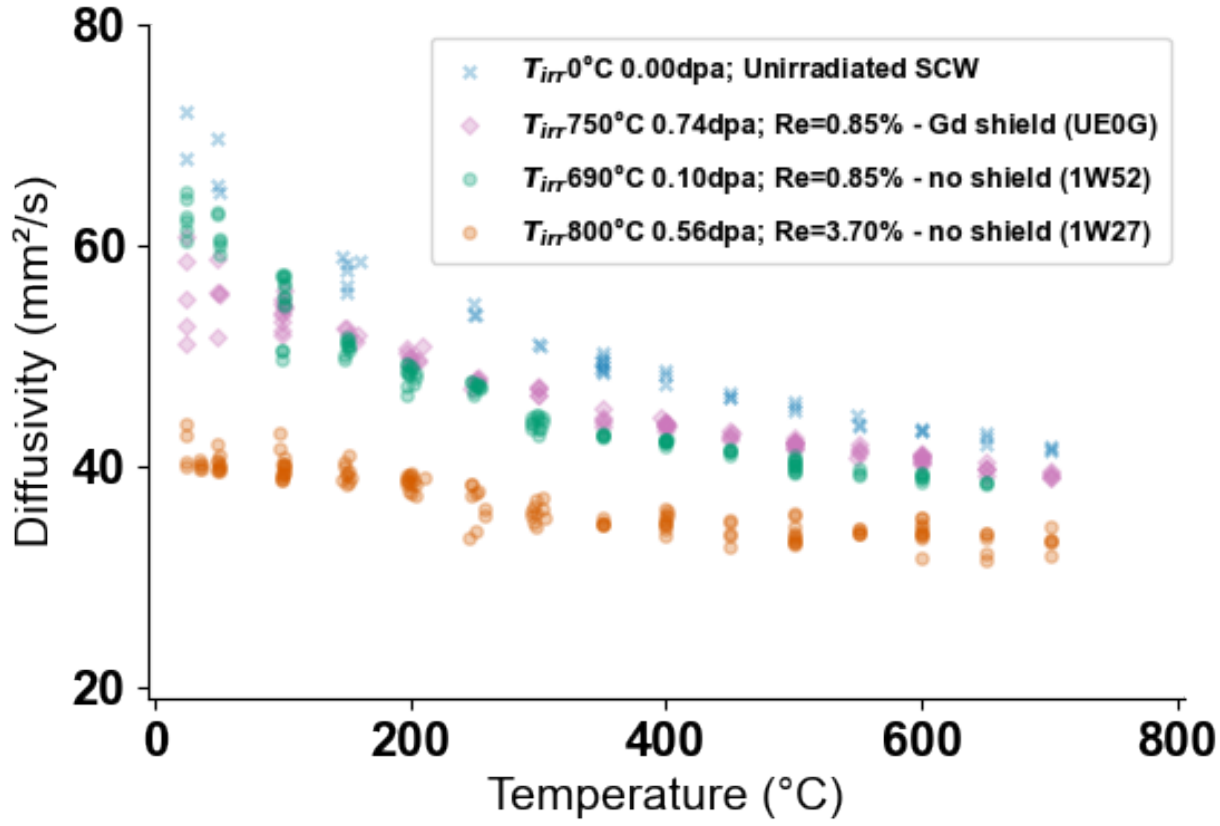

Figure 2. Temperature dependent thermal diffusivity of irradiated, unirradiated, shielded, and unshielded SCW.

From this point, the model can be adapted into the electronic component of the thermal diffusivity (κ_e) by using the Wiedemann–Franz law:

$$\frac{\kappa_e}{\sigma} = LT$$

Where σ is electrical conductivity (inverse resistivity), T is temperature, L is a material-dependent proportionality constant called the Lorenz number. This thermal diffusivity model is shown in Figure 4, alongside thermal diffusivity measurements of W-Re alloys from the literature [6-8] and converted values from electrical resistivity measurements of W-Re-Os alloys [4, 5, 9]. These predictions slightly

underestimate observed W-Re alloy thermal diffusivity, but generally follow closely with observed trends in unirradiated material. The W-Re alloy deviation is attributed to 1) the phonon-phonon and electron-phonon scattering contributions not accounted for by the model and 2) slight differences in the Lorenz number for Re and Os, which are not yet accounted for.

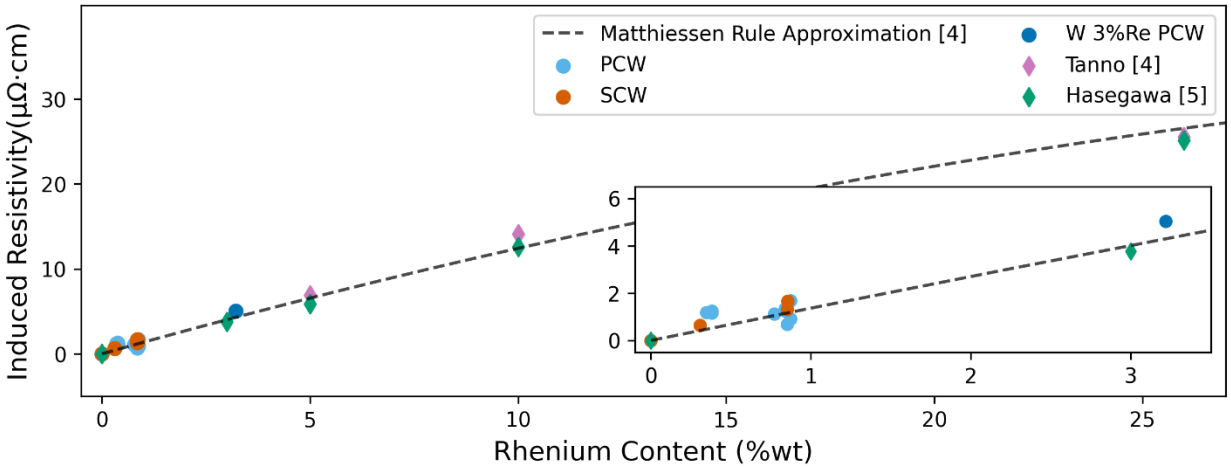

Figure 3. Visualization of room-temperature modelling utilizing Matthiessen's rule for electrical resistivity. Results are consistent with both literature data and observed electrical resistivity for unirradiated and irradiated W and W-Re alloys. [4, 5]

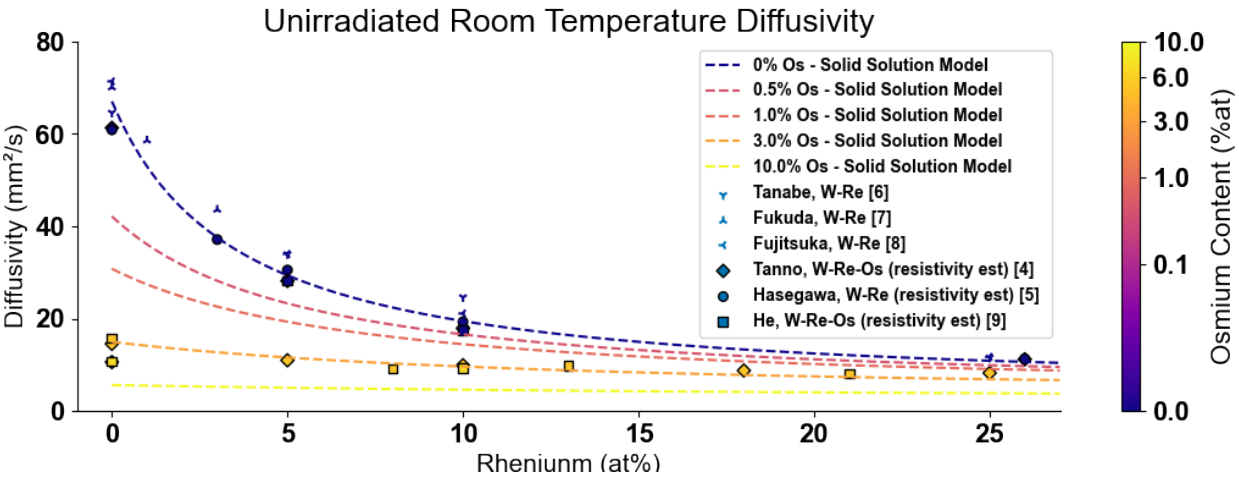

Figure 4. Applying the Matthiessen's rule model with the Wiedemann–Franz law can generate predictions for solid-solution W-Re-Os systems. Literature observations of W-Re thermal diffusivity are shown with y-shaped markers [6-8]. Diffusivity conversions from electrical resistivity values of W-Re-Os alloys are shown in the larger markers with the color bar scale representing Os content [4, 5, 9].

Finally, this model is compared with the room-temperature diffusivity data taken in this work in Figure 5. To separate out the effects of lattice defects, this figure is reproduced separately for samples which were irradiated at temperatures above/below the vacancy migration threshold [10] (~650°C). Several important takeaways from this are as follows:

1) The model appears to reasonably predict the diffusivity of low-Os (<0.1 at%) samples irradiated above the vacancy migration threshold.
2) High-Os samples deviate significantly from the model. This is assumed to be the result of significant Re-Os precipitates observed in such samples [1, 4]. As a result, the thermal diffusivity degradation of Os is significantly lower than would be expected for a system in solid solution.
3) Low-Os, low temperature samples have lower diffusivities. These differences can be used to directly quantify irradiation defect contributions to thermal diffusivity (and define A coefficients) by comparing diffusivity results below the vacancy migration threshold to the expected diffusivity.

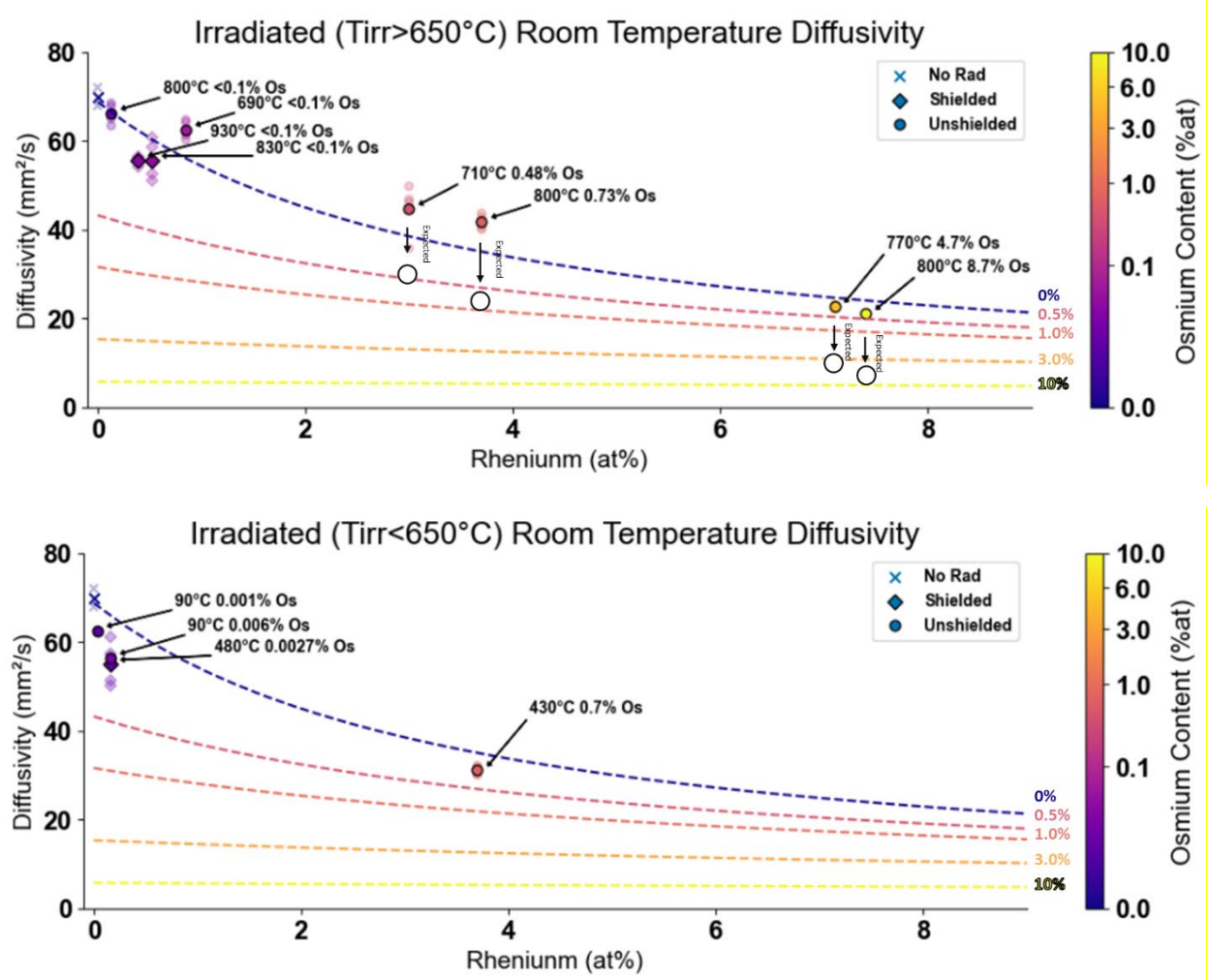

Figure 5. Room temperature thermal diffusivity data with Re indicated on horizontal axis and Os content indicated with the color bar. (Top) Data from irradiations above the vacancy migration threshold (~650°C). (Bottom) Irradiations below this threshold.

Future Work

Future work will involve measuring unirradiated W-Re-Os alloys and adapting the model to account for precipitates, grain boundaries, lattice irradiation defects, and measurement temperature.

References

[1] Katoh, Y., et al. "Response of unalloyed tungsten to mixed spectrum neutrons." Journal of Nuclear Materials 520 (2019): 193-207.
[2] Echols, J.R., et al. “4.3 Electrical conductivity evaluation of neutron irradiated tungsten materials from the PHENIX collaboration.” DOE/ER-0313/70 – Volume 70 ORNL/SPR-2021/2151 (2021): 47-51.
[3] Echols, J.R., et al. “4.5: Electrical conductivity evaluation of neutron irradiated tungsten materials from the PHENIX campaign” DOE/ER-0313/69 – Volume 69 ORNL/SPR-2021/1910 (2020): 137-140.
[4] Tanno, T., et al. "Effects of transmutation elements on the microstructural evolution and electrical resistivity of neutron-irradiated tungsten." Journal of Nuclear Materials 386 (2009): 218-221.
[5] Hasegawa, Akira, et al. "Property change mechanism in tungsten under neutron irradiation in various reactors." Journal of nuclear materials 417.1-3 (2011): 491-494.
[6] Tanabe, T., et al. "Temperature dependence of thermal conductivity in W and W–Re alloys from 300 to 1000 K." Materials Letters 57.19 (2003): 2950-2953.
[7] Fukuda, Makoto, et al. "Microstructural development of tungsten and tungsten–rhenium alloys due to neutron irradiation in HFIR." Journal of Nuclear Materials 455.1-3 (2014): 460-463.
[8] Fujitsuka, M., et al. "Effect of neutron irradiation on thermal diffusivity of tungsten–rhenium alloys." \ Journal of nuclear materials 283 (2000): 1148-1151.
[9] He, Jian-Chao, et al. "Fabrication and characterization of W-Re-Os alloys for studying transmutation effects of W in fusion reactors." Materials transactions 45.8 (2004): 2657-2660.
[10] L.K. Keys, et al. “High-Temperature Recovery of Tungsten after Neutron Irradiation.” Physical Review. 176 (1968). https://doi.org/10.1103/PhysRev.176.851.

4.5 PROGRESS REPORT ON RE-STARTING HOT-ROLLING AND CONTINUED CHARACTERIZATION OF TUNGSTEN HEAVY ALLOY AT PNNL—J. Wang, R. Prabhakaran, C. H. Henager, Jr., W. Setyawan (Pacific Northwest National Laboratory)

OBJECTIVE

The objective of the project is to understand the deformation behavior of ductile phase toughened tungsten heavy alloys, such as W-NiFe, for applications in fusion reactor divertor and plasma-facing components.

SUMMARY

This report summarizes the progress in fabricating new batches tungsten heavy alloy, also known as ductile phase toughened (DPT), W-NiFe alloys at PNNL, and preliminary characterization and testing results. The microstructure of new hot-rolled W-NiFe alloys were examined using SEM and EBSD, at 60% and 88% thickness reductions, respectively. Thermal annealing was also briefly explored. The resulting microstructure is almost identical to previous batches of hot-rolling, despite a slightly different annealing temperature. Microhardness testing was also performed, and the preliminary results are presented.

PROGRESS AND STATUS

Previously, 90W-NiFe samples, in which W powders were embedded in a Ni-Fe matrix, were hot-rolled at PNNL to 62%, 74%, and 87% thickness reduction to attain a lamellar structure and have been used in FY20 and FY21 to collect experimental data to understand the effects of hot rolling and deformation behavior of DPT W-NiFe alloys. Near the end of FY21, we started to reproduce a new batch of hot-rolled DPT W-NiFe due to specimens running low. Due to retirement of key personnel, and some equipment stayed idle for a long period of time, a brief pilot run was initiated, and the resulting materials were examined and compared with previous samples.

Hot rolling of DPT W-NiFe specimens was restarted near the end of FY21. However, due to the downtime of instruments, COVID-19 pandemic, heat waves in the region, the progress is delayed. Several as-received 90W-0R specimens were cut into strips with ~0.25 inches in thickness. Before rolling, the sample was pre-heated to around 1150 °C in a furnace. After 2 passes, a part of the sample was then annealed with H_2/Ar 50/50 mix to 1200 °C for 3 hours. Figure 1 shows pictures taken during hot rolling and after annealing. Thickness reduction was targeted at ~10% each pass, with a goal at ~87%. During hot rolling, a part of the sample was cut at intermediate thickness reduction, around 60%, for inspection as well.

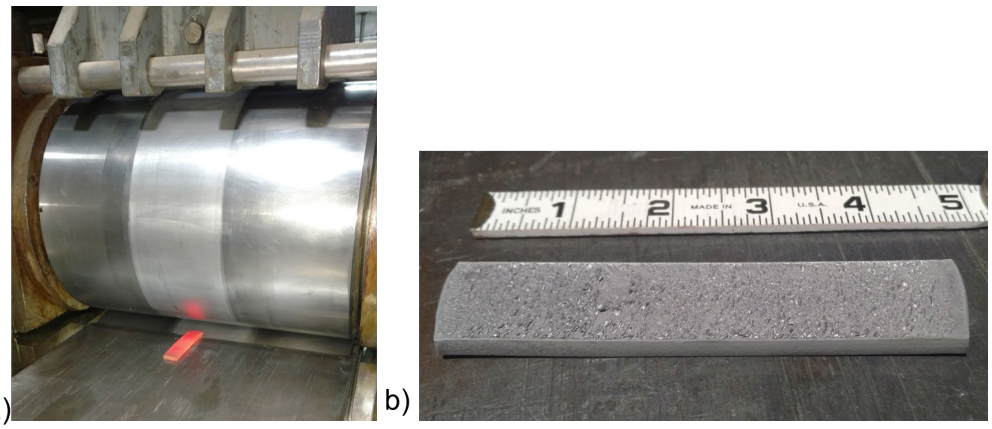

Figure 1. Pictures of a) hot-rolling mill; b) rolled specimen after 2 passes with 10% thickness reduction in each pass.

The SEM examinations on DPT W-NiFe samples were carried out using a JEOL 7600 field emission SEM at PNNL. Samples for characterization were polished to a 0.05 μm colloidal silica finish. A low-angle backscatter electron (BSE) detector was utilized to examine the general microstructure at various locations. The results were processed and analyzed using the AZtec software package from the Oxford Instruments. Fractography was performed on selected samples as is without any tampering of the fracture surfaces. The specimen matrix in this report is listed in Table 1, and the corresponding specimen orientations are shown in Figure 2.

Table 1. Specimen matrix in this report

Specimen ID	Details
90W-0R	90 wt% W, as received, powder purchased from MiTech, sintered at PNNL
90W-60R-RD-Annealed	90 wt% W, hot rolled to 60% thickness reduction, ND-RD orientation, annealed
90W-60R-Plan-Annealed	90 wt% W, hot rolled to 60% thickness reduction, TD-RD orientation annealed
90W-85R-RD-Annealed	90 wt% W, hot rolled to 85% thickness reduction, ND-RD orientation, annealed
90W-85R-Plan-Annealed	90 wt% W, hot rolled to 85% thickness reduction, TD-RD orientation, annealed
90W-85R-RD-As-Rolled	90 wt% W, hot rolled to 85% thickness reduction, ND-RD orientation, as-hot-rolled
90W-85R-Plan-As-Rolled	90 wt% W, hot rolled to 85% thickness reduction, TD-RD orientation, as-hot-rolled

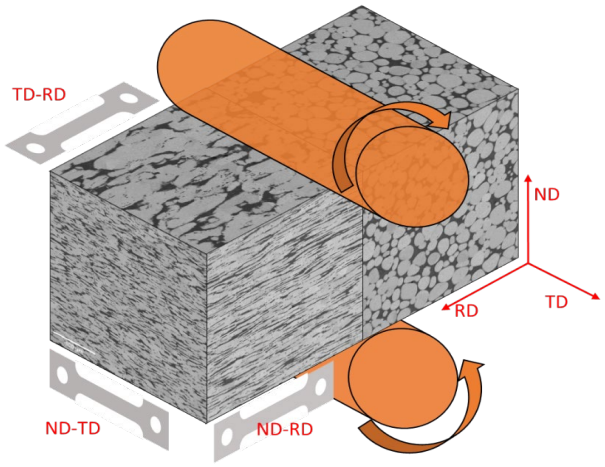

Figure 2. Tensile specimen orientations in 90W-87R [1]. The 90W-87R-Plan features the TD-RD orientation while the 90-87R-RD features the ND-RD direction. (RD = Rolling Direction, TD = Transverse Direction, ND = Normal Direction).

Figure 3 shows the microstructure of the surface of as-sintered W-NiFe (90W-0R) specimens and surfaces of samples from previously hot-rolled W-NiFe (TD-RD for 90W-87R-Plan and ND-RD for 90W-87R-RD, as illustrated in Figure 2). The microstructure resembles two typical phases in this set of materials: a NiFe phase, which serves as the ductile matrix; and a W phase, which provides strength and high-temperature mechanical performance. It shows that along the rolling direction, the W phase deforms significantly into a plate-like structure. In the as-sintered 90W-0R, the W-phase is mostly spherical-like and some W-W grain boundaries exist, while in the hot-rolled W-NiFe samples, the W-phase deforms into a plate-like

morphology. The NiFe ductile phase shows significant grain refinement in the hot-rolled samples compared to the as-sintered ones.

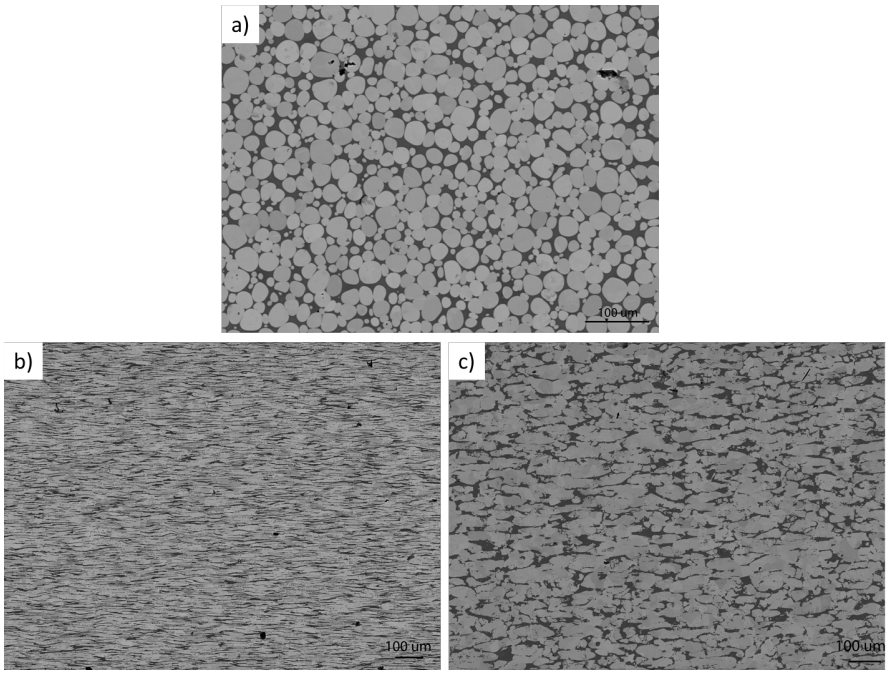

Figure 3. Back-scattered electron (BSE) images of a) 90W-0R; and previously fabricated b) 90W-87R-RD, and 90W-87R-Plan.

Specimens were taken at 60% thickness reduction to investigate intermediate stages of microstructure evolution during hot-rolling. Figure 4 and Figure 5 show SE and BSE images of the microstructure on the ND-RD and TD-RD surfaces at two different magnifications. The microstructure starts to show some levels of anisotropic features, especially in the ND-RD, due to rolling, while it is less significant on the TD-RD surface. In addition, the BSE contrast shows that new grains/subgrains starts to form within relatively well-maintained W particles. The observation indicates hot-rolling not only pushes W particles together to form new W/W grain boundaries, but also introduces new W/W boundaries internally.

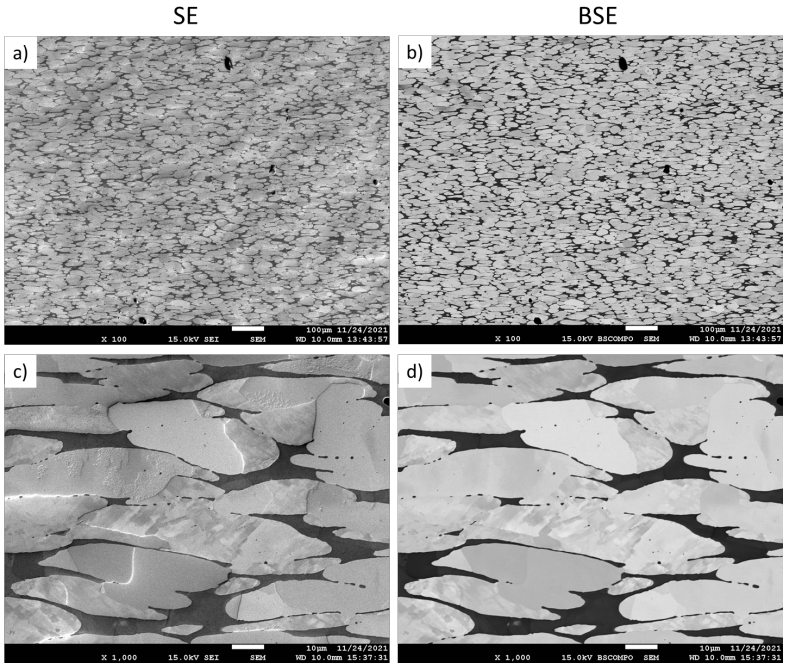

Figure 4. Secondary electron (SE) and back-scattered electron (BSE) images for 90W-60R-RD-Annealed at two different magnifications, showing microstructure of ND-RD surfaces.

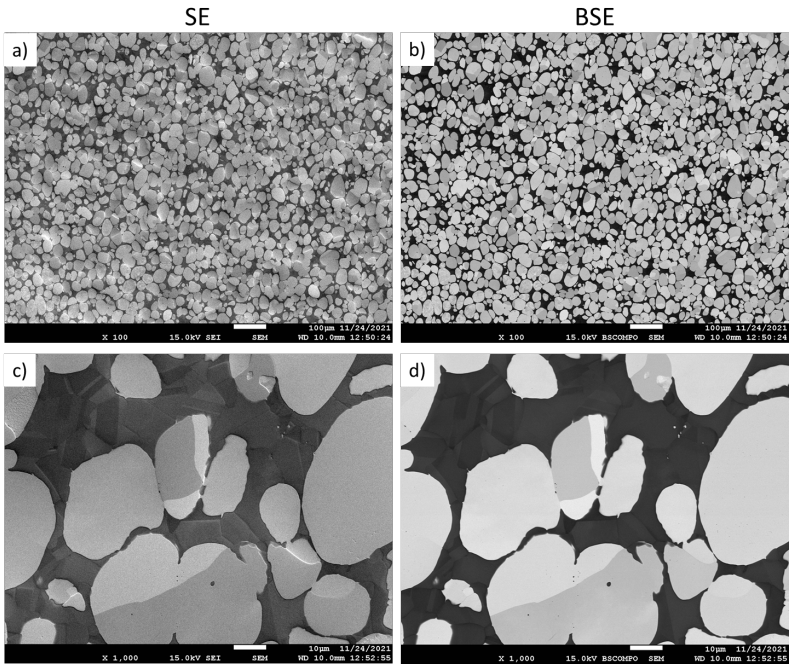

Figure 5. Secondary electron (SE) and back-scattered electron (BSE) images for 90W-60R-Plan-Annealed at two different magnifications, showing TD-RD surfaces.

Figure 6 and Figure 7 show SE and BSE images of the microstructure on the ND-RD and TD-RD surfaces for DPT W specimens after 85% thickness reduction, followed by thermal annealing. The resulting microstructure is consistent with previously hot-rolled specimens to 87%. Compared with 60% specimens,

the W grains are more elongated in both orientations. Although the ND-RD surface shows that W/NiFe interface morphologies are like the as-received materials at the SEM scale, the look at TD-RD surface shows a "fuzzier" W/NiFe interface morphology after severe thickness reduction. The observation suggests that the interfaces between W/NiFe suffered from deformation anisotropically. For example, one implication could be more crack initiation sites on the side wall of W phase compared to a pristine microstructure. However, since W particles in any way provide little crack resistance in pure tungsten form, the "fuzzier" microstructure may lead to increased surface to volume ratio locally. The W/W grain contiguity is also noticeably increased.

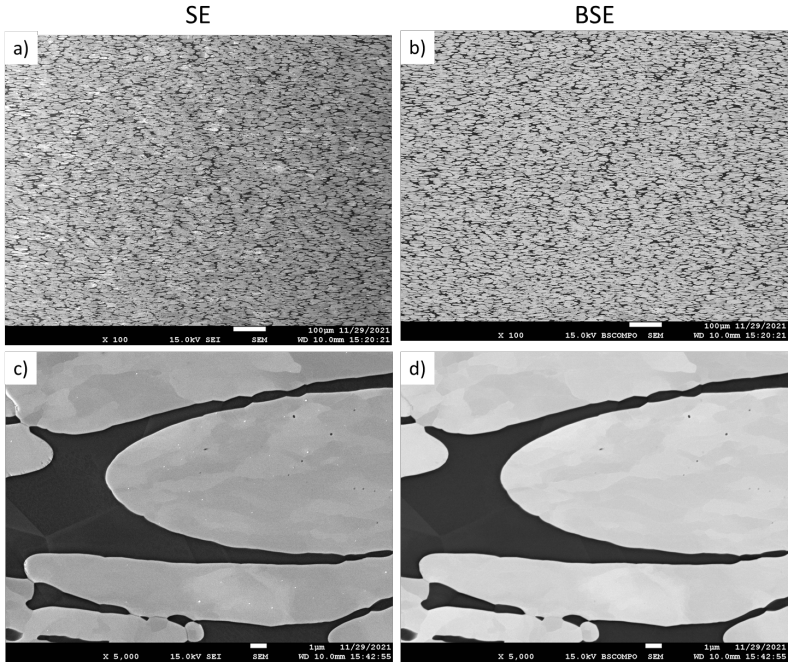

Figure 6. Secondary electron (SE) and back-scattered electron (BSE) images for 90W-85R-RD-Annealed at two different magnifications, showing microstructure of ND-RD surfaces.

Figure 8 and Figure 9 are displayed to show microstructure in as-rolled 90W-85R, as a quick comparison to previously shown annealed ones. In both SE and BSE, the results are almost identical to the annealed microstructures. Figure 10 and Figure 11 show comparison of EBSD inverse pole figures between previously rolled and newly rolled DPT W specimens. Again, the annealed specimens looks similar, but the as-rolled DPT W specimen seems to suffer from larger residual strains in the W phase. Table 2 summarize the grain statistics between annealed and as-rolled specimens from the newly hot-rolled batch. The smaller grain size in the annealed 85% reduction sample is probably due to bad statistical sampling in such a small region. Future characterization will be performed to acquire a larger area to ensure better counting statistics.

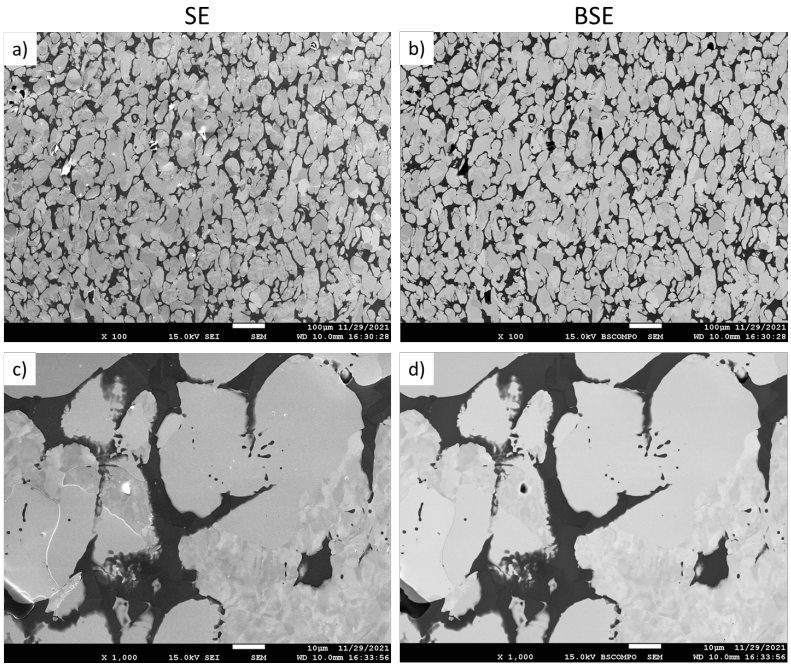

Figure 7. Secondary electron (SE) and back-scattered electron (BSE) images for 90W-85R-Plan-Annealed at two different magnifications, showing TD-RD surfaces.

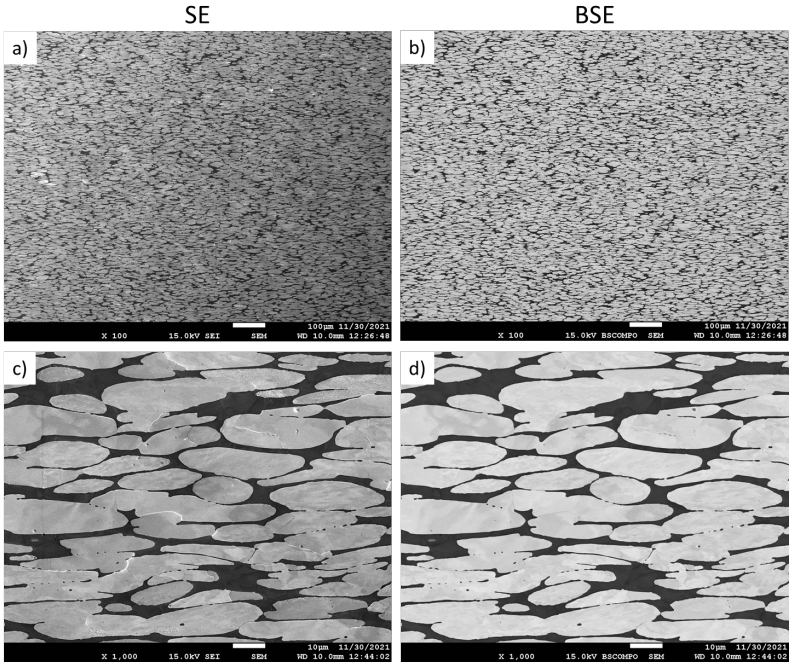

Figure 8. Secondary electron (SE) and back-scattered electron (BSE) images for 90W-85R-RD-As-Rolled at two different magnifications.

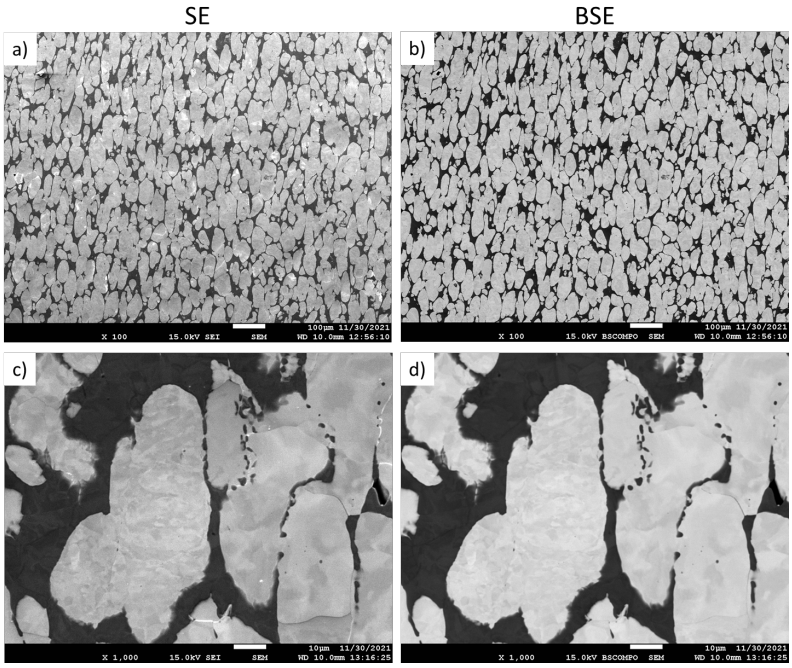

Figure 9. Secondary electron (SE) and back-scattered electron (BSE) images for 90W-85R-Plan-As-Rolled at two different magnifications.

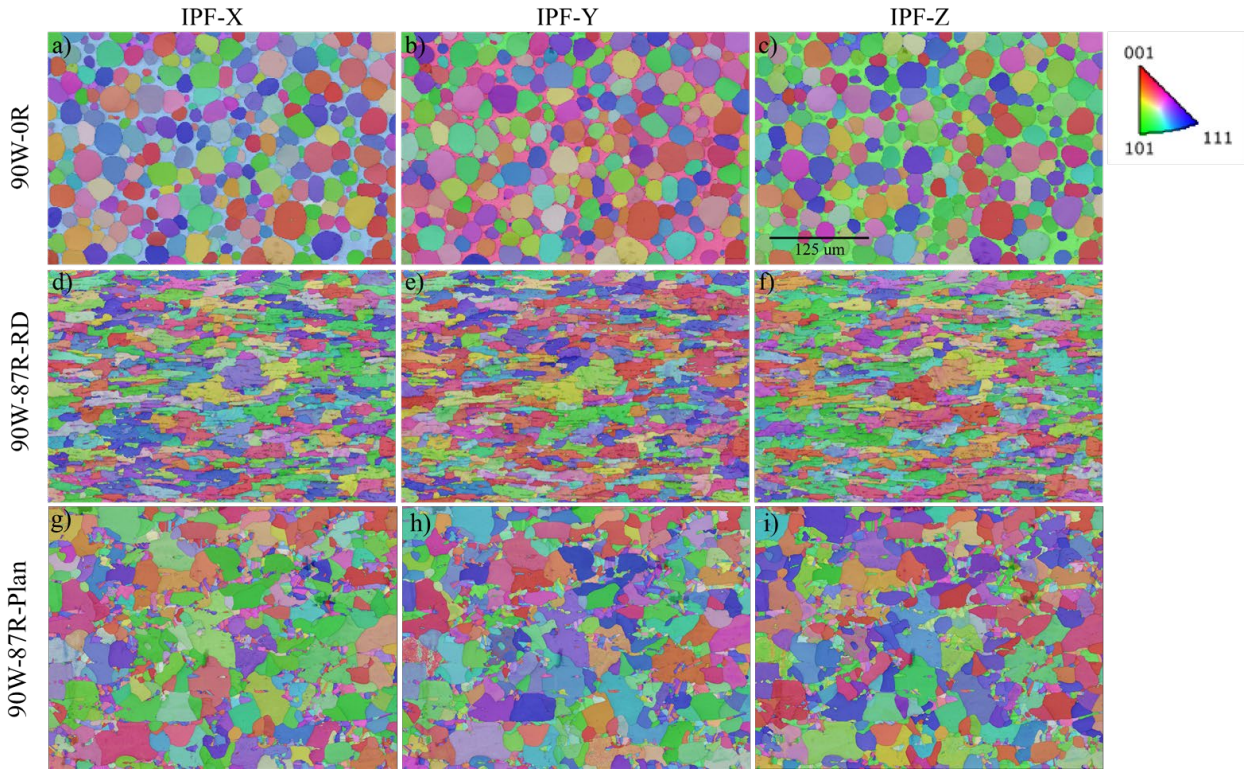

Figure 10. Inverse pole figure (IPF) maps for as-received 90% DPT W (90W-0R) and previously hot-rolled DPT W (90W-87R-RD and 90W-87R-Plan).

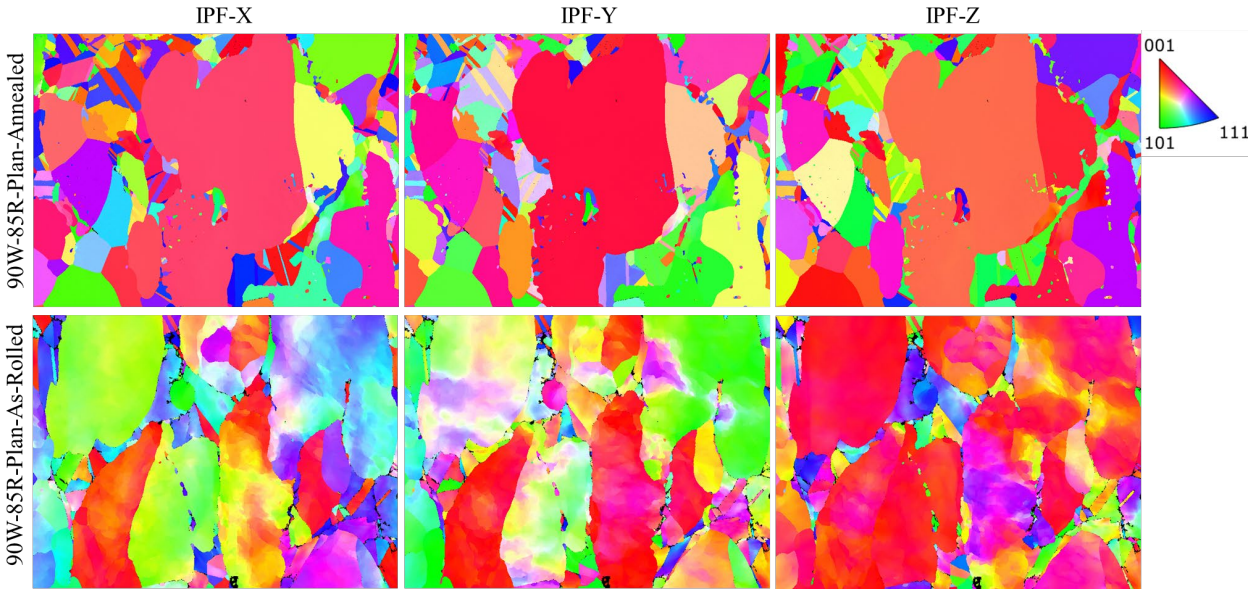

Figure 11. Inverse pole figure (IPF) maps for 90W-85R-Plan-Annealed and 90W-85R-Plan-As-Rolled.

Table 2. Number of detected grains and grain sizes are listed to investigate effects of annealing

	W		NiFe	
	No. Grains	Ave. Grain Size (um)	No. Grains	Ave. Grain Size (um)
90W-85R-Plan-Annealed	54	8.74	357	2.24
90W-85R-Plan-As-Rolled	16	15.52	164	2.68
90W-87R-Plan-Annealed	-	~15	-	~5

Microhardness Test

Microhardness was performed on as-received and previously hot-rolled DPT W specimens using a Vickers hardness tester. The polished specimen was mounted on an aluminum puck (SEM sample holder) using crystal bond. Vickers microhardness testing (15 s dwell) was performed on this mounted and polished specimen using two loads (500-gf and 1000-gf) to study the effect of load. Due to the W and NiFe phase sizes and indenter sizes are comparable, it is not feasible to extract hardness data for each individual phase in current setup. In future, a nanoindentation will be utilized to evaluate hardness of each phases and the effects of hot rolling on them.

Optical images of indentation sites after tests are displayed in Figure 12 and the obtained hardness data are presented in Table 3. For a 500-gf load, the average indent sizes were on the order of ~50 μm, which covers an area with a few W particles and NiFe matrix. The average HV for all three specimens are within a narrow range of 306-317 HV and the associated standard deviations are relatively small. This is consistent with previous tensile tests which show similar tensile strengths among as-received and hot-rolled

specimens, with the hot-rolled samples having slightly higher values. Currently, additional Vickers microhardness testing is being performed at different loads on the remaining samples.

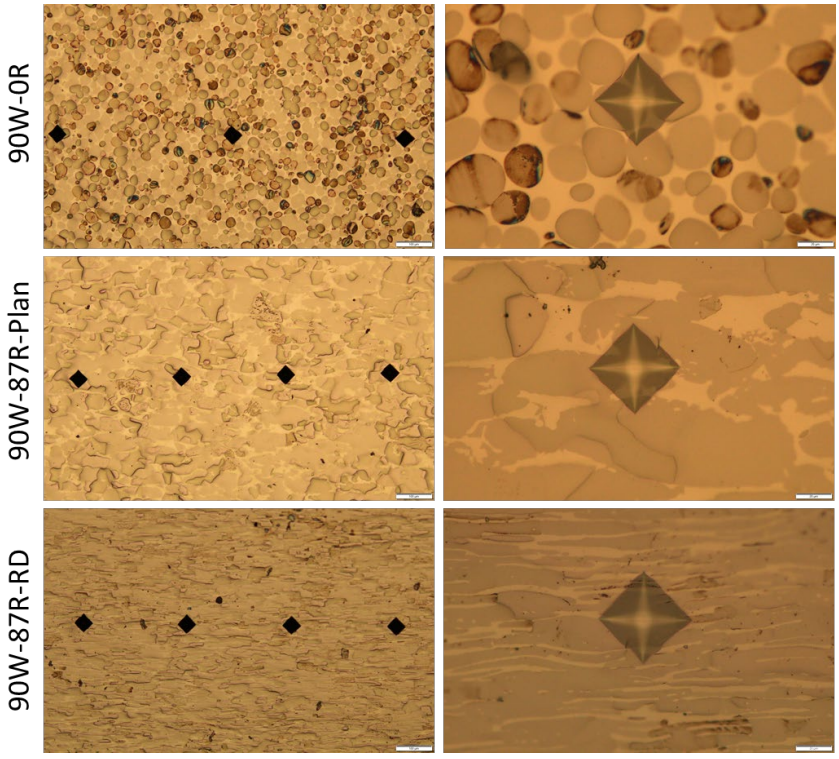

Figure 12. Optical images of tested DPT W specimens and indentation sites after tests.

Table 3. Vickers microhardness test results

Material	Test Load (gf)	Dwell time (s)	Average HV	Standard deviation
90W-0R	500	15	306	11.31
90W-R87-Plan	500	15	313	9.97
90W-R87-RD	500	15	317	7.55

Acknowledgment

This research was supported by the Office of Fusion Energy Sciences, U.S. Department of Energy (DOE) under Contract DE-AC05-76RL01830.

Reference

[1.] James V. Haag IV, et al., In-situ mechanical testing and interfacial characterization of ductile-phase toughened tungsten, in Fusion Materials Semiannual Progress Report For the Period Ending December 31, 2019. 2019. p. 78-85.

4.6 STATUS OF THE ELEVATED TEMPERATURE MECHANICAL TEST FACILITY SETUP AT PNNL

—R. Prabhakaran, J. Wang, C. H. Henager, Jr., W. Setyawan (Pacific Northwest National Laboratory)

OBJECTIVE

The objective of this task is to setup an elevated temperature mechanical test facility at PNNL and design appropriate fixtures so that various types of mechanical testing (tensile, bend, fracture toughness) could be performed to understand the mechanical behavior of ductile phase toughened tungsten heavy alloys, such as W-NiFe, for applications in fusion reactor divertor and plasma-facing components.

SUMMARY

This report summarizes the progress in the elevated temperature mechanical test facility setup (furnace, utility connections and test frame) at PNNL and designing of various mechanical test fixtures to perform tensile, bend and fracture toughness testing of ductile phase toughened (DPT) W-NiFe alloys.

PROGRESS AND STATUS

Introduction

The DPT is a fracture toughness improvement concept being utilized to develop tungsten-based composites for fusion reactor divertor and plasma-facing materials. Tungsten (W) is a promising candidate material for fusion reactor component applications due to its excellent high-temperature strength, low sputtering rate, and high melting temperature.[1-2] However, the potential application of tungsten as a structural material is limited due to its low ductility that could further degrade after irradiation.[3] Hence, introducing a ductile phase for developing a tungsten composite could serve as an alternative route to overcome its limitations.

Previous mechanical tests have been performed at room temperature using an Instron 5582 servo-mechanical test frame equipped with an Epsilon ONE optical extensometer and the results could be found in our previous reports.[4-6] Currently, efforts are ongoing to understand the mechanical behavior of DPT W-NiFe alloys at elevated temperatures (up to 1200-1300°C) and this report is focused in documenting the status of the elevated temperature mechanical test facility setup at PNNL.

Elevated Temperature Mechanical Test Facility Setup

Instron 8801 servo hydraulic mechanical test system

The Instron 8801 is a compact servo hydraulic fatigue testing system that could be employed for performing static and dynamic mechanical testing. This frame has been utilized for testing several materials at ambient and elevated temperatures (600°C). This system has both Bluehill Universal and WaveMatrix software for performing axial static and dynamics tests.

Features

- Double-acting servo hydraulic actuator with force capacity up to ±100 kN (±22 kip).
- High-stiffness, precision-aligned load frame with twin columns and actuator in the lower base.
- 150 mm (6 in) of usable stroke.
- Designed for both dynamic and static testing on a variety of materials and components.
- Choice of hydraulic configuration and dynamic performance to suit the application.
- Extra-height frame option for testing longer load strings.
- Adjustable upper crosshead with hydraulic lifts and locks fitted as standard for easy adjustment of daylight.

- Patented Dynacell advanced load cell technology for faster testing and reduction of inertial errors.
- Compact servo hydraulic fatigue test system – frame requires less than 0.5 m² (5.4 ft²) of floor space.
- Hydrostatic bearing actuators for higher side-load resistance or material critical applications, such as low cycle fatigue (LCF).
- Compatible with a large range of grips, fixtures, chambers, video extensometers, protective shields, and other accessories.

MRF Model M-4x6-M-1600-V&G Furnace

The PNNL has an Materials Research Furnaces, Inc. (MRF) Model M-4x6-M-1600-V&G front-loading furnace with a usable work zone of 3.5" dia. x 4.0" high, and a maximum operating temperature of 1600°C.

The furnace chamber has the following features:

- Rectangular, and made of double-walled, water-cooled 304L stainless steel.
- Ports to accommodate the temperature thermocouples, vacuum sensors, vacuum system etc.
- Right hand hinged front opening door.
- Two 1/2"x2" slotted sight window on the front and rear centered to the hot zone.
- The hot zone is a 180° split design with tungsten mesh heating elements for operation in vacuum (50-100 milliTORR) and inert gas.
- Ar, N_2, or Ar/O_2 gas mixture.
- Four water-cooled copper power feed-throughs that which supplies power to the heating element.

This furnace was purchased several decades ago, and it was not used for a longer time. Currently, efforts are ongoing to restore and install this furnace to a compatible state with the existing mechanical test frame in the lab. The tungsten mesh heating elements were damaged. The insulation of water-cooled power cords was also not in good condition. Hence, new heating elements and power cords were recently ordered and installed. The replacement items had a long lead time. The PNNL electricians checked the electrical connections and thermocouples. Due to the COVID-19 pandemic, ordering components and working with the building support staff have been greatly hampered.

The MRF furnace requires the following power: 23 kVA, 480V/1ph/60 Hz. 60 Amps (maximum). This required substantial modification to the existing power outlet in the lab. The furnace had to be placed next to the Instron mechanical test frame and the power outlet was several feet away. After getting necessary approval from the electrical SME (subject matter expert), longer cables were utilized, and electrical panels were changed to get the required power supply for the furnace.

Argon gas lines (2 CFM/56 LPM and 30 psig inlet pressure) were connected to the furnace through gas flowmeters. The MRF furnace needs water at the rate of 4 GPM @ 70°F and 50-60 psig (max). The water lines were also replaced and then checked for leaks. The water lines were connected to the building's chilling water supply. A water flow meter was recently purchased and connected to the furnace. Currently, water flow rate is about 2 GPM (due to nearby lab's test setup requirements and longer travel distance) and permission was obtained to install a small pump in the lab to get the required flow rate. The water sensor (that could be set to the required GPM) that acts as a safety switch (to shut off the furnace in the event of water loss) malfunctioned. Hence, it was replaced with an appropriate water sensor. The vacuum pump was also checked by the PNNL staff. A vacuum gage was recently added to the furnace to monitor the level of vacuum.

Once the new water pump is installed (early February 2022), the furnace will be ready to begin system verification testing. Once the verification is complete, we then will test the furnace at various temperatures.

Figure 1 shows the photographs of the high-temperature furnace located in the new lab space. Figure 2 shows the exterior and interior view of the MRF furnace.

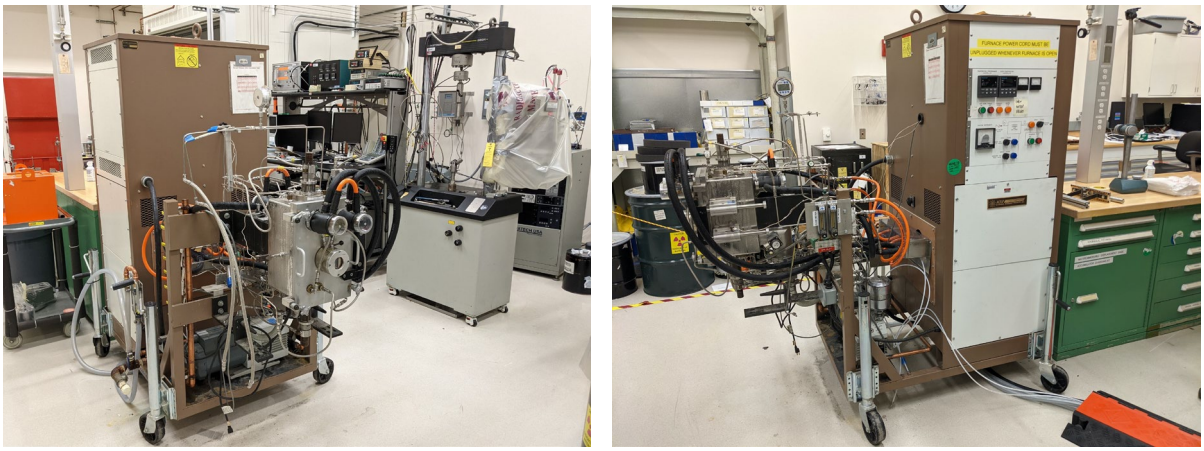

Figure 1. MRF furnace (1600°C) along with Instron 8801 mechanical test frame.

Figure 2. Exterior and interior view (tungsten mesh heating elements) of the MRF furnace.

Tensile specimen and test fixture

Previous ambient temperature tensile testing was performed using age hardened Inconel 718 fixture (using the shoulder-loaded design), as shown in Figure 3. The tensile specimens were shoulder-loaded instead of pin-loaded to avoid tear-out at the pin-hole as well as warping of the pins.

A batch of tensile specimens was recently fabricated by using wire EDM to perform intermediate temperature tensile testing (500-600°C) using the existing tensile fixture. Once the furnace installation is complete, we will begin the intermediate temperature tensile testing. A similar age hardened Inconel 718 fixture has been employed successfully to test irradiated samples in the PNNL hot cell using manipulators at 430°C.

Efforts are also ongoing to perform tensile testing at around 1000°C and slightly higher. The SiC tensile fixture can perform well at these elevated temperatures (1200-1300°C); however, the cost of machining is high, and durability is low. For this Fiscal Year, the goal is to identify a metallic material and fixture design that would allow to utilize the furnace and perform tensile testing at the maximum possible operating temperature (based on a metallic fixture).

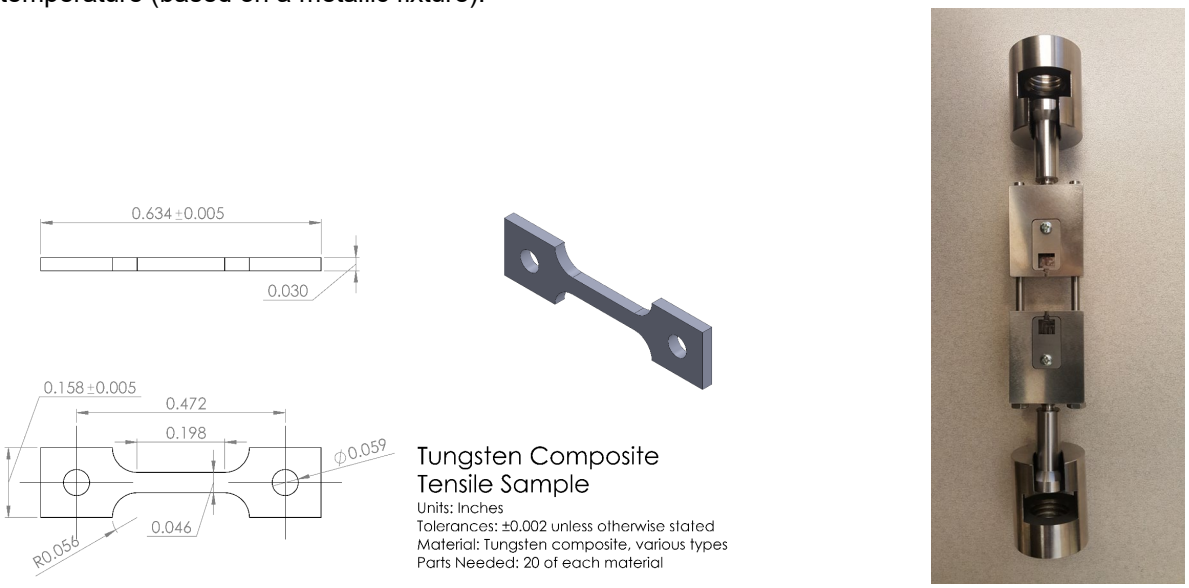

Figure 3. Tensile specimen geometry (left) and shoulder-loaded tensile fixture (right).

Bend test specimen and test fixture

The PNNL has several three and four-point bend test fixtures. Figure 4 shows two types of four-point bend test fixtures: (a) SiC fixture for testing at elevated temperatures (over 1000°C) and (b) Inconel or Hasteloy-X fixture that uses SiC pins for load transfer. Currently, efforts are ongoing to determine the type of metallic alloy by referring the old records.

In the past, different types of specimens were employed by various fusion materials researchers for several studies:

- The W-Cu composite was machined into 3.30-mm × 1.67-mm × 16.05-mm single-edge notched bend (SENB) specimens and as-sintered W-Ni-Fe alloy was machined into 4-mm × 3-mm × 20-mm bend bars and three-point bend tests were conducted.[7]
- Four-point SENB specimens measuring 25.4-mm × 1.75-mm × 4.0-mm were cut from pieces of hot rolled W-Ni-Fe materials.[8]
- Room temperature fracture toughness tests were conducted on the small, fatigue pre-cracked, single-edge notch bend bar specimens with a nominal length (L) x width (W) x thickness (B) dimensions of 25.4-mm × 4.0-mm × 1.75-mm.[9] Researchers at UCSB (University of California, Santa Barbara) expressed interest in sending samples to PNNL so that elevated temperature fracture toughness testing could be performed.

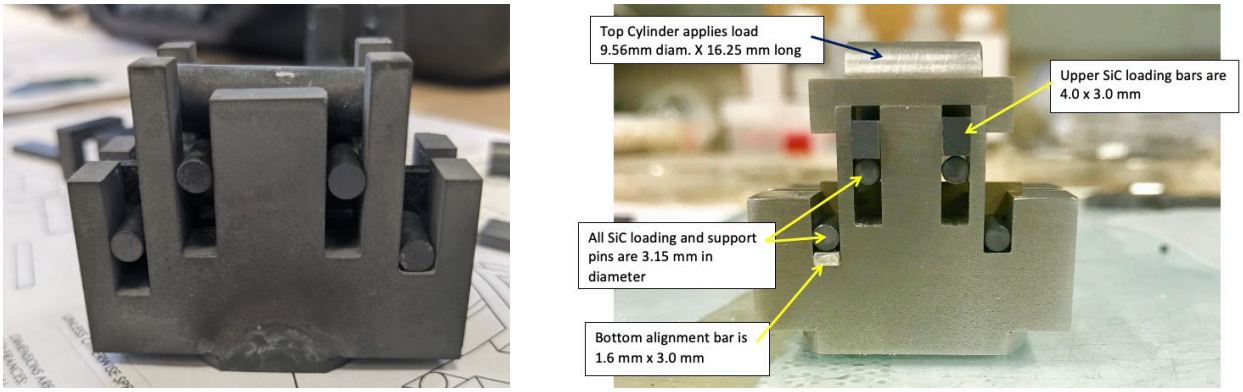

Figure 4. Four-point bend fixtures: SiC fixture (left) and Inconel or Hasteloy-X fixture (right).

The PNNL researchers have also employed an Inconel 718 fixture (see Figure 5) for three-point bend testing of notched stainless-steel samples (13 mm x 5 mm x 3 mm). Currently, efforts are ongoing to modify this fixture to accommodate four-point bend testing of unnotched bars for a different project. This modified fixture design concept could also be employed for the fusion materials program.

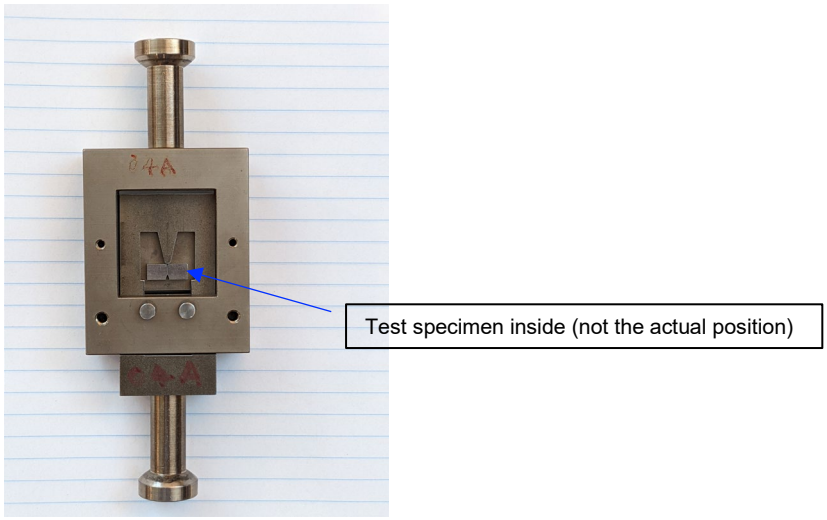

Figure 5. Three-point age bend fixture made of Inconel 718.

Acknowledgment

This research was supported by the Office of Fusion Energy Sciences, U.S. Department of Energy (DOE) under Contract DE-AC05-76RL01830.

References

[1.] Wurster, S., et al., *Recent progress in R&D on tungsten alloys for divertor structural and plasma facing materials.* Journal of Nuclear Materials, 442(1-3): p. S181-S189, 2013.

[2.] Stork, D., et al., *Developing structural, high-heat flux and plasma facing materials for a near-term DEMO fusion power plant: the EU assessment.* Journal of nuclear materials, 455(1-3): p. 277-291, 2014.

[3.] Hasegawa, A., et al., *Neutron irradiation effects on the microstructural development of tungsten and tungsten alloys.* Journal of Nuclear Materials, 471: p. 175-183, 2016.

[4.] Wang, J., et al., *Tensile testing and microstructural characterization of ductile phase toughened W-NiFe alloys*, in *Fusion materials Semiannual Progress Report for the Period Ending June 30, 2020*. 2020.
[5.] Wang, J., et al., *Microstructural characterization and mechanical testing of ductile-phase toughened tungsten*, in *Fusion materials Semiannual Progress Report for the Period Ending December 31, 2019*. 2019.
[6.] Wang, J., et al., *Microstructure-Mechanical Property Correlation in Ductile Phase Toughened W-NiFe Heavy Alloy*, in *Fusion Materials Semiannual Progress Report for the Period Ending December 31 2020*, D. Clark, Editor. 2020.
[7.] K.H. Cunningham, K. Fields, D. Gregg and T. Roosendaal, 4.1, Volume 54: *Recent Progress in the Development of Ductile-Phase Toughened Tungsten for Plasma-Facing Materials*, DOE/ER-0313/54-Volume 54, Semiannual Progress Report, June 30, 2013, edited by F.W. Wiffen, R. Godfrey and B. Waddell, US DOE, ORNL, TN, vol. 54, chapt. 4.1, pp. 95-107, 2013.
[8.] Henager, C. H., et al., *Ductile-phase toughened tungsten for plasma-facing materials in fusion reactors*, International Journal of Powder Metallurgy, Volume 53, No. 2, 2017.
[9.] Alam, M.E., et al., *The effect of hot rolling on the strength and fracture toughness of*
[10.] *90W-7Ni3Fe tungsten heavy metal alloys*, Materials Science & Engineering A 824, 141738, 2021.

4.7 METHOD DEVELOPMENT AND PREPARATION OF TUNGSTEN FIBERS FOR IRRADIATION—L. M. Garrison (Oak Ridge National Laboratory), J. Riesch (IPP-Garching)

OBJECTIVE

The goal was to develop a method to irradiate thin tungsten wires and fibers. The method was then used to prepare the materials for irradiation in the FRONTIER campaign.

SUMMARY

A method for keeping thin tungsten wires and fibers straight during preparation and irradiation was developed. A fixture was designed for preparing a bundle of 16 μm diameter tungsten fibers to be inserted into a 1.2 mm diameter opening in a tungsten tube for irradiation. Six tungsten tubes, each containing 36 tungsten wires with 150 μm diameter and 24 pieces of 16 μm diameter tungsten fiber were prepared for irradiation. The details of the wire and fiber preparation and loading list for each of the six tungsten tubes are recorded here.

PROGRESS AND STATUS

Tungsten wires and fibers are an important component in tungsten composites. Their behavior after irradiation generally determines the behavior of the composite, so studying them individually is beneficial. The challenge is that the tungsten wires and fibers used are 150 μm and 16 μm diameter, respectively. This is too small to individually engrave or to insert directly in most irradiation capsules. Therefore, within an irradiation capsule, a smaller container must be designed to keep the fibers straight and accounted for during and after the irradiation.

Experimental Procedure

Materials

Three types of tungsten wires and one tungsten fiber were used. Previously in the PHENIX irradiation campaign, three types of tungsten wires were irradiated and referred to as Type 1, Type 2, and Type 3. In FRONTIER, more of the Type 1 and Type 3 material was irradiated, as well as a new type, Type 4, as below. The same starting material was used to produce the Type 4 wire and the fiber. Tungsten's properties depend not only on the material but also strongly on the processing method and grain size, so both the Type 4 wire and the fiber are useful to test. These wires and fibers were provided by IPP-Garching, so their label is also indicated for tracking purposes. The content of K doping is reported as measured by High Resolution Gas Discharge Mass Spectroscopy of the parent ingots that the wires or fibers were drawn from.

Table 1. Information about the three wire and one fiber type that were included in the FRONTIER irradiation

	Type 1	Type 3	Type 4	Fiber
Composition	W 73 ppm K	W	W 66 ppm K	W 66 ppm K
Straightening method	Plastic deformation	Plastic deformation	Plastic deformation	As-produced and wound on a spool (not straightened)
IPP-Garching Label	Wire No. 13	Wire No. 9	Wire No. 28	Wire No. 27
Diameter	150 μm	150 μm	150 μm	16 μm
Length	37 mm	35.5 mm	34 mm	approx. 37.5 mm
Note	Same as "Type 1" wire used in PHENIX	Same as "Type 3" wire used in PHENIX	Same material as the fiber	Same material as Type 4 wire

Cutting

All types of the 150 μm diameter wires were received in ~30 cm long pieces. A cutting guide was made by printing lines of the desired length on a paper. To cut the wires to the desired length, they were lined up on top of the corresponding marking, gently held in place by hand, and the cut made with small wire cutters. To be able to differentiate the wires after irradiation, each type of wire was cut to a slightly different length, which are 1.5 mm different from each other (Type 1: 37, Type 3: 35.5, Type 4: 34 mm). This same method of different lengths was used successfully to differentiate the wires irradiated in the PHENIX campaign.

The 16 μm diameter fiber was loaded from the spool into the tube for irradiation, as described below. Because the fiber is very flexible and will curl and tangle if a length of it is cut from the spool, it could not be loaded in the same way as the wires and the new procedure described here had to be developed.

Cleaning

After the 150 μm diameter wires were cut to the proper size, they were placed in shallow metal dishes for cleaning. Acetone was sprayed into the dishes, the dishes were gently agitated by hand to make sure the acetone reached all surfaces, and the acetone was allowed to evaporate in the fume hood (about five minutes). The procedure was repeated with methanol or ethanol (depending on availability in the lab). The last drops of the methanol were absorbed with a kimwipe, using very light pressure to avoid bending the wires.

The 16 μm diameter fiber was sprayed with acetone after being wound on the loading frame and allowed to dry in the fume hood. In most cases, a kimwipe sprayed with acetone was used to gently touch the fibers since they could not be submerged.

Winding fibers and loading tubes

To irradiate the wires and fibers, they must be contained somehow within the capsule to prevent any damage to them and to keep track of the small pieces. Previously in the PHENIX campaign, a small graphite tube was used to load the tungsten wires. After irradiation, the wires were unloaded from graphite tube in LAMDA. A similar approach was used here, except there was a concern about carbon contamination of the fibers, so a tungsten tube was desired. The capsules for FRONTIER also required a different geometry of tube than was used previously. A tungsten tube with an outer rectangular shape and a central round hole was fabricated to fit inside the irradiation capsule designed for fracture toughness bars. The tungsten tube replaces one row of three bars and is 37.5 mm in length and has a cross section that matches the dimensions of the bars, 2 by 2.67 mm. The central hole in the tube is 1.2 mm diameter (Figure 1).

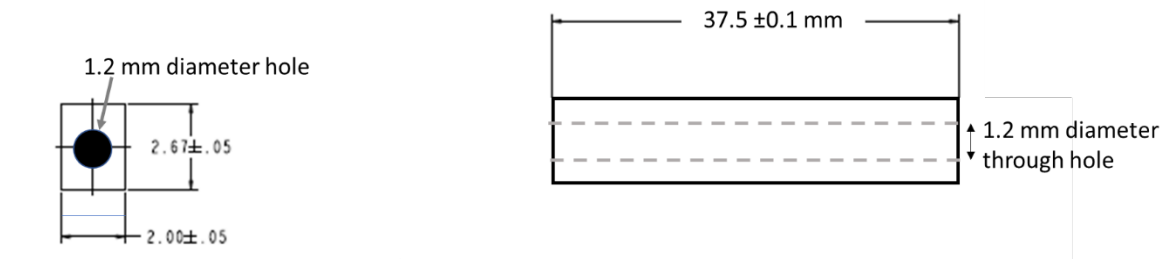

Figure 1. Dimensions of the tungsten tube for holding the fibers and wires during irradiation.

The tungsten wires retain their straight shape when moved, so only required a pair of tweezers to load into the small tube. However, the tungsten fiber will curl if it is cut from the spool and does not have the stiffness to be able to be pushed into the tube, so a different method for loading the fibers was needed. In fact, if the tungsten fiber is released from gentle tension, it will tangle and twist onto itself and cannot be straightened again; any force used to try to untangle it will more likely damage or break the fiber and then the pieces cannot be used for testing. The loading method needed to always keep the fiber straight and with a gentle tension on it to maintain the fibers in good condition.

The procedure was developed to wind the fiber around two supports and then transfer the fibers into the tube while always maintaining a light tension on them. The fiber winding fixture has a 60 mm span between the two posts and two screws in the base plate to serve as the starting and ending points for winding the fiber (Figures 2-3). Each of the posts unscrews from the base plate, which allows the fiber bundle to be removed from the fixture after it is wound. After the fibers were loaded into the tungsten tube, the tungsten wires Type 1, 3, and 4 were added with tweezers into the tube. The detailed steps of the fiber winding and loading are described and illustrated below.

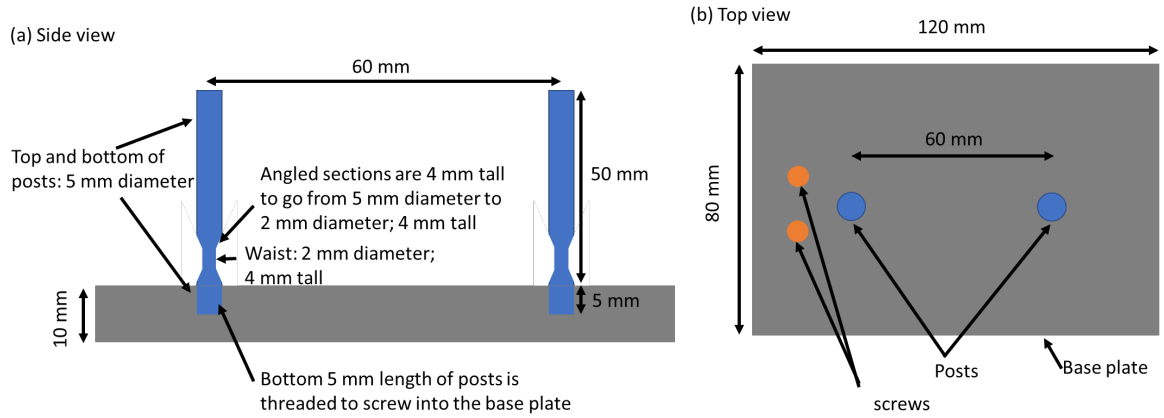

Figure 2. Illustration of the fiber winding fixture (not to scale).

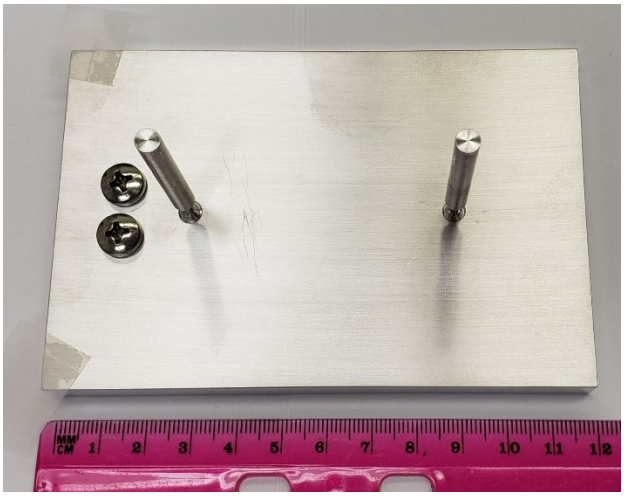

Figure 3. Fiber winding fixture.

Procedure for fiber winding and loading for irradiation

All the images shown in the procedure were taken during the loading of tungsten tube with ID 21-06.

Prepare the workspace and secure the end of the fiber.

The workspace should have a large clear area to give room for winding. Place blank paper under the fiber fixture and write the engraved identification of the tube and make an area to keep track of rotations. In this way, any of the images will be traceable to the individual tube and the step in the process. To start the winding, secure the end of the fiber under the top screw on the left of the fixture, and put a small piece of tape on the fiber to secure it more fully to the base plate. Gently keep a small amount of tension on the fiber as the spool is unwound to the right (Figure 4).

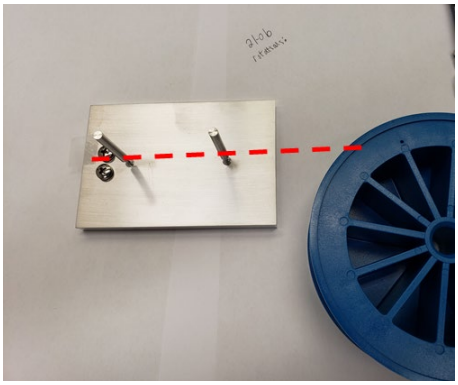

Figure 4. The starting end of the fiber has been secured under the screw and a piece of tape on the left, and the fiber spool (blue) is on the right of the fixture. No rotations have been completed yet. The path of the fiber is overlaid with the red dotted line because it is too small to be seen in the image.

Continue winding the fiber clockwise around the two posts for a total of 12 rotations.

Each time the spool reaches the location shown in Figure 5, add a tick mark to the tally of rotations. It is important to record each carefully in case there is a fiber break, and the winding needs to be resumed in the middle. At all times keep gentle pressure on the fiber as the spool is rotated around the fixture to avoid

the fiber developing any kinks, loops, or tangles. In Figure 5 six rotations have been completed; in Figure 6, all twelve rotations have been completed. On rotation 12, the spool is kept on the left side instead of fully circling the post. The fiber is strong for its size, but it can only hold ~1 N, so it can be broken by a person if too much tension is applied to it. If this happens, and the fiber unwinds or tangles badly, the winding will have to be started again from the beginning. In many cases, however, if there is a break, the broken end of the fiber can be pulled gently to take out any slack that might have developed in the fiber that has already been wound. Then, the end can be secured to the nearest screw; either completing the current rotation and securing it under the closer screw if it is long enough, or unwinding the last half turn and again securing it under the closer screw. No ends can be taped or attached in any way to the base plate of the fixture except where the screws are on the left. Then, pick up the new end on the spool and secure it to the top screw. Finally, continue with the rotations until the remainder of the windings are completed.

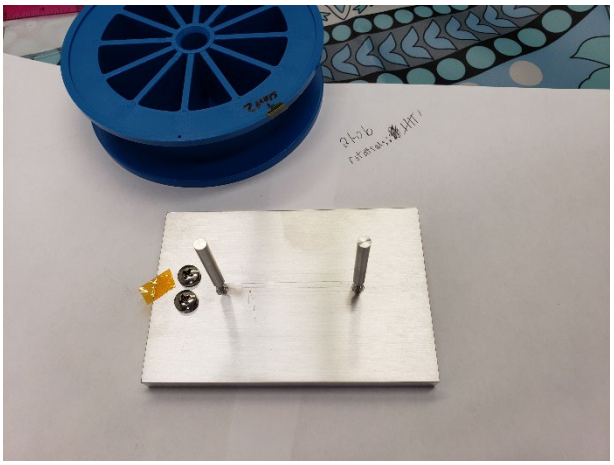

Figure 5. Six rotations have been completed. A tick is added to the rotation tally each time the spool is in the position shown.

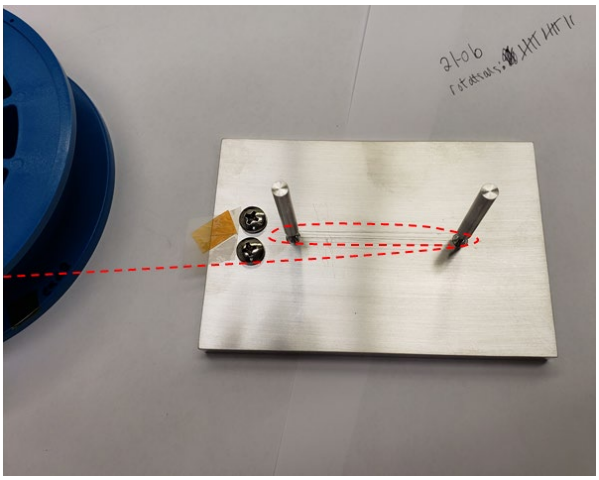

Figure 6. For the final (twelfth) rotation, the spool ends on the left side rather than the top. In this position, it is easier to guide the fiber under the bottom screw on the left and secure it with tape before cutting the spool free. The approximate path of the final rotation of the fiber is illustrated with the red dotted line.

<u>Secure the end of the fiber and cut free from the spool.</u>

When the final rotation is in the position in Figure 6, gently slide the fiber under the lower screw (closer to the operator) and tighten the screw. Add a small piece of tape to secure the fiber to the base plate of the fixture to the left of the screw. Put a small piece of tape about a centimeter away from the fixture and hold with one hand while the other hand cuts the fiber in between the base plate and the second piece of tape. In this way, a light tension remains on the rest of the fiber on the spool until the end with the tape can be secured on the edge of the spool. Once the spool is cut and its end secured, it can be put away. The fiber bundle is now completely on the winding fixture (Figure 7).

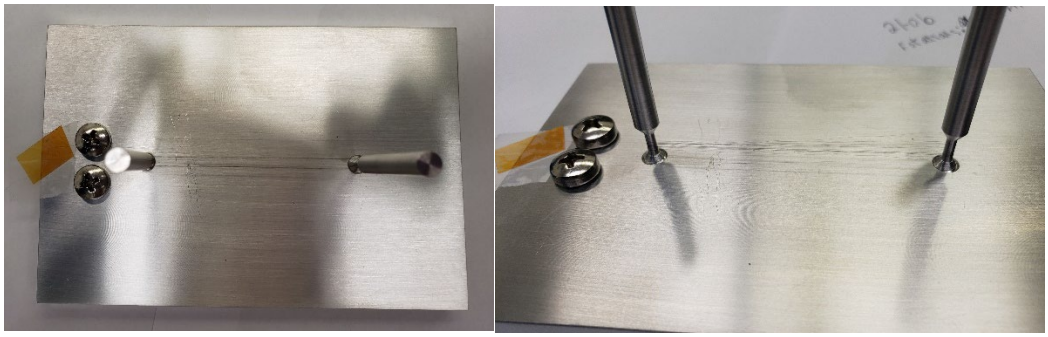

Figure 7. Top and side views of the completed twelve winds of the fiber. The end has been secured and the fiber leading to the spool was cut.

Clean fibers while on the frame by spraying alcohol on them and wiping excess.

Once the fibers are all wound on the frame and the spool has been removed, move the fixture with fibers to a fume hood. Spray acetone on the center of the fibers between the two posts, avoiding the screws and tape on the left. Use a kimwipe to gently dab away excess and allow to dry in the fume hood.

Use a sewing needle to loop thread through the right end of the fiber bundle.

After the fibers are clean, remove the fixture from the fume hood and return to the workspace. Use any sewing thread and a sewing needle >38 mm long. Here, the thread is yellow so it can be easily seen while working and in images. Thread the thread through the eye of the needle and tie the two ends together in a single knot. The length of the thread should be ~80-100 mm. The length is not critical, but it is useful for the thread to be longer than the tungsten tube length, but not too long. Gently pass the sewing needle under and through the middle of the fibers (Figure 8). Bring the needle all the way through the gap in the middle of the fibers, and then pass the point through the two yellow threads. Gently pull on the needle until the knot is secure around the bundle of fibers.

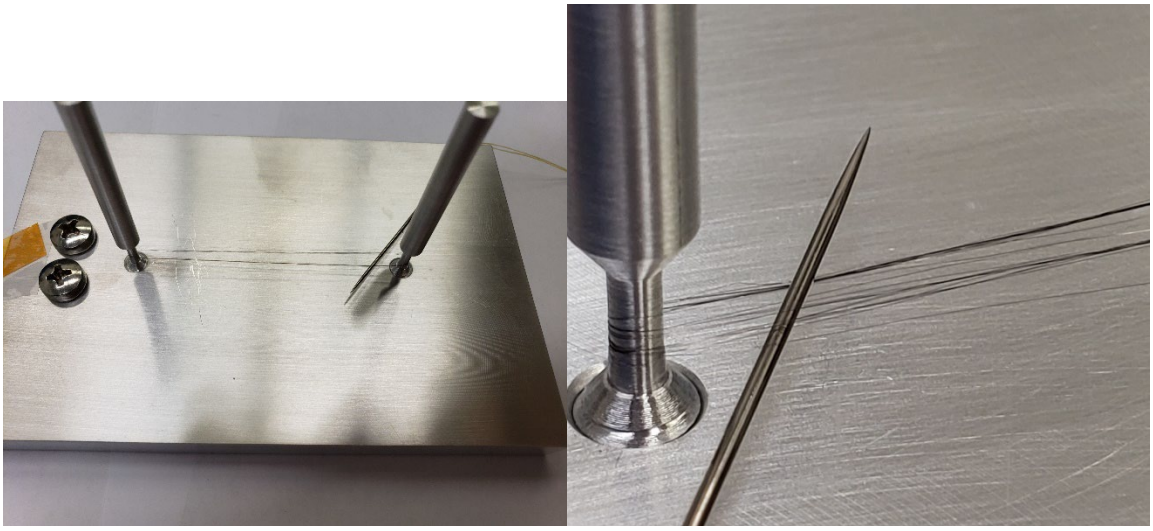

Figure 8. (Left) View from the front of the fixture showing the needle partially inserted below the back group of fibers, coming up through the middle, and ending on top of the front group of fibers. (Right) Close-up view from the back of the fixture with the needle in the same position; here the fibers in the foreground are on top of the needle and the fibers in the background are below the needle.

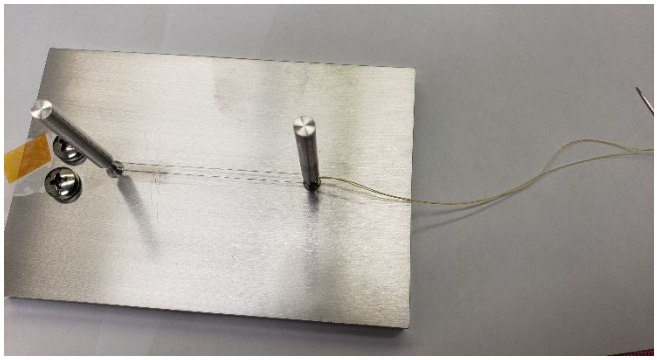

Figure 9. The knot in the thread is secure around the fibers next to the right post of the fixture. The needle is mostly out of the frame on the right.

Slide tube onto needle and thread.

This is shown in Figure 10.

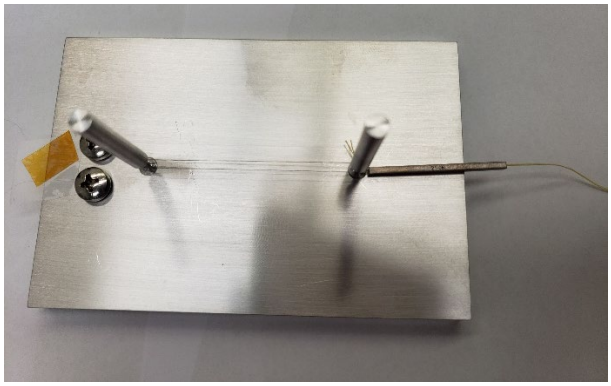

Figure 10. Tungsten tube has been slid over the needle and onto the thread.

Remove right post, keeping hold of the thread with right hand.

While holding the thread with gentle pressure with the right hand, use the left hand to unscrew the right post. Carefully slide the tube to the left slightly and then out from between the fibers; set post aside. As soon as the post is removed and continuing through the next couple steps, gentle tension must be kept on the fibers by holding the thread on the right side (Figure 11).

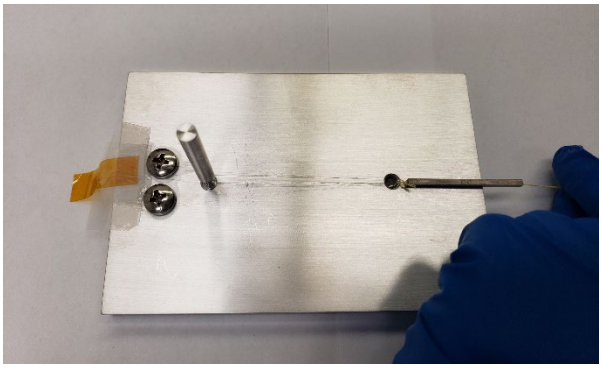

Figure 11. The right post has been removed. The hand is holding the yellow thread, which is putting a light tension on the fibers.

Slide tube onto fibers.

While keeping the hand holding the thread and applying a gentle tension on the fibers in place, use the left hand to slide the tungsten tube over the knot in the thread and onto the bundle of fibers (Figure 12). The twelve rotations of fibers create 24 lengths of fiber inside the tube, and this only takes up a small fraction of the space inside the tube, so the gentle tension is still required to prevent the fibers from curling or tangling inside the tube.

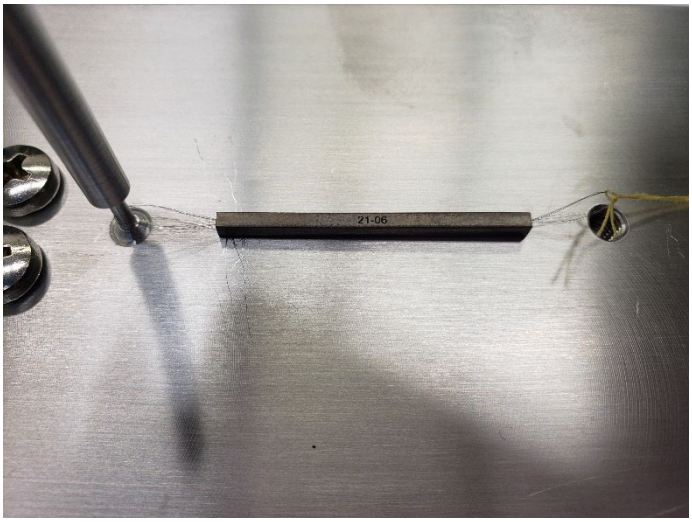

Figure 12. The tube has been slid onto the bundle of fibers. The yellow thread is being gently pulled to the right, which keeps the fibers straight in the tube.

Add 150 μm wires, leaving part out of tube until all loaded and then slide in the rest of the way.

Next, use tweezers to slide the 150 μm wires into the right side of the tube. It may be useful to switch the left hand to keep the slight tension on the thread while the right hand uses tweezers to load the wires. Here, 12 of Type 1, 12 of Type 3, and 12 of Type 4 wires were loaded into each tube. It is useful to not push the wire fully into the tube so the next wire can be placed on top of it (Figure 13). If the wires are pushed all the way into the tube, it is likely that the next wire loaded may push out an earlier wire rather than sliding into the tube. In a trial loading of the wires without the fibers, the end of the tube was imaged (Figure 14). Once all 36 wires have been loaded, then can be gently pushed the rest of the way into the tube. Again, keep gentle tension on the thread so the fibers do not move when the wires are slid into place.

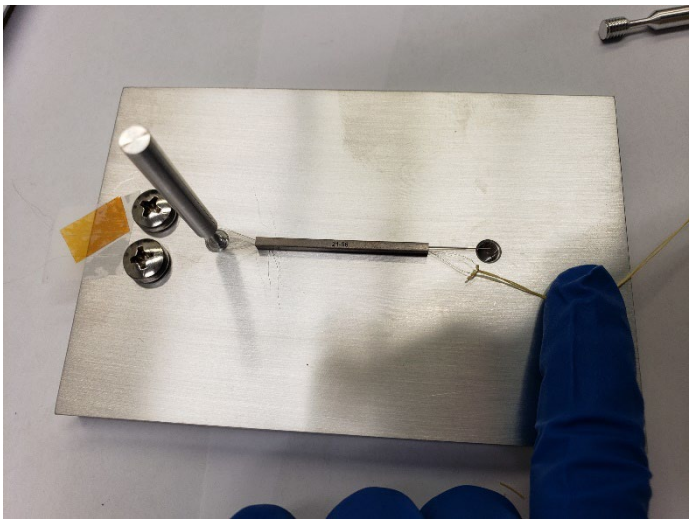

Figure 13. Some of the wires have been loaded and are sticking a few millimeters out of the tube on the right.

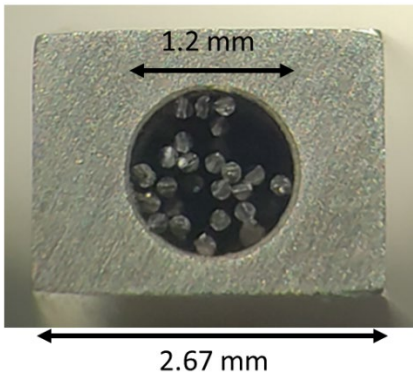

Figure 14. End view of a practice loading of the 150 μm wires into the tungsten tube without the fibers.

Remove left post, cut ends connected to tape, cut thread so it is shorter.

Once all the wires have been loaded, it is not a tight fit, but it is not easy for the fibers or wires to slide out. At this stage, the left post can be unscrewed from the fixture. The two screws on the left should be loosened, and the ends of the fibers under the tape should be cut. The thread does not need to be removed, only cut shorter. The fiber and wire loading is now complete (Figure 15). The ends of the fibers remain outside the tube until the end caps are secured by the capsule build group. After the end caps are put on, the fiber tails are cut to be flush with the ends of the tube.

Figure 15. A tungsten tube that has been completely loaded with tungsten wires and fibers and is ready for the end caps to be put in place.

Below are the final contents of the six tubes that were prepared for the FRONTIER irradiations. In cases where the fiber winding had to be completed with material from different spools, the number of lengths from each spool is indicated. This happened in cases where there was an accidental break and where one spool was finished, and another needed to be opened to complete the windings for one tube. In the table, “lengths” are noted because that is the final contents of the tube. One rotation or one circle around the winding fixture results in two lengths of fiber in the tube. Thus for 12 rotations on the winding fixture, the result is 24 lengths of fiber.

Table 2. Final contents of fibers and wires in tungsten tubes for FRONTIER irradiation

	Tube: 21-06 Completed 8/2/21
Wire No. 27 spool 2010-04-A part 2	24 lengths
Type 1; 37 mm long	12 wires
Type 3; 35.5 mm long	12 wires
Type 4; 34 mm long	12 wires

	Tube: 21-01 Completed 8/3/21
Wire No. 27 spool 2010-04-A part 2	2 lengths
Wire No. 72 spool 2010-04-A part 1	18 lengths
Wire No. 27 spool 2010-04-B	4 lengths
Type 1; 37 mm long	12 wires
Type 3; 35.5 mm long	12 wires
Type 4; 34 mm long	12 wires

	Tube: 21-02 Completed 8/3/21
Wire No. 27 spool 2010-04-B	24 lengths
Type 1; 37 mm long	12 wires
Type 3; 35.5 mm long	12 wires
Type 4; 34 mm long	12 wires

	Tube: 21-03 Completed 11/19/21
Wire No. 27 spool 2110-02	24 lengths
Type 1; 37 mm long	12 wires
Type 3; 35.5 mm long	12 wires
Type 4; 34 mm long	12 wires

	Tube: 21-04 Completed 11/22/21
Wire No. 27 spool 2110-02	14 lengths
Wire No. 27 spool 2110-03	10 lengths
Type 1; 37 mm long	12 wires
Type 3; 35.5 mm long	12 wires
Type 4; 34 mm long	12 wires

	Tube: 21-05 Completed 12/10/21
Wire No. 27 spool 2110-03	24 lengths
Type 1; 37 mm long	12 wires
Type 3; 35.5 mm long	12 wires
Type 4; 34 mm long	12 wires

4.8 CHARACTERIZATION OF DISCONNECTION CONTENT ASSOCIATED WITH GRAIN BOUNDARY MOTION IN TUNGSTEN—I. S. Winter, T. Frolov, T. Oppelstrup, R. E. Rudd (Lawrence Livermore National Laboratory)

Extended abstract of a manuscript titled "Characterization and visualization of grain boundary disconnections" completed and submitted to Acta Materialia with our FES funding

OBJECTIVE

The objective of this study is to develop a new computational methodology to predict the motion of grain boundaries in tungsten associated with recrystallization. This approach accounts recently discovered high-temperature grain boundary phases in tungsten and other metals and alloys. This paper [1] reports the initial work in the project that developed a novel technique for molecular dynamics to characterize disconnections, dislocation-like defects in grain boundaries that mediate grain boundary motion. Grain boundary properties are needed for a thermomechanical model of recrystallization of tungsten for magnetic fusion applications.

SUMMARY

Tungsten is a material of interest to meet the requirements for tokamak first-wall materials due to its high thermal conductivity, acceptable activation levels, high melting temperature, mechanical strength at elevated temperatures, and resistance to surface sputtering. However, conventionally processed tungsten is not mechanically robust at desired operating conditions, and the path forward to improve its performance is work in progress. Recrystallization and embrittlement are important remaining challenges. Plasma-facing components need to operate below their recrystallization temperature to prevent grain growth and embrittlement. Grain growth involves the motion of grain boundaries, and their motion can be affected by structural changes due to grain boundary phase transformations [2-6]. Molecular dynamics can provide predictions of the motion of grain boundaries, both through explicit simulations and through the identification of mechanisms that can be used to construct analytic models.

In this paper submitted for publication we describe the development of a new technique to characterize dislocations that works not only for bulk dislocations, but for disconnections that lie within grain boundaries. Techniques to visualize bulk dislocations have proven to be powerful tools in the analysis of plasticity in molecular dynamics simulations. Often those simulations produce such copious data that it is overwhelming without powerful analysis methods, and visualization and quantification techniques like OVITO and DXA are extremely valuable in managing the vast data and reducing it to an essence that is relevant and visual. Unfortunately, the standard techniques do not work in grain boundaries, where the interface itself is a defect and its discontinuities thwart standard quantitative techniques using Burgers circuits. There is a need for similar techniques that work for dislocations whether in the bulk or in grain boundaries. This paper describes a new technique that does just that.

Specifically, we have developed a new method for characterizing and visualizing dislocation content in grain boundaries that requires no prior knowledge of a given grain boundary's atomic structure. As a proof of concept, we describe application of this method to grain boundaries in body-centered cubic tungsten, as well as to a disconnection in face-centered cubic copper. We show that the technique works on phase junctions between different grain boundary phases, currently a hot topic. We show the dislocation content of these systems to be well characterized by our method, revealing not only the presence of dislocations within a grain boundary, but the dislocation type as well. The method uses an atomistic Nye tensor approach based on the displacement shift complete (DSC) lattice. This method promises to be of great use to the field, enabling a broad range of future studies into polycrystalline plasticity, the kinetics of boundary migration and new possibilities for grain boundary engineering.

Future Plans

We are applying the disconnection characterization technique to the results of large-scale molecular dynamics simulations, analyzing disconnection mechanisms associated with grain boundary motion as well as the nucleation and growth processes associated with grain boundary phase transformations. These results will inform analytic models of grain boundary motion.

Acknowledgments

This work was performed under the auspices of the U.S. Department of Energy by Lawrence Livermore National Laboratory under Contract DE-AC52-07NA27344. This material is based upon work supported by the U.S. Department of Energy, Office of Science, Office of Fusion Energy Sciences. Computing resources for this work came from the LLNL Institutional Computing Grand Challenge program.

References

[1] I. S. Winter, T. Oppelstrup, T. Frolov, and R. E. Rudd, "Characterization and visualization of grain boundary disconnections," submitted to Acta Materialia (2022). arXiv:2201.13441.
[2] I. S. Winter, T. Oppelstrup, T. Frolov, and R. E. Rudd, Phys. Rev. Lett. 128, 035701 (2022).
[3] T. Frolov, Q. Zhu, T. Oppelstrup, J. Marian, and R. E. Rudd, Acta Mater. 159, 123 (2018).
[4] T. Frolov et al., Nanoscale 10, 8253 (2018).
[5] T. Meiners, T. Frolov, R. E. Rudd, G. Dehm, and C. H. Liebscher, Nature 579, 375-378 (2020).
[6] Q. Zhu, A. Samanta, B. Li, R. E. Rudd, T. Frolov, Nature Comm. 9, 467 (2018).

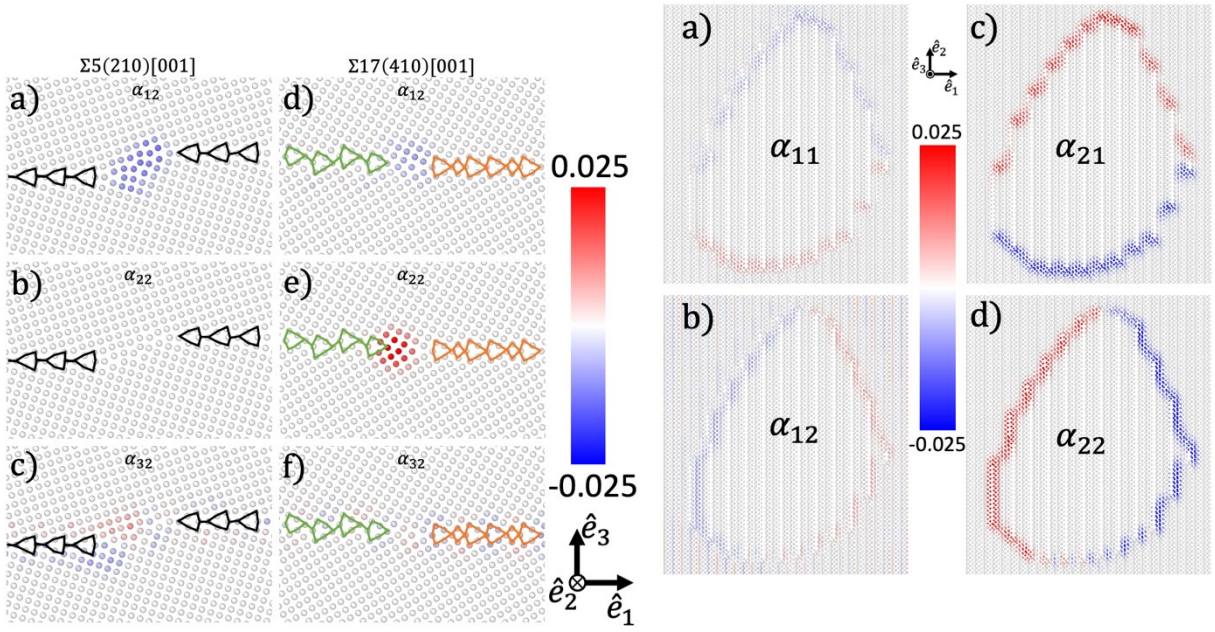

Figure 1. (left panel) Visualization of disconnections in two tungsten grain boundaries: Σ5(210)[001] (left column) and Σ17(410)[001] (right column). The circles denote columns of atoms, colored by the atomistic Nye tensor values α_{ij} using our DSC-based technique. The solid lines trace structures characteristic of the grain boundary. The Σ5 boundary has the kite structure on both sides of the disconnection; the Σ17 boundary has kites on the left and kites and squares on the right. The sum over atoms of α_{i2} gives the Burgers vector: $-1.35e_x$ Å (Σ5) and $-0.57e_x+1.62e_y$ Å (Σ17), where e_x and e_y are unit vectors in x and y, respectively. (right panel) Whereas the left panel views the grain boundary side on along the disconnection line, the right panel has the Σ17 grain boundary in plain view, showing the staircased morphology of the disconnection loop.

4.9 TRANSMISSION ELECTRON MICROSCOPY ANALYSIS OF A HEAVY ION IRRADIATED TUNGSTEN HEAVY ALLOY—J. V. Haag IV, M. Murayama (Virginia Tech), M. J. Olszta, D. J. Edwards, W. Jiang, W. Setyawan (Pacific Northwest National Laboratory)

OBJECTIVE

This work is aimed at the observation of radiation damage in a 90 wt.% W tungsten heavy alloy after sequential Ni^+ and He^+ ion irradiations.

SUMMARY

A dual phase 90W-7Ni-3Fe tungsten heavy alloy was subjected to Ni^+ then He^+ ion irradiations to mimic the displacements per atom (dpa) and He production values expected after a simulated five years of service in the DEMO-1 reactor. Focused ion beam (FIB) lamellae specimens were prepared from the irradiated region for transmission electron microscopy (TEM) and energy dispersive x-ray spectroscopy (EDS) mapping. These analyses have revealed a high density of cavities in the W and Ni-Fe-W phases, and defect segregation at the interphase boundaries (IPBs). There is also evidence of precipitation at the IPB in the irradiated region, but the exact crystallography and chemistry of this phase remains unknown. The implications of the IPB acting as a sink site for defects are concerning as segregation and precipitation could reduce the adhesion between BCC W and FCC Ni-Fe-W, leading to reduced ductility and fracture toughness post-irradiation.

PROGRESS AND STATUS

Introduction

Tungsten heavy alloys have been proposed as candidates for the replacement of monolithic tungsten as plasma facing material components (PFMCs) for fusion reactors [1,2]. While these alloys have been the subject of multiple mechanical and microstructural observations [3,4,5], there is very little data available on the behavior of these alloys post-irradiation, or on the irradiation behavior of multi-phase materials in general. In the proposed implementation of multiphase materials for the damaging environment of the fusion reactor, it is a major concern that the interface between the different phases may act as a sink site for the accumulation of damage, leading to decreased adhesion between the phases. This is especially concerning as prior study of these alloy systems indicates that the surprising strength and ductility of these systems owes to a strong bond which exists between the BCC W and FCC Ni-Fe-W phases [5]. It is then necessary to study the extent to which irradiation will affect this material.

To do this, a liquid phase sintered specimen of 90W-7Ni-3Fe (wt.%) has been subjected to sequential ion irradiations at Texas A&M to better understand the behavior of WHA microstructures post-irradiation. This specimen was subjected first to Ni then He ion irradiations at 700°C to simulate the damage incurred throughout five years of service in a fusion reactor. The conditions selected for the ion irradiations are based on calculations by Jiang, *et al* in [6]. Ni^+ irradiation was done with 1.2 MeV ions to a fluence of 2.15×10^{16} Ni^+/cm^2. This equates to a peak damage dose of 27.3 dpa at ~192nm of depth below the surface in the W phase, and 30.6 dpa at ~296nm below the surface in the Ni-Fe-W phase. Next, He implantation was done at 90keV to a fluence of 6.5×10^{15} He^+/cm^2. This equates to approximately 0.48 at.% He at a depth of ~215nm in the W phase, and 0.39 at.% He at a depth of ~295nm in the Ni-Fe-W phase. These imposed conditions produce a specimen with a relatively shallow peak damage with the region of interest for irradiation damage characterization lying at approximately 200-300nm below the surface.

Experimental Procedure

To characterize the defect structures present post-irradiation, specimens were prepared via a FIB lift out technique and affixed to a gold TEM grid to facilitate future flash electropolishing trial work for the removal of surface damage from FIB preparation. To accommodate for the difference in FIB milling rates between

the two phases, extra care was taken during the thinning steps to minimize thickness differentials in final foils. These foils have been observed in TEM and are seen to possess remarkably different defect structures between the W and Ni-Fe-W phases. An example of this is included in Figure 1 below, with a series of TEM micrographs of each individual phase 'through focus', or at sequential imaging conditions corresponding to under-focus, in-focus, and over-focus. This is done to take advantage of Fresnel fringes to aid in the visualization of radiation damage in TEM mode. The features can be noted with corresponding dark or light fringes in the over and under-focus images respectively, and their contrast value inverts due to the change in the strength of the objective lens, and thereby focus condition. The interior of the Ni-Fe-W phase grains clearly possess an abundance of faceted voids (>5nm), and the W phase interior presents a high density of bubble type defects (<2nm) in size. Qualitatively, the size, distribution, and density of cavities in each phase appears identical to that of the results presented in a Ni and He irradiated thermomechanically processed (R87) WHA alloy of the same composition reported by Jiang *et al*. in [7]; yet quantitative comparison analyses of damage distribution in this sample is yet to be conducted.

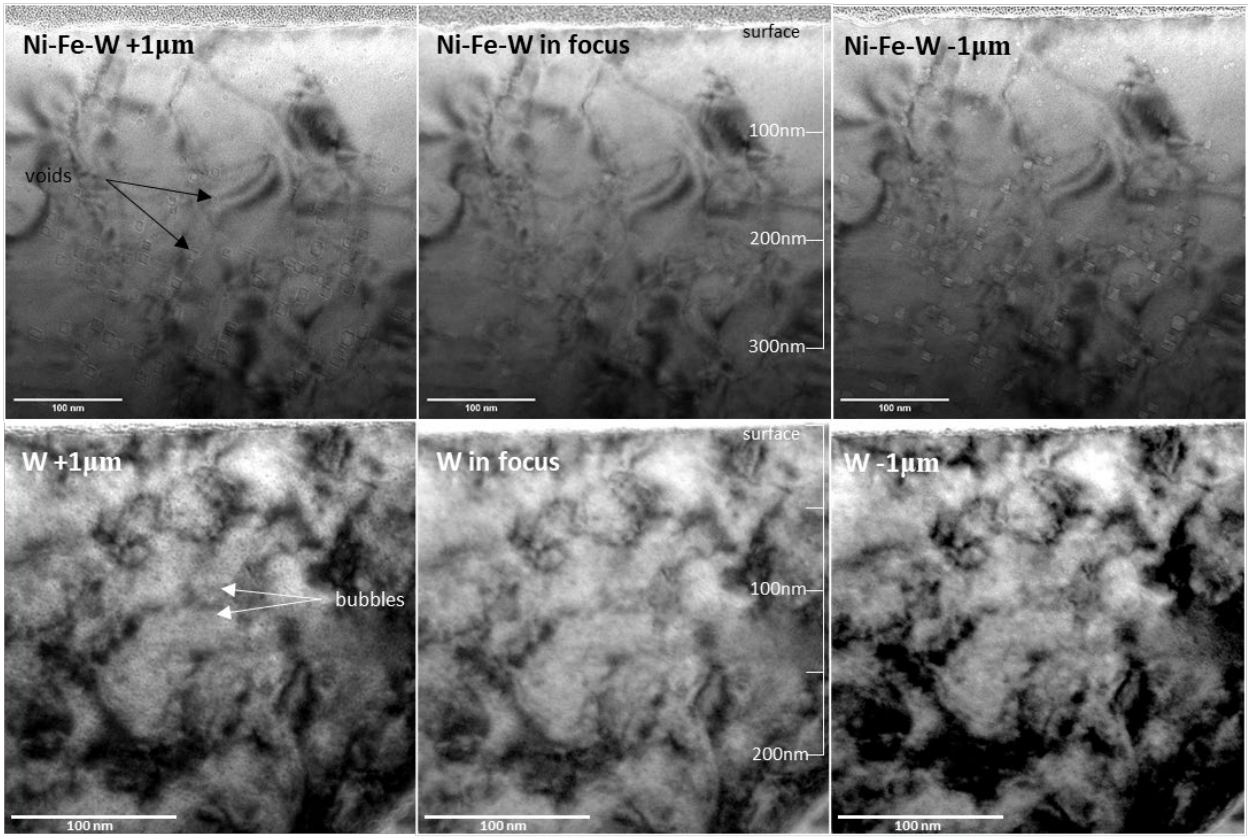

Figure 1. Through focus bright field TEM imaging of defects in Ni and He ion irradiated WHA. Top row shows under, in, and over-focus conditions to visualize voids in the Ni-Fe-W phase. Bottom row shows over, in, and under-focus conditions to visualize bubbles in W phase.

Of paramount interest in this analysis is the behavior of the interphase boundary between the W and Ni-Fe-W phases post-irradiation. The IPB is essential in the expression of the ductile phase toughening effect in these alloy systems, and potential radiation damage accumulation at these sites could be detrimental for the mechanical behavior of these alloys. In the observation of multiple IPBs, there does appear to be a high density of cavities at the boundary plane. Figure 2 highlights this IPB region in the Ni and He irradiated specimens. Tilting of this boundary with respect to the incident electron beam reveals that the cavities appear to only lie on the Ni-Fe-W side of the IPB, with every cavity on the IPB exhibiting a wetted droplet morphology onto the W side of the grain boundary. This morphology is shown more clearly in the schematic

Figure 3 with the shape of the white cavities at the IPB. It is postulated that the one-sided appearance of these cavities may owe to the lower formation energy of vacancy clusters in the Ni-Fe-W over W.

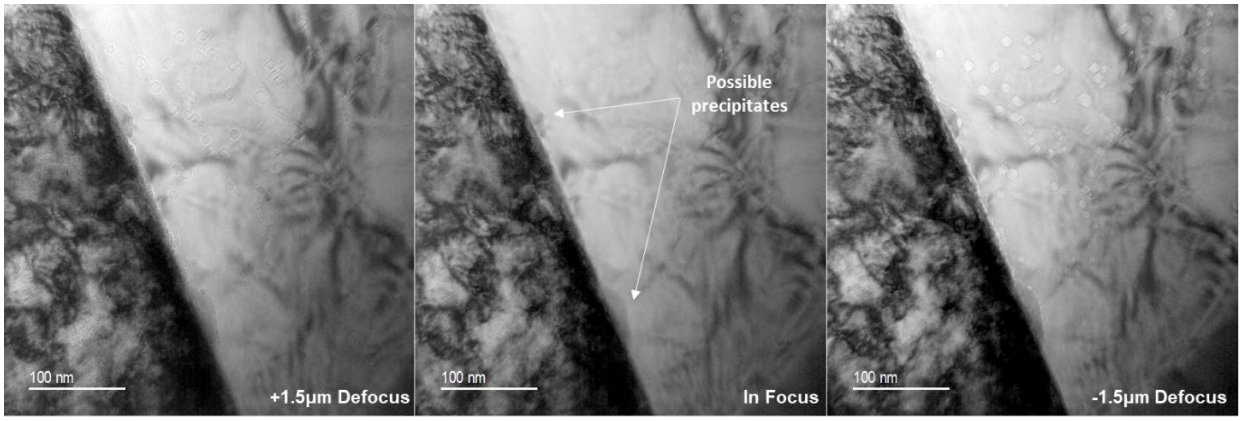

Figure 2. Through focus bright field TEM imaging of IPB region from Ni and He ion irradiated WHA. From left to right shows the under, in, and over-focus conditions to visualize the cavities.

In further observation of these IPB sites in the irradiated region, there is evidence of precipitation at the IPB plane. This precipitation, shown with arrows at the IPB in Figure 2 as well as in Figure 4. It should also be noted here that of the four IPB planes which have been analyzed from this specimen, each has presented noticeable precipitation at the IPB. Figure 4 highlights the depth at which these precipitates are found as well as providing a sense of the structure of these precipitates. The fact that these precipitates seem to stop after approximately 400nm below the surface and not continue beyond that point suggests that their formation mechanism at least partially owes to the irradiation conditions rather than solely due to thermal effects. To the knowledge of the authors, this represents the first-time irradiation induced precipitation has been noted in tungsten heavy alloy systems. To probe more deeply into these boundary precipitates the specimen was tilted in the TEM stage to find a strong diffraction condition by which to image these phases. The bright field scanning transmission electron microscope (STEM) image in the right frame of Figure 4 shows that these precipitates are crystalline, with the presence of lattice fringes across the domain. At this imaging condition, the domain is oriented to an unknown zone axis with visible lattice spacings corresponding to approximately 2.12 Angstroms. This spacing does not correspond to any low index lattice plane calculated from the W or Ni-Fe-W crystal structures but does lie reasonably close to both the W (110) and Ni-Fe-W (111) spacings at 2.25 and 2.08 Angstroms respectively. It can also be observed that multiple cavities with the same morphology of those found at the boundary between W and Ni-Fe-W exist between the precipitates and the Ni-Fe-W. These cavities are shown in the right frame of Figure 4, and clearly sit on the precipitates and protrude out into the Ni-Fe-W phase.

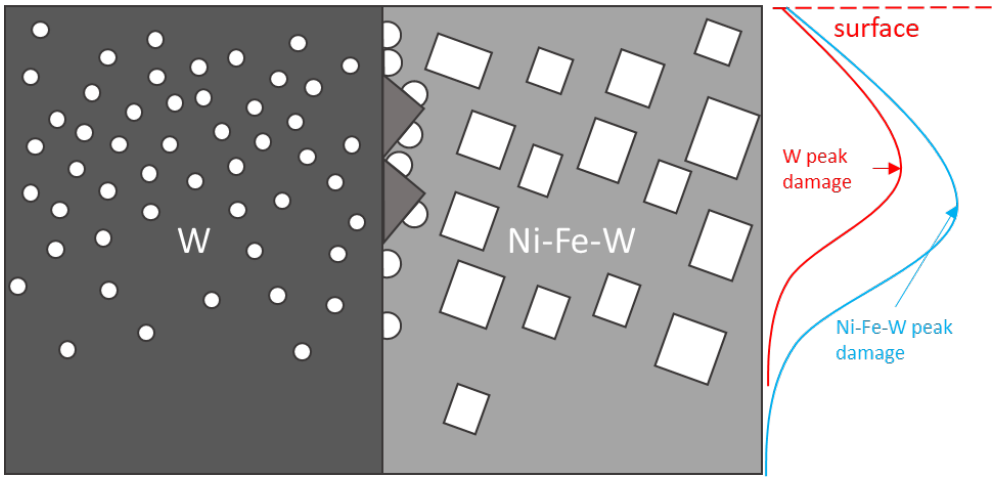

Figure 3. Schematic of the extent of irradiation damage in a WHA. The interface exhibits a high density of cavities lying on the Ni-Fe-W side of the boundary with fin-shaped precipitates at the boundary. W exhibits a high density of bubbles, and the Ni-Fe-W exhibits large, faceted voids. The spectra on the left represents the damage curve for both phases proceeding into the depth of the specimen.

To further aid in the identification and characterization of these boundary precipitates, STEM energy dispersive x-ray spectroscopy (EDS) mapping has been conducted on the IPB. While tilting analyses of these precipitates have revealed that in most cases they are small (<50nm) and these domains at the boundary do not go entirely through the thickness of the TEM foil, EDS is still a valuable tool in the identification of the approximate chemistry, as well as to reveal any enrichment of a particular elemental species or an abundance of a particular contaminant. An EDS map of this region is included in Figure 5. While there is no evidence of significant impurity element segregation at the IPB, the precipitates do appear to be enriched in W and depleted in both Ni and Fe as compared to the surrounding Ni-Fe-W phase. This result agrees with the characteristic mass-thickness contrast present in the acquired high angle annular dark field (HAADF) STEM micrographs from these regions and allows for further restriction and refinement in the identification of these boundary precipitates to phases which contain only W, Ni, and Fe. Further chemical and crystallographic identification analyses are currently in process to characterize these precipitates and will be a large focus in the upcoming reporting period.

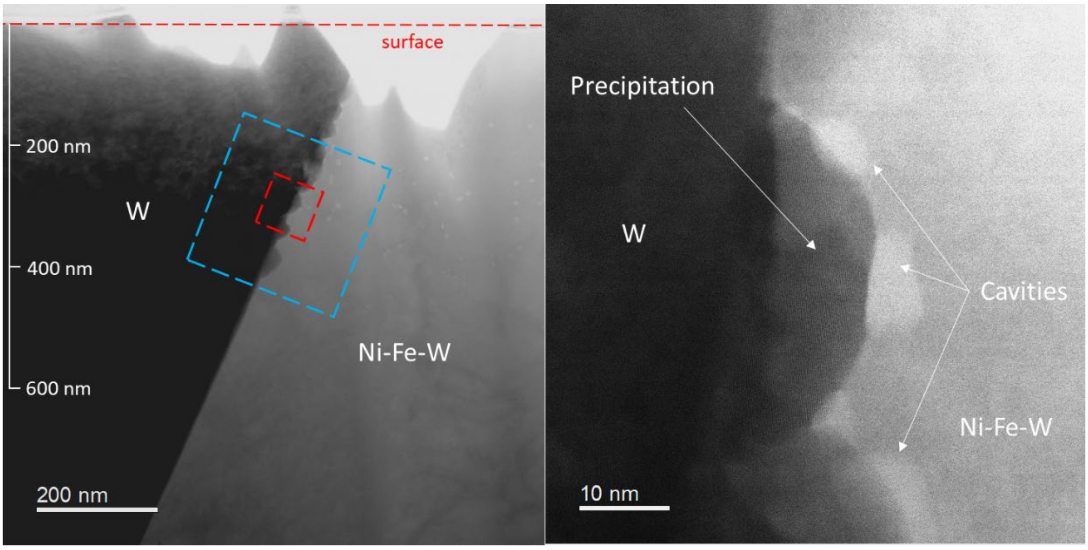

Figure 4. (left) low magnification bright filed STEM image of Ni and He irradiated TEM foil. Red dashed box is region shown in frame to the right. (right) is enlarged frame showing structure of precipitate at IPB with cavities sitting on the precipitate. The blue dashed box is the region of the boundary shown in the EDS map from Figure 5.

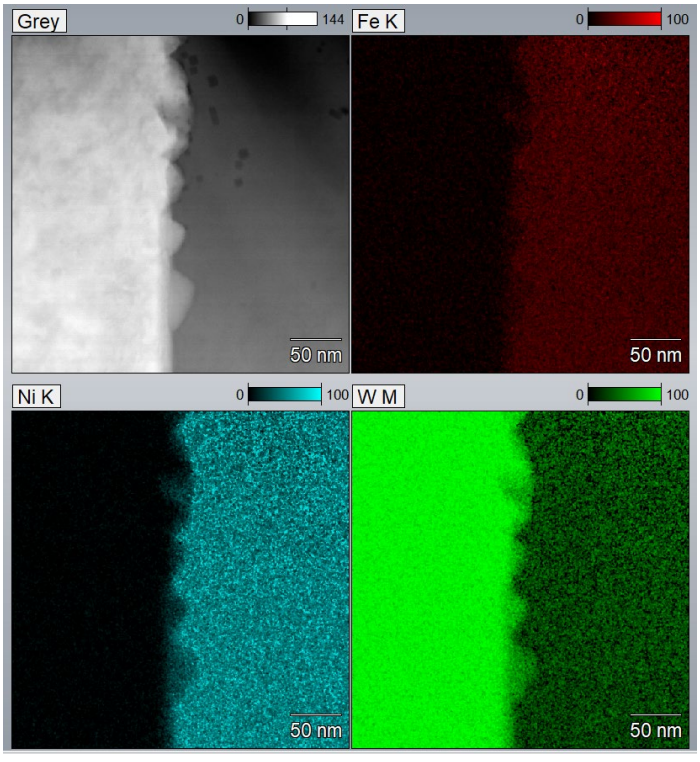

Figure 5. STEM EDS map of boundary region shown in blue box in Figure 4. Fe is shown in red, Ni is blue, and W is green. There was no evidence of significant impurity segregation. The precipitates appear to be enriched in W and depleted in Ni and Fe.

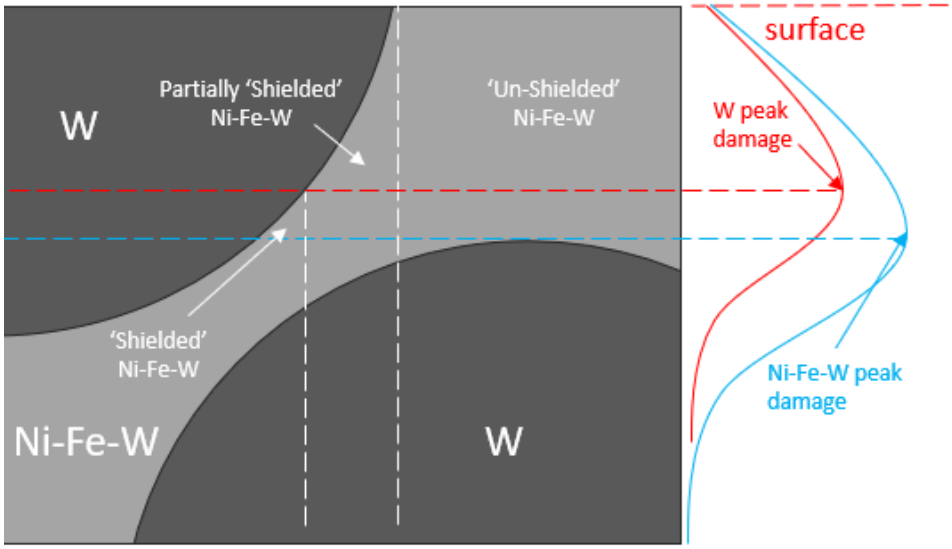

Figure 6. Schematic of the effects of morphological dispersion in the irradiation of multiphase materials.

One final item which warrants further discussion is the explicit identification of additional variables which add to the complexity of studying multi-phase material irradiation damage accumulation. In the analysis of these alloy systems, not only must both phases and the interfaces which exist between them be considered, but so must the morphology. As can be seen from Figure 6, it is anticipated that the individual W domains at or near the surface of the material may exhibit a 'shielding' effect upon the Ni-Fe-W below it. There is potential that this geometry shown in Figure 6 allows the W domain in the upper left to mitigate the damage in, or even fully protect, the underlying Ni-Fe-W. This geometry may also contribute to the IPB precipitation noted in Figure 4. It is possible that the incident irradiation could penetrate through the W domain in the partially shielded region, leading to a ballistic mixing of additional tungsten into the Ni-Fe-W matrix. It is possible this intermixing in the partially shielded region is the driving force behind the formation of tungsten rich precipitates on the Ni-Fe-W side of the IPB. The extent of these effects and their bearing upon overall material behavior are expected to be largely dependent on the imposed irradiation conditions, but this additional variable of morphological dispersion in the study of these materials must be discussed and further complicates the analysis of multi-component systems during irradiation.

References

[1] R. Neu et al., "Investigations on tungsten heavy alloys for use as plasma facing material," Fusion Engineering and Design, vol. 124, pp. 450–454, Nov. 2017, doi: 10/gct8g6.

[2] C. H. Henager et al., "DUCTILE-PHASE TOUGHENED TUNGSTEN FOR PLASMA-FACING MATERIALS IN FUSION REACTORS," International Journal of Powder Metallurgy, vol. 53, no. 2, p. 18, 2017.

[3] M. E. Alam and G. R. Odette, "On the remarkable fracture toughness of 90 to 97W-NiFe alloys revealing powerful new ductile phase toughening mechanisms," Acta Materialia, vol. 186, pp. 324–340, Mar. 2020, doi: 10/ggqgkk.

[4] M. E. Alam, J. Wang, C. H. Henager, W. Setyawan, and G. R. Odette, "The effect of hot rolling on the strength and fracture toughness of 90W–7Ni3Fe tungsten heavy metal alloys," Materials Science and Engineering: A, vol. 824, p. 141738, Sep. 2021, doi: 10/gmx9wf.

[5] J. V. Haag, D. J. Edwards, C. H. Henager, W. Setyawan, J. Wang, and M. Murayama, "Characterization of ductile phase toughening mechanisms in a hot-rolled tungsten heavy alloy," Acta Materialia, vol. 204, p. 116523, Feb. 2021, doi: 10/ghpnzr.

[6] W. Jiang, W. Setyawan, K. Kruska, L. Kovarik, D. Zhang, “Self-ion and He ion irradiation of ductile-phase toughened tungsten composites,” DOE Fusion Reactor Materials Program Semiannual Progress Report. DOE/ER-0313/68 (2020) 96-101.
[7] W. Jiang, D. Li, D. Zhang, B. Matthews, W. Setyawan, “Microstructures in 87R DPT W irradiated with Ni^+ and He^+ ions,” DOE Fusion Reactor Materials Program Semiannual Progress Report. DOE0313/70 (2021) 140-145.

4.10 CHARACTERIZATION OF HELIUM CAVITIES IN He^+ ION IRRADIATED DUCTILE-PHASE TOUGHENED TUNGSTEN—W. Jiang, L. Kovarik, K. Kruska, W. Setyawan (Pacific Northwest National Laboratory)

OBJECTIVE

The aim of work is to explore methods for quantifying helium density and pressure in He cavities and determining the size distribution of the cavities in He^+ ion irradiated ductile-phase toughened tungsten.

SUMMARY

A hot-rolled, 87% thickness reduced ductile-phase toughened tungsten (87R DPT W) composite (90W-7Ni-3Fe) was irradiated with 90 keV He^+ ions to 1.0×10^{17} He^+/cm^2 at 973 K. The material contains two phases of W at 88 wt.% and NiFeW at 12 wt.%. The ductile NiFeW phase consists of 54.68 wt.% Ni, 22.57 wt.% Fe, and 22.75 wt.% W. Helium cavities distributed over a thickness of ~8 nm were imaged using convergent-beam scanning transmission electron microscopy (CB-STEM). In contrast to the conventional TEM under a defocus condition, the CB-STEM allows for the determination of cavity size without the need for correction; very small cavities can be imaged, and the cavity numbers can be counted more accurately. In addition, STEM-EELS (Electron Energy Loss Spectroscopy) has been explored to quantify He density and pressure in the He cavities. Further efforts to resolve the He K edge core-loss peak, which is very weak due to limited He concentration in this study, are underway.

PROGRESS AND STATUS

Introduction

Conventional TEM under a defocus condition has been applied to characterize the size of He bubbles or cavities in materials. In our previous study of ion irradiated 87R DPT W [1], the observed size was corrected for the defocus values based on simulation results. If the cavity number density is high, there is a large probability, due to projection, for cavities to be stacked within the foil thickness that is significantly larger than the average cavity size. This would create a high risk for underestimation of the cavity number density. This study explores a CB-STEM method that could determine He cavity size and number density more accurately.

Walsh, Yuan and Brown [2] have developed a method for measuring the He density and pressure in nanometer-sized bubbles in irradiated materials based on STEM-EELS. It measures the scattering probability of an electron because of exciting a 1s electron in He to the 2p state. He K edge is located at 21.218 eV, where there is a high-intensity plasmon peak from the matrix. To obtain a He K edge core-loss spectrum, two EELS spectra are usually taken, one from the bubble center and the other from the matrix close to the bubble. After normalization and subtraction of the former from the latter, the difference represents the He core-loss peak. The amount of He atoms N could be determined [2] by $N = I_{He}/(I_0\sigma d)$, where I_{He} is the area of the He peak, σ is the He cross section and d is the He cavity diameter. This method has been successfully applied to characterize He bubbles in a tritiated $Pd_{90}Pt_{10}$ alloy [3] and a He^+ ion implanted martensitic steel [4]. It has also been extended to study the association of H with He bubbles in zirconium [5] as well as a simultaneous analysis of He and T inside bubbles in beryllium [6]. To date, similar characterizations of He cavities in W or NiFeW have not been reported. In this study, the Walsh-Yuan-Brown method is explored to determine the He density and pressure in He cavities.

Experimental Procedure

SRIM Simulation

To estimate dose rates and He atomic distributions in W and NiFeW phases, quick Kinchin-Pease (K-P) SRIM13 (Stopping and Range of Ions in Matter, version 2013 [7]) simulations were carried out for 90 keV

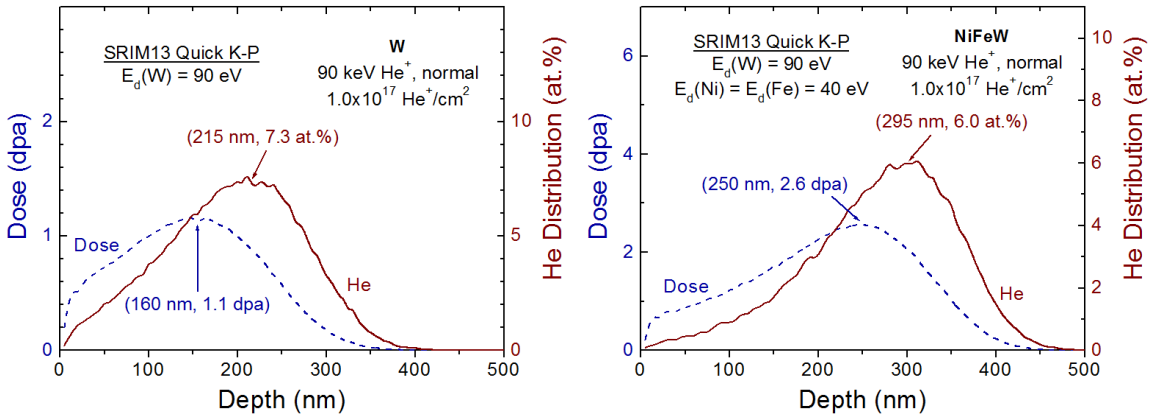

Figure 1. Depth profiles of the dose and He atomic percentage from a quick Kinchin-Pease SRIM13 simulation of 90 keV He^+ irradiation in W and NiFeW to 1.0×10^{17} He^+/cm^2.

He^+ ions in W and NiFeW, where the threshold displacement energies of E_d(W)=90 eV and E_d(Ni)=E_d(Fe)=40 eV were adopted [8]. The lattice binding energy was set to 0 eV [9]. The theoretical densities were assumed to be 19.25 g/cm^3 (or 6.3×10^{22} at./cm^3) and 9.50 g/cm^3 (or 8.3×10^{22} at./cm^3) for body-centered cubic W and face-centered cubic NiFeW, respectively. Simulation results for 1.0×10^{17} He^+/cm^2 in W and NiFeW are shown in Figure 1. The peak dose corresponds to 1.1 dpa at 160 nm in W and 2.6 dpa at 250 nm in NiFeW. The maximum He concentrations are 7.3 at.% at 215 nm and 6.0 at.% at 295 nm in W and NiFeW, respectively. Note that SRIM simulations are performed at the temperature of 0 K. The real He depth profiles are expected to be broader in W and NiFeW due to diffusion during He^+ ion irradiation, especially at an elevated temperature. In addition to the interaction of He atoms and vacancies and the aggregation of He atoms to form He cavities, some of the He atoms are also likely to diffuse to the surface and escape from the sample.

He^+ Ion Irradiation and Sample Characterizations

A full-density 87R DPT W composite with a nominal composition of 90W-7Ni-3Fe was fabricated at the Pacific Northwest National Laboratory (PNNL) [10] with metal powders obtained from Mi-Tech [11,12]. A ductile phase NiFeW Included in a brittle phase W in the composite can prevent or inhibit crack

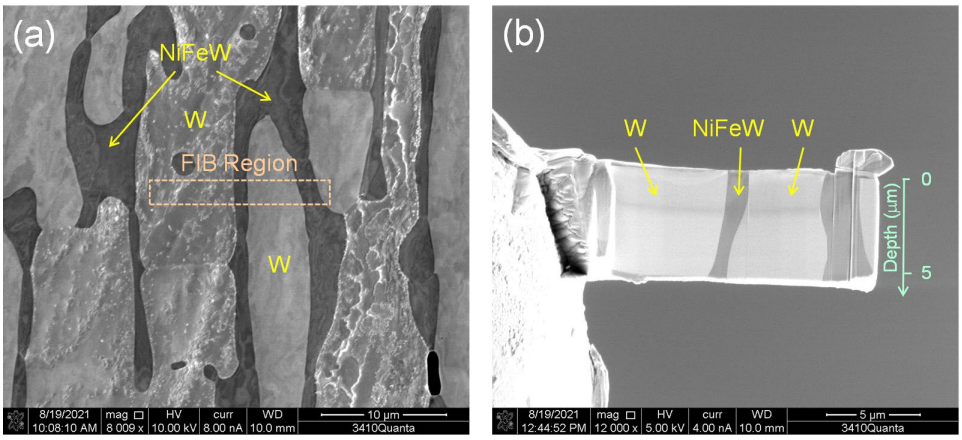

Figure 2. (a) SEM image of 87R DPT W sample surface with a FIB region indicated, irradiated with 90 keV He^+ ions to 1.0×10^{17} He^+/cm^2 at 973 K, and (b) SEM image of a cross-sectional FIB lift-out with multiple W and NiFeW interphase boundaries.

propagation by crack blunting, crack bridging, crack deflection, and crack branching [10]. The material was rolled to an 87% thickness reduction at high temperatures, cut into small samples, and polished on one side. Ion irradiation of the sample was performed at Texas A&M University (TAMU) with 90 keV He^+ ions at normal incidence to 1.0×10^{17} He^+/cm^2 at 973 K using a rastering system to achieve a uniform irradiation over a large area. A resistance heater was located behind the copper plate on which the sample was mounted. The average ion flux was 3.6×10^{12} $(He^{2+}/cm^2)/s$.

A cross-sectional TEM sample of the irradiated 87R DPT W was prepared using a FEI Quanta dual-beam focused ion beam (FIB) microscope. A lamella was sliced with multiple interphase boundaries from the indicated area, as shown in Figure 2(a). Figure 2(b) shows the microstructure of the FIB sample with a distinct contrast of W (white) and NiFeW (dark) phases. Due to a significantly higher sputtering rate from NiFeW than W, additional thinning for W was also performed. A few keV Ga^+ ion beam was used for the final polishing of the FIB sample. The FIB sample was examined using a Themis STEM from Thermo Fisher Scientific with a spatial resolution of 0.05 nm. Both STEM and STEM-EELS were performed at an accelerating voltage of 300 kV.

Results

High-angle annular dark-field (HAADF) CB-STEM was performed for the irradiated 87R DPT W. Figure 3(a) shows a low-magnification image near a phase boundary. Figures 3(b) and 3(c) show HAADF high-resolution CB-STEM images of W and NiFeW, respectively. Under the focusing conditions, cavities are imaged in real size within a thickness of ~8 nm. Cavities in both components are clearly visible and the contrast is a result of the thickness difference, but not the Fresnel diffraction from a defocused beam. Helium cavities show a darker contrast due to imaging a smaller thickness. The CB-STEM imaging of

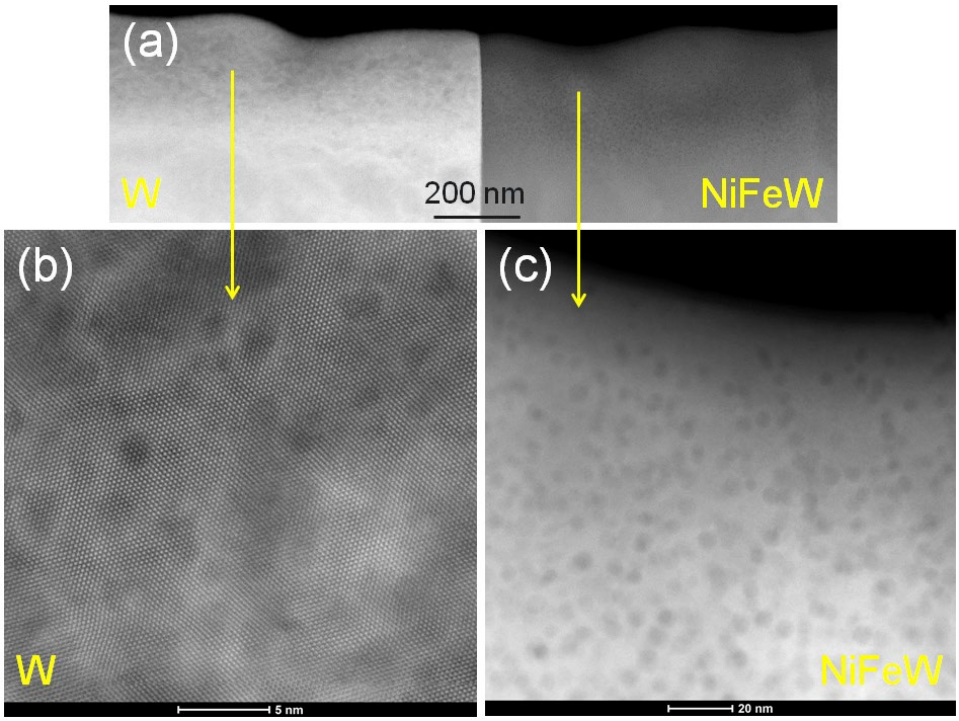

Figure 3. (a) A low-magnification HAADF STEM image of 87R DPT W near a W and NiFeW interphase region irradiated with 90 keV He^+ ions to 1×10^{17} He^+/cm^2 at 973 K. (b) and (c) are the higher-magnification HAADF CB-STEM images of irradiated W and NiFeW, respectively. The imaging focus span is ~8 nm.

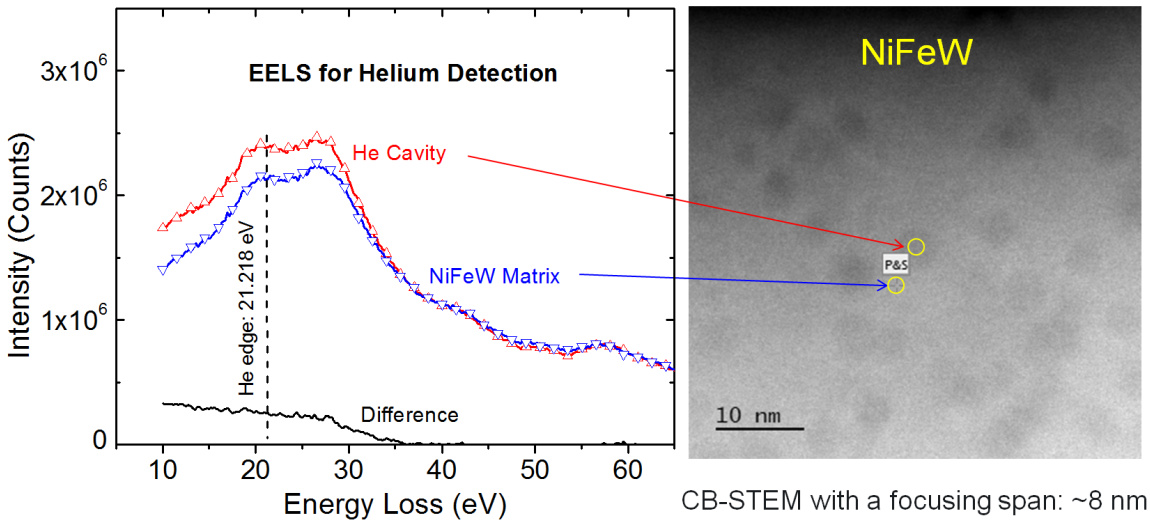

Figure 4. STEM-EELS spectra from two close-by areas with and without a He cavity in NiFeW within 87R DPT W irradiated with 90 keV He^+ ions to 1×10^{17} He^+/cm^2 at 973 K. The difference represents the He K edge core-loss spectrum from the subtraction of the two spectra.

small cavities represents a new method that has not been reported as a tool to determine cavity distributions to date. Compared to imaging cavities in a thicker foil, e.g., 100 nm, using a conventional TEM under a defocus condition, CB-STEM technique can show much smaller cavities without image overlapping. This can help count the cavity numbers more accurately and determine the number density with smaller errors. From Figure 3, the average cavity diameters in W and NiFeW are estimated to be 20-30 % smaller than from our previous study [13], where a conventional TEM was used, and cavity size correction was made. The cavity number densities estimated from Figure 3 are about one and two orders of magnitude higher than those from the conventional TEM [13] in W and NiFeW, respectively. Part of the reason might be that a large amount of small He cavities that could be resolved by CB-STEM were invisible to conventional TEM under the defocus conditions.

The STEM-EELS has also been performed from the center of a cavity (He-rich) and the NiFeW matrix (He-free) close to the cavity and the data are shown in Figure 4. This procedure is consistent with what has been reported in the literature [3-6]. Intensity normalization was performed in the energy-loss region from 35 to 45 eV. Subtraction of the cavity spectrum from the matrix spectrum yields a difference spectrum, which is also shown in the figure. The difference spectrum represents the He K edge core-loss spectrum that is peaked at 21.218 eV. In this study, however, the He spectrum overlaps with a broad, strong plasmon peak centered at ~25 eV. The He peak is not resolved under the experimental conditions, likely because the He density in the cavity is not high enough because of He diffusion and release during He^+ ion irradiation at 973 K. The STEM-EELS data suggest a challenge to quantify the He density in small He cavities in NiFeW. It is expected that He quantification in W is more difficult because the cavity size is even smaller.

Future Work

More efforts are underway to further thin the FIB sample, which should help reduce the plasmon peak intensity. In addition, we will study temperature effects on the plasmon peak shift. The data might help to reduce the background yield at the He K edge position (21.218 eV) by shifting the plasmon peak position. If successful, we will proceed with the characterization of He cavities in W. Our goal would be to generate data that can be used to validate the prediction from a model calculation that shows different He retention behavior in NiFeW and W. In addition, a series of CB-STEM for the FIB sample will be performed at different depths over the depth region of interest. Analysis of the data will lead to distributions of the cavity size and cavity number density as a function of depth or dose.

Acknowledgements

This research was supported by the Office of Fusion Energy Sciences, U.S. Department of Energy and performed at PNNL under Contract DE-AC05-76RL01830. We are grateful to Charles Henager at PNNL for providing the 87R DPT W samples and to Xuemei Wang and Zhihan Hu at TAMU for ion irradiation.

References

[1] W. Jiang, *et al*. J. Nucl. Mater. 550 (2021) 152905.
[2] C.A. Walsh, *et al*. Philos. Mag. A 80 (2000) 1507.
[3] D. Taverna, *et al*. Phys. Rev. Lett. 100 (2008) 035301.
[4] S. Fréchard, *et al*. J. Nucl. Mater. 393 (2009) 102.
[5] M.S. Blackmur, *et al*. Scripta Mater. 152 (2018) 102.
[6] M. Klimenkov, *et al*. Micron 127 (2019) 102754.
[7] J.F. Ziegler, J.P. Biearsack, U. Littmark, *The stopping and Range of Ions in Solids* (Pergamon Press, New York, 1985); available at: http://www.SRIM.org/.
[8] ASTM, ASTM Standard E521-96 (2009), *Standard Practice for Neutron Radiation Damage Simulation by Charged-Particle Irradiation,* ASTM International, West Conshohocken, PA (2009).
[9] R.E. Stoller, *et al*. Nucl. Instrum. Meth. Phys. Res. B 310 (2013) 75.

[10] C.H. Henager, Jr. *et al*. Ductile-phase toughened tungsten for plasma-facing materials in fusion reactors, Int. J. Powder Metall. 53 (2017) 53.
[11] https://www.mttm.com/tungsten-alloys.
[12] A. Pathak, *et al*. Int. J. Refract. Met. Hard Mater. 75 (2018) 43.
[13] W. Jiang, *et al*. J. Nucl. Mater. 561 (2022) 153565.

4.11 NEUTRON IRRADIATION-ENHANCED GRAIN GROWTH IN TUNGSTEN AND TUNGSTEN ALLOYS—H. Gietl, T. Koyanagi, Y. Katoh (Oak Ridge National Laboratory), X. Hu (Sichuan University), M. Fukuda (National Institutes for Quantum Science and Technology), A. Hasegawa (Tohoku University)

Abstract of a manuscript in Journal of Alloys and Compounds (In Press, doi.org/10.1016/j.jallcom.2021.163419)

To understand the microstructural stability of candidate plasma-facing materials under fusion-relevant environments, neutron irradiation of W and W-3%Re alloys with and without K and La dopants was performed in the mixed-spectrum High Flux Isotope Reactor at nominal temperatures of ~850 °C and ~1,100 °C to calculated doses between 0.42 and 0.47 dpa. To the best of our knowledge, this study presents the first experimental evidence of radiation-enhanced recrystallization in W and undoped W–Re alloys at ~850 °C, conditions where thermal annealing does not cause any grain growth in a similar timescale. Potassium- or lanthanum-doped tungsten alloys showed more resistance to radiation-enhanced grain growth. We explain the acceleration of grain growth by analyzing the self-diffusion constant under atomic displacement environments. The microstructural observations of the studied W variants suggest that La doping is more effective than K doping for mitigating recrystallization. This study also found that radiation-enhanced recrystallization is an important consideration when designing and applying W to plasma-facing components in future nuclear fusion reactors.

5. ADVANCED MANUFACTURING

5.1 FABRICATION OF CERAMIC AND METAL MATRIX ENHANCED SHIELD THROUGH DIRECT CURRENT SINTERING—J.M. Gentile, B. Cheng, D.J. Sprouster, J. R. Trelewicz, L.L. Snead (Stony Brook University)

OBJECTIVE

In this report, we discuss progress made toward developing ceramic and metal matrix entrained hydride shields for enabling compact superconducting Tokamaks. Using direct current sintering (DCS), we show that a combination of sintering aids suppresses the consolidation temperature of ceramic and metal matrices, which can be brought down to suitable levels for entraining metal hydrides that are historically beneficial for neutron absorption and moderation applications.

PROGRESS AND STATUS

Tokamaks require shielding to minimize neutron damage and heat deposition to the delicate superconducting magnets necessary for sustaining fusion [1-5]. Current generation shields employ a combination of light or heavy elements and neutron absorbers such as W, H_2O, and ^{10}B. However, H_2O is effectively ruled out for compact reactors, and B-based compounds suffer from inherent irradiation instability and burnout. Due to the limitations of conventional shields, enhanced shields are necessary to drive the efficiency, reliability, and cost-effectiveness of next generation fusion reactors. Our proposed solution involves the use of radiation stable ceramic and metal matrices to entrain otherwise irradiation unstable metal hydrides, which ironically exhibit high performance for neutron moderating and absorption applications. In essence, these composite materials will combine the benefits of low activation, radiation stable matrices with the superior neutron stopping performance of the entrained hydride phase in turn mitigating the risk associated with their radiation instability.

In the previous semi-annual report, we presented a systematic sintering study of MgO ceramic and Ni matrix composites. For the MgO we effectively reduced the sintering temperature by 600°C. Here, we build upon these procedures, and present our results for co-sintering MgO with 25%HfH_2, and Fe with 25%HfH_2, at different peak sintering temperatures. The SEM and XCT are used to characterize the morphology, and XRD is used to examine phases in the sintered specimens with the phase fraction quantified using Rietveld analysis. Finally, the total hafnium hydride fraction in the sintered articles is presented to demonstrate the successful retention of hydride using our advanced processing route.

Experimental Procedure

Ceramic composites

The MgO matrix powder for the co-sintering of MgO with HfH_2 was adapted from the recipe in our last report, while the HfH_2 powder was purchased from Stanford Advance Materials (99% purity). The matrix MgO powder was mixed with 25 volume percent HfH_2 powder using a speedmixer. The powder mix was then cold-pressed under 100MPa for 10min and then transferred into a 25mm graphite sintered die. Graphite foil was used to prevent the reaction between the sample and graphite die. The sintering was carried out using direct current sintering equipment under vacuum (<10Pa) and 20MPa compressive pressure. The sintering die was heated to 800°C, 900°C, 1000°C and 1100°C peak sintering temperature using a heating rate of 100°C/min and held for 10min. The sintered articles were clean using sandblasting and polished following standard metallographic procedure for SEM and XRD analysis. The density was determined by measuring the weight and dimension of the samples. A small slab was cut from sample for the XCT characterization.

Metal Matrix Composites

During this semiannual reporting period for the metal matrix – metal hydride composites, we focus on the synthesis of composites employing low activation matrix materials such as RAFM. Fe powders (Alfa Aesar) were loaded into a 25mm graphite die, and into a DCS system (Sinterland LABOX-3010KF, Japan) placed under vacuum. For all experiments, only the maximum sintering temperature was varied from 700-1000°C and the heating rate, pressure, and hold time were fixed at 100°C/min, 50MPa, and 10min, respectively. A second set of experiments was conducted up to 1200°C with the addition of 25V% HfH_2 into the Fe powder. To provide a connection to our last report on Ni-based MMCs, a single sample employing a Ni matrix with 25V% HfH_2 was synthesized at 800°C. Following synthesis, x-ray diffraction (XRD) was performed on all samples using a Bruker D8-Advance to determine the phase structure of the compacts while microstructure was assessed for macroscopic defects through optical and x-ray microscopy.

Results

Ceramic Composite

Figure 1 (a) shows the displacement of graphite punch as a function of heating temperature for the MgO+25%HfH_2 sample sintered under different peak temperatures. The positive displacement indicates the powder shrinkage or densification, whereas the negative displacement is associated with the thermal expansion of graphite punch and powder. Compared to pure MgO, the onset of sintering temperature of MgO+25%HfH_2 delayed 300°C to 700°C, which might be related to the increase of sintering activation energy due to the addition of HfH_2. For all the samples, the displacement kept increasing after reaching the peak sintering temperature. The final displacement scales with the peak sintering temperature until 1000°C and then plateaued. Figure 1(b) shows the relative density as a function of peak sintering temperature. The relative density was calculated using measured density divided by ideal density determined by rule-of-mixture. The relative density increased with increasing peaking sintering temperature agreeing with the final displacement shown in Figure 1(a). At 1100°C, we achieved a highly dense sintered article with a relative density above 97%.

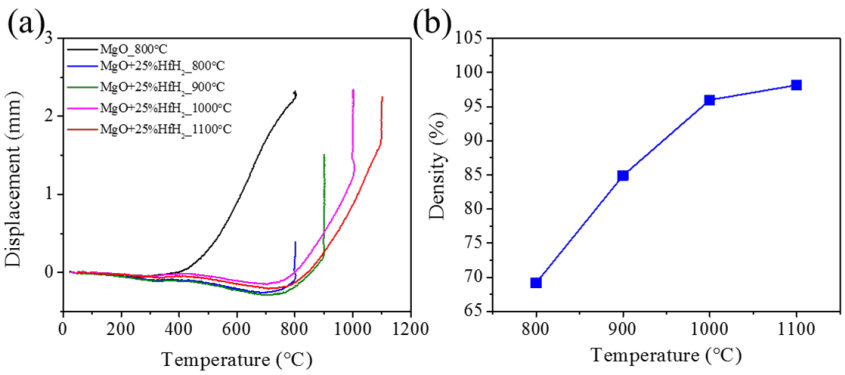

Figure 1. (a) The displacement-temperature curves of MgO and MgO+25%HfH_2 samples sintered at different peak sintering temperatures (b) The relative density as a function of peak sintering temperature.

Figure 2 (a) displays an SEM micrograph of MgO+25%HfH_2 sintered at 1100°C, where the bright particles are HfH_2, and the grey region is the MgO matrix. Despite few HfH_2 agglomerates, the microstructure of MgO+25%HfH_2 is homogenous and free of cracks. A high magnification SEM micrograph of this sample is shown in Figure 2(b), where we observed HfH_2 particles surrounded by the MgO matrix suggesting an excellent infiltration of the MgO. The grain size of the MgO matrix is fine and around ~1μm. There are some tiny voids in the MgO matrix, which might result from polishing due to the brittleness of MgO. In addition,

there are some nanoparticles (~70nm) on the MgO matrix, and we still do not know what it is. Further investigation is needed. Representative XCT cross sections of the sample are shown in Figure 2 (c) and (d). XCT shows that the sample is homogenous and free of cracks. This suggests that we achieved a complete encapsulation of HfH_2 using a high-density MgO matrix.

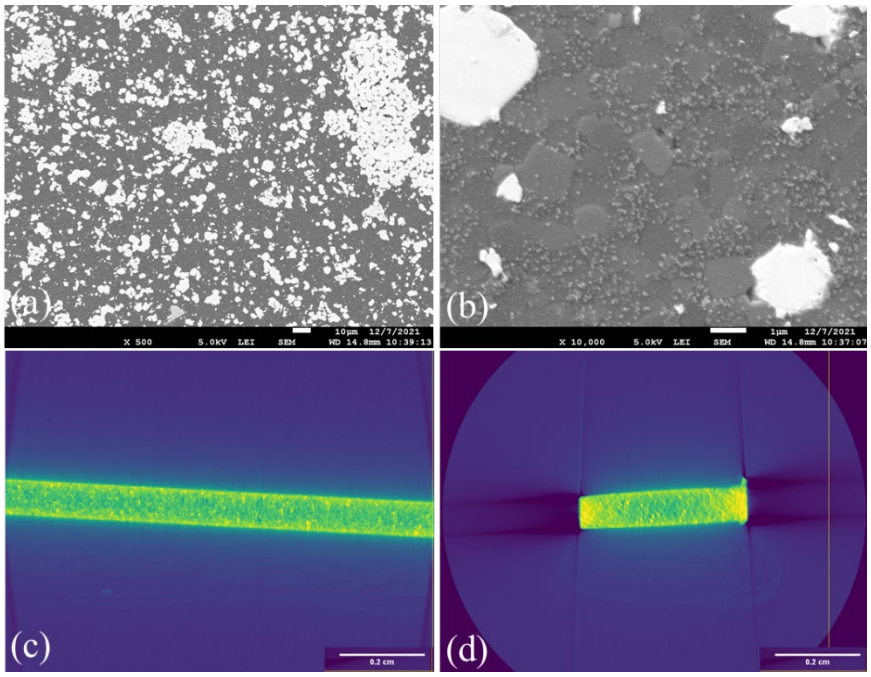

Figure 2. (a) low and (b) high-magnification secondary electron SEM micrographs and (c) the cross-sectional and (d) top-down plane XCT scan images of the MgO+25%HfH_2 sample sintered at 1100°C for 10 min.

Figure 3(a) show the XRD patterns of MgO+25%HfH2 samples sintered at 800°C, 900°C, 1000°C and 1100°C. There are five phases presented in the XRD patterns. Reflections from MgO, $HfH_{1.9}$, $HfH_{1.6}$, and HfO_2 are visible in all specimens, while metallic Hf is only seen in the samples sintered above 900°C. The HfH_2 phase evolves into two hydride populations: $HfH_{1.9}$ and $HfH_{1.6}$. The HfO_2 phase is present the in HfH_2 feedstock, and the peak intensity increases after sintering. The Hf metal phase resulted from the decomposition of the HfH_2 phase. Rietveld quantification of the Hf-rich phases are shown in Figure 3(b). $HfH_{1.9}$ phase decreases, while the metallic Hf phase increases with increasing sintering temperature (from 800°C to 1000°C). After 1100°C, these two phases stabilized. The phases evolution potentially results from the desorption of hydrogen of hafnium hydride, which then forms hafnium metal. The $HfH_{1.6}$ and HfO_2 phases are relatively stable across the four sintering temperatures. In general, the unwanted phases, which are Hf and HfO_2, are minor phases whose amount is less than 8 wt.%.

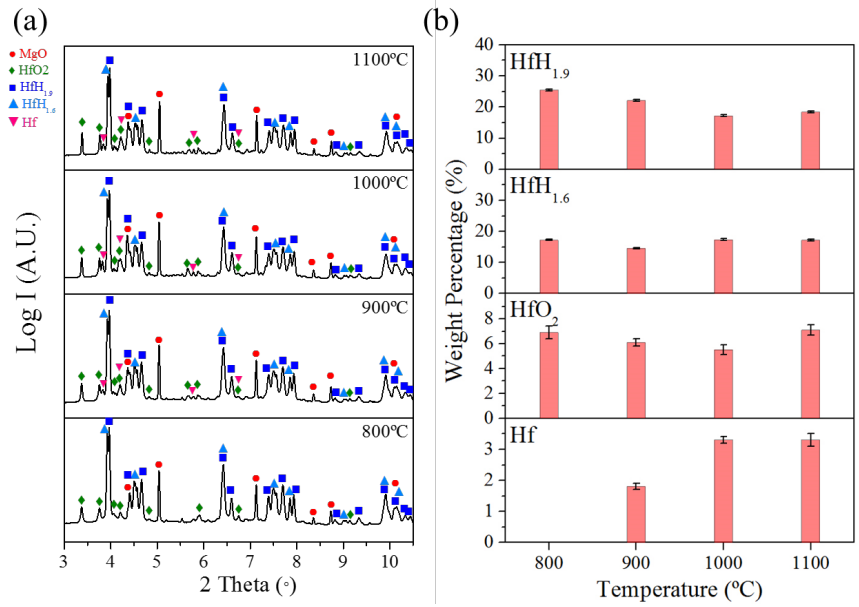

Figure 3. (a) The XRD patterns and (b) the phase quantification of MgO+25%HfH_2 samples sintered at different peak sintering temperatures).

The hafnium hydride retention in the sintered articles is a crucial factor determining the performance of MgO-HfH_2 composite shielding. After sintering, the original HfH_2 phase decomposed to $HfH_{1.9}$ and $HfH_{1.6}$, which is termed HfH_{1-x}. The total weight percent of $HfH_{1.9}$ and $HfH_{1.6}$ is the hafnium hydride retention in the sintered article, and they are shown in Figure 4 upper panel. The pre-sintered specimens have 48.5wt% HfH_2 phase (25vol%). ~75% hydride retention is quantified from XRD analysis after sintering above 1000°C.

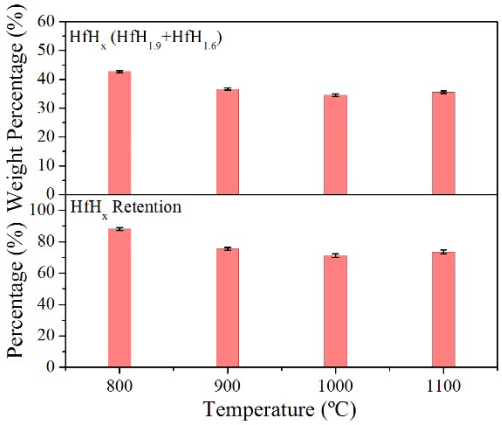

Figure 4. The HfH_2 phase retentions in the MgO+25%HfH_2 samples sintered at different peak sintering temperatures.

Metal Matrix

To acquire an optimized set of process parameters for DCS consolidation of the Fe matrix, the sintering temperature was mapped to relative density, calculated as the measured Archimedes density of the Fe compact normalized by the measured gas pycnometry density of the Fe powder. The relative density of the Fe specimens is given in Figure 5. A fully dense compact is signaled by the plateau achieved at 800°C. In

seeking to entrain metal hydrides within the Fe matrix, we target the temperature range of 800-1200°C to achieve a fully dense matrix and subsequently study the effects of process temperature on the metal-hydride phase through XRD.

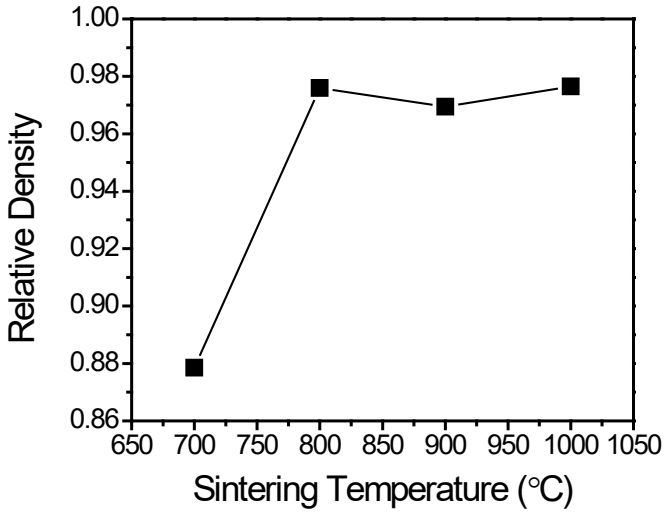

Figure 5. Relative density plotted against sintering temperature for the pure Fe powder with particle size distribution of -45µm. A fully dense matrix is achieved at 800°C.

The XRD results for DCS consolidation of individual Ni and Fe metal matrices with the addition of 25V% HfH_2 at 800°C are shown in Figure 6 in the left and right panels, respectively. The XRD results provide evidence that the Ni matrix reacted with the HfH_2 during sintering, in turn forming a NiHf intermetallic which leads to significant loss of the initial hydrogen loading. In contrast, the Fe matrix does not promote the formation of intermetallic phases, and largely retained the high initial hydrogen loading. These findings suggest that low activation steels may be used in the production of MMC enhanced shields for the processing windows required to mitigate hydrogen loss of the metal hydride inclusions.

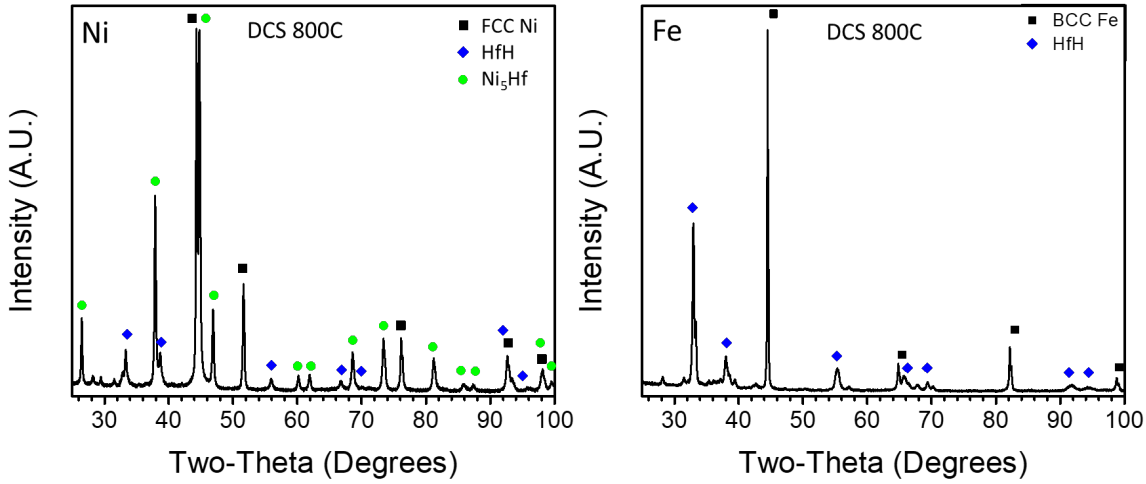

Figure 6. XRD patterns for the Ni matrix with 25V% HfH_2 (left) and Fe matrix with 25V% HfH_2 (right) both sintered at 800°C. The MMC employing a Ni matrix shows the formation of a NiHf. The Fe matrix does not have intermetallic phases.

To study the effects of sintering temperature on the phase evolution and hydrogen loading of the Fe-25V% HfH_2 MMC, we employ XRD with results illustrated in Figure 7 and major phases indexed. From 800-1000°C, we observe a gradual phase transformation from $HfH_{1.9}$ to $HfH_{1.6}$, with gradual increase in intensity of the reflections from $HfH_{1.6}$ and reduction in the $HfH_{1.9}$ peaks. At 1200°C, we observe the loss of Fe due to partial melting in the graphite die and the more prominent presence of HfO_2 relative to samples processed at lower temperatures. Given that the MMC sample processed at 1000°C qualitatively illustrates a high degree of hydride phase fraction without Fe loss, its microstructure was analyzed through optical and XCT. Figure 8 shows a representative cross section through the XCT volume, with bright regions associated with the hydrides. No visible macroscopic defects are observed from the XCT indicating that the processing leads to highly dense matrix with little porosity and a fully entrained metal-hydride phase.

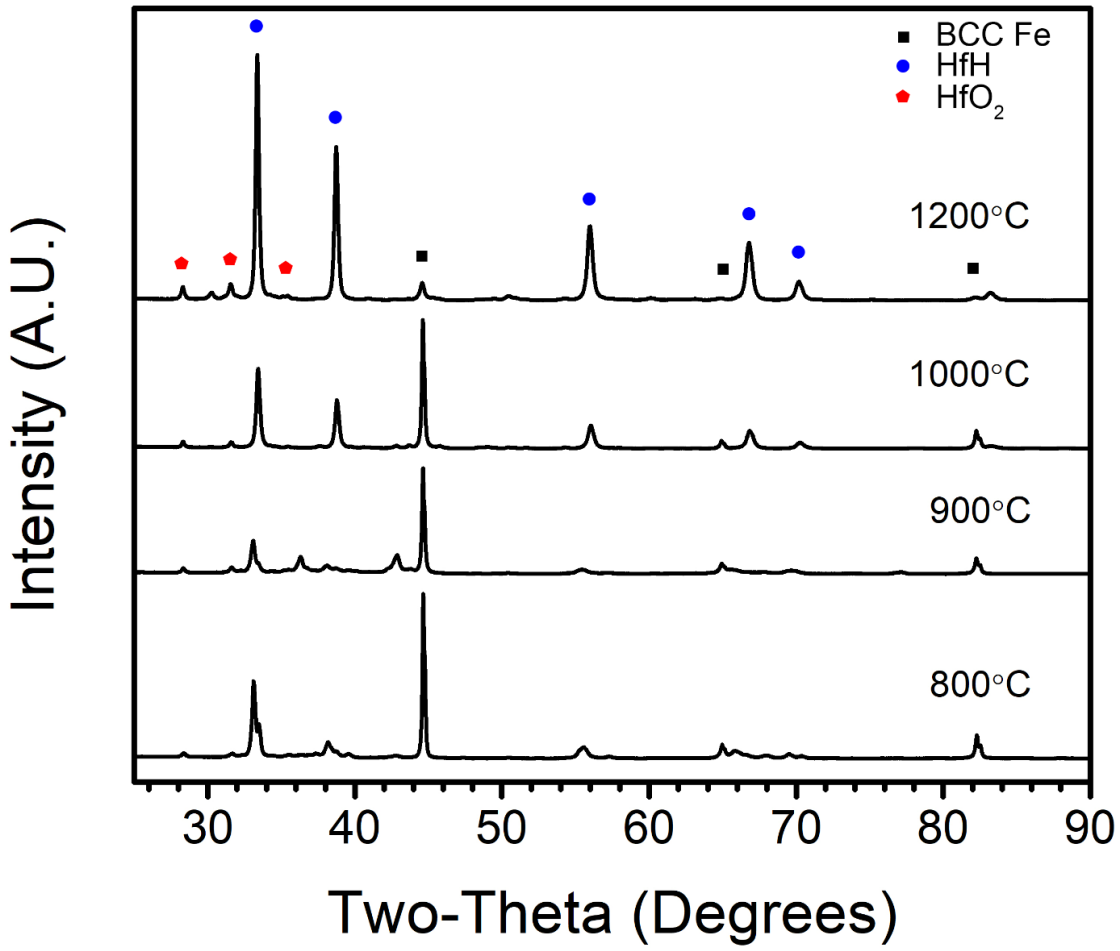

Figure 7. Indexed XRD patterns of the Fe-25V% HfH_2 MMCs processed through DCS from 800-1200°C, illustrating a gradual phase transformation from $HfH_{1.9}$ to $HfH_{1.6}$, which manifests in the diffraction data as convergence from split peaks to more discrete and uniform peaks. Fe loss is noted for the MMC processed at 1200°C.

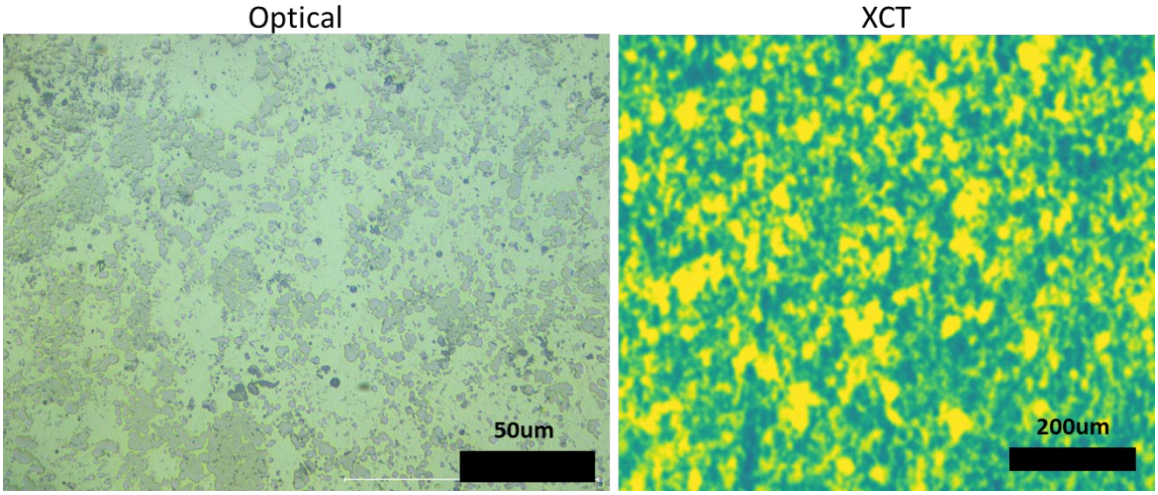

Figure 8. Optical and XCT micrographs of the Fe-25V% HfH_2 MMC consolidated at 1000°C. The absence of voids and cracks indicates a highly dense Fe matrix encapsulating the metal-hydride phase.

SUMMARY

In summary, we demonstrated the successful manufacturing of Ceramic (MgO) and Metal (Fe) Matrix Composite Shields, with 25% HfH_{1-x} and high densities. The high densities were achieved by sintering at appropriate temperatures. Characterization results from a combination of SEM, XCT, and optical microscopy reveal that the ceramic and metal matrix composites are crack free with homogenously distributed HfH_{1-x} particles. XRD results show most hafnium hydride phases are retained after high temperature sintering, with minor amount of HfO_2 and Hf phases. The high hydride retention quantified from the XRD highlights that our processing routes are effective in retaining the majority of hydride phase in the composite structure. Future work will focus on thermophysical properties testing and hydrogen concentration measurements of the composites.

Acknowledgements

This work was supported by the Advanced Research Projects Agency-Energy (ARPA-E) Galvanizing Advances in Market-Aligned Fusion for an Overabundance of Watts (GAMOW) program under contract DE-AR0001381. The authors gratefully acknowledge the use of instrumentation at the Center for Functional Nanomaterials, a U.S. Department of Energy (DOE) Office of Science User Facility operated for the DOE Office of Science by Brookhaven National Laboratory under Contract No. DE-SC0012704.

6. EFFECTS OF IRRADIATION

6.1 UPDATE ON CAVITY EVOLUTION IN TEMPERED MARTENSITIC STEELS UNDER DUAL ION-BEAM IRRADIATION—T. Yamamoto, G. R. Odette (University of California, Santa Barbara), Y. Du, K. Yoshida (Tohoku University), K. Yabuuchi (Kyoto University)

OBJECTIVE

The objective of this research is to characterize how cavity and other microstructural evolutions in irradiated candidate 9Cr tempered martensitic steels (TMS) are influenced by the starting microstructure and irradiation variables, including temperature, displacements per atom (dpa), dpa rate, and the helium/dpa (He/dpa) ratio. This report updates recent observations on 500°C dual ion irradiated (DII) microstructures in F82H IEA heat nominally at 82 dpa and 3700 appm He.

SUMMARY

Conventional TEM and scanning TEM (STEM) microstructures in TMS F82H IEA heat 500°C irradiated and He implanted in DII, nominally to 82 dpa and 3700 appm He, have been characterized. The cavity microstructures were imaged by through-focus series bright field (BF) TEM, as well as by high angular annual dark field (HAADF) STEM, while dislocations were characterized using weak-beam (WB) dark-field STEM. The images were taken in areas ≈ 600 to 800 nm from the irradiation surface. Under-focus cavity images across the entire sample indicated local variations of the cavity formation, while detailed imaging of WB and HAADF STEM and through-focus BF TEM was carried out at selected locations. Preliminary quantitative analyses in one location indicated the cavity volume fraction, $f_v \approx 0.5\%$, which is typical of low swelling cases with presumable injected self-interstitial effects. With dislocation density, $\rho \approx 2.9 \times 10^{14}$ m^{-2}, along with sink densities of bubbles and voids 2.0 and 3.3×10^{14} m^{-2}, respectively, and a factor of ≈ 0.2 for possible injected interstitial effect, predict a swelling rate of ≈ 0.018%/dpa, which is reasonably consistent with the low swelling case trend of ≈ 0.014%/dpa.

PROGRESS AND STATUS

As reported previously [1-5], we have been carrying out DII studies at 500°C in DuET facility in Kyoto University at various nominal He/dpa and dpa rates (defined at the depth of 600 nm) in TMS F82H. The dual ion database includes 234 alloy-dpa-He/dpa conditions for irradiations up to ~ 82 dpa and 3700 appm helium. The large "scatter" observed in f_v is primarily due to local microstructural variations, especially those that shield regions at shallower depths from the effects of injected interstitial atoms, which would otherwise reduce f_v. The highest f_v data, at a specified dpa and He/dpa, presumably providing the most appropriate measures of swelling trend unperturbed by injected self-interstitial atoms, indicated that the dose dependence of f_v can be described by an incubation dpa_i, marking the onset of significant void swelling, and a post-incubation swelling rate, $f_v' = d[f_v]/d[dpa]$. Both dpa_i and f_v' decrease with increasing He/dpa. The f_v' is quantitatively consistent with a simple model treating defect partitioning between bubble, void, and biased dislocation sinks. Here we update the DII database with a new observation of cavity and dislocation microstructures in F82H IEA heat at the highest nominal dpa and He condition including the test of the new data with the sink balance model.

Experimental Procedure

While details of alloys and DII experiments can be found in [1-5], Table 1 summarizes nominal He and dpa conditions at two reference depth locations encompassed by the current DII microstructure database. The dpa are based on SRIM using the Kinchin-Pease with Fe displacement energy of 40 eV [6-8]. The sample used in this report is the F82H IEA heat irradiated in DI16A+19A experiments to nominally 82 dpa and 3700 appm He. Fisher Scientific Helios Focused Ion Beam (FIB) tool was used to micro-machine < 100 nm thick electron transparent ~ 5 μm wide and ~ 5 μm deep lift-outs, which included both damaged-implanted and undamaged regions. Final FIBing at 5.5pA of 2kV Ga beam removing the higher energy ion damage, was

followed by nano-milling by Ar ions at energies down to 300 eV. The F82H IEA sample previously observed to the area 100 to 300 nm from the irradiation surface [4,5] has been further nano-milled to reveal 600 to 800 nm region electron transparent. Through-focus series cavity images were observed using a TEM JEOL JEM-2100-Plus, while STEM BF, WB and HAADF images were obtained in a spherical aberration-corrected JEOL ARM 200F STEM, both located in Oarai International Research Center of Tohoku University. The details of the TEM optics and detectors for WB-STEM, recently developed by Yoshida et al. [5,9,10]. The foil thickness was measured by the convergent beam electron diffraction (CBED) method [11] at a reference location ≈ 90 nm from the milled sample edge.

Table 1. Irradiation Conditions

Exp ID	T (°C)	Nominal Condition (@550-650nm)				Peak He (@1000-1100 nm)			Alloys
		dpa	He (appm)	He/dpa	dpa/s	dpa	He (appm)	He/dpa	
DI10B1	500	26	1210	47	5.0×10^{-4}	45	2100	47	M3
DI10B2	500	9.9	457	46	5.2×10^{-4}	17	795	46	M3
DI10B3	500	10	480	47	5.1×10^{-4}	18	840	47	M3
DI13A	500	26	390	15	5.1×10^{-4}	44	670	15	IEA M3
DI13B1	500	30	848	29	1.5×10^{-3}	51	1467	29	IEA M3
DI14A1	500	30	1200	47	1.3×10^{-3}	45	2100	47	IEA M3
DI14B	500	45	1290	28	8×10^{-4}	79	2230	28	IEA M3
DI15A1	500	51	1360	27	8.6×10^{-4}	88	2350	27	IEA M3
DI16A	500	52	2327	45	6.5×10^{-4}	89	4020	45	IEA M3
DI16A+19A	500	82	3700	45	6.5×10^{-4}	142	6400	45	IEA M3

Results

Figure 1a shows example under-focus images of cavity microstructures across a part of the thinnest region, located at 550 to > 750 nm depth relative to the irradiation surface, which shows local variation in cavity evolution. Figures b and c show corresponding STEM HAADF images at two locations. Relatively large cavities are clearly identified in both HAADF STEM and under-focus TEM images as darker objects and brighter objects with dark fringes, respectively, while small cavities were more identifiable in under-focus TEM images. Figure 2 shows examples of STEM of a and d) bright-field (BF); b and e) weak beam (WB) darkfield; and c and f) high angle annual dark field (HAADF) images at two locations.

Out of the observation, preliminary quantitative analysis was carried out at a location. Figure 3 shows a complete set for the analysis including a) STEM BF; b) STEM WB; c) STEM HAADF; d) TEM under-focus images for the quantitative analysis. Figure 3e shows traces of dislocations based on images a and b, while Figure 3f shows cavities marked based on images c and d, from which dislocation density and cavity volume fraction, average size and number densities (for bubbles and voids assuming d_c = 4nm) were derived as shown in Table 2. Figure 4 compares the $f_v \approx 0.5\%$ in this analysis with the other data in the database. Clearly, the data belongs to the lower swelling rate group, which presumably is subjected to significant effects of injected self-interstitial atoms. The table also shows the sink densities for the observed microstructural features, k_d, k_b, k_v,and the predicted swelling rate, f_v', using a simple point defect balance-based model [5] shown below.

$$f_v' \approx C\eta k_v k_d (B_d - B_b)/[(k_d + k_b + k_v)\{k_d(1 + B_d) + k_b(1 + B_b) + k_v(1 + B_b)\}] \quad (1)$$

Here, C is a roll-up factor of various effects and assumed to be 0.2 for significant injected interstitial effects and η is the fraction of point defects assumed to survive in-cascade recombination, that is nominally 0.33[5].

For the net dislocation bias, $B_d - B_b = 0.015 \pm 0.005$ [5], the predicted, $f_v' = 0.18 \pm 0.06$ %/dpa, which is consistent but slightly higher than the trend of the lower swelling population, which is ≈ 0.15 ± 0.05%/dpa.

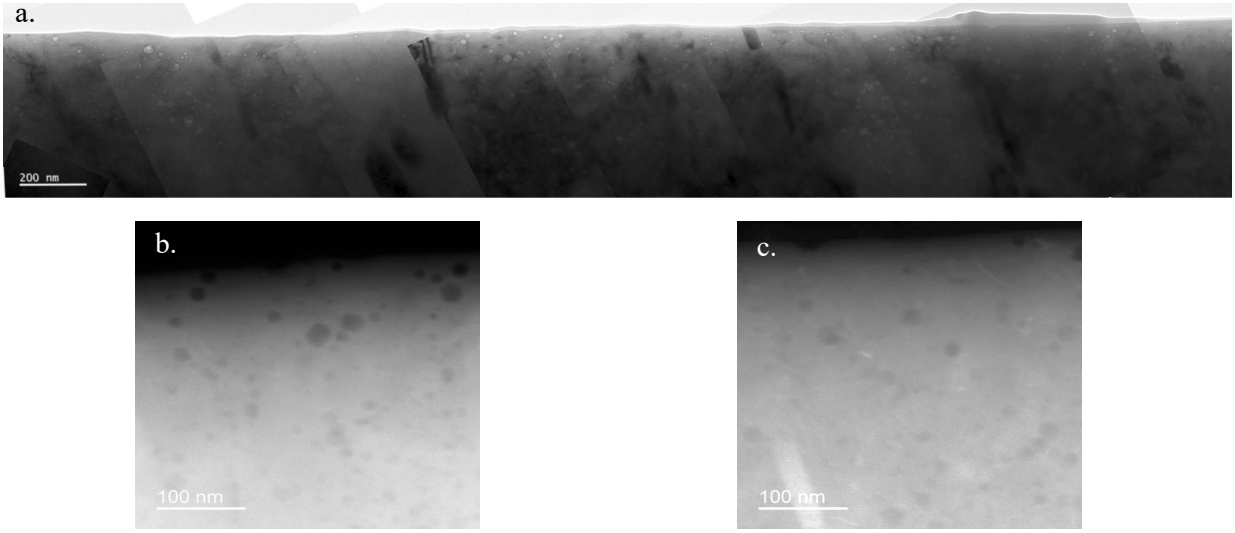

Figure 1. a) Example under-focus images of cavity microstructures across the thinnest region, from 550 to > 750 nm deep region relative to the irradiation surface; and b and c) STEM HAADF cavity images at two locations.

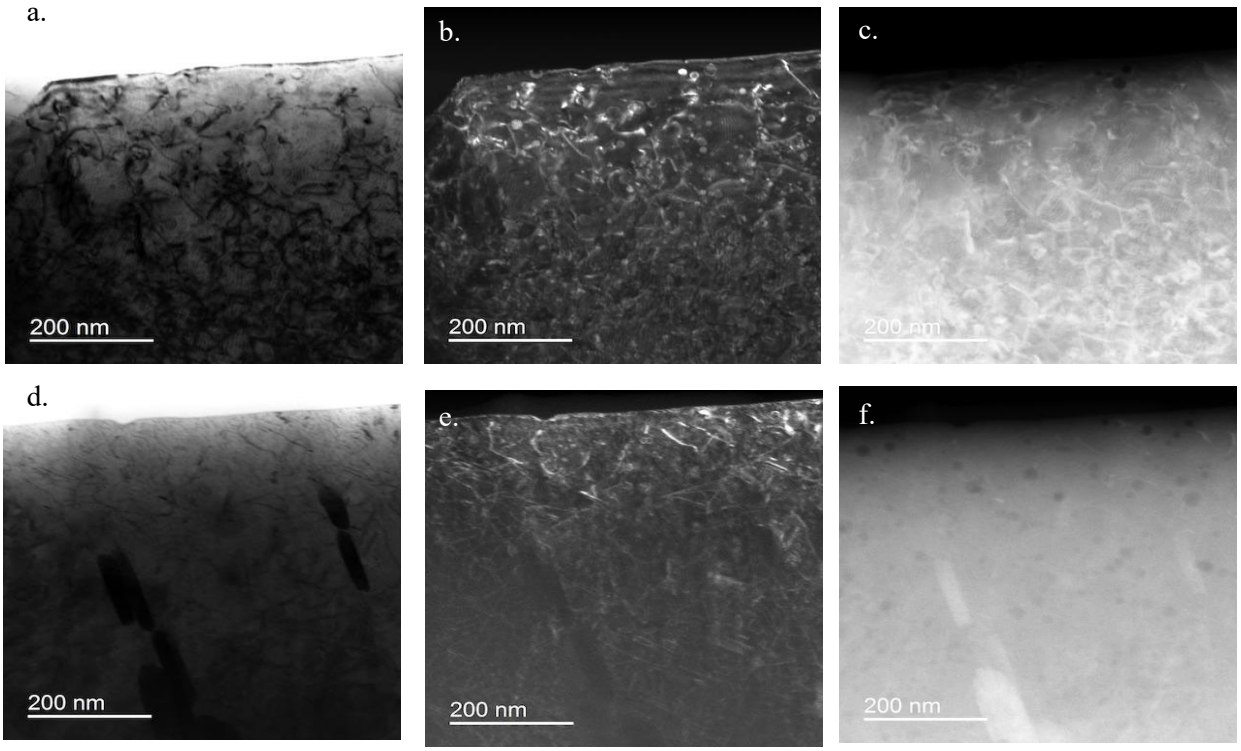

Figure 2. STEM examples of a and d) bright field (BF); b and e) weak beam (WB) dark field; and c and f) high angle annual dark field (HAADF) images at two locations.

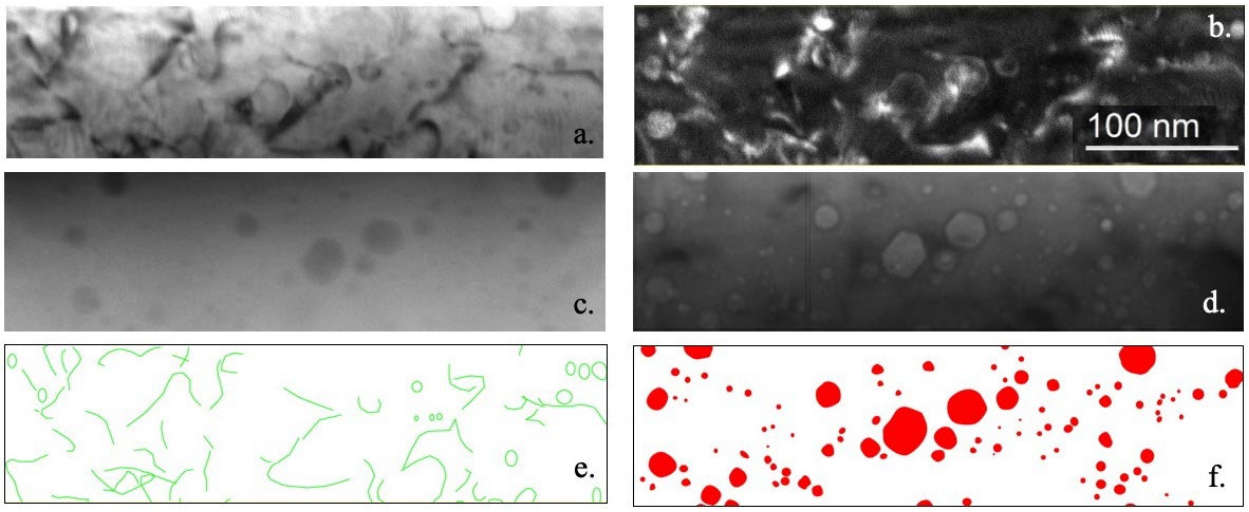

Figure 3. A set of a) STEM BF; b) STEM WB; c) STEM HAADF; and d) TEM under-focus images for quantitative analysis; e) traces of dislocations based on images a and b; f) cavities marked based on images c and d.

Table 2. Quantitative results of microstructural features and the swelling rate prediction

	For d_c = 4 nm	For d_c = 6 nm
$<d_b>$	3.1 nm	3.8 nm
N_b	5.4×10^{21} m^{-3}	8.6×10^{21} m^{-3}
$<d_v>$	8.8 nm	12.2 nm
N_v	7.4×10^{21} m^{-3}	4.2×10^{21} m^{-3}
f_v	0.53%	0.51%
ρ (=k_d)	2.9×10^{14} m^{-2}	2.9×10^{14} m^{-2}
k_b	1.0×10^{14} m^{-2}	2.0×10^{14} m^{-2}
k_v	4.1×10^{14} m^{-2}	3.3×10^{14} m^{-2}
f_v'	0.018 %/dpa	0.014 %/dpa

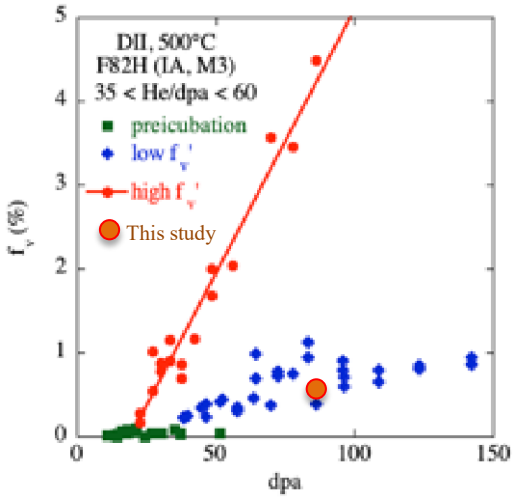

Figure 4. f_v for the reports compared with other data [5] in the DII database.

Figure 5 shows the size distribution of all the cavities. This case, a gap of two populations corresponding to the smaller bubbles and larger voids is observed at $d_c \approx 6$ nm. The reason for a d_c larger than the typical value is not clear at this moment; thus Table 4 also shows the results of the analysis using the value for d_c. The predicted $f_v' \approx 0.014 \pm 0.005$ %/dpa is more consistent for the observation. Further analysis including other areas are underway and will be discussed in the future report.

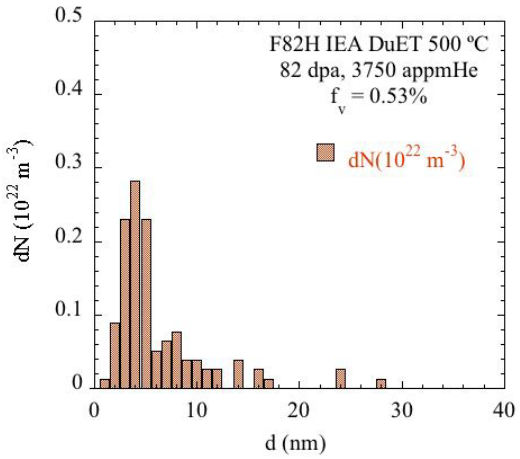

Figure 5. Size distribution of the cavities observed in the area shown in Figure 3.

Future Work

Recent updates on the TEM and STEM observations of the cavity and dislocation microstructures in DII irradiated F82H IEA are reported. Preliminary quantification shows that the analyzed area belongs to the lower swelling rate group in the database, which is presumably due to the injected self-interstitial atoms. The sink densities of dislocations, bubbles, and voids are consistent with the average swelling rate, ≈ 0.015%/dpa, of the group assuming the roll-up swelling reduction factor of 0.2 mainly due to the injected interstitial effect.

Acknowledgments

The dual ion-beam irradiations were conducted under the support of the "Joint Research Program on Zero-Emission Energy Research, Institute of Advanced Energy, Kyoto University (ZE2021A-32). The work performed at UCSB was supported by the U. S. Department of Energy, Office of Fusion Energy Sciences, under contract DE-FG03-94ER54275. TEM and STEM work were carried out in support of the International Research Center for Nuclear Materials Science, Tohoku University (Oarai, Japan).

References

[1] T. Yamamoto, Y.Wu, G.R. Odette, K. Yabuuchi, S. Kondo, A. Kimura, "A Dual Ion Irradiation Study of Helium-DPA Interactions on Cavity Evolution in Tempered Martensitic Steels and Nanostructured Ferritic Alloys," J. Nucl. Mater. 449 (2014) 190.

[2] G.R. Odette, T. Yamamoto, Y. Wu, S. Kondo, A. Kimura, "On the Effects of Helium-DPA Interactions on Cavity Evolution in Tempered Martensitic Steels and Nanostructured Ferritic Alloys Under Dual Ion-beam Irradiation," *Fusion Materials Semiannual Report 6/30/2015* DOE/ER-313/57 (2015) 8.

[3] T. Yamamoto, Y. Wu, G.R. Odette, S. Kondo, A. Kimura, "Effects of Helium-DPA Interactions on Cavity Evolution in Tempered Martensitic Steels Under Dual Ion-Beam Irradiation," *Fusion Materials Semiannual Report 6/30/2014* DOE/ER-313/56 (2014) 194.

[4] Takuya Yamamoto, Yuan Wu, G. Robert Odette, Kiyohiro Yabuuchi, Sosuke Kondo, Akihiko Kimura, "On the Effects of Helium-DPA Interactions on Cavity Evolution in Tempered Martensitic Steels Under Dual Ion-beam Irradiation," *Fusion Materials Semiannual Report 6/30/2016* DOE/ER-313/60 (2016) 12.

[5] Takuya Yamamoto, Yuan Wu, Kiyohiro Yabuuchi, Jack Haley, Kenta Yoshida, Akihiko Kimura, G. Robert Odette, "Cavity Evolution and Void Swelling in Dual Ion Irradiated Tempered Martensitic Steels," submitted to J. Nucl. Mater.

[6] F. Ziegler, M.D. Ziegler, J.P. Biersack, "SRIM - The stopping and range of ions in matter (2010)," Nucl. Instr. Methods Phys. Res. B 268 (2010) 1818.

[7] ASTM E521-96 (2009), ASTM.

[8] R.E. Stoller, M.B. Toloczko, G.S. Was, A.G. Certain, S. Dwaraknath, F.A. Garner, Nuc Instr Methods Phys Res B 310 (2013) 75.

[9] K. Yoshida, M. Shimodaira, T. Toyama, Y. Shimizu, K. Inoue, T. Yoshiie, K.J. Milan, R. Gerard, Y. Nagai, "Weak-Beam Scanning Transmission Electron Microscopy for Quantitative Dislocation Density Measurement in Steels," Microscopy (2017) 120.

[10] M. Shimodaira, T. Toyama, K. Yoshida, K. Inoue, N. Ebisawa, K. Tomura, T. Yoshiie, M.J. Konstantinovic, R. Gerard, Y. Nagai, "Contribution of Irradiation-Induced Defects to Hardening of A Low Copper Reactor Pressure Vessel Steel," Acta Mater. 155 (2018) 402.

[11] D. Williams and C. Carter, "Transmission Electron Microscopy," ISBN: 0-306-45324-X, 1996. Springer.

6.2 THE DEPTH DEPENDENT ALPHA PRIME DISTRIBUTION IN Fe18Cr AFTER ION IRRADIATIONS—Y. Zhao, S. J. Zinkle (University of Tennessee), A. Bhattacharya (Oak Ridge National Laboratory)

OBJECTIVE

The objective of this work is to study the effect of the free surface and injected ions on the formation of α' precipitates, so that the safe analysis region can be determined for ion irradiations.

SUMMARY

Fe18Cr alloys were irradiated with 8 MeV Fe ions to a midrange (~1 um) dose of 0.37 or 3.7 displacements per atom (dpa) at 350-450 °C and 10^{-4} dpa/s. Following irradiation, atom probe tomography (APT) was employed to characterize the Cr-rich clusters. The results obtained at the mid-range depths were summarized previously [1]. The surface was observed to reduce α' formation within a relatively narrow temperature-dependent depth (~10 nm at 450 °C). Pronounced suppression of α' precipitation due to implanted ions (injected interstitials) was observed within ~500 nm of calculated mean ion range.

PROGRESS AND STATUS

3 Fe18Cr specimens were selected for detailed analysis of α' precipitation at multiple depths by APT. Their irradiation conditions are listed in Table 1.

Table1. The specimens characterized by APT in this reporting period

Irradiation temperature (°C)	Mid-range dose rate (dpa/s)	Mid-range dose (dpa)
350	10^{-4}	0.37
350	10^{-4}	3.7
450	10^{-4}	3.7

Experimental Procedure

The specimen preparation procedures, and details related to ion irradiation experiments, can be found in a prior report [1]. After ion irradiation, the samples were characterized by APT. The APT needles were prepared by focused ion beam (FIB) technique. A thin layer of Ni atoms was deposited on the sample surface before the FIB milling, so that the original ion irradiated surface could be marked and protected. For all other deeper depths, the corresponding lengths below the Platinum protection layer was removed during the final polishing step, so that the target depths can be easily achieved. The Cr-enriched α' precipitates were identified and quantified through a solute concentration-based cluster analysis algorithm written with Python codes. Details regarding this Python code will be documented in a separate publication [2].

Results

<u>α' precipitates denuded zone near the surface</u>

Figure 1 shows the reconstructions of APT needles extracted from the near-surface depth of the 3 specimens. The original sample surfaces were marked and located just below the Ni cap. A thin layer of precipitate denuded zone can be observed near the surface region in all 3 specimens. The extent of this layer is around 3-4 nm after irradiation at 350 °C for both fluences and around 10 nm after irradiation at 450 °C to the high fluence.

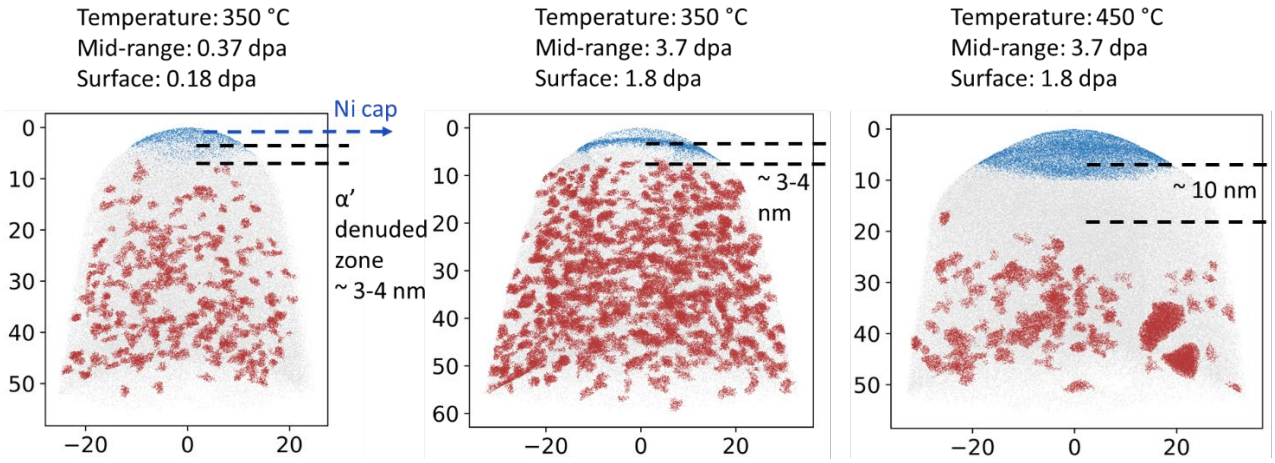

Figure 1. Reconstructions for needles taken from the surface-depth of 3 specimens. α' denuded zones are visible in the near-surface region.

Suppression of α' precipitation at and beyond the peak damage region

Figure 2 presents cross-sections of the depth-dependent distribution of α' precipitates in Fe18Cr after ion irradiation at 350 °C to the lower fluence, along with the injected ion concentration and displacement damage profiles calculated by SRIM. The α' precipitates can be observed at all investigated depths, including the peak-damage region and the location with highest injected ion concentrations. However, the number density of α' precipitates decreased significantly in the 1.5-2 μm depths (implanted ion and peak damage region) compared to their mid-range value.

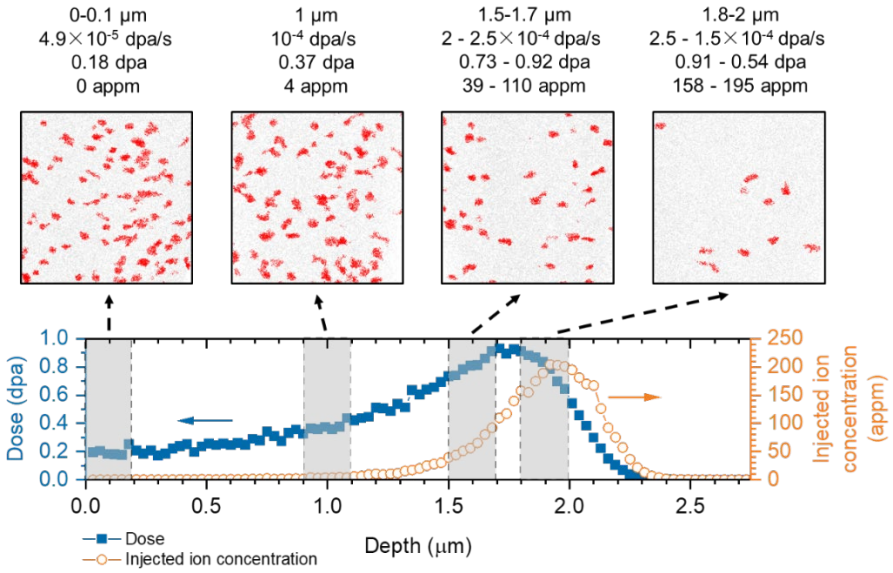

Figure 2. Cross-sections showing the distribution of α' at different depths in Fe18Cr after irradiation at 350 °C to the lower fluence. Imaged volume is 40×40×10 nm^3 for each cross section. The local dose rate, dose and injected ion concentration are given above each cross-section image.

Figure 3 shows the distribution of α' after ion irradiation at 350 °C and 450 °C to the high fluences. At 350 °C, α' precipitates were observed only at depths shallower than ~1.2-1.4 μm. The absence of α' precipitation

at the near peak implanted ion/ peak damage region and deeper locations may indicate strong suppression effects. At 450 °C, α' formation were detected at depths up to 1500 nm. Characterizations of α' at deeper depths haven't been completed and are planned to be done in near future.

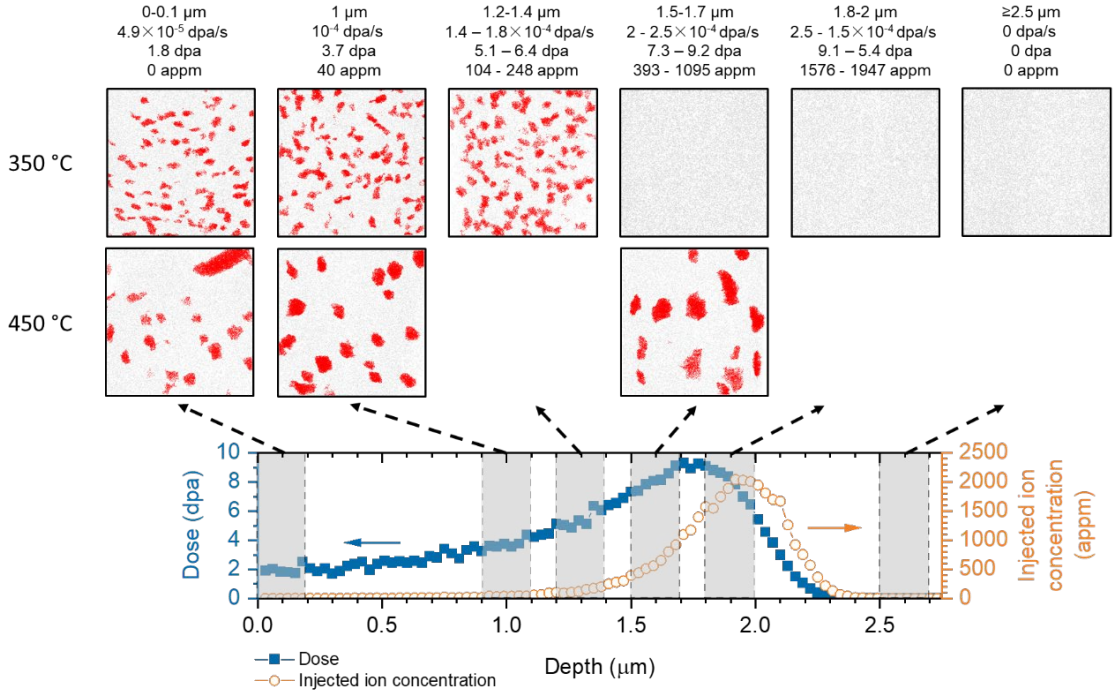

Figure 3. Cross-sections showing the distribution of α' at different depths in Fe18Cr after irradiation at 350 °C and 450 °C to the high fluences. Imaged volume is 40×40×10 nm^3.

The radius, number density and volume fraction of α' precipitates were determined through a cluster searching algorithm by selecting the cluster atoms above a threshold solute concentration. The Cr concentration in precipitates and matrix phases were calculated using the proximity histogram method using a threshold Cr concentration of 24 at. %. The results are plotted in Figure 4. At 350 °C, there is no obvious change on the sizes of precipitates over the entire range of investigated depths. The number densities of α' are nearly constant at depths shallower than 1.2 μm for both ion fluences, above which they started to decrease for the low fluence condition and dropped below the APT volumetric density detection limit (~$10^{22}/m^3$) for the high fluence condition. The volume fractions of the α' precipitate phase show a similar trend. Although there is no clear difference among the precipitate Cr contents measured at different depths, the matrix Cr content increased at depths >1.5 μm due to the decreased Cr clustering. At 450 °C, both smaller-sized (radius ~1 nm) and large-sized precipitates (radius ≥1.5 nm) were present in the near-surface region (~0-200 nm depths), while mainly large precipitates were found in the depths of 1-1.5 μm, which resulted in a smaller average radius and a lower volume fraction of α' in the former case. As for the Cr contents in precipitate and matrix phases, there is no clear trend with respect to depth up to 1.5 μm.

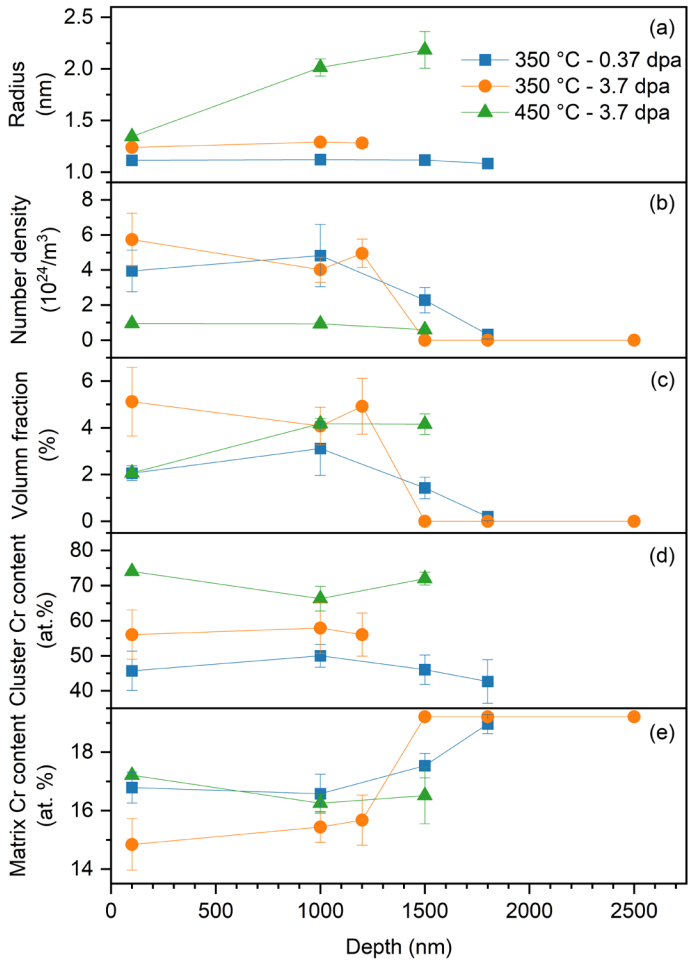

Figure 4. The evolution of (a) radius, (b) number density, (c) volume fraction, (d) Cr concentration in precipitates and (e) matrix with irradiation depth.

Discussion and Conclusion

Three Fe18Cr specimens irradiated at a constant 8 MeV Fe ion flux (corresponding to a mid-range dose rate of 10^{-4} dpa/s) were selected for studying the effect of surface and injected ions on α' precipitate formation: two specimens irradiated at 350 °C to mid-range doses of 0.37 dpa and 3.7 dpa, and one specimen at 450 °C to 3.7 dpa, After ion irradiations, the α' distributions at different depths were characterized using APT. Precipitate denuded zones in the near surface region were observed in all 3 specimens. The thicknesses of the near-surface denuded zones are ~3-4 nm at 350 °C and ~10 nm at 450 °C, and the irradiation dose has no identifiable effect. These measured thicknesses are much narrower than the void denuded zones typically observed after ion irradiations near these temperatures, which are ~100-500 nm in FeCr alloys [3]. Since the formation of voids requires a substantial net supersaturation of vacancies relative to interstitials, while only high vacancy concentrations are needed for the radiation-enhanced precipitation process, it is expected that the conditions for precipitate formation would be easier to be achieved compared to the formation of voids, and thus leads to a narrower denuded zone. Our investigation indicates that for studies focusing on precipitation behavior under ion irradiations, the artifacts related to surface are not very important and can be easily avoided.

Suppression of α' precipitation at the near peak damage region was revealed after ion irradiation at 350 °C. Especially in the high fluence case, no α' was observed beyond the depth of 1.5 μm. However, this suppression effect is not obvious after irradiation at 450 °C at depths up to 1.5 μm. According to our previous results, the higher dose rate in the implanted ion region alone is not sufficient to suppress α' formation, because pronounced α' precipitation was observed in the midrange regions of 8 MeV Fe ion irradiated Fe18Cr after irradiation at the same temperature and a higher dose rate of 10^{-3} dpa/s [4]. Similar α' precipitation suppression behaviors near the implanted ion region have been observed by multiple researchers, and there were different explanations without reaching an agreement. Tissot et al. inferred suppression of α' formation by injected interstitials by showing the decrease in precipitate number density and volume fraction in the ion implanted region of a Fe-15Cr specimen after ion irradiation at ~2-6.1×10^{-5} dpa/s and 300 °C to doses of ~0.3-1 dpa [5]. Pareige et al didn't detect any α' in Fe-12Cr alloy after irradiation at 2.2×10^{-4} dpa/s and 300 °C to 0.5 dpa using Fe ions with energies of 0.5, 2 and 5 MeV (to achieve relative flat displacement damage and injected ion profiles), which was attributed to the injected interstitials that were almost everywhere at this condition [6]. The suppression behavior observed in the analyzed regions was attributed to a decreased radiation enhanced diffusion rate due to the injected interstitials which recombine with vacancies or form interstitial clusters that act as sinks and further decrease the local vacancy supersaturation level [5]. Harrison et al. studied the effect of cascade sizes and proposed that the shorter mean free paths between collisions at the end of range led to a higher probability of cascade overlap, which can more effectively dissolve the precipitates [7]. The experiments summarized in this report compared the α' distribution after irradiation at 350 °C and 10^{-4} dpa/s to final doses that are 10 times different. The stronger suppression effect at the high fluence condition indicates that the accumulation of injected ions or displacement damage is the most important factor that leads to the disappearance of α', and thus it agrees more with the physical mechanism proposed by Tissot et al. Since the temperature, injected ion energy and flux were almost the same, if cascade overlap is the main reason, similar suppression effect should be observed after irradiation to both doses, The less significant suppression effect at 1.5 μm after irradiation at 450 °C might be attributed to the higher radiation enhanced diffusion rate. Therefore, to avoid implanted ion related artifacts, the analysis region should be limited to ≤1.2 μm at 350 °C for 8 MeV Fe ions (i.e., the analysis depths should be at least 700 nm away from the peak in the implanted ion distribution). At 450 °C, the regions that can be safely analyzed extends up to 1.5 μm based on our current results. If the bombarding ion species is different from the "self-ion" Fe beam, chemical effects associated with implanted ions might also need to be considered.

Future Work

1. The TEM characterization of the dislocation loops at different depths of the 3 specimens will be performed, so their potential influence on radiation enhanced diffusion coefficient can be calculated and the overall depth-dependent point defect sink strengths can be quantified.
2. The α' distribution at 1800 nm of the 450 °C sample will be performed by APT.
3. The APT characterizations will be performed on FeCr specimens irradiated by protons, so that the phase boundary between α and α+α' could be evaluated for low (proton) versus high (Fe ion) average primary knock-on energy conditions.

References

[1] Zhao Yajie et al. "A study on the stability of Alpha-prime (α') precipitates in high purity Fe-18Cr alloys after ion irradiation" Fusion materials semiannual progress report for the period ending Dec. 31, 2019, DOE/ER-0313/67, p. 33.
[2] Y. Zhao, S. Levine, C. Pareige, A. Bhattacharya, Z. Jiao, S. Zinkle, APT Cluster Analysis Using Open Source Programs (in progress).
[3] Y.-R. Lin, A. Bhattacharya, D. Chen, J.-J. Kai, J. Henry, S.J. Zinkle, Temperature-dependent cavity swelling in dual-ion irradiated Fe and Fe-Cr ferritic alloys, Acta Mater. 207 (2021) 116660.

[4] Y. Zhao, A. Bhattacharya, C. Pareige, C. Massey, P. Zhu, J.D. Poplawsky, J. Henry, S.J. Zinkle, Effect of heavy ion irradiation dose rate and temperature on α' precipitation in high purity Fe-18%Cr alloy, Acta Materialia, under review (2022).
[5] O. Tissot, C. Pareige, E. Meslin, B. Décamps, J. Henry, Influence of injected interstitials on α′ precipitation in Fe–Cr alloys under self-ion irradiation, Mater. Res. Lett. 5(2) (2016) 117-123.
[6] C. Pareige, V. Kuksenko, P. Pareige, Behaviour of P, Si, Ni impurities and Cr in self ion irradiated Fe–Cr alloys – Comparison to neutron irradiation, J. Nucl. Mater. 456 (2015) 471-476.
[7] R.W. Harrison, A.W. Carruthers, J.A. Hinks, M.G. Burke, S.E. Donnelly, Cascade size and dose rate effects on α′ precipitation in ion-irradiated Fe14Cr alloy, Scr. Mater. 172 (2019) 33-37.

6.3 APT STUDY ON THE FORMATION OF CHROMIUM-ENRICHED PRECIPITATES IN DUAL-ION IRRADIATED Fe-14Cr FERRITIC ALLOYS—Y. Lin, A. Bhattacharya (Oak Ridge National Laboratory), S. J. Zinkle, Y. Zhao (University of Tennessee)

OBJECTIVE

The primary objective of the current study is to examine if α' precipitates formed in dual ion irradiated Fe-14Cr at 400°C with dose and dose rate of 30 dpa, and 1.4×10^{-3} dpa/s, respectively.

SUMMARY

The Cr-enriched precipitates or irradiation-altered α' precipitates were observed in the Fe-14Cr sample irradiated at 400°C. Although the cluster core Cr content of the observed precipitates (~44-56 at.%) were lower than the thermal equilibrium α' precipitates (~80-90 at.%), comparison with recent low-dose (~0.35-3.5 dpa) results on ion-irradiated Fe-Cr alloys at a similar dose rate of $\sim10^{-3}$ dpa/s suggests that the precipitate evolution may have reached a steady-state and the precipitates are stable at dose rates $\sim10^{-3}$ dpa/s for doses up to at least 30 dpa. The formation of α' precipitates in the Fe-14Cr sample with a high strength above 10^{15} m^{-2} can likely reduce the cavity swelling significantly.

PROGRESS AND STATUS

In our previous study [1], we applied dual 8 MeV Ni ions and 3.55MeV He ions to irradiate a series of ultra-high purity bcc Fe and Fe-Cr alloys with Cr content ranging from 3-14% Cr at 470-550°C. Based on the Fe-Cr phase diagram estimated by using the Thermo-Calc software (Figure 1), Fe-14Cr irradiated at 400°C has the highest possibility for α' precipitation compared to other samples; at temperatures above 400°C the predicted α-α'solvus rapidly increases to Cr levels >14%. Although clear evidence for α' was not visible in the Fe-10Cr and Fe-14Cr samples by TEM or STEM-EDS, the Fe-14Cr sample irradiated at 400°C was selected for APT analysis to examine if precipitates formed during irradiation. As shown in Figure 2, Cr-enriched precipitates were observed in all four APT needles extracted from the midrange (~1 μm) region of the same irradiated Fe-14Cr sample. The midrange dose and dose rate were 30 dpa and 1.4×10^{-3} dpa/s, respectively. The information on the Cr-rich precipitates, including the precipitate size, number density, and the Cr content of the precipitate/matrix, is listed in Table 1. The average number density and average atomic radius are 1.6×10^{-23} m^{-3} and 1.53 nm, respectively.

In the irradiated Fe-14Cr sample, Cr-enriched precipitates were observed by APT but not by conventional or analytical TEM (EDS and EELS). The reason why precipitates in the Fe-14Cr sample were undetectable under TEM is most likely due to the slight lattice parameter mismatch between α (a=0.2886 nm) and α' (a=0.2885 nm) phase, and the tiny atomic number difference between Fe (Z=56) and Cr (Z=52). The observation of these irradiation-altered α' precipitates by APT in Fe-14Cr at such a high dose rate is consistent with recent low-dose (~0.35-3.5 dpa) results on ion-irradiated Fe-Cr alloys [3, 4]. It is also worth noting that the Cr concentration in the clusters is 44-56 at% (Table. 1), much lower than the 80-90 at% for typical α' precipitates as estimated by the thermal equilibrium phase diagram. This could be due to an artifact of APT analysis for small precipitates (radius <2 nm) or because the Cr-enriched precipitates are radiation-altered α' precipitates (not thermal equilibrium α' precipitates) whose chemical content could be altered by prolonged displacement cascade-induced ballistic mixing events with the Fe-rich matrix. Regardless, the observation of these Cr-enriched precipitates with precipitate sizes and densities comparable to that observed much lower dose (0.35-3.5 dpa) ion irradiation studies on binary Fe-Cr alloys [3, 4] suggests the precipitate evolution may have reached a steady-state and in any case was not dissolved under the severe displacement damage to 30 dpa at dose rates $\sim10^{-3}$ dpa/s. With different irradiation conditions (e.g., dose, dose rate, temperature, or using proton source), further examination of how dose rate and irradiation temperature affect the precipitate ballistic dissolution and radiation enhanced diffusion would be valuable.

Previous studies have reported that when the point defect sink strength associated with nanoparticles, etc. is above ~10^{15} m^{-2}, the cavity swelling could be suppressed [5, 6, 7]. If irradiation-altered α' precipitates are effective point defect sinks like oxides or MX type particles, the average size and density of the α' precipitates observed in the irradiated Fe-14Cr sample translates to a sink strength of 6.2×10^{15} m^{-2}. Therefore, the formation of α' precipitates in the Fe-14Cr sample with such a high strength above 10^{15} m^{-2} can likely reduce the cavity swelling significantly. Based on the Fe-Cr phase diagram (Figure 1), the Fe-10Cr and Fe-14Cr materials with relatively higher Cr content are favorable for α' precipitation at 400-435°C. Additional APT analyses are needed to confirm if α' phase precipitation occurred in Fe-10Cr. In addition, in this study, we only examined the α' precipitates in the 0.1 appm He/dpa irradiated sample. Although the presence of helium is expected to have a minor effect on second phase precipitation, it remains an open question if a higher helium production rate could indirectly affect the formation of α' precipitates.

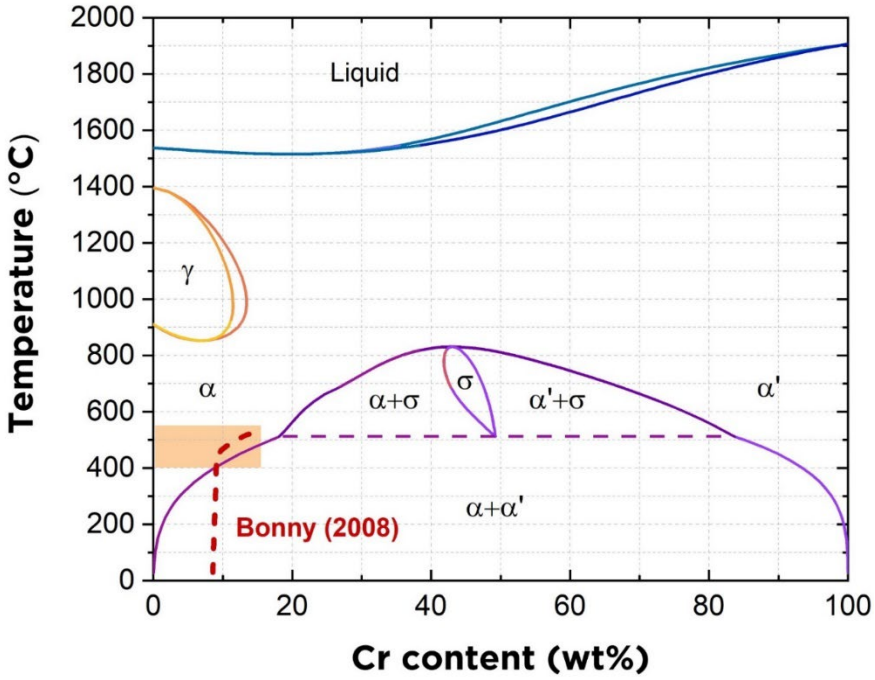

Figure 1. Fe-Cr phase diagram predicted by Thermo-Calc software. The dashed red curve is the boundary estimated by Bonny et al. [2] The orange shaded area indicates the irradiation temperature range and the Cr content range of the materials used in this study.

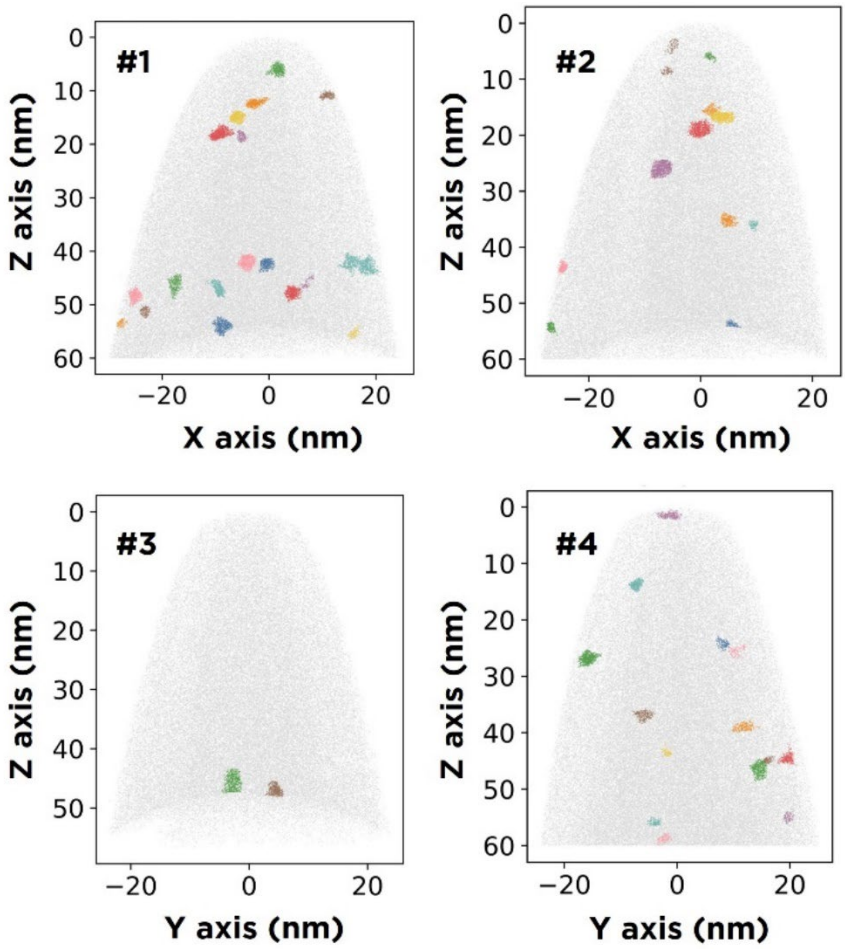

Figure 2. APT reconstruction of the Fe-14Cr irradiated at 400°C (30 dpa, 0.1 appm He/dpa, 1.4×10^{-3} dpa/s). The colored clusters represent the Cr-enriched precipitates.

Table 1. Quantification of Cr-enriched precipitates in Fe-14Cr irradiated at 400°C with 0.1 appm He/dpa

Sample #	Number density (m^{-3})	Atomic radius (nm)	Cluster core Cr (at.%)	Matrix Cr (at.%)
1	1.9×10^{23}	1.27	47.91	14.85
2	1.7×10^{23}	1.41	44.11	15.07
3	4×10^{22}	1.82	56.26	14.93
4	2.3×10^{23}	1.61	44.67	15.12
Average	1.6×10^{23}	1.53	48.24	14.99
Standard deviation	8.3×10^{22}	0.24	5.60	0.12

Future Plans

To evaluate the Q ratio (the ratio of biased sink strengths to neutral sink strengths) effect on cavity swelling, two sets of dual ion irradiated samples at 30 dpa and 10 appm He/dpa are selected for further characterization of dislocation loops and network dislocations. The first set is Fe-10Cr irradiated at 400-550°C, and the second is Fe and Fe-Cr (3-14 wt%) irradiated at 470°C.

References

[1] Y. Lin, A. Bhattacharya, D. Chen, J. Kai, J. Henry, S.J. Zinkle, "Temperature-dependent cavity swelling in dual-ion irradiated Fe and Fe-Cr ferritic alloys", Acta Mater., 207 (2021), 116660
[2] G. Bonny, D. Terentyev, L. Malerba, On the α–α′ miscibility gap of Fe-Cr alloys, Scripta Materialia 59(11) (2008) 1193-1196.
[3] Y. Zhao, A. Bhattacharya, C. Pareige, C. Massey, P. Zhu, J.D. Poplawsky, J. Henry, S. Zinkle, Effect of Heavy Ion Irradiation Dose Rate and Temperature on α' Precipitation in High Purity Fe-18%Cr Alloy, Acta Materialia (under review).
[4] R.W. Harrison, A.W. Carruthers, J.A. Hinks, M.G. Burke, S.E. Donnelly, Cascade size and dose rate effects on α′ precipitation in ion-irradiated Fe14Cr alloy, Scripta Materialia 172 (2019) 33-37.
[5] Y. Lin, W.-Y. Chen, L. Tan, D.T. Hoelzer, Z. Yan, C.-Y. Hsieh, C.-W. Huang, S.J. Zinkle, Bubble formation in helium-implanted nanostructured ferritic alloys at elevated temperatures, Acta Materialia 217 (2021) 117165.
[6] S.J. Zinkle, L.L. Snead, Designing Radiation Resistance in Materials for Fusion Energy, Annual Review of Materials Research 44(1) (2014) 241-267.
[7] Y. Dai, G.R. Odette, T. Yamamoto, 1.06 - The Effects of Helium in Irradiated Structural Alloys, in: R.J.M. Konings (Ed.), Comprehensive Nuclear Materials, Elsevier, Oxford, 2012, pp. 141-193.

6.4 RESPONSE OF CANDIDATE FUSION BLANKET MATERIALS TO DUAL AND TRIPLE ION IRRADIATION TO UNDERSTAND THE SYNERGIES BETWEEN H, He AND RADIATION DAMAGE—L. N. Clowers, Z. Jiao, G. S. Was (University of Michigan)

OBJECTIVE

The objective of this project is to understand the synergy between transmutation gasses H and He on cavity evolution in ferritic-martensitic fusion blanket materials.

SUMMARY

Three ferritic/martensitic alloys were studied to understand the synergistic effect between single ion beam (Fe^{2+}), dual ion beam (Fe^{2+}+He^{2+} and Fe^{2+}+H^{+}), and triple ion beam (Fe^{2+}+He^{2+}+H^{+}) irradiations on cavity evolution in F82H, CNA3, and model alloy Fe8Cr2W. Irradiations were conducted to 50 dpa at $1x10^{-3}$ dpa/s with He/H injection rates of 10/40 appm/dpa between 450 and 600°C. In all three alloys, hydrogen co-injection with helium resulted in an increased cavity number density and cavity size, producing an increase in swelling over that from helium injection alone that peaks between 450 and 500°C. Electron energy loss spectroscopy (EELS) elemental mapping revealed hydrogen forming a halo-like structure about the periphery of the cavities and helium residing within the cavities themselves. This observation suggests that hydrogen reduces the surface energy of helium-filled cavities which results in both increased cavity number density and cavity size in triple beam irradiation over dual beam irradiation.

PROGRESS AND STATUS

To determine the effects of beam composition, that is, the individual levels of H and He injection, a series of single, dual, and triple ion irradiations were conducted at 500°C to 50 dpa at $1x10^{-3}$ dpa/s. A visual comparison of the evolution in cavity microstructures across each alloy and irradiation condition is shown in the STEM-HAADF images in Figure 1, from which several clear distinctions can be made. In the case of single ion irradiation, most cavities were observed within the first ~300 nm of the material, likely due to the oversaturation of vacancies near the sample surface due to loss of interstitials, promoting their growth. There were very few resolvable cavities within the depth region of interest for this condition, however, in the CNA3 (~43 nm at ~$4x10^{18}$ m^{-3}) and Fe8Cr2W (~24 nm at ~$5x10^{19}$ m^{-3}) alloys, some large cavities were measured leading to observed swelling values of 0.02% and 0.39% in those alloys, respectively. In the dual beam (Fe + H) case, low densities of cavities were observed in F82H (~23 nm at ~$3x10^{19}$ m^{-3}) and Fe8Cr2W (~62 nm at ~$3x10^{19}$ m^{-3}) at much larger sizes than those in the single ion irradiated case, resulting in respective swelling values of 0.044% and 0.716% for each alloy.

Unlike the single and dual (Fe + H) conditions, the dual (Fe + He) and triple ion irradiated samples exhibited much higher cavity densities, on the order of 100x higher across all three alloys. Cavities from diameters as low as <1 nm to as large as 40 nm were measured via TEM-BF and STEM-HAADF in both irradiation conditions involving He injection. For the purposes of differentiation, the small cavities (<5nm) of highest density will be referred to as bubbles while those larger cavities (>5nm) or lower densities will be referred to as voids. The cavity size distributions (Figure 2) for the dual/triple beam irradiated alloys were qualitatively similar although the triple beam irradiated case was observed to have significantly higher densities of both smaller bubbles (<3nm) and larger voids (>20nm), the latter being more responsible for the swelling difference of 0.72% for dual and 0.93% for triple ion irradiation for F82H, although the results for this alloy

are within error bars. The increase in total swelling between dual and triple ion irradiation seemed to be more apparent in the CNA3 (0.46% to 1.6%) and Fe8Cr2W (1.03% to 2.14%) alloys.

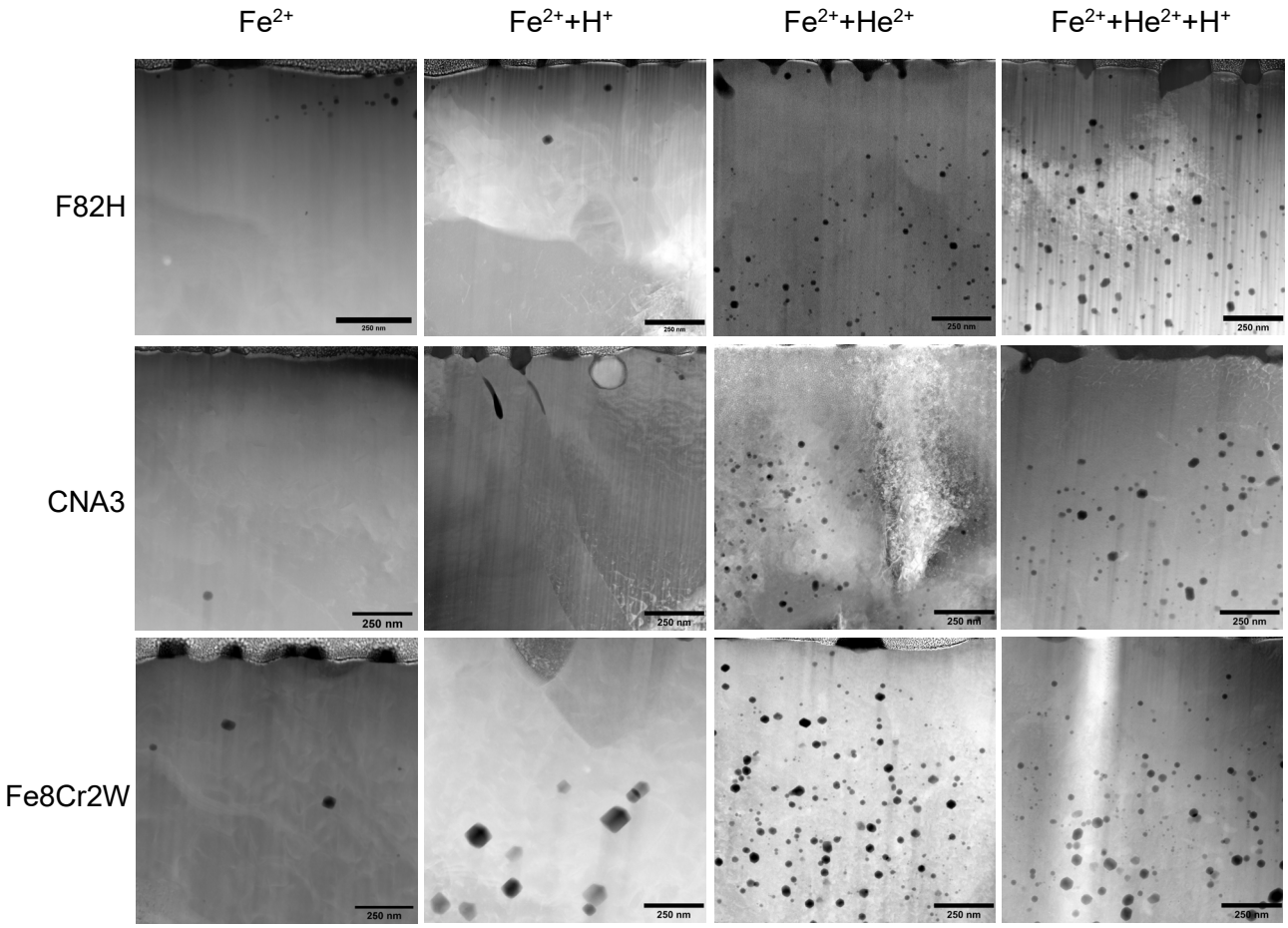

Figure 1. HAADF images of cavities in single beam, dual beam (Fe^{2+}+H^{+}, Fe^{2+}+He^{2+}) and triple beam (Fe^{2+}+He^{2+}+H^{+}) irradiated F82H, CNA3, and Fe8Cr2W at 500°C.

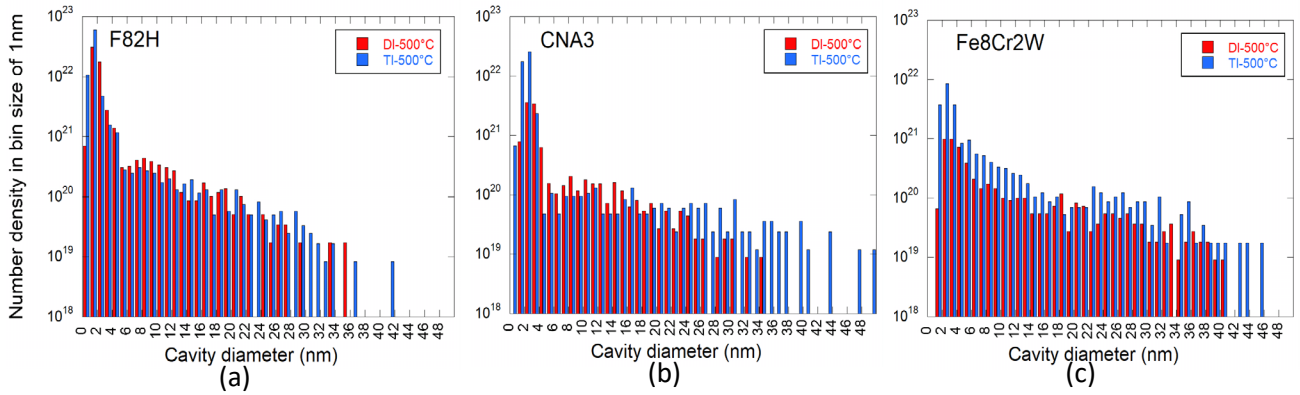

Figure 2. Comparison of cavity size distribution in dual beam and triple beam irradiated (a) F82H, (b) Fe8Cr2W and (c) CNA3 alloys at 500°C.

To determine the location of hydrogen in the irradiated microstructure of triple ion irradiated RAFM steels, a series of EELS scans were taken in very thin regions of Fe8Cr2W samples irradiated at 450°C to 50 dpa and 80/10 appm/dpa of D/He to provide 2D elemental maps of hydrogen and helium around cavities. These elemental maps are shown for two adjoined cavities each of ~15-20 nm in diameter, in Figure 3. The H-K signal appears to form a shell-like structure around the outside of the cavities while the He-K signal appears to reside mainly within the center of the cavity. A comparison of the raw EELS spectra and the PCA recombined spectra for this entire region of interest is shown in Figure 4.

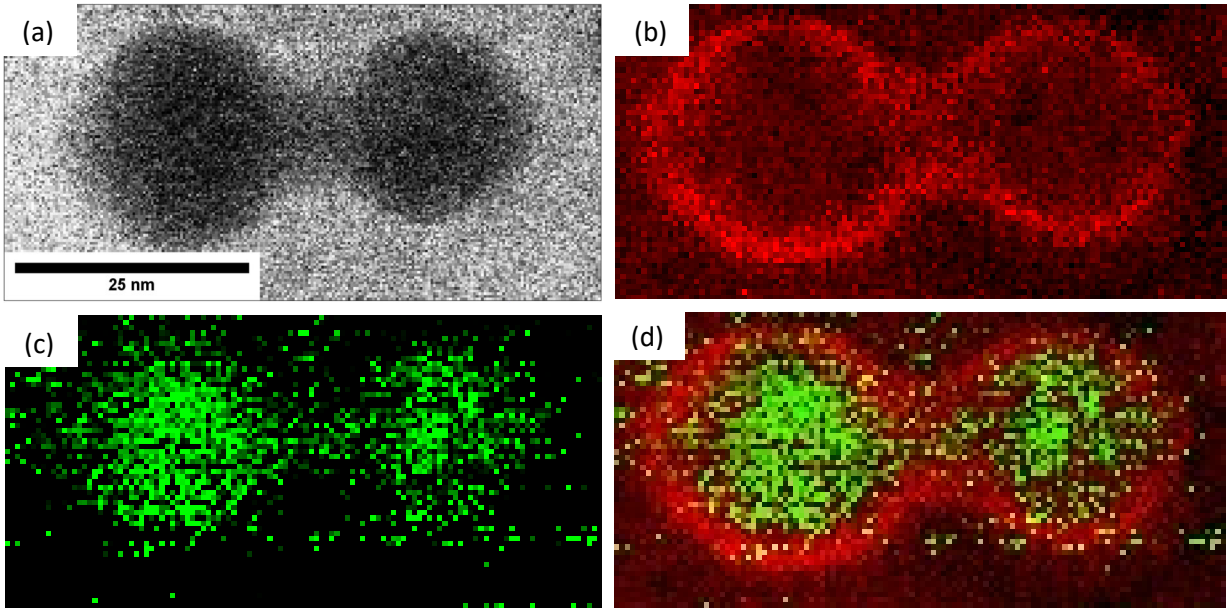

Figure 3. (a) STEM-HAADF image of cavities in triple ion irradiated Fe8Cr2W, EELS spectral map integrated for the (b) H-K peak (11-14 eV) and (c) He-K peak (21-24 eV), and (d) composite of H-K and He-K EELS spectral maps.

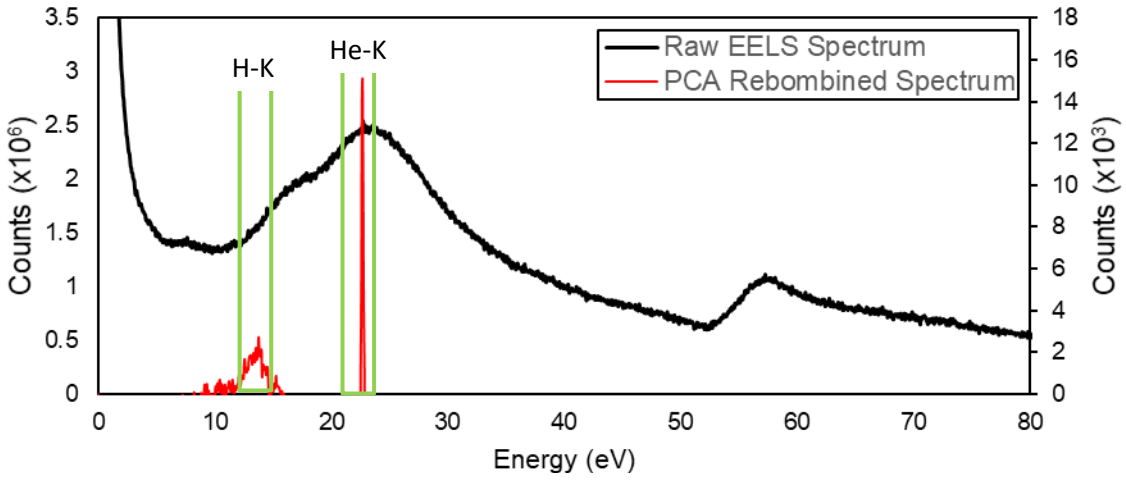

Figure 4. Raw EELS spectrum and PCA recombined EELS spectrum from region of interest containing cavities showing the extracted H-K and He-K edges with the ranges of spectrum integration marked accordingly for H and He.

Given that swelling is consistently higher in triple beam irradiation vs. dual beam, the question then becomes; what is the mechanism by which hydrogen enhances swelling? Explanations for the observed effect of hydrogen on swelling vary considerably, in part due to the conflicting behaviors observed in these studies. In cases where H was observed to result in higher swelling, it has been proposed that the effect of hydrogen may be to reduce the critical cavity size, increase the number of small cavities, accelerate the bias driven cavity growth of helium bubbles, or change the diffusion bias for vacancy accumulation. An increase in cavity density coupled with a reduction in critical cavity size would increase the promotion of bubbles to cavities and result in higher swelling. However, an enhancement of bubble density without a decrease in critical cavity size would suppress swelling by increasing the sink strength [1]. These observations also must be evaluated in light of recent work by *Kohnert et al.* [2] who showed a strong bias for single interstitial atom (SIA) absorption by small voids that can be alleviated in over-pressurized gas bubbles.

While *Garner et al.* [3] postulated that bubbles in stainless steels irradiated in a PWR, FFTF and HFIR contained hydrogen stored in the form of H_2 gas. *Hayward and Deo* found no evidence of direction interaction between He and H bubbles [4] . Rather, they found that H is attracted to the stress fields created by pressurized bubbles and in doing so, stabilizes the cavities. Clusters of all sizes have the same structure consisting of a core of helium surrounded by a shell of hydrogen atoms. *Farrell and Lee* [5] postulated that H could facilitate helium bubble nucleation by reducing the surface energy. Since the critical bubble size (according to the critical bubble model) is proportional to the surface energy, any reduction in surface energy will produce a commensurate reduction in the critical bubble size. Their assertion that H is trapped at bubble interfaces is supported by measurements of de-trapping of deuterium from an iron sample containing He clusters. *Myers et al*. [6] conducted de-trapping experiments on D in He-implanted Fe and found a de-trapping enthalpy of 0.75 eV. This measurement is supported by those of *Hirth* [7] who calculated the energy for chemisorption of H on an internal free surface to be 0.73 eV. *Abramov and Eliezer* [8] considered that hydrogen is attracted to helium-filled bubbles by the tensile stress around the bubble. From this model they calculated the trapping energy between H atoms, and He bubbles to be 0.71eV. That hydrogen trapping is due to the stress field around a bubble is also supported by the observation of *Takahashi et al.* [9], who showed via APT that deuterium in steel is trapped only at semi-coherent VC platelets with misfit dislocation cores. The increase in cavity density among alloy three alloys at 500°C is an indication that hydrogen may stabilize small He-V clusters. The increase in cavity diameter indicates easier growth, resulting in increased swelling for all three alloys.

The EELS mapping results in Figure 3 appear to show the presence of helium at the core of the cavity, as is generally expected to be the mechanism by which bubbles/cavities form and grow through direction interaction between vacancies and matrix insoluble He atoms, while hydrogen appears to be present as a shell, or halo, around the cavity itself. This has also been observed with similar techniques by *Judge, et al.* [10] and *Zimber, et al.* [11] in their investigations of the interactions between hydrogen and helium bubbles in irradiated X-750 Ni base alloys and Eurofer-97 RAFM steel, respectively. Judge asserts that, if hydrogen is truly at the surface of bubbles, it may be lowering the interfacial surface tension of the nickel matrix around the bubble [10]. By lowering the surface energy around the bubble, it will then alter the He-V ratio necessary to form stable bubbles in the alloy.

The temperature dependence of the H effect must also be considered. The F82H alloy shows a swelling peak at intermediate temperature and a drop off at high temperature, similar to the Fe-12Cr alloy in ref. [12]. The striking difference between dual and triple beam irradiations is in the cavity number density. While the number density falls off with temperature in the dual ion irradiation case, it remains essentially unchanged in the triple beam case. While it has been postulated that at high temperature, hydrogen diffuses too quickly to interact with these clusters [13], the data appears to indicate otherwise even when at 600°C cavities are mostly confined to the grain boundaries resulting in significantly reduced swelling. In fact, detrapping of hydrogen from a cavity surface is expected to occur by 327°C [6,7]. The observation of hydrogen at cavity surfaces in a 500°C irradiation (Figure 3) may be explained by the attraction of both H and He to vacancies as noted by Ortiz [14] and Marian [13]. That is, the combination of H trapping by the stress field of the He-filled cavity surface combined with the stability of V-He-H clusters may explain why H remains at these locations above the detrapping temperature. While more measurements and modeling need to be done, these results lend support to the role of hydrogen in reducing surface energy to enhance bubble nucleation as well as growth.

Future Work

Further experiments are planned that include dual ion irradiation (Fe^{2+} + H^{+}) at 500°C and additional temperatures and H/He concentrations. Irradiation experiments are also being designed to isolate the role of hydrogen. The future characterization will help understand the role of hydrogen in cavity swelling. Thus far, the significant role of hydrogen in swelling has not been confirmed.

References

[1] R.E. Stoller, G.R. Odette, Analytical solutions for helium bubble and critical radius parameters using a hard sphere equation of state, J. Nucl. Mater. 131 (1985) 118–125. https://doi.org/10.1016/0022-3115(85)90450-7.

[2] A.A. Kohnert, M.A. Cusentino, B.D. Wirth, Molecular statics calculations of the biases and point defect capture volumes of small cavities, J. Nucl. Mater. 499 (2018) 480–489. https://doi.org/10.1016/j.jnucmat.2017.12.005.

[3] F.A. Garner, E.P. Simonen, B.M. Oliver, L.R. Greenwood, M.L. Grossbeck, W.G. Wolfer, P.M. Scott, Retention of hydrogen in fcc metals irradiated at temperatures leading to high densities of bubbles or voids, J. Nucl. Mater. 356 (2006) 122–135. https://doi.org/10.1016/j.jnucmat.2006.05.023.

[4] E. Hayward, C. Deo, Synergistic effects in hydrogen–helium bubbles, J. Phys. Condens. Matter. 24 (2012) 265402. https://doi.org/10.1088/0953-8984/24/26/265402.

[5] K. Farrell, E.H. Lee, Ion Damage in a Fe-10Cr-6Mo-0.5Nb Ferritic Steel, Radiation-Induced Chang. Microstruct. 13th Int. Symp. (1987) 498–507. https://doi.org/10.1520/STP33839S.

[6] S.M. Myers, F. Besenbacher, J. Bottiger, Deuterium in He-implanted Fe: Trapping and the surface permeation barrier, Appl. Phys. Lett. 39 (1981) 450–452. https://doi.org/10.1063/1.92735.

[7] J.P. Hirth, Effects of hydrogen on the properties of iron and steel, Metall. Trans. A. 11 (1980) 861–890. https://doi.org/10.1007/BF02654700.

[8] E. Abramov, D. Eliezer, Trapping of hydrogen in helium-implanted metals, J. Mater. Sci. Lett. 7 (1988) 108–110. https://doi.org/10.1007/BF01730586.

[9] J. Takahashi, K. Kawakami, T. Tarui, Direct observation of hydrogen-trapping sites in vanadium carbide precipitation steel by atom probe tomography, Scr. Mater. 67 (2012) 213–216. https://doi.org/10.1016/j.scriptamat.2012.04.022.

[10] C.D. Judge, H. Rajakumar, A. Korinek, G.A. Bickel, On the Potential Synergies of Helium and Hydrogen on the Nucleation and Stability of Cavity Clusters in Inconel X-750® Irradiated in a High Thermal Neutron Flux Spectra, in: 19th Int. Conf. Environ. Degrad. Mater. Nucl. Power Syst. - Water React. EnvDeg 2019, 2019: pp. 688–694. https://doi.org/10.18699/gpb2020-66.

[11] N. Zimber, P. Vladimirov, M. Klimenkov, U. Jäntsch, R. Vila, V. Chakin, F. Mota, Microstructural evolution of three potential fusion candidate steels under ion-irradiation, J. Nucl. Mater. 535 (2020). https://doi.org/10.1016/j.jnucmat.2020.152160.

[12] M. Ando, E. Wakai, T. Sawai, H. Tanigawa, K. Furuya, S. Jitsukawa, H. Takeuchi, K. Oka, S. Ohnuki, A. Kohyama, Synergistic effect of displacement damage and helium atoms on radiation hardening in F82H at TIARA facility, J. Nucl. Mater. 329–333 (2004) 1137–1141. https://doi.org/10.1016/j.jnucmat.2004.04.290.

[13] J. Marian, T. Hoang, M. Fluss, L.L. Hsiung, A review of helium-hydrogen synergistic effects in radiation damage observed in fusion energy steels and an interaction model to guide future understanding, J. Nucl. Mater. 462 (2015) 409–421. https://doi.org/10.1016/j.jnucmat.2014.12.046.

[14] C.J. Ortiz, R. Vila, J.M. Pruneda, Ab initio study of helium and hydrogen interactions in α -Fe, (2018) 1–5.

6.5 TENSILE PROPERTIES OF HFIR IRRADIATED F82H VARIANTS AND ODS STEELS SHOW IRRADIATION HARDENING AND LOSS OF DUCTILITY—A. Bhattacharya, J. Reed, D.T. Hoelzer, J.W. Geringer (Oak Ridge National Laboratory), H. Tanigawa, T. Nozawa (QST), S.M. Levine, S.J. Zinkle (University of Tennessee)

OBJECTIVE

Different variants of F82H steel, such as F82H-IEA, mod3, BA12 and ODS steels (MA957, 12YWT, PM2000) were neutron irradiated in numerous HFIR irradiation experiments in collaboration with QST. These irradiation experiments include RB19J, RB15J, JP26, JP27, JP29, F8B2 and F11B3. Previously, Vickers hardness data on these steels was reported. Here, results from the tensile tests at room temperature (RT) and irradiation temperature (T_{irr}) for these alloys are presented. The irradiations were performed in HFIR on SS-J3 type flat tensile samples, with doses ranging between ~3.5 to ~75 dpa at target irradiation temperatures of 300, 400 and 500 °C. This report details the dose and temperature dependent hardening and loss of ductility of the studied materials. It should be noted that the MA957 is from Plansee, 12YWT is from Kobelco and PM2000 is also from Plansee.

SUMMARY

Tensile tests were completed on F82H-IEA, F82H-mod3 and F82H-BA12 that were irradiated in HFIR in RB19J, JP29, RB15J, F8B2 and F11B3 irradiation experiments (~3.5 to ~75 dpa, target T_{irr} = 300 °C). Moreover, 14% Cr base MA957, 12% Cr base 12YWT and 18% Cr-5.5%Al base PM2000 from JP26 and JP27 experiments were also characterized (4.5 - 13.1 dpa, T_{irr} = 300, 450 and 500 °C). This report summarizes the uniaxial properties of the tested steels after irradiation and quantifies the irradiation hardening/loss of ductility behavior of the different steels. The results show significant increase in yield stress and loss of tensile ductility due to irradiation in all the F82H variants. The behavior of B12 is like IEA heat, while the high dose results show no significant difference between hardening in IEA and mod3 variants – suggesting all these steels behave similarly in terms of uniaxial properties. The report also shows significant irradiation hardening in ODS steels detected up to 450-500 °C, which might emerge as a design challenge for the first-wall/blanket that target ODS steels in future fusion devices. The results validate previously reported Vickers hardness data on the HFIR irradiated ODS steels showing hardening in this class of materials up to high irradiation temperatures, where RAFM steels do not show much hardening (T_{irr} > 350-400 °C). The results suggest different underlying irradiation damage mechanisms might be operating in the high Cr based ODS steels compared to RAFM steels.

PROGRESS AND STATUS

Numerous F82H steel variants and ODS alloys were neutron irradiated at ORNL in various irradiation experiments to map the dose-temperature dependent irradiation behavior of these materials. Here, irradiated tensile properties are summarized. Uniaxial tensile tests were performed in the hot cells at RT and 300°C with guidance from ASTM E8 Standard Test Methods for Tension Testing of Metallic Materials and ASTM E21 Standard Test Methods for Elevated Temperature Tension Tests of Metallic Materials using a strain rate of 10^{-3} s^{-1} (5×10^{-3} mm/s extension rate). The tangent modulus method was used to provide accurate values for the yield strength (σ_{YS}), uniform plastic elongation (UEp) and total plastic elongation (TEp) in the absence of gauge extensometry for miniature tensile samples. The specimens were shoulder loaded for testing using an Instron 5967 tensile machine equipped with a 5 kN load cell and connected with an Instron Bluehill3 analysis software. RT tests were performed in air. Elevated temperature tests were performed in vacuum at pressures ≤5×10^{-6} torr. For tensile tests at 300 °C, the temperatures were measured using two thermo-couples welded onto the fixture. The temperature ramp-up time from room to test temperature was typically between ~25–30 min. The tests were performed only when the sample temperature stabilized to the set-point of 300±5°C. Table 1 summarizes the result of the tests.

Table 1. Summary of the irradiated tensile properties of F82H steel variants and ODS steels. The target temperatures of one of the JP26 experiments was 400 °C but SiC thermometry data shows capsules were at 450 °C (latter is taken as the irradiation temperature). These values are highlighted in red in the table below. T_{irr} = irradiation temperature, T_{test} = tensile test temperature, σ_{YS} = yield stress, σ_{UTS} = ultimate tensile stress, UE_p = uniform plastic elongation, TE_p = total plastic elongation, σ_{UTS}/σ_{YS} = strain hardening ratio figure-of-merit. For F82H, the doses below represent the target capsule design values.

Experiment	Material	IDs	Target dose (dpa)	T_{irr} (°C)	T_{test} (°C)	σ_{YS} (Mpa)	σ_{UTS} (Mpa)	UE_p (%)		TE_p (%)	σ_{UTS}/σ_{YS} ratio
RB15J	F82H-IEA	OX1	4.5	300	300	752	766	0.30		11.20	1.02
RB15J	F82H-IEA	OX2	4.5	300	300	732	736	0.08		10.10	1.01
F8B2	F82H-IEA	OXM	50	300	300	950	978	0.50		8.60	1.03
F8B2	F82H-IEA	OXN	50	300	300	965.2	973	0.60		6.60	1.01
JP29	F82H-IEA	O64	~75	300	300	862.	880	0.40		7.80	1.02
JP29	F82H-IEA	O65	~75	300	300	880	888	0.20		8.20	1.01
F11B3	F82H-IEA	O92	20	300	300	832	871	0.60		9.20	1.05
F11B3	F82H-IEA	O91	20	300	24	1011	1026	0.50		9.20	1.01
JP29	F82H-mod3	H64	~75	300	300	865	871	0.20		10.20	1.01
JP29	F82H-mod3	H65	~75	300	300	897	904	0.30		10.40	1.01
RB19J	F82H-BA12	TV66	2.5	300	300	738	744	0.70		12.00	1.01
RB19J	F82H-BA12	TV67	2.5	300	300	729	744	1.00		12.00	1.02
JP26	12YWT	ZP01	4.5	300	24	1537	1582	0.50		9.50	1.03
JP26	12YWT	ZP10	5.5	450	24	1492	1572	0.50		8.80	1.05
JP26	12YWT	ZP21	8.7	500	24	1384	1408	0.40		12.70	1.02
JP27	12YWT	ZP30	13.1	300	24	1530	1540	0.60		4.40	1.01
JP26	MA957	ZQ01	4.5	300	24	1210	1260	8.50		14.60	1.04
JP26	MA957	ZQ10	5.5	450	24	1241	1261	6.10		12.50	1.02
JP26	MA957	ZQ21	8.7	500	24	1081	1126	8.80		18.80	1.04
JP27	MA957	ZQ30	13.1	300	24	1285	1345	8.40		15.50	1.05
JP26	PM2000	ZR21	8.7	500	24	879	890	0.08		2.20	1.01

Experimental Procedure

Comparing dose dependent hardening in F82H variants and ODS alloys for T_{irr} ~ 300 °C

A compilation of dose dependent σ_{YS} is shown in Figure1 for all the F82H variants and ODS steels tested in this study. For F82H-IEA, irradiation hardening increases sharply with dose and saturates for doses > ~15-20 dpa. The comparison of mod3 and F82H results at high doses suggest no major differences in the σ_{YS} of these two alloys – implying hardening behavior between these variants is likely similar despite different starting metallurgical and processing conditions. The results also compare the newer F82H heat, BA12, that was irradiated in the RB15J capsules. At low doses (< 5 dpa), the σ_{YS} of both IEA and BA12 is very similar – implying no major differences in irradiation hardening behavior between these two variants.

Figure 1 also shows σ_{YS} of HFIR irradiated 12YWT and MA957. These two alloys show significant irradiation hardening upon irradiation. For MA957, hardening seems to continuously increase with doses up to ~13.1 dpa, while 12YWT seems to show saturation already between 4.5 -13.1 dpa. High dose data is needed to identify the saturation hardening doses for these two materials. It should be noted that the MA957 alloy irradiated at HFIR were tensile samples extracted along the extrusion direction from tubes. Figure 1 compares the MA957 results from HFIR with previous research on bar type samples after irradiations in OSIRIS and BOR60 reactors where some differences between their hardening behavior can be seen. Although this difference is likely due to test temperature effects on measured irradiation hardening – HFIR samples were tested at RT while BOR60/OSIRIS samples were tensile tested at T_{irr}.

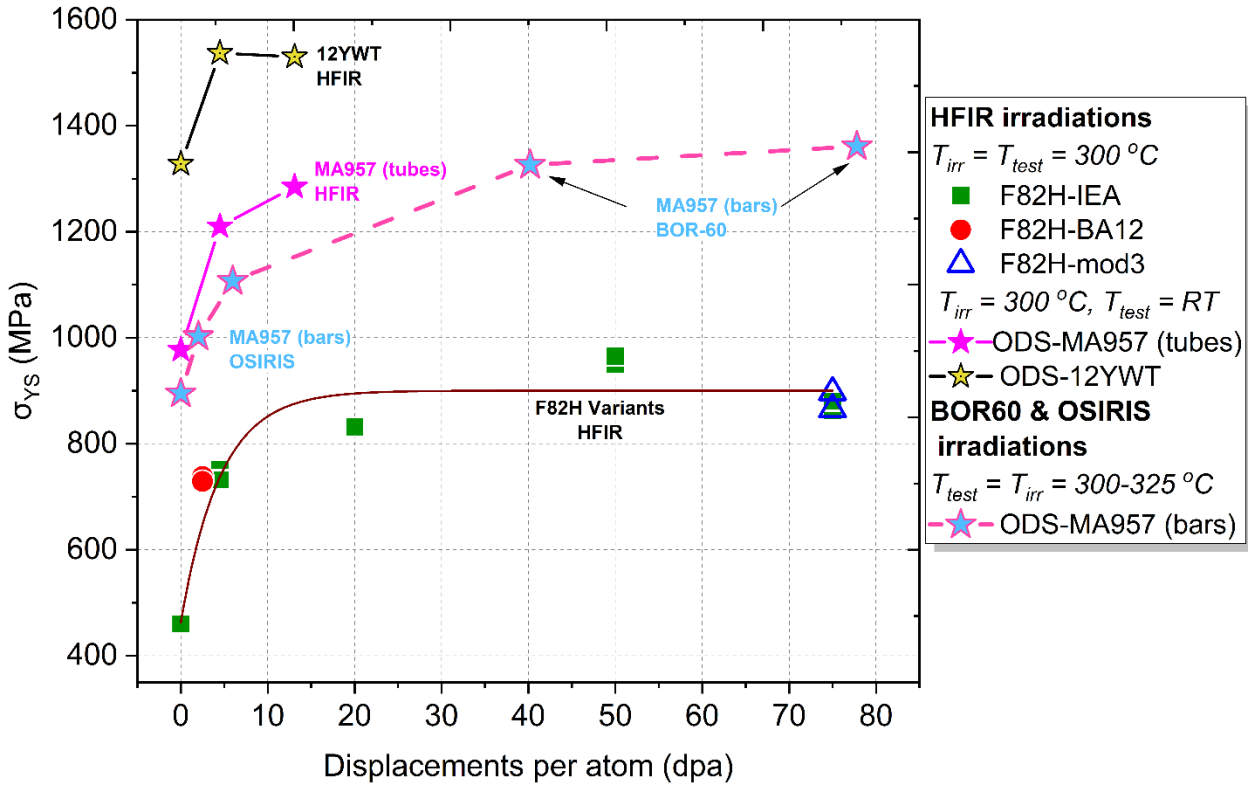

Figure 1. Dose dependent yield stress in F82H steel variants (IEA, BA12 and mod3), and ODS steels (MA957, 12YWT) after HFIR neutron irradiations at 300 °C. Literature results on MA957 are also plotted, with data taken from Refs. [1,2].

Figure 2 presents the dose dependent ductility (UEp and TEp). For All the F82H variants, there is a significant reduction of UEp – which is well known to occur in RAFM steels. The UEp decreases sharply with dose and then saturates at values mostly lower than ~0.5-0.6%. The TEp remained higher, between 8-12% - further highlighting that the primary ductility remaining in RAFM steels after neutron irradiation is necking ductility as previously shown for other RAFM steels such as Eurofer97 [3]. Because of the extremely low UEp remaining in the F82H variants, the strain hardening figure of merit (σ_{UTS}/σ_{YS}) decreases sharply with irradiation – which remains as a critical challenge for first-wall/blanket designing.

For ODS steels, the elongation properties were vastly material dependent. The 12YWT alloy behaved very similar to RAFM steels, showing an initial sharp loss in UEp and thereafter a tendency to saturate around ~0.4-0.6%. However, TEp of 12YWT seems to reduce continually with dose at least till ~13.1 dpa, with values much lower than those measured for RAFM steels. For 14%Cr based MA957, the ductility was remarkably better than RAFM steels and 12YWT after irradiation. Initially, there is irradiation induced reduction of both UEp and TEp. However, the UEp remains higher than 8% for doses as high as 13.1 dpa. The UEp seems to saturate at such high values between ~4.5 to 13.1 dpa. The ductility of MA957 after irradiation in HFIR are compared with literature data after irradiations in OSIRIS and BOR60 reactors. The behavior is material dependent: overall the samples from MA957 tubes irradiated in HFIR performed better than samples taken from bars that were irradiated in BOR60/OSIRIS. For the bar type specimens, the UEp is still higher than typical values for RAFM steels like F82H. It should be noted that for all three neutron irradiation experiments (HFIR, BOR60 and OSIRIS), the samples were machined along the extrusion direction implying this was the best-case scenario for tensile ductility. In ODS alloys, properties can be direction dependent, and it is likely the behavior may be different if samples perpendicular to the direction of extrusion were extracted.

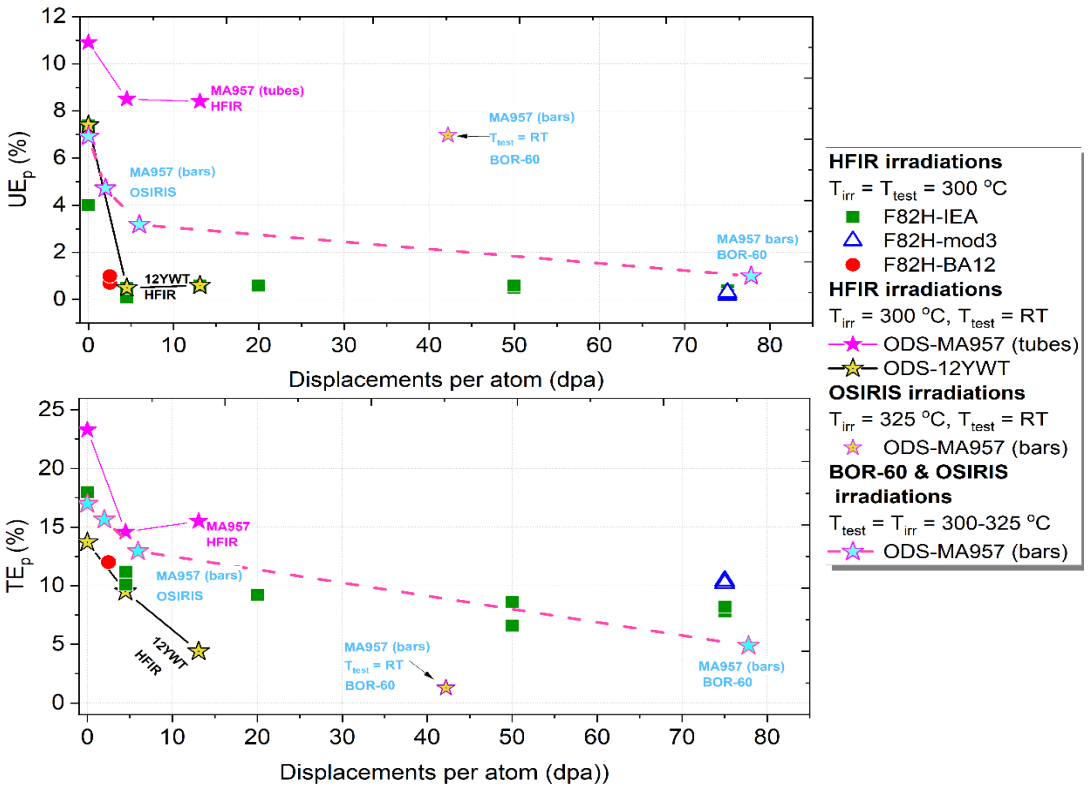

Figure 2. Dose dependent loss in uniform and total plastic elongations in F82H steel variants (IEA, BA12 and mod3), and ODS steels (MA957, 12YWT) after 300 °C HFIR neutron irradiations. Literature results on MA957 is also plotted, with data taken from Refs. [1,2].

Effect of irradiation temperature on irradiation hardening

The MA957, 12YWT and PM2000 were also neutron irradiated at 450 and 500 °C in the JP26/27 irradiation experiments. For the target 400 °C irradiations, the actual temperature estimated using SiC thermometry was ~450 °C. The raw hardness data reported previously [5] is re-compiled in Figure 3 and now compared with literature in various RAFM steels [5,6]. The results suggest hardening in ODS steels up to high temperatures of 450 and 500 °C – which required validation with tensile testing.

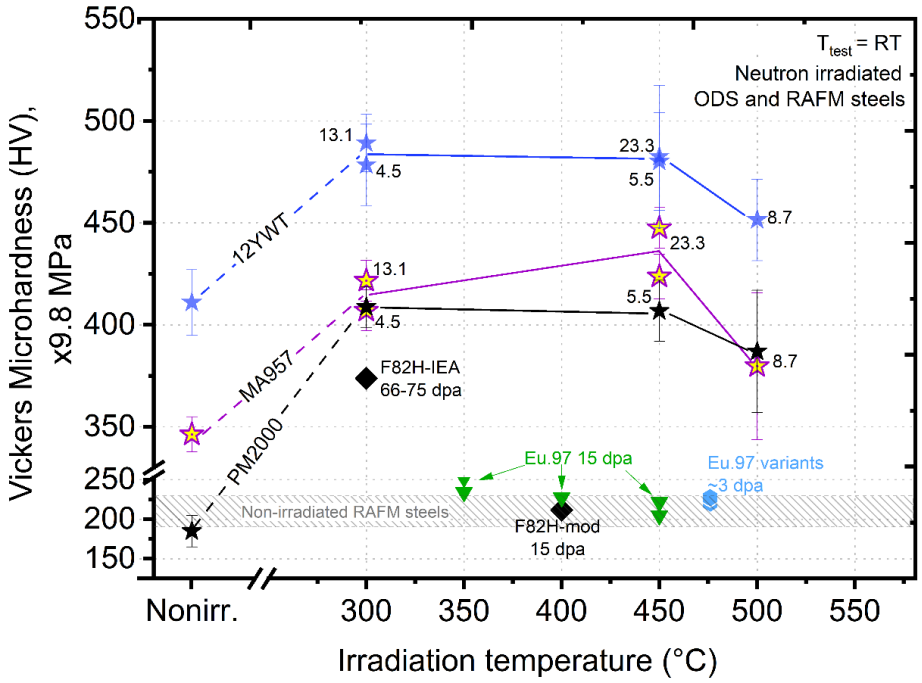

Figure 3. Compilation of temperature dependent irradiation hardening in HFIR irradiated ODS steels and compared with RAFM steels from literature. Literature data taken from Refs. [5,6].

To complete the T_{irr} dependent mechanical property analysis, tensile tests were performed on the HFIR irradiated ODS steels that were previously tested for hardness. Figure 4 compiles the measured irradiation hardening, taken as the difference between nonirradiated and irradiated σ_{YS} of the ODS alloys and compares their properties to RAFM steels data in literature. The results in ODS steels are fully consistent with Vickers hardness – that there is significant irradiation hardening in MA957 and 12YWT alloys at high temperatures. Between 300 and 450 °C, there is not much recovery in hardening behavior. At 500 °C, there is reduction in hardening, but it's not completely recovered. This is a remarkable observation because for temperatures as high as 450-500 °C, irradiation hardening is not a major problem for RAFM steels (as shown in Figure 4). In fact, at such high temperatures, RAFM steels may often show softening. Similar results are reported in literature for low dose (0.01-0.75 dpa) JMTR irradiated Fe-Cr and Fe-Cr-Al based ODS steels [7]. The combined HFIR and JMTR results highlight that ODS steels with Cr concentrations > 12 wt.% will continue to harden profusely for temperatures as high as ~450 °C, and higher temperatures will be needed to suppress this problem. Because hardening is directly related to degradation in fracture toughness, continued hardening up to high temperatures may pose a challenge to fusion first-wall/blanket designing with ODS alloys. Figure 4 shows that the 12YWT alloy, which has lower Cr concentration as compared to MA957, shows lower hardening. This is expected because lower Cr level implies lower fraction of embrittling Cr rich α' phase formation in this alloy.

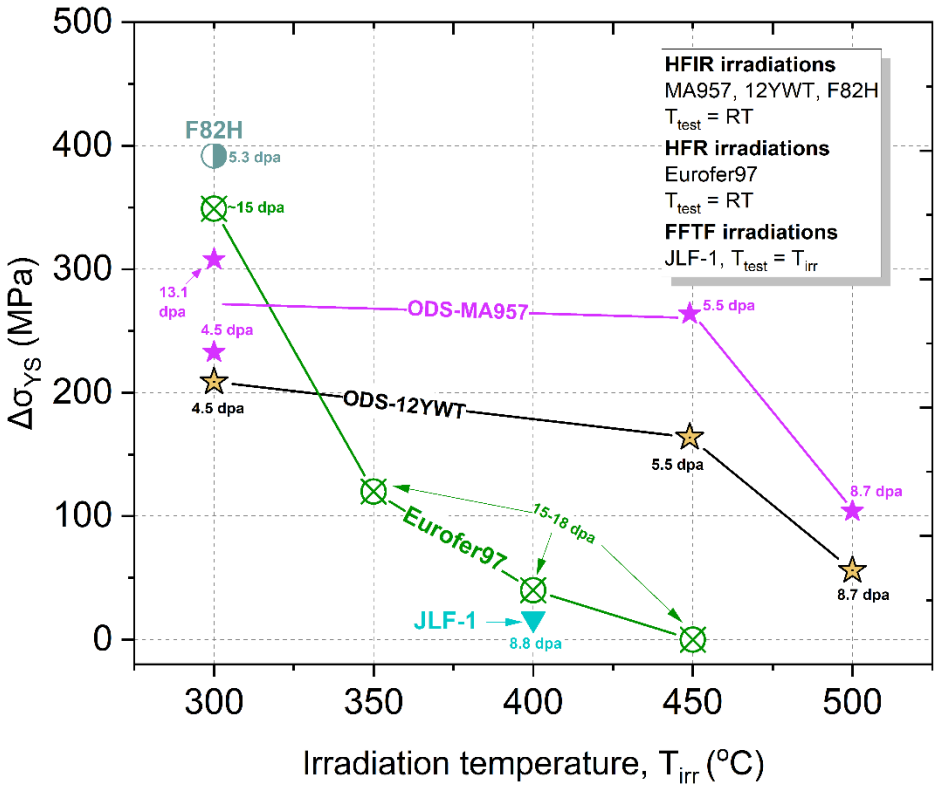

Figure 4. Temperature dependent irradiation hardening in HFIR irradiated ODS steels compared with literature on RAFM steels. Literature data taken from Refs. [5,6].

Future Work

The APT data sets were collected from all the HFIR irradiated ODS steels. Their data analysis is ongoing. STEM investigation will also be performed to holistically develop structure-property relationship of the HIFR irradiated ODS steels.

References

[1] J. Henry, X. Averty, A. Alamo, Tensile and impact properties of 9Cr tempered martensitic steels and ODS-FeCr alloys irradiated in a fast reactor at 325 C up to 78 dpa, J. Nucl. Mater. 417 (2011) 99-103.
[2] A. Alamo, J.L. Bertin, V.K. Shamardin, P. Wident Mechanical properties of 9Cr martensitic steels and ODS-FeCr alloys after neutron irradiation at 325 C up to 42 dpa. J. Nucl. Mater. 367-370 (2007) 54-59.
[3] A. Bhattacharya, X. Chen et al. Irradiation hardening and ductility loss of Eurofer97 steel variants after neutron irradiation to ITER-TBM relevant conditions, Fus. Eng. Des. 173 (2021) 112935.
[4] A. Bhattacharya, J. Reed, X. Chen, J.W. Geringer, Y. Katoh, T. Nozawa and H. Tanigawa *Neutron irradiation induced hardening in RAFM and ODS steels, Fusion Reactor Materials Program Semi-Annual Report, DOE/ER-0313/69 (2020).*
[5] X. Chen, L. Clowers et al. Post-irradiation evaluation of eurofer97 fracture toughness using miniature multinotch bend bar specimens *American Society of Mechanical Engineers, Pressure Vessels and Piping Division (Publication) PVP* vol 1 pp 1–8 (2020).
[6] I. Sacksteder , H.-C. Schneider and E. Materna-Morris, Determining irradiation damage and recovery by instrumented indentation in RAFM steel , *J. Nucl. Mater.* 417 (2011) 127–30.
[7] H.S. Cho, R. Kasada, A. Kimura, Effects of neutron irradiation on the tensile properties of high-Cr oxide dispersion strengthened ferritic steels, J. Nucl. Mater. 367-370 (2007) 239-243.

7. PLASMA-MATERIAL INTERACTIONS

No contributions this reporting period.

8. CORROSION AND COMPATIBILITY IN FUSION SYSTEMS

8.1 LIQUID METAL COMPATIBILITY OF PRE-OXIDIZED FeCrAl IN FLOWING Sn—B. A. Pint, M. Romedenne (Oak Ridge National Laboratory)

OBJECTIVE

The goal of this research was to investigate the compatibility of liquid Sn with FeCrAl alloys and the viability of a thermally grown alumina scale to prevent dissolution and mass transfer. A thermal convection loop (TCL) was fabricated from a commercial FeCrAlMo alloy and pre-oxidized specimens of this alloy and two ODS FeCrAl alloys were exposed in the flow path with a peak temperature of 400°C.

SUMMARY

This first TCL experiment with liquid Sn completed 1000 h with a peak temperature of 400°C and additional characterization is reported from the FeCrAlMo (Kanthal alloy APMT) and ODS FeCrAl specimens exposed in APMT tubing. The mass losses in the hot leg were relatively high and the observed pitting suggests that localized failure of the preformed surface oxide caused metal loss. Post exposure room temperature tensile testing showed limited impact of the Sn exposure on the 12Cr ODS FeCrAl alloy, comparable to a 1000 h anneal at 400°C.

PROGRESS AND STATUS

Introduction

An assessment of candidate liquid metals for plasma-facing components down selected Sn as an attractive candidate for further study because of its low vapor pressure [1]. However, Sn is very corrosive to most structural alloys [2]. To improve liquid metal compatibility, one strategy that has been used with Pb-17at.%Li is to form a stable, adherent surface oxide such as α-Al_2O_3 on FeCrAl alloys or using an Al-rich coating on steels [3-8] to prevent direct contact between the structural alloy and the liquid. This strategy has shown very promising results for Pb-Li and static testing was initiated in Sn. Initial screening used Sn in Mo capsules for 1000 h at 400°C [8]. As expected, a large mass loss (368 mg/cm^2) was observed for a reduced activation ferritic-martensitic (RAFM) F82H steel specimen exposed to high purity Sn. In contrast, the mass loss was much lower for APMT (composition in Table 1) specimens with almost no mass change for the specimen pre-oxidized for 2h at 1000°C to form an external alumina scale [7,8]. A similar small mass change was observed for pre-oxidized APMT specimens after capsule testing at 500°C for 1000 and 2000 h. To complete the Sn compatibility assessment, a thermal convection loop (TCL) made of APMT has been fabricated and coupon and tensile specimens of APMT and two ODS Fe-(10-12)Cr-6Al+Zr alloys were included in the hot and cold legs of the TCL in a ~55°C temperature gradient with a peak temperature of 400°C. The TCL experiment was completed, and initial characterization was previously presented [9] as part of Task 3 in the Japan-US FRONTIER program. This report updates the post-exposure examination.

Table 1. Alloy compositions measured using inductively coupled plasma and combustion analyses

Alloy	Fe	Cr	Al	Ni	Si	C	Other
APMT	69.0	21.6	4.9	0.12	0.53	0.03	2.8Mo,0.1Mn,0.2Hf,0.1Y,0.1Zr
APMT tube*	70.0	21.4	4.9		0.34	0.04	3.1Mo, 0.2Mn, 0.02Cu
ODS FeCrAl†	83.6	9.8	6.0			0.06	0.22Y,0.27Zr,0.10O,0.04N
ODS FeCrAl	80.8	11.6	6.2	0.03	0.02	0.03	0.39Zr, 0.38Y, 0.49Ti, 0.02Mn

* reported by manufacturer [6] † heat 4H795C

Experimental Procedure

This TCL experiment followed similar procedures as detailed previously [6-11]. Chains of 20 specimens were exposed in the hot leg (HL) and cold leg (CL) of the TCL for 1000 h with a peak hot leg temperature of 400°C. Coupon specimens were 15 x 25 x 2 mm, and the tensile specimens were 25 mm long SS-3 type and alternated between APMT and two different ODS alloys [12,13] with low-Cr to avoid issues with α' embrittlement. Chemical compositions of the three alloys and APMT tubing are given in Table 1. All the specimens were pre-oxidized for 2 h at 1000°C in laboratory air [7,8]. The APMT loop was pre-oxidized for 8 h at 1050°C, as part of the standard heat treatment [6]. After the exposure, the Sn was dumped into a stainless-steel tank and residual Sn was removed by dipping specimens in liquid Li at ~250°C in an Ar-filled glovebox. There is some concern that the Li would remove the alumina scale [14], which was <0.5µm thick and difficult to detect using X-ray diffraction. Residual Li was removed using ethanol. Specimens were weighed before exposure and after cleaning using a Mettler Toledo X205 balance with an accuracy of ±0.04 mg. Selected specimens were metallographically mounted and polished and then imaged using light microscopy and a TESCAN model MIRA3 scanning electron microscope (SEM) equipped with energy dispersive X-ray spectroscopy (EDS) to determine the reaction products and depth of attack. Room temperature tensile tests used a strain rate of 0.015/min per ASTM E8-13.

Results

Specimen mass change of the specimens in the hot leg (HL) and cold leg (CL) are reported in Figure 1 after cleaning in Li and then ethanol. With each specimen exposed at a slightly different temperature, large mass losses were measured in the HL, especially above 380°C. Figures 2 and 3 show representative light microscopy images from cross-sectioned ODS 10Cr specimens. Figure 2 contrasts specimens from the bottom of the HL and top of the CL where the temperature was ~366°C in both locations. At low magnification, the CL specimen shows little attack with a mass loss of 4.2 mg/cm^2, Figures 2a and 2b. In contrast, the HL specimen lost 36 mg/cm^2 and is heavily pitted, Figures 2c and 2d. A recurring theme in HL specimens of all three alloys is that there are flat regions which appeared relatively unaffected and have retained a surface oxide, Figure 3d, while the pitted areas appear to have lost the oxide layer, Figure 3c.

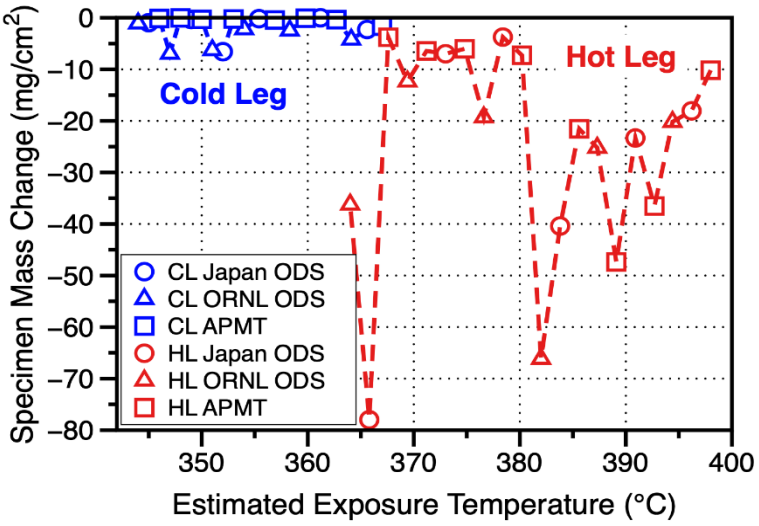

Figure 1. Specimen mass change of TCL specimens as a function of estimated temperature in the hot leg (HL) and cold leg (CL) of the Sn TCL experiment.

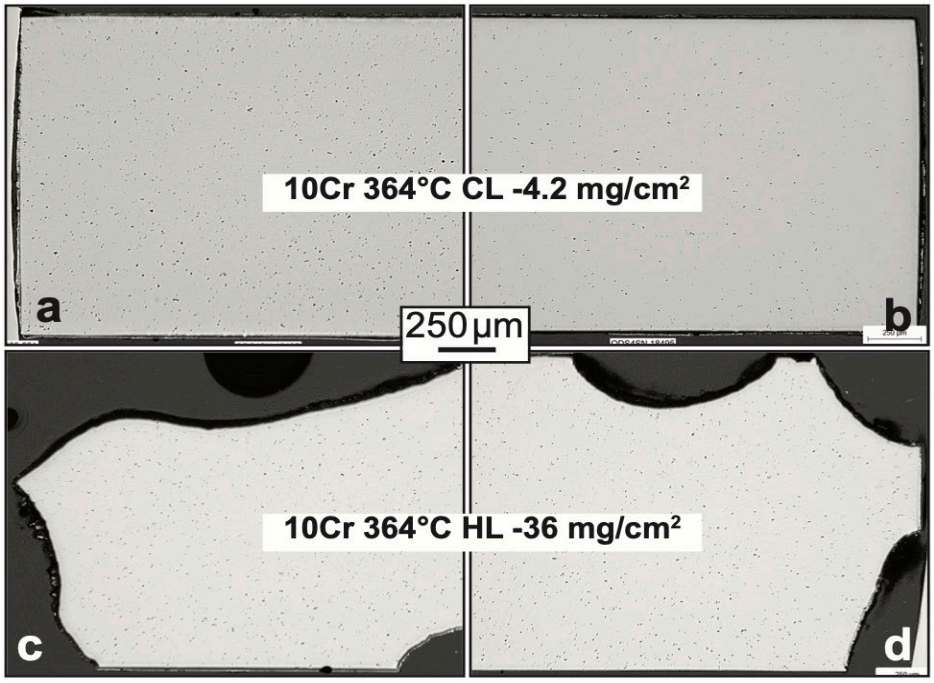

Figure 2. Light microscopy of ODS 10Cr specimens after exposure at ~366°C in the (a,b) cold leg and (c,d) hot leg.

To confirm this observation, SEM/EDS was performed on several specimens. Figure 4 shows the APMT specimen from the top of the HL. In Figure 4a, a thin surface layer was observed, and EDS maps detected Al and O, Figures 4b and 4c. In contrast, Figure 4e shows a pitted region with no clear surface oxide layer as confirmed by associated EDS maps, Figures 4f and 4g. Finally, some pitted areas appeared to have reaction products in some locations. Figure 5a shows a low magnification SEM image where the flat unaffected specimen surface is shown on the far right and the Cu-plated pit region is featured across the

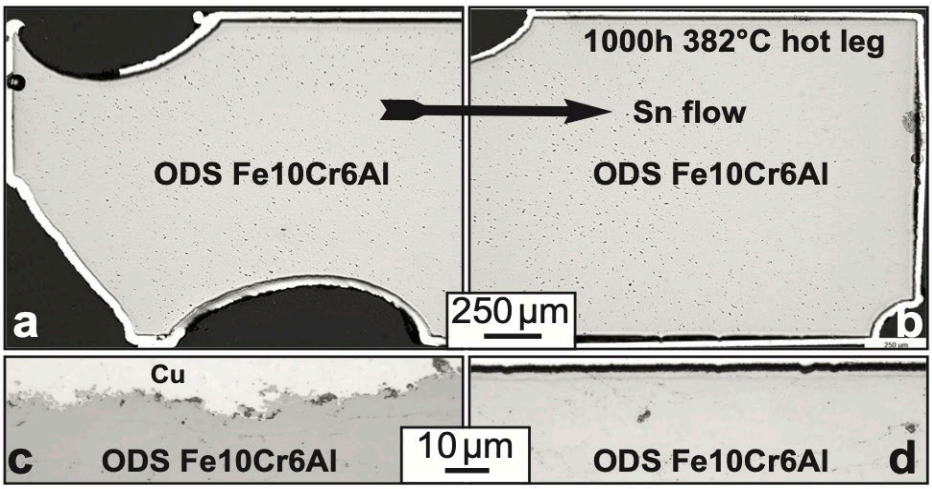

Figure 3. Light microscopy of ODS 10Cr specimen after exposure at ~382°C in the hot leg. The mass loss for this specimen was 66 mg/cm^2.

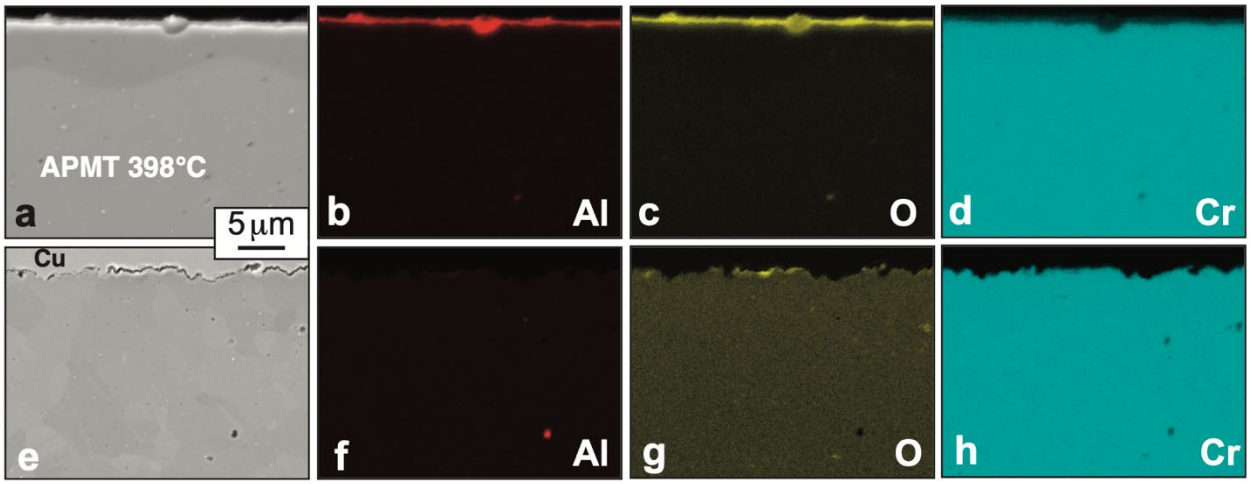

Figure 4. SEM images (a,e) from two areas of the APMT specimen exposed in flowing Sn at 398°C and (b-d,f-h) associated EDS maps.

image. Maps were taken from the small box in Figure 5a and are shown in Figures 5b-5f. In this region, there appeared to be Al-rich precipitates, perhaps oxides, and some Sn was retained in the rough surface region, Figure 5f.

The post-exposure room temperature tensile data are summarized in Figure 6 with the focus on the total elongation and the ultimate tensile stress. Results for all three alloys are shown. The green shaded regions show the range of values measured for three pre-oxidized specimens of each alloy without Sn exposure. The blue shaded region shows the range of values measured for three pre-oxidized specimens of each alloy after annealing for 1000 h at 400°C in an Ar-filled quartz ampoule. These specimens are intended to

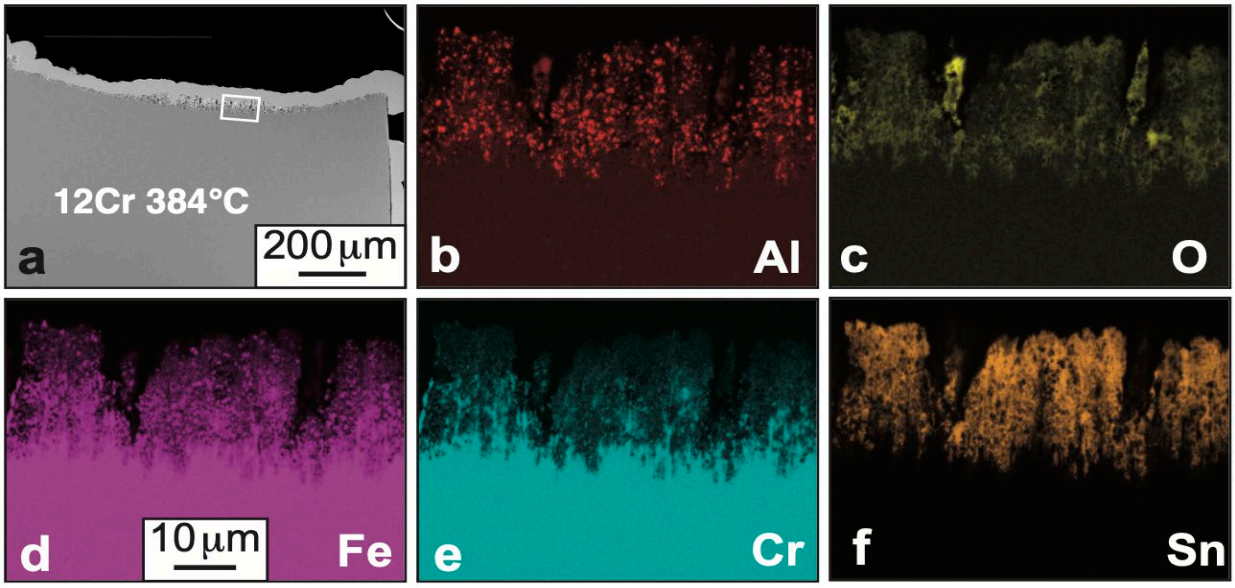

Figure 5. SEM image (a) from the ODS 12Cr specimen exposed in flowing Sn at 384°C and (b-f) associated EDS maps from the box in (a). Some Sn was retained in this pitted area.

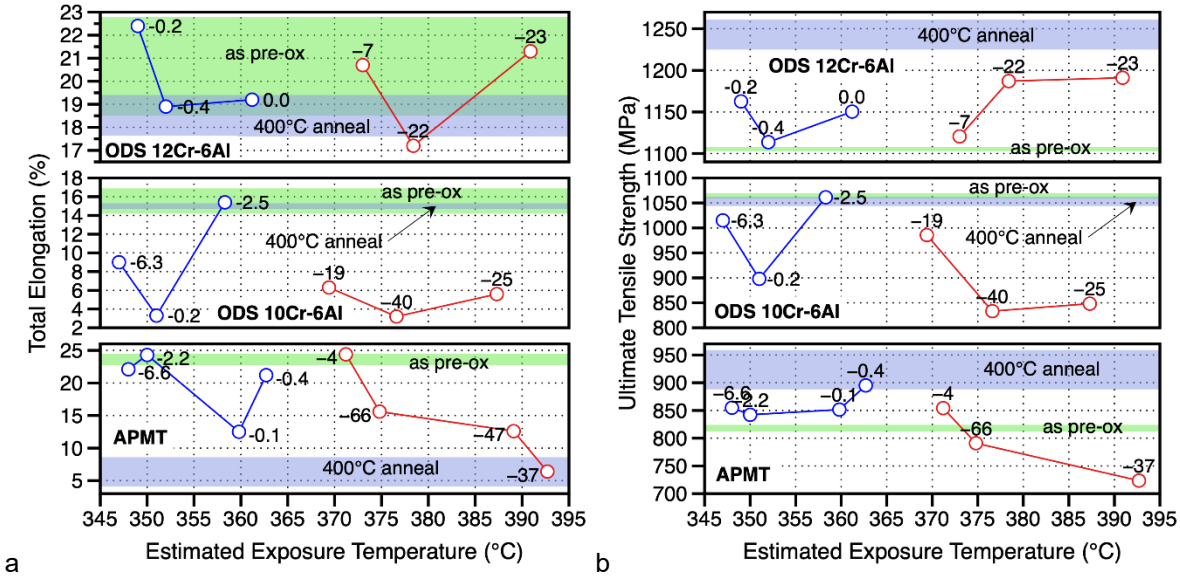

Figure 6. Room temperature tensile data for specimens exposed to flowing Sn (a) total elongation and (b) ultimate tensile strength (UTS) plotted as a function of estimated exposure temperature in the hot leg (red) and cold leg (blue). The mass change for each specimen is noted.

isolate the thermal effect from any effect of the Sn exposure. For the ductility results in Figure 6a, only the APMT specimens were strongly affected by the 400°C anneal. The ODS alloy with 12Cr appeared unaffected by the Sn exposure in both strength and ductility. The ODS alloy with 10Cr showed lower ductility for most of the specimens in the CL as well as the HL, where large mass losses were observed. For the UTS data shown in Figure 6b, the anneal tended to increase the UTS values. Again, the ODS 10Cr specimens appeared to be degraded by the Sn exposure as were the APMT HL specimens with high mass losses. Since every specimen was exposed at a slightly different condition, it is difficult to draw many conclusions for the 6-8 specimens of each alloy exposed in this experiment.

No further compatibility experiments are planned for Task 3 at this time. The remaining experiment is to expose these three pre-oxidized materials with and without Sn in HFIR [15].

References

[1] M. Kondo, M. Ishii and T. Muroga, Fus. Eng. Design 98–99 (2015) 2003.
[2] S. J. Zinkle and N. M. Ghoniem, Fus. Eng. Design, 51-52 (2000) 55.
[3] H. Glasbrenner, Z. Peric and H. U. Borgstedt, J. Nucl. Mater. 233-237 (1996) 1378.
[4] W. Krauss, J. Konys, N. Holstein and H. Zimmermann, J. Nucl. Mater. 417 (2011) 1233.
[5] W. Krauss, J. Konys, S.-E. Wulf, J. Nucl. Mater. 455 (2014) 522.
[6] S. J. Pawel and K. A. Unocic, J. Nucl. Mater. 492 (2017) 41.
[7] J. Jun, K. A. Unocic, M. J. Lance, H. M. Meyer and B. A. Pint, J. Nucl. Mater. 528 (2020) 151847.
[8] B. A. Pint and J. Jun, Oxid. Met. 96 (2021) 231.
[9] B. A. Pint and J. Jun, DOE-ER-0313/70 (2021) 151.
[10] B. A. Pint, J. Jun and M. Romedenne, Fus. Eng. Design 166 (2021) 112389.
[11] B. A. Pint, J. Jun, E. Cakmak, D. J. Sprouster, N. Olynik and L. L. Snead, Fus. Sci. Tech. 77 (2021) 761.
[12] B. A. Pint, S. Dryepondt, K. A. Unocic and D. T. Hoelzer, JOM 66 (2014) 2458.

[13] S. Dryepondt, K. A. Unocic, D. T. Hoelzer, C. P. Massey, B. A. Pint, J. Nucl. Mater. 501 (2018) 59.
[14] R. J. Lauf and J. H. DeVan, J. Electrochem. Soc., 139 (1992) 2087.
[15] M. Kondo, et al., Plasma Fus. Res. 16 (2021) 2405040.

8.2 LIQUID METAL COMPATIBILITY OF SiC AND ALUMINIZED F82H IN FLOWING PbLi—M. Romedenne, B. A. Pint (Oak Ridge National Laboratory)

OBJECTIVE

This goal is to move compatibility testing in flowing PbLi towards more realistic blanket materials. The first thermal convection loop (TCL) experiment with a peak temperature of 700°C showed a strong dissimilar materials interaction between SiC and FeCrAl. The second TCL experiment reduced the peak temperature to 650°C and included aluminized F82H (Fe-8Cr-2W) specimens.

SUMMARY

The TCL experiment using Kanthal APMT (Fe-21Cr-5Al-3Mo) tubing and CVD SiC and aluminized F82H specimens completed 1000 h with a peak temperature of 650°C. The aluminized specimens were pre-oxidized for 2 h at 800°C in air to further minimize the interaction between the steel and liquid. Compared to the previous TCL experiment with a peak temperature of 700°C, where severe metal loss was observed on ODS FeCrAl specimens and large mass gains on CVD SiC specimens, much smaller mass changes were observed at the lower temperature. Characterization of the specimens is in progress.

PROGRESS AND STATUS

Introduction

Intensive research has been accumulated on the compatibility of austenitic and ferritic steels for use in Pb-17at%Li (PbLi)-metal blankets of fusion reactors. Studies from the 1980s [1-4] and 1990s [5-7] observed dissolution, intergranular penetration, interstitial element transfer, and mass transfer caused by thermal and concentration gradients in Thermal Convection Loops (TCLs) and Forced Convection Loops (FCLs). The corrosion behaviors and dissolution rates of austenitic steels (316 type), ferritic steels (HT9, 9Cr1Mo types), and, more recently, RAFM (Reduced Activation Ferritic-Martensitic steels) (Manet and F82H types) were evaluated. Although lower dissolution rates were measured for the ferritic and RAFM steels (HT9, 9Cr1Mo types) than austenitic steels in PbLi, high corrosion rates [1-10] and metallurgical considerations [1] limit their use as blanket material below 475 °C [1,8].

Different strategies have been investigated to improve liquid metal compatibility above 500°C such as alloying to form FeCrAl alloys [11-13] and the use of Al-rich coatings on RAFM-type steels [21-23]. Either alloying or coating enables the formation of an adherent surface oxide such a-Al_2O_3 [13,18-20] that prevents the direct contact between steel and liquid. These strategies have shown very promising results in static and flowing Pb-Li [11-13]. For SiC, most studies have shown good Pb-Li compatibility for both monolithic SiC (e.g., high purity chemical vapor deposited (CVD) material) and SiC-SiC composites [14-17]. However, only a few studies have exposed SiC to PbLi in the presence of Fe or Cr, which both form more stable carbides than SiC. Previous capsule testing showed some changes when SiC was exposed in Fe capsules [15]. To further explore a possible dissimilar material interaction between low-Cr ODS FeCrAl [19,20] and CVD SiC, a TCL experiment was conducted with flowing Pb-Li at a peak temperature of 700°C [18]. Like results with only APMT in the TCL, significant metal dissolution occurred at >650°C [23]. With SiC specimens present in the TCL, Fe and Cr dissolved from the FeCrAl specimens reacted with the SiC coupons forming thick carbide and silicide layers [18]. In the next experiment, the peak temperature was

lowered to 650°C and the ODS FeCrAl specimens were replaced with pack aluminized F82H (Fe-8Cr-2W) specimens [24]. The current results after 1,000 h operation are presented.

Experimental Procedure

Thermal convection loop and materials

The sixth TCL experiment followed similar procedures as detailed previously [13,17-19,23]. Chains of 20 specimens were exposed for 1000 h in the hot leg (HL) and cold leg (CL) with a peak hot leg temperature of 650°C in a TCL made from APMT tubing (26.7 mm outer diameter, 3.1 mm wall thickness). The APMT loop was pre-oxidized for 8 h at 1050°C [11]. Coupon specimens were 15 x 25 x 2 mm, and the dog bone tensile specimens were 25 mm long SS-3 type. Chemical compositions of the specimens and APMT tubing are given in Table 1. Six coupon specimens of CVD SiC were added to each chain along with aluminized F82H coupons and tensile specimens and W spacers were placed at the bottom of the chain to prevent the specimens from floating. Four APMT coupons were included for comparison to the previous monometallic TCL experiment. Commercial Pb-17 at.%Li was melted in a stainless-steel fill tank. Six thermowells at the top, middle, and bottom of each leg were used to estimate each specimen temperature, and the peak temperature of 650°C ± 1°C was controlled at the top of the HL. During operation, temperatures were measured by thermocouples in thermowells at the top (T), middle (M) and bottom (B) of the hot leg (HL) and cold leg (CL), which are shown as thick black lines in the schematic (Figure 1a). A summary of the measured temperatures during the experiment is shown in Figure 1b. The temperature distribution was slightly different than the previous monometallic APMT TCL experiment because half of the middle furnace on the HL failed and could not be replaced during the experiment. As a result, the middle of the HL was cooler than normal, but the bottom temperature was nearly identical. The temperature gradient was ~24°C, and hot spot tests [11] measured a Pb-Li velocity of 0.77 ± 0.07 cm/s (Figure 2).

Table 1. Alloy compositions measured using inductively coupled plasma and combustion analyses in wt.%

Alloy	Fe	Cr	Al	Ni	Si	C	Other
APMT	69.0	21.6	4.9	0.12	0.53	0.03	2.8Mo,0.1Mn,0.2Hf,0.1Y,0.1Zr
APMT tube*	70.0	21.4	4.9		0.34	0.04	3.1Mo, 0.2Mn, 0.02Cu
F82H	88.9	8.1	0.02	0.06	0.08	0.10	1.8W, 0.45Mn, 0.20V,0.09Ta, 0.01N
CVD SiC				0.01	69.8	30.2	0.003 O

* reported by manufacturer [11]

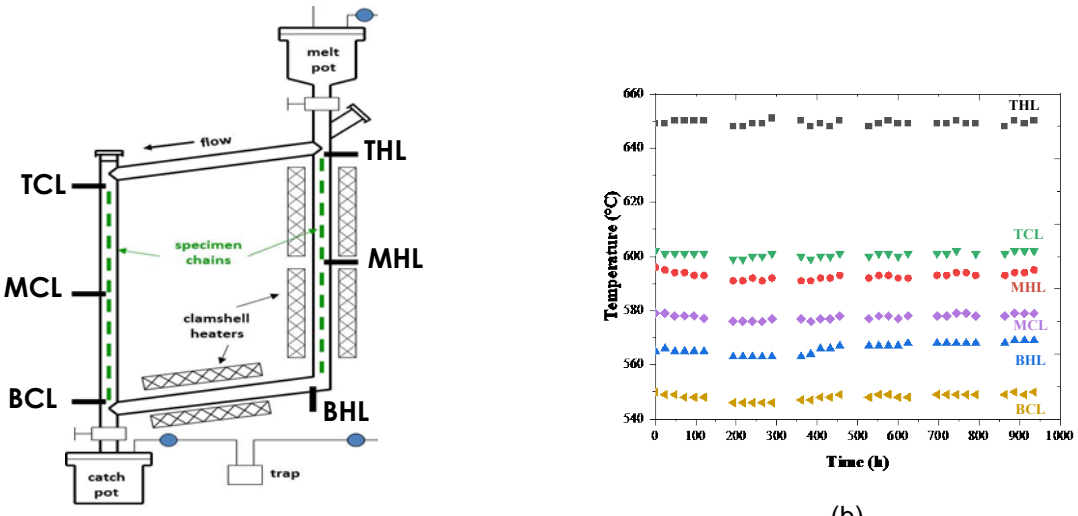

Figure 1. TCL schematic and (b) measured temperatures as a function of experiment time from the six thermowells in the TCL.

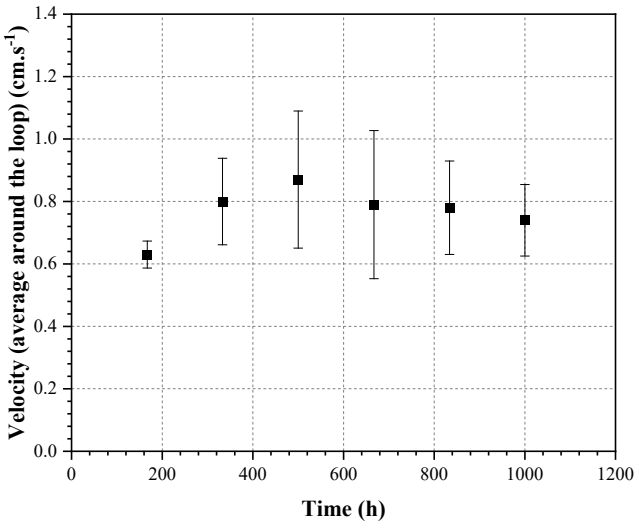

Figure 2. Velocity measurements (average around the loop) from hotspot tests.

Coating and pre-oxidation procedures

The F82H specimens were aluminized using pack cementation [24] for 30 min at 1050°C in a pack containing 20wt.% Cr-10wt.%Al powder, 2% NH_4Cl activator and 78% Al_2O_3 filler. After coating, the specimens were pre-oxidized for 2h at 800°C in air to form an alumina layer prior to PbLi exposure. The APMT coupons were pre-oxidized for 2h at 1000°C [13].

Tensile tests and characterizations

After 1,000 h, the PbLi was drained into a stainless-steel tank, and the TCL was cleaned using the standard solution of acetic acid, ethanol, and hydrogen peroxide [11-13]. Specimens were weighed before and after

exposure using a Mettler Toledo X205 balance with an accuracy of ±0.04 mg. The surface of the coupon was analyzed using conventional X-ray diffraction (XRD) using a Malvern PANalytical X'Pert PRO diffractometer with Cu Kα radiation in the Bragg-Bentano geometry. Polished specimen cross sections were characterized using light microscopy and scanning electron microscopy (Tescan model MIRA3) equipped with energy dispersive X-ray spectroscopy (EDS). Postexposure room temperature tensile testing was performed with a strain rate of 0.015/min per ASTM E8-13, "Standard Test Methods for Tension Testing of Metallic Materials," ASTM International.

Results

Mass change

The specimens mass change data is reported in Figure 3. Compared to the previous TCL experiment with a peak temperature of 700°C, the mass changes were much lower. Previously, the ODS FeCrAl specimens lost 20-160 mg/cm^2 in the HL and the CVD SiC specimens gained 20-60 mg/cm^2. Most of the SiC specimens gained mass while most of the aluminized F82H specimens had very small mass gain. Two of the SiC coupons may have been damaged during handling thus affecting the mass change and explaining the large mass loss for the specimen at the top of the HL. Nevertheless, the mass gains for the SiC specimens at <600°C suggest that some interaction with SiC occurred in flowing PbLi. Overall, the mass changes in this experiment were minimal and like the previous monometallic APMT experiment with a 650°C peak temperature where the average mass loss was -0.2 mg/cm^2 [13]. The four APMT coupons exposed in the current loop showed mass changes ranging from -0.09 to +0.05 mg/cm^2.

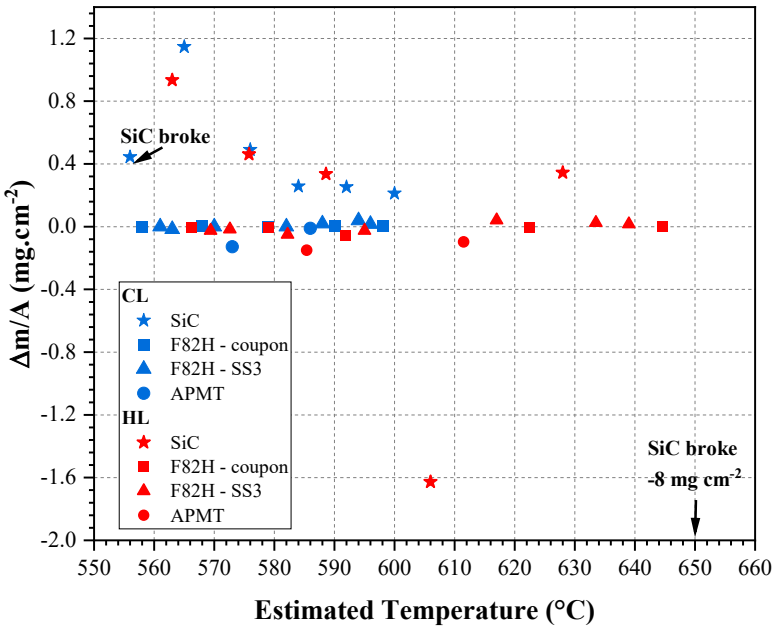

Figure 3. Specimen mass change of TCL specimens in flowing PbLi after 1000 h as a function of estimated temperature in the hot and cold legs. The CVD SiC specimens are shown with close stars, the pre-oxidized and aluminized F82H specimens are close squares and triangles and APMT open circles.

Microstructure after exposure

Figure 4 shows SEM images of the coatings before and after pre-oxidation and the phases were identified using EDS mapping (not shown here). The coatings appeared very uniform with a depth of ~100-120 µm. The thin outer layer of coating grows by Fe outward transport but most of the coating formed by Al inward diffusion [24]. The N in the steel reacts with Al to form AlN precipitates [25]. Figure 5 shows the Al EDS profiles measured from the oxide-coating towards the underlying F82H substrate. In agreement with the observed very low mass changes in Figure 3, the Al-rich oxide layer was still present on the surface of the specimen and the composition of the coating remained unchanged after 1,000 h in flowing PbLi with no significant interdiffusion (Figure 5) [26].

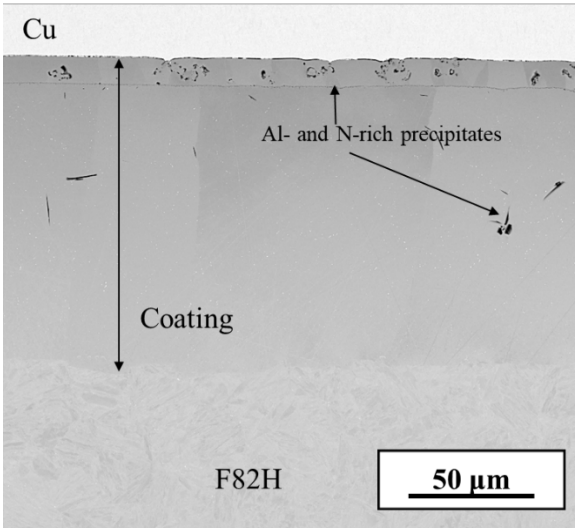

(a)

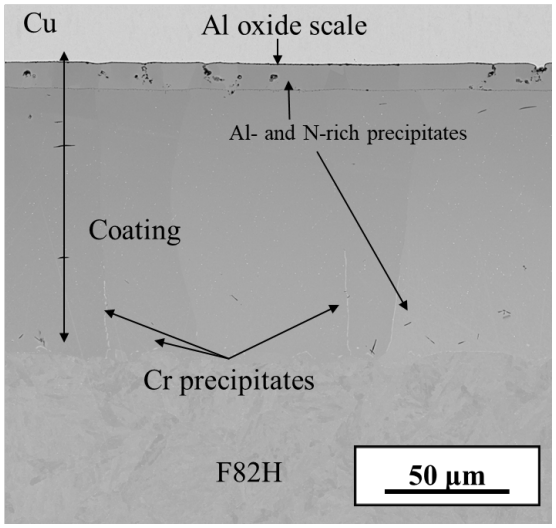

(b)

Figure 4. SEM images of polished cross-sections of the Al-rich coatings on F82H (a) as-deposited and (b) after pre-oxidation.

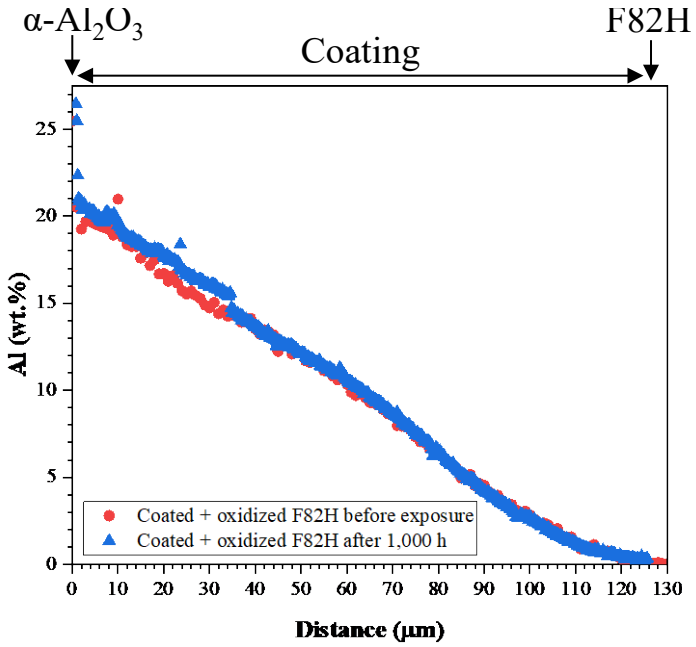

Figure 5. Al EDS elemental profiles measured in coated and pre-oxidized F82H before and after 1,000 h in flowing PbLi.

Currently, only 2 SiC coupons from the CL have been characterized (565 and 592 °C), Figure 6. In agreement with previous observations [18], the surface of the exposed SiC after 1,000 h in flowing PbLi was covered with a Fe-, Cr-, Mn-, Ni-, C- and O-rich corrosion product (Figure 6 and Figure 7). The thickness of the surface reaction layer decreased with increasing temperature as seen in Figure 6. Cracks were also visible below the corrosion layer and going through the SVD SiC (Figure 6). Preliminary XRD analyses suggest the formation of Cr_3C_2, Cr_3Si and Fe_8SiC (Figure 8) while thermodynamic calculations at 650 °C suggested the formation of Cr_3C_2, Cr_3Si, Cr_5Si_3 and Fe_8Si_2C. Because of the thin reaction products, TEM characterization will be performed to study their structure and composition.

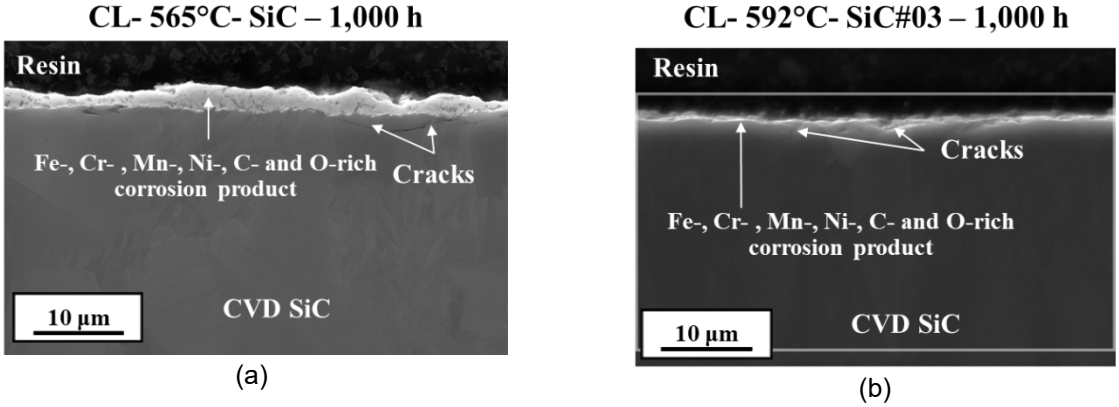

(a) (b)

Figure 6. SEM images of SiC coupons after 1,000 h in the cold leg of the APMT loop filled with flowing PbLi at (a) 565 °C and (b) 592 °C.

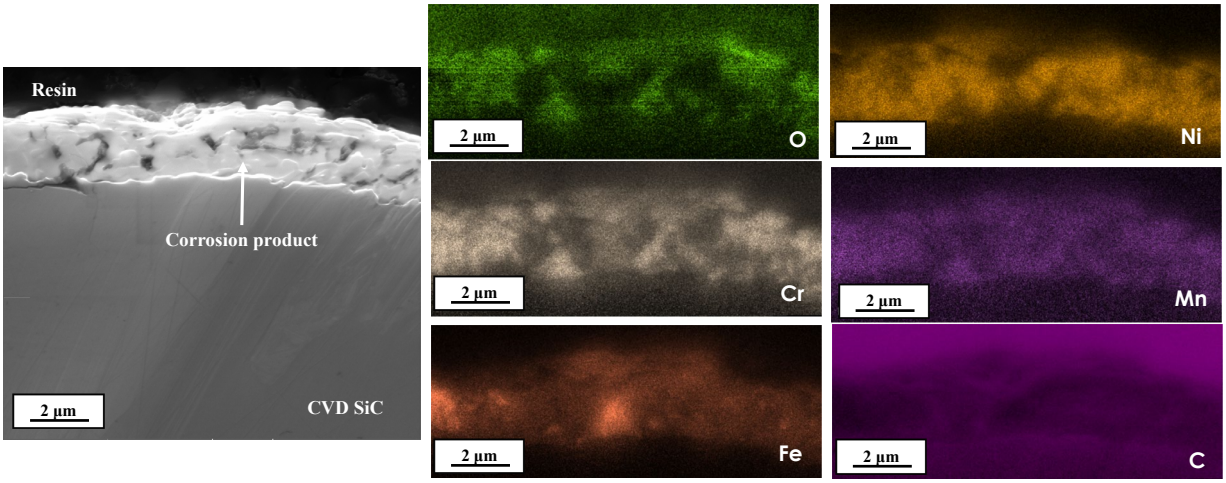

Figure 7. BSE image and EDS ZAF quantified elemental maps of the corrosion product on the surface of the exposed SiC coupon after 1,000 h in the cold leg of the APMT loop filled with flowing PbLi at 565 °C.

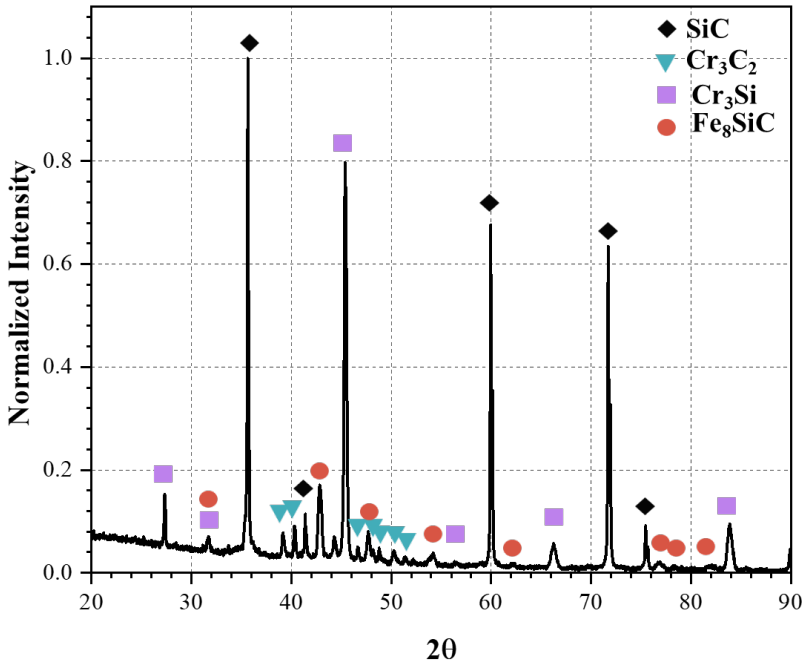

Figure 8. XRD surface analysis of exposed SiC after 1,000 h in the APMT loop filled with flowing PbLi at 556 °C.

Tensile properties

Before PbLi exposure, the tensile properties of coated F82H with and without pre-oxidation were evaluated before and after annealing in Ar at 550 and 650 °C (Figure 9). The pre-oxidation of the coated F82H resulted in a ~50 % decrease in the ultimate tensile stress (UTS) and a ~40 % increase in the total elongation (Figure 9). Annealing in Ar for 1,000 h at 550 or 650 °C did not significantly affect the UTS or the total elongation. After exposure to PbLi, the UTS and total elongation remained largely unchanged (Figure 10).

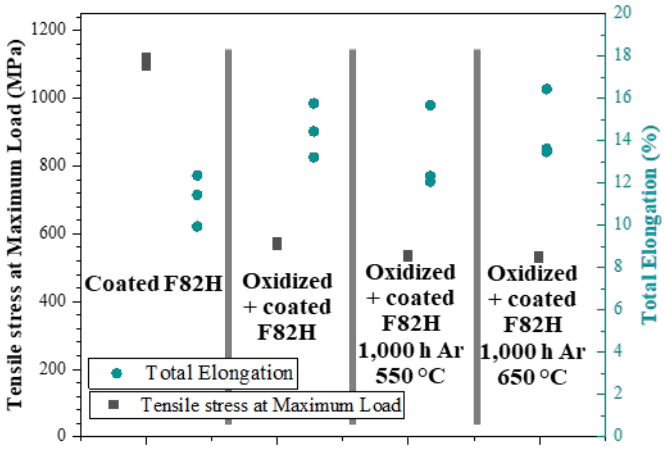

Figure 9. Tensile stress at maximum load and Total elongation of coated and pre-oxidized and coated F82H before exposure and after 1,000 h in Ar at 550 and 650 °C.

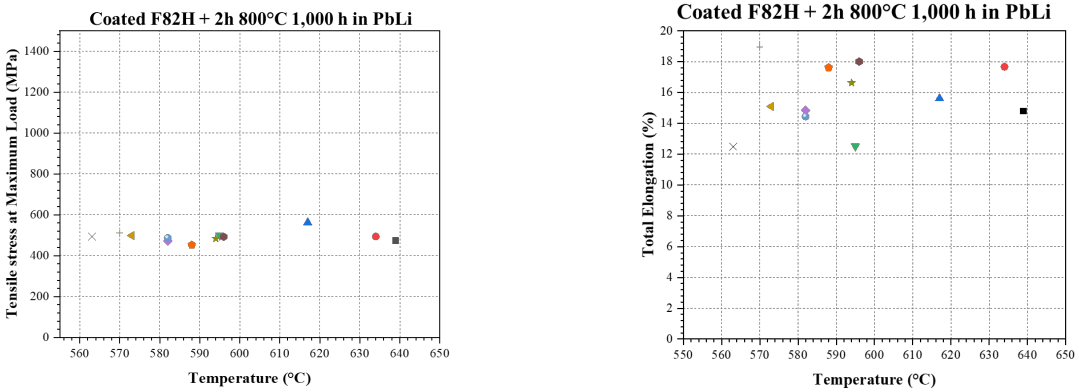

(a) (b)

Figure 10. (a) Tensile stress at maximum load and (b) Total elongation of coated and pre-oxidized F82H after 1,000 h in APMT loop filled with flowing PbLi.

References

[1] O. K. Chopra, P. F. Tortorelli, J. Nucl. Mater. **123** (1984) 1201.
[2] P.F. Tortorelli and J.H. De Van, J. Nucl. Mater. 141-143 (1986) 592.
[3] G.M. Gryaznov, V.A. Evtikhin, L.P. Zayval'skii, N.V. Samsonov and A.A. Gusakov, Atomnaya Energiya. 355-358 (1985) 59.
[4] H.U. Borgstedt, G. Drechsler, G. Frees and Z. Peric, J. Nucl. Mater. 155-157 (1988) 728-731.
[5] J. Sannier, M. Broc, T. Flament and A. Terlain, Fus. Eng. Design 299-307 (1991) 14.
[6] J. Sannier, T. Dufrenoy, T. Flament and A. Terlain, J. Nucl. Mater. 191-194 (1991) 975-978.
[7] P. F. Tortorelli, J. Nucl. Mater. 191-194 (1992) 965-969.
[8] J. Konys, W. Krauss, H. Steiner, J. Novotny and A. Skrypnik, J. Nucl. Mater. 1191-1194 (2011) 417.
[9] J. Konys and W. Krauss, J. Nucl. Mater. S576-S579 (2013) 442.

[10] P. Chakraborty, V. Kain, P. K. Pradham, R.K. Fotedar and N. Krishnamurthy, J. Fus. Eng. 371-378 (2015) 34.
[11] S. J. Pawel and K. A. Unocic, J. Nucl. Mater. 492 (2017) 41.
[12] K. A. Unocic and B. A. Pint, J. Nucl. Mater. 455 (2014) 330.
[13] J. Jun, K. A. Unocic, M. J. Lance, H. M. Meyer and B. A. Pint, J. Nucl. Mater. 528 (2020) 151847.
[14] T. Yoneoka, S. Tnaka and T. Terai, Mater. Trans. 1019-1023 (2001) 42.
[15] B.A. Pint and K.A. Unocic, J. Nucl. Mater. 442 (2013) S572.
[16] P. Chakraborty, S. Kumar, R. K. Fotedar and N. Krishnamurthy (2013, June) *Interaction of α-silicon carbide with lead-lithium eutectic.* AIP Conference Proceedings 538, 34, Carbon Materials, Granada, Spain.
[17] S. Tosti, A. Moriani and A. Santucci, Fus. Eng. Design 2479-2483 (2013) 88.
[18] B. A. Pint, J. Jun and M. Romedenne, Fus. Eng. Design 166 (2021) 112389.
[19] B. A. Pint, S. Dryepondt, K. A. Unocic and D. T. Hoelzer, JOM 66 (2014) 2458.
[20] S. Dryepondt, K. A. Unocic, D. Hoelzer, C. P. Massey, B. A. Pint, J. Nucl. Mater. 501 (2018) 59.
[21] H. Glasbrenner, Z. Peric and H. U. Borgstedt, J. Nucl. Mater. 233-237 (1996) 1378.
[22] W. Krauss, J. Konys, S.-E. Wulf, J. Nucl. Mater. 455 (2014) 522.
[23] B. A. Pint, J. Jun, E. Cakmak, D. J. Sprouster, N. Olynik and L. L. Snead, Fus. Sci. Tech. 77 (2021) 761.
[24] B. L. Bates, Y. Q. Wang, Y. Zhang and B.A. Pint, Surf. Coat. Technol. 204 (2009) 766.
[25] Y. Zhang, B. A. Pint, K. M. Cooley and J. A. Haynes, Surf. Coat. Technol. 200 (2005) 1231.
[26] Y. Zhang, A. P. Liu and B. A. Pint, Mater. Corr., 58 (2007) 751.

9. MODELING AND COMPUTATIONAL STUDIES

9.1 THE EFFECTS OF IRRADIATION ENHANCED THERMAL SOFTENING AND He RE-HARDENING ON THE CREEP PROPERTIES OF 9Cr TEMPERED MARTENSITIC STEELS—M.E. Alam, T. Yamamoto, G.R. Odette (University of California, Santa Barbara)

OBJECTIVE

The objective of this study is to model the effect of higher temperature irradiation softening and re-hardening by He on the primary creep properties of Grade 91 type tempered martensitic steels.

SUMMARY

Acceleration of thermal creep rates by irradiations above ≈ 450 °C could have a deleterious effect on the creep properties of Grade 91 type 9Cr tempered martensitic steels (TMS), such as Eurofer97. Here, first, we model the effects of softening on the creep rate and strain-time curves. The softening, and its effect on creep, is approximately athermal between 450 and 550 °C. The effects of softening are mainly manifested at higher primary strains and failure metrics like the dpa onset of tertiary creep. Then we have integrated the He re-hardening model with the softening model considering that He makes an approximately athermal contribution to hardening above 450 ºC, starting at a threshold of ≈ 430 appm and increasing with the √He. He re-hardening would be expected to extend the creep life if softening failure does not occur before about the mentioned threshold He appm, which is typical for the first wall as He/dpa ≈ 10 at ≈ 43 dpa. Integrated with softening model, the He re-hardening model is then applied to predict the creep curves, strain rate vs. dpa curves, re-hardening initiation stress, and creep stopper stress as a function of various σ, ε, and T.

BACKGROUND

We previously reported a comprehensive model for the effects of irradiation on the constitutive properties of TMS, with a focus on changes in the yield stress, σ_y, including for fusion relevant irradiation conditions as $\Delta\sigma_y$ = f(dpa, He/dpa, T), where T is the irradiation and test temperatures [1]. Typical fission reactor irradiations, with He(appm)/dpa ratios << 1, cause hardening at T ≤ 400 °C, while at higher T the steels can gradually soften. At fusion first wall relevant He/dpa ≈ 10, the steels initially irradiation soften, but begin to re-experience increases in $\Delta\sigma_y$ at He > ≈ 400 appm. We showed the likely reason for the softening at such low T is radiation enhanced diffusion (RED); RED shifts purely thermal softening regime (> 600°C > 10^3 h) to lower temperatures and shorter times. We further noted that the main effects of softening are expected to be increases in thermal creep rates (ε'), since ε' is proportional to $[\sigma/\sigma]^n$, where n is a large number (typically ≥ 15). We also previously reported models to predict a variety of creep properties for a range of TMS heats [2]. We found that creep could be best modeled based on a normalized stress power law, $\varepsilon' \alpha (\sigma/\sigma_u)^n$, where σ_u is the ultimate tensile stress of steel at the creep temperature. Here, we combine the softening and creep models to assess the effect of irradiation on the creep strains (ε_x) as a function of dpa. The basic creep model was previously fitted to a Eurofer97 creep database [3] and $\sigma_y(dpa)/\sigma_{yo} \approx (\sigma_u(dpa)/\sigma_{uo})$ was fitted to data from 450 to 600°C irradiations. The combined model was used to calculate the creep strain (ε) and creep rate (ε') as a function of dpa for T = 450, 500 and 550ºC at various σ, both with and without softening. To a good approximation, the dpa to specified strain ε_x with softening (dpa_s) is given by a relation in the form $dpa_s = C dpa_t^m$, where dpa_t is the corresponding pseudo dpa at ε_x without irradiation enhanced softening. As expected, the effect of softening increases with increasing dpa. For example, for ε_x = 2% (close to the thermal tertiary creep strain), $dpa_s = 1.3284(dpa_t)^{0.735}$. Thus, if dpa_t = 100 dpa, without softening, dpa_s would be ≈ 39 dpa [4]. On the contrary, He contributes for hardening above 450 ºC after ≈ 430 appm which might greatly extend the creep life of the component if the material survives beyond He/dpa ≈ 10 at ≈ 43 dpa. Therefore, in this study, first, the irradiation enhanced thermal softening has been estimated and then integrated with the He induced re-hardening model.

PROGRESS AND STATUS

The primary creep models

In our previous study, we have developed three primary creep models that include: 1) the Larson-Miller parameter (LMP); 2) the applied stress (σ) normalized to the temperature (T) dependent 0.2% tensile yield stress, [$\sigma/\sigma_y(T)$] or ultimate tensile strength, [$\sigma/\sigma_u(T)$]; and 3) threshold stress that scales with σ_y, (σ-$C\sigma_y$) or σ_u as (σ-$C\sigma_u$) [2]. These models were calibrated to a database total of 17 heats of 9Cr TMS (including 8 heats of Eurofer97, reported by Rieth et al. [3]). It has been seen that the normalized [$\sigma/\sigma_u(T)$] model predicts the best creep stress with ≈11 MPa SD, ≈ 0 MPa mean error (ME) and 1:1 M-P (measured vs predicted) lines at 0 MPa interception for a larger dataset with creep time, t_x>10h, T = 375 to 550 ºC and strains (ε_x) from 0.2 to 2 % (Figure 1a). For all three primary creep models development, approach and results can be found elsewhere [2]. Here, the basic approach for the primary creep σ/σ_u model for Rieth's database has been summarized below:

The most common approach to fitting data at higher σ and lower T, in the dislocation creep (climb-glide) regime, is the use of the simple Norton power-law model as:

$$\varepsilon' = A\sigma^n \exp(-Q/RT) \quad (1)$$

While the parameters A, the stress exponent n and the activation energy Q are often assumed to be constant, they actually depend on the combination of σ and T. The Norton model is usually used for t_r and ε_m (minimum creep) data correlations. Here a modified Norton model, proposed by Wilshire [5], where the σ is normalized by dividing it by tensile strength, σ_u in equation (2) as σ/σ_u and has been used to predict time using Rieth's FZK primary creep dataset [3].

$$\varepsilon' = A(\sigma/\sigma_u)_n \exp(-Q/RT) \quad (2)$$

First, $\varepsilon' \exp(Q/RT)$ vs. σ/σ_u are plotted for the measured 6 different strains (0.1, 0.2, 0.5, 1, 2 and 5%) for FZK database that gives slope (A) and power (n) at each mentioned strain. The modified equation for the strain rate-based model is then:

$$\varepsilon'(x) = (A_1 + A_2\varepsilon + A_3\varepsilon^2) * (\sigma/\sigma_u)^{[n_1 + n_2 \ln(\varepsilon)]} * \exp(-Q/RT) \quad (3)$$

Here, A_i'a and n_i's are the slope and power of the fit parameters and Q is the effective activation energy. The model is optimized for time (h) by dividing ε(x) by ε'(x) and the least square fit (LSF) approach was used to minimize standard deviation between predicted (P) and measured (M) time at each strain. Figure 1b shows the P vs M time for the 450 ºC FZK primary creep strains using equation (3). While the times are a bit scattered, the model predicts a robust trend. Figure 1c shows an example of predicted and measures ε(t) at 450 °C for creep stress, σ = 320 MPa, and ultimate stress, σ_u = 458 MPa.

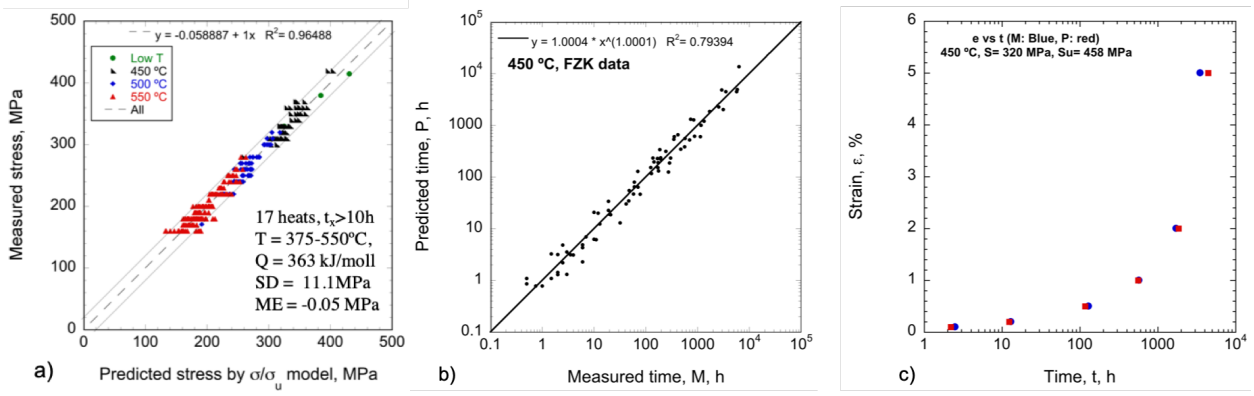

Figure 1. The σ/σ_u model showing: a) predicted (P) vs measured (M) σ for the 17 heats of 9Cr steels for t_x >10 h; b) measured vs predicted time for 450 ºC; and, c) measured (blue dots) and predicted (red square) creep curve (ε vs t) at 450 ºC for σ = 320 MPa and σ_u = 458 MPa.

The softening model

The effect of high temperature exposures for long times leading to softening both with (under creep) and without (under thermal aging) stress is well established [6–13]. Thermal aging effects are generally manifested above ≈ 600°C and time in excess of 10,000 h. Softening under stress also occurs near and beyond the tertiary creep strain and time. While there are a number of different microstructural evolution mechanisms leading to thermal softening, they generally share a common rate-controlling dependence on the thermal diffusion coefficient (D_{th}). Thus, the excess defects produced by displacement damage result in higher radiation enhanced diffusion (RED) coefficients (D*). The RED shifts the microstructural evolutions to lower temperatures and shorter times. Figure 2a shows the best estimate D_{th} and D* as a function of 1/T. The banded region marks temperatures ranging from 450 to 550 °C, where D* is nearly athermal. It has also been found that thermal and irradiation softening data can be superimposed by a temperature adjustment with an activation energy of about 260 kJ/mole. Thus, softening, which begins thermally at about 600 °C, would be expected to start at about 400 °C under irradiation. While the thermal softening rates increase with a temperature above ≈ 600 °C, the corresponding kinetics under irradiation would be expected to be roughly athermal at lower temperatures. The softening model was developed by fitting both the long-term thermally-aged [6–13] and RED adjusted [1] σ_y/σ_{yo} at 450, 500, 550 and 600 ºC as shown in Figure 2b.

$$\sigma_y/\sigma_{yo} = A - B \log (dpa) \qquad (4)$$

Here σ_{yo} is the unirradiated yield stress. The data is highly scattered but yields the fits summarized in Table 1. The fit results are very similar for the 450 to 550°C data, which is not surprising given the athermal D*. The average slope (B) and offset (A) over this temperature range for equation (4) is also shown in Table 1. In these cases, σ_y/σ_{yo} falls below 1 at > ≈ 4.6 dpa and σ_y/σ_{yo} = 0.85 at 200 dpa. The softening slope is larger and the dpa at σ_y/σ_{yo} = 1 is smaller for the 600 °C data. Thus, the overall softening process is described by a bilinear function shown in Figure 2c. The σ_u/σ_{uo} is assumed to be the same as σ_y/σ_{yo}. Time and dpa are related, based on an assumed dpa rate of 10^{-6} /s. The dashed lines show the effect of re-hardening by a He/dpa ratio of 10 appm/dpa.

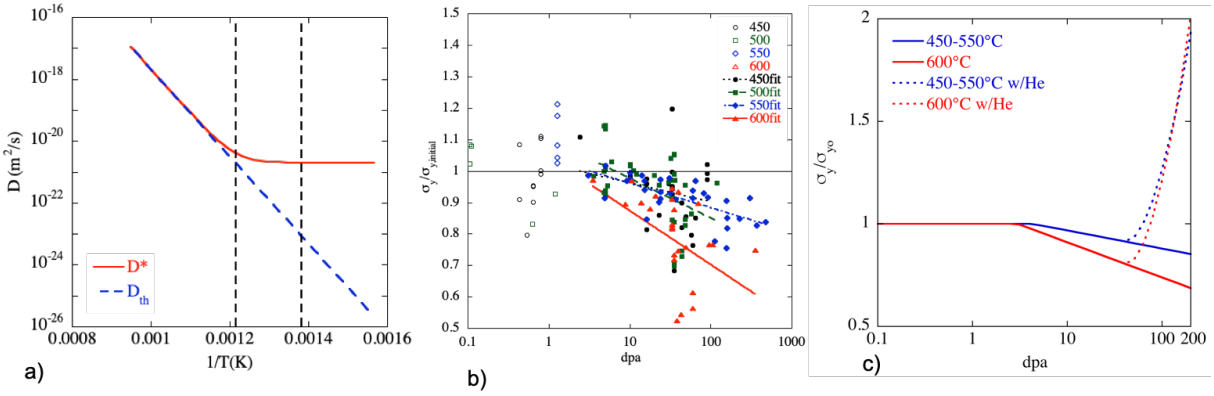

Figure 2. a) D_{th} and D* as a function of 1/T; b) σ_y/σ_{yo} vs dpa for combined thermally-aged and RED-adjusted softening; and c) the average softening from 450 to 550 and 600 °C (solid line) and re-hardening at He/dpa = 10 in units of appm/dpa (dashed line).

Table 1. Parameters for softening model

Parameters	450 ºC	500 ºC	550 ºC	Average of (450-550 ºC)	600 ºC
A (offset)	1.029	1.1037	1.0372	1.05659	1.08175
B (slope)	-0.06055	-0.1266	-0.07791	-0.08835	-0.17135

The effect of irradiation softening is estimated by simply by replacing the unirradiated constant σ/σ_u with the σ/σ_u(dpa) ratio in equation (3), which increases with dpa. The ε' is adjusted in small ε increments (0.01%) from 0.1 to 5% and LSF is used to predict ε' (dpa) for the softening case. Again, predicted time in terms of dpa for softening is then measured by dividing (ε/ε') x10^{-6}. Since it results in longer creep times and dpa, the effect of softening increases with decreasing σ. At least 10 to 15 creep stress (σ) at each temperature (T) has been estimated to observe the strain, initial dpa and temperature effect. Figure 3a shows an example of unsoftened (black) and softened (green) creep curves for 550 ºC at σ = 140 MPa and σ_u = 350 MPa, and 3b shows a log-log plot of the non-softening vs. softening dpa at 0.2, 0.5, 1, 2, 3, 4 and 5% strains. Here the results are restricted from 10 to 1000 dpa. The detailed irradiation enhanced thermal softening results for 3Ts (450, 500 and 550ºC) as a function of σ and ε_x can be found elsewhere [4].

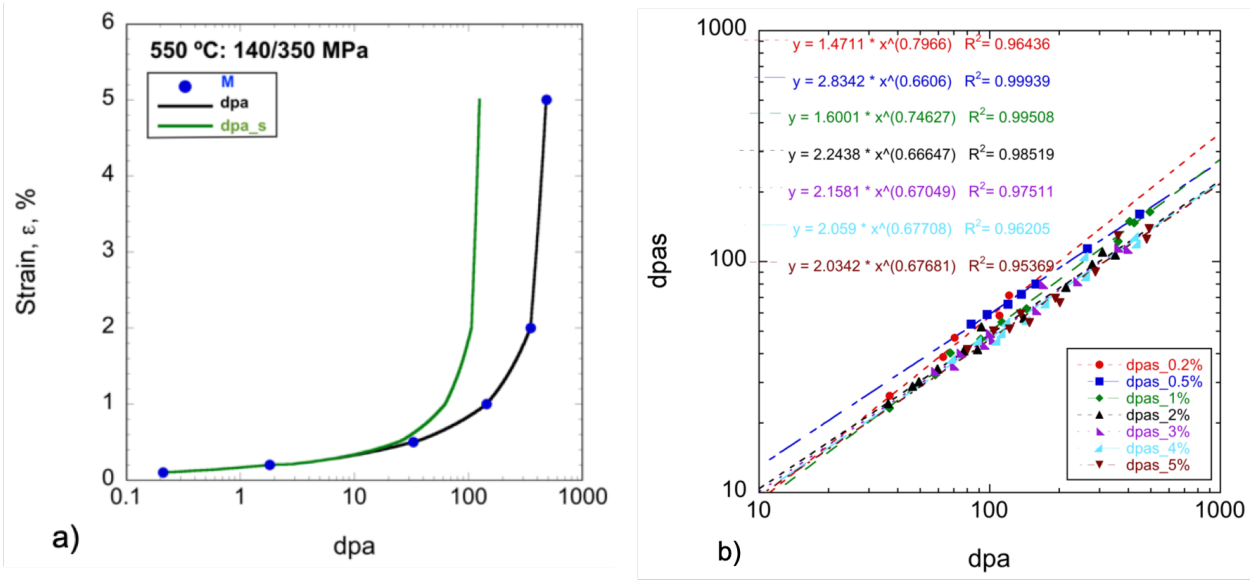

Figure 3. a) Softening and non-softening curves at 550 °C at σ = 140 MPa and σ_u = 350 MPa, and b) Creep dpa before and after softening from 0.2 to 5 % strains at varying T and σ.

The re-hardening model

The results mentioned above in Figure 3 do not consider the effects of re-hardening by He illustrated in Figure 2c. Helium makes an approximately athermal contribution to hardening above 450 °C starting at a threshold of a threshold of ≈ 430 appm and increasing with the √He. Thus, He re-hardening would be expected to greatly extend the creep life if softening failure (by whatever criteria) does not occur before about the threshold of 500 appm He. For typical first wall He/dpa ≈10, 43 dpa is a good metric for when the beneficial (to creep) effects of He to begin to emerge. We have used the same approach as softening by using equation (3) to first measure the ε' using hardened σ/σ_u and then divided ε by ε' for time prediction which is then converted to dpa by dividing by 10^6. Figure 4a and b show an example for thermal creep (TC, black), softened (S, green), and hardened (H, red) creep curves, and strain rate, ε' vs. dpa, respectively, for 550 °C at σ = 140 MPa and σ_u = 350 MPa. The hardening starts to jump abruptly after reaching ≈ 500 dpa. Figure 4c-i) shows the softened (green) and hardened (red) dpa vs. thermal creep up to 500 dpa at different ε from 0.2 to 5% for all σ and T that shows the hardening jump at each mentioned ε. Note, higher hardening dpa (where creep nearly stops) corresponding to softened dpa is not plotted here.

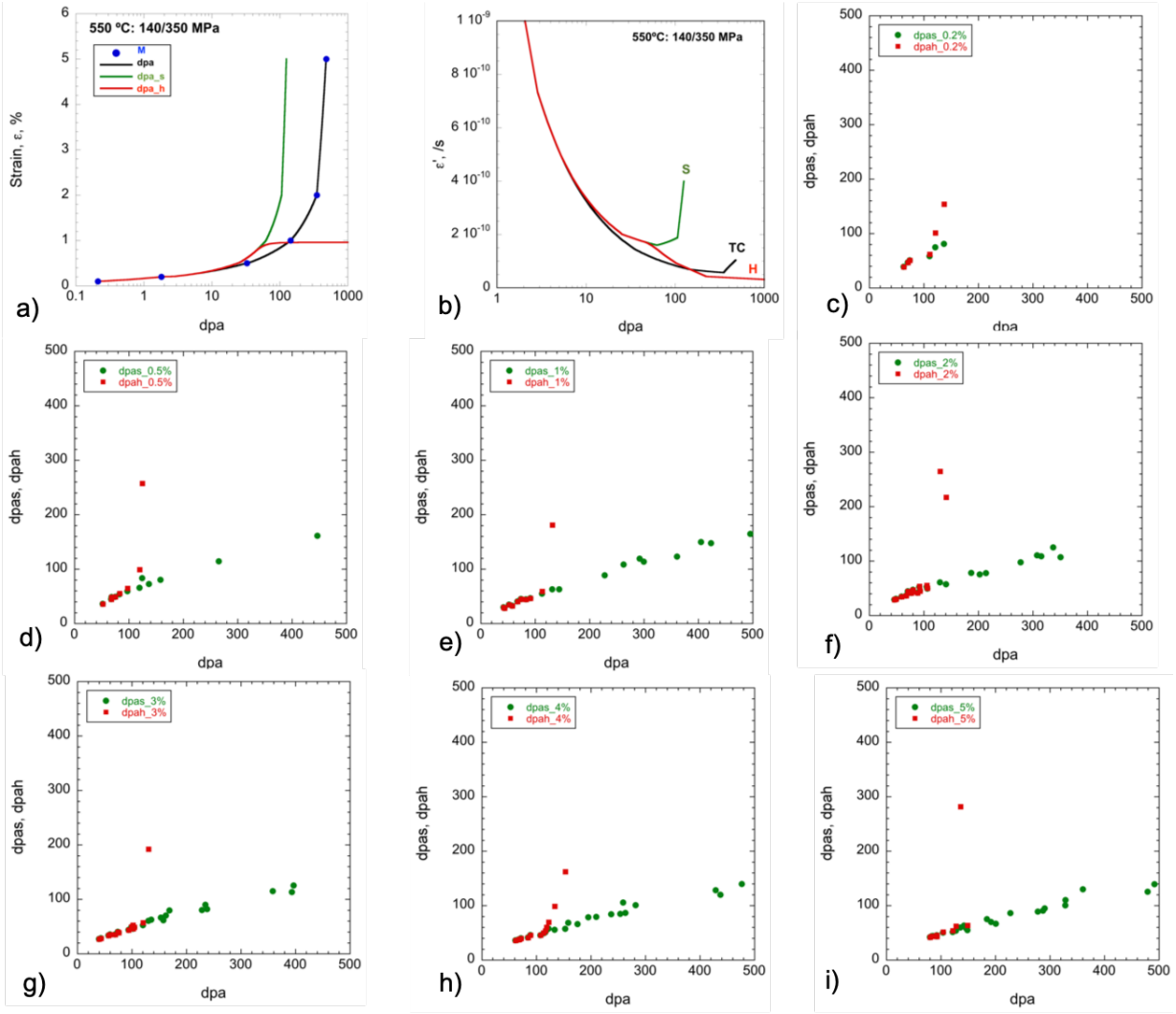

Figure 4. Thermal creep (TC, black), softened (S, green), and hardened (H, red) creep curves in a) and strain rate, ε' vs. dpa in b), respectively, for 550 °C at σ = 140 MPa and σ_u = 350 MPa. Figure 4c-i) shows the softened (green) and hardened (red) dpa vs. thermal creep up to 500 dpa.

As mentioned earlier, the re-hardening mostly initiates at ≈ 43 dpa. Therefore, in our next iteration, we have calculated the initiation re-hardening stress (for the given σ_u) at different strains (ε = 0.2, 0.5, 1, 2 and 5%) at all three T. Figure 5a-c) shows examples for the re-hardening initiation stress at ε = 1% as 248, 178.5 and 146 MPa for 450, 500 and 550ºC, respectively, whereas 5d summarized the re-hardening initiation stresses as a function of ε, and T. Note, σ_u used in these cases are 464, 424 and 350 MPa for 450, 500 and 550 ºC, respectively.

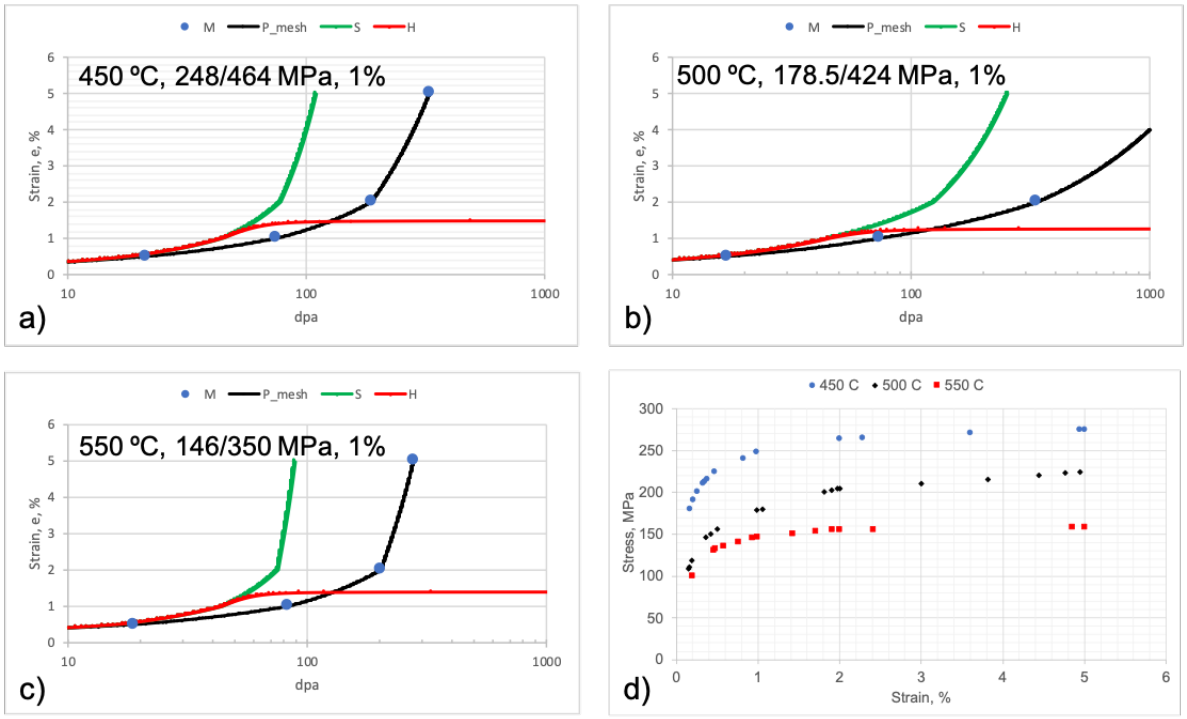

Figure 5. a-c) The re-hardening initiation stress at ε = 1% for 450, 500 and 550 ºC, respectively. Here, thermal creep (P, black), softened (S, green), and hardened (H, red) are used to show creep curves. Figure 5d summarize the re-hardening initiation stress as a function of ε, and T.

For softening dpa > 43, the re-hardening takes control over softening and the hardening strain rate goes down exponentially that literary stops creep. Therefore, in our next iteration, we have calculated the σ need to stop creep at the specific strains (ε = 0.2, 0.5, 1 and 2%) at each T. Figure 6a-c shows the example for creep stopper σ at ε = 1% for 450, 500 and 550 ºC, respectively, whereas Figure 6d and f summarizes the creep stopper stresses σ and normalized σ/σ_u, respectively, as a function of ε and T. Note, normalized stresses are close at higher T (Figure 6f).

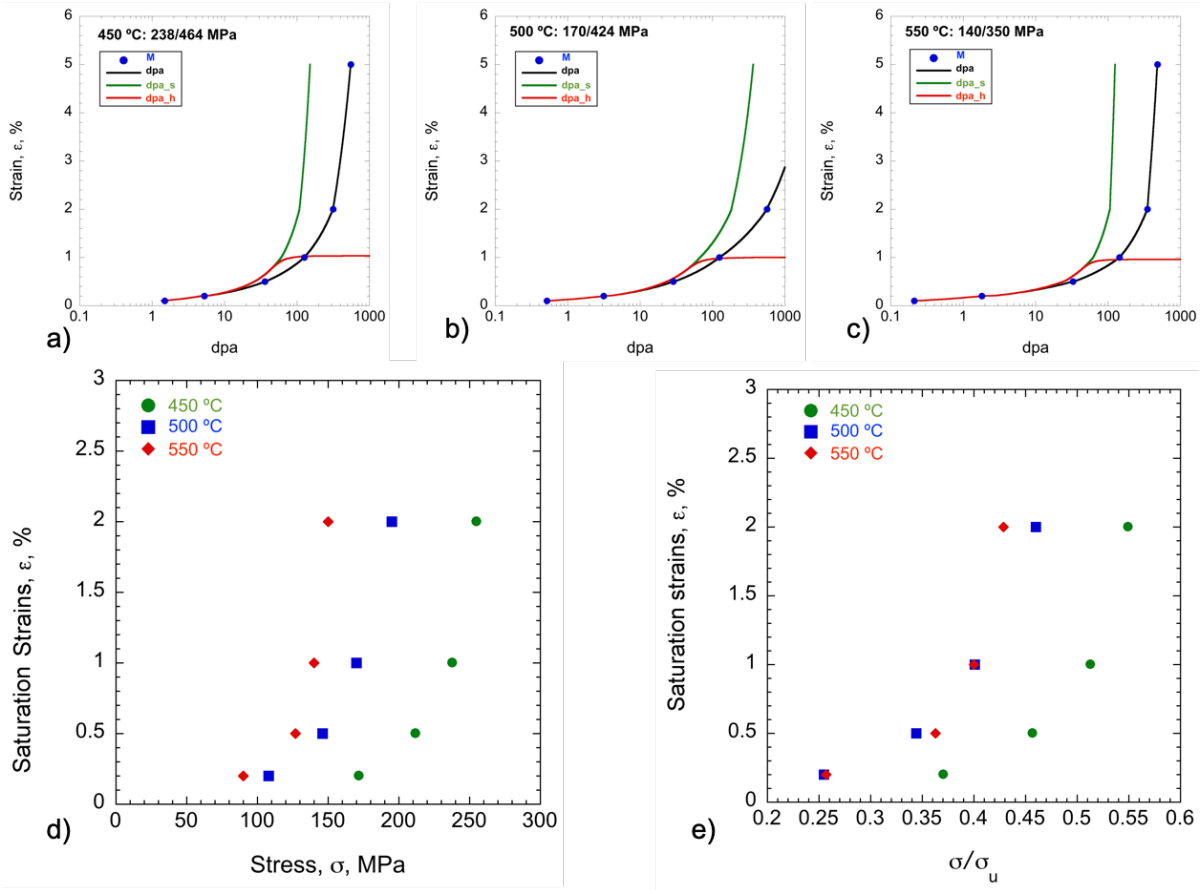

Figure 6. a-c) The hardening stopper stresses at ε = 1% for 450, 500 and 550 ºC, respectively. Here, thermal creep (black), softened (green), and hardened (red) is used to show creep curves. Figure 6d and f summarize the creep stopper stresses σ and normalized σ/σ_u, respectively, as a function of ε and T.

Results

At high temperatures the softening effects of irradiation must be considered. However, high He/dpa ≈ 10 would have a beneficial effect on creep times if the failure criteria are not met before ≈ 43 dpa. Therefore, the irradiation enhanced thermal softening model is integrated with the He re-hardening effect to develop an integrated re-hardening model for various creep stress, strain and temperatures. Thermal, softening and hardening creep curves and creep strain rates vs. dpa are measured for 450, 500 and 550 ºC for 0.2, 0.5, 1, 2, 3, 4, 5 % strains at variable creep stresses. The integrated re-hardening model also predicts the initiation hardening, hardening jump and creep stopper stresses for all these mentioned temperatures and strains which will help to predict the load for a certain condition.

Acknowledgment

We acknowledge the support provided by U.S. Department of Energy through the Office of Fusion Energy Sciences (8-442520-22419-3).

References

[1] T. Yamamoto, G.R. Odette, Constitutive models for hardening of tempered martensitic steels irradiated at 300 to 500 °C up to high dpa abd He, DOE Fusion React. Mater. Progr. Semiannu. Prog. Rep. DOE/ER/68 (2020) 55–67.

[2] M.E. Alam, T. Yamamoto, G.R. Odette, Global Thermal Creep Models Derived from a Comprehensive Multiple Heat Database on 9Cr Tempered Martensitic Steels, DOE Fusion React. Mater. Progr. Semiannu. Prog. Rep. 69 (2020) 24–37.

[3] M. Rieth, M. Schirra, A. Falkenstein, P. Graf, S. Heger, H. Kempe, R. Lindau, H. Zimmermann, EUROFER 97. Tensile, charpy, creep and structural tests, in: (No. FZKA--6911). Forschungszentrum Karlsruhe GmbH Technik und Umwelt (Germany). Inst. fuer Materialforschung., 2003.

[4] M.E. Alam, T. Yamamoto, G.R. Odette, On the Effects of Irradiation Enhanced Thermal Softening on the Creep Properties of 9Cr Tempered Martensitic Steels, DOE Fusion React. Mater. Progr. Semiannu. Prog. Rep. DOE0313/70 (2021) 15–22.

[5] B. Wilshire, P.J. Scharning, A new methodology for analysis of creep and creep fracture data for 9-12% chromium steels, Int. Mater. Rev. 53 (2008) 91–104.

[6] C.G. Panait, W. Bendick, A. Fuchsmann, A.F. Gourgues-Lorenzon, J. Besson, Study of the microstructure of the Grade 91 steel after more than 100,000 h of creep exposure at 600 °C, Int. J. Press. Vessel. Pip. 87 (2010) 326–335.

[7] F. Masuyama, T. Yamaguchi, New ferritic steels beyond Grade 92 and its creep degradation assessment by hardness method for Grade 91, in: ASME Symp. Elev. Temp. Appl. Mater. Foss. Nucl. Petrochemical Ind., 2014: pp. 1–8.

[8] H.-Y. Lee, W.G. Kim, Influence of Thermal Aging on Material Strength Behavior in Grade 91 Steeel, in: Transacctions Korean Nucl. Soc. Autumn Meet., 2015: pp. 3–5.

[9] J. Zhao, J. Gong, A. Saboo, D.C. Dunand, G.B. Olson, Dislocation-based modeling of long-term creep behaviors of Grade 91 steels, Acta Mater. 149 (2018) 19–28.

[10] S. Khayatzadeh, D.W.J. Tanner, C.E. Truman, P.E.J. Flewitt, D.J. Smith, Influence of thermal ageing on the creep behaviour of a P92 martensitic steel, Mater. Sci. Eng. A. 708 (2017) 544–555.

[11] M. Li, W.Y. Chen, Microstructure-based prediction of thermal aging strength reduction factors for grade 91 ferritic-martensitic steel, Mater. Sci. Eng. A. 798 (2020) 140116.

[12] T. Nagasaka, M. Ando, H. Tanigawa, H. Sakasegawa, T. Tanaka, T. Muroga, A. Sagara, Tensile properties of F82H steel after aging at 400–650 °C for 1000–30,000 h, Fusion Eng. Des. 124 (2017) 1011–1014.

[13] Y. Yano, T. Tanno, Y. Sekio, H. Oka, S. Ohtsuka, T. Uwaba, T. Kaito, Tensile properties and hardness of two types of 11Cr-ferritic/martensitic steel after aging up to 45,000 h, Nucl. Mater. Energy. 9 (2016) 324–330.

9.2 CALCULATION OF DEPTH DEPENDENT ACTIVATION ENERGY BARRIERS OF TRAP MUTATION REACTIONS IN W(110) SURFACE—G. Nandipati, K. J. Roche, R. J. Kurtz, W. Setyawan (Pacific Northwest National Laboratory), K. D. Hammond (University of Missouri), D. Maroudas (University of Massachusetts), B. D. Wirth (University of Tennessee)

OBJECTIVE

This task aims to use object kinetic Monte Carlo (OKMC) simulations to study the evolution of the helium-bubble microstructure in the near-surface region of the plasma-exposed tungsten surface. The KSOME (kinetic simulations of microstructural evolution) [1-3], an OKMC code, is used to simulate spatially relevant near-surface microstructures to experimentally relevant time scales under isothermal and variable temperature conditions caused by Edge-Localized Modes (ELMs).

SUMMARY

This report documents the calculation of depth-dependent activation energy barriers and prefactors of trap-mutation processes, based on their relative occurrence probabilities reported in Refs. 3 and 4, for He clusters of size 2 to 7 in the near-surface region of W(110) surface.

PROGRESS AND STATUS

Introduction

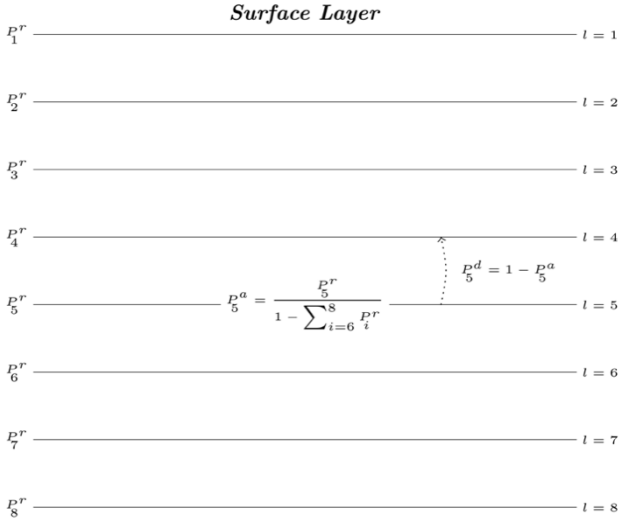

Figure. 1. P_i^r, where $i=1,\cdots,8$, are the relative occurrence probabilities of TM events that occur at various depths. P_5^a is the absolute occurrence probability for a TM event that occurs at a depth of $l = 5$. P_5^d is the absolute probability for the diffusion of the He cluster from the depth of $l = 5$ to $l = 4$.

In the studies reported in Refs. 4 and 5, several hundred molecular dynamics (MD) simulations of the dynamics of isolated He_n clusters (n = size) towards W free surfaces were performed. Individual outcomes of these simulations can be trap mutation (TM) reactions and/or cluster dissociation reactions. Unlike W(100) (see previous report [6]), for W(111) [7] and W(110) surfaces, partial and complete dissociations are rare. The outcome of individual MD simulation runs for the He_n ($1 \le n \le 7$) clusters was recorded to obtain the overall occurrence probabilities of individual reactions. Accordingly, for a given cluster size, the occurrence probabilities for TM events at a particular depth reported in Refs. 4 and 5 depend on the occurrence probabilities of those that occur at lower depths. However, to calculate the activation energy

barriers and prefactors for these reactions at a particular depth, the probabilities of all competing processes (referred to as absolute probabilities) at that depth are required. Accordingly, the sum of these absolute probabilities should be equal to one. Absolute occurrence probabilities for TM events at a given depth can be calculated as shown in Figure 1. More importantly, as cluster diffusion towards the surface is the primary competing process against TM events, the probability of non-occurrence of TM events is taken as the occurrence probability for the cluster to hop to an upper layer.

Expressions Used to Calculate Activation Barriers and Prefactors

When the average time scale (Δt_{avg}) or the average rate (R_T) of a process at a given temperature *T* and its activation barrier (E_a) are known, then the prefactor (D_0) is expressed using Eq. (1)

$$D_0 = \frac{1}{\Delta t_{avg}} exp\left(\frac{E_a}{k_B T}\right) = R_T exp\left(\frac{E_a}{k_B T}\right) \qquad (1)$$

However, if the rate R_T of a process at a given temperature *T* and its prefactor are known, then the activation barrier, E_a for this process can be calculated using Eq. (2)

$$E_a = k_B T\ ln\left(\frac{D_0}{R_T}\right) \qquad (2)$$

If the rates of a process R_{T_1} and R_{T_2} at two different temperatures T_1 and T_2 are known, then the activation barrier for this process can be calculated using Eq. (3)

$$E_a = \frac{k_B T_2 T_1}{T_2 - T_1} ln\left(\frac{R_2}{R_1}\right) \qquad (3)$$

If the ratio of the rates (R_T^{ab}) of two competing processes *a* and *b* at two different temperatures T_1 and T_2 are known, then the difference of their activation energy barriers is given by Eq. (4)

$$\Delta E_{ba} = E_b - E_a = \frac{k_B T_1 T_2}{T_2 - T_1} ln\left(\frac{R_{T_1}^{ab}}{R_{T_2}^{ab}}\right) \qquad (4)$$

where $R_{T_i}^{ab} = \frac{R_a}{R_b}\Big|_{T_i}$ at a temperature T_i where *i=1,2*.

If the ratio of rates of two different processes, R_a and R_b is known at a given temperature *T*, the difference in their activation energy barriers is given as

$$E_a - E_b = k_B T\ ln\left(\frac{R_{\boldsymbol{b}} D_0^a}{R_{\boldsymbol{a}} D_0^b}\right) \qquad (5)$$

Note that the present calculation of the activation energy barrier considers the effect of elastic interaction between the He cluster and the free surface, [9, 10], and temperature on the barriers for competing diffusion processes. [8] Furthermore, all prefactors were assumed to be temperature independent.

Activation Energy Barriers and Prefactors for Trap Mutation Reactions

He_1

In the near-surface region of W(110), single He atoms do not trap-mutate and desorb with 100%.

He_2 and He_3 Clusters

For the He_2 cluster, the TM reaction occurs at *I = 3* with a probability of 67.1% (for a sample size of 225 trajectories). If either the TM reaction or diffusion occurs with 100%, then the probability for the He atom to hop away from *I = 3* is 100 − 67.1 = 32.9%. Furthermore, under this assumption, the ratio of the rates of

TM reaction (R_{TM}) and the competing diffusion process (R_{Diff}) is equal to the ratio of their occurrence probabilities (p), that is,

$$\frac{R_{TM}}{R_{Diff}} = \frac{p_{TM}}{p_{Diff}} = \frac{67.1}{32.9} = 2.040$$

Since it is not possible to calculate the prefactor and the activation energy barrier simultaneously, the prefactors for the TM reaction and diffusion process are taken to be equal. Then using eq. (5), the activation energy barrier for the TM reaction $E_{TM}^{He_2} = 0.38\ eV$. Following a similar approach for the He_3 cluster, $E_{TM}^{He_3} = 0.334\ eV$. Energy barriers and the corresponding prefactors for TM reactions for He_2 and He_3 are shown in Table 1

Table 1. TM reactions and their relative probabilities, undergone by He_2, and He_3 clusters near W(110) surface. *I = 1* corresponds to the *surface layer*.

Reaction	Probability	T (K)	E_{TM} (eV)	D_0 (s^{-1})
$He_2 \rightarrow He_2V$ (*I* = 3)	67.1%	1200	0.38	1.3×10^{13}
$He_3 \rightarrow He_3V$ (*I* = 5)	72.8%	1200	0.334	2.3×10^{13}

<u>He_4 He5 and He_6 clusters</u>

For He_n clusters for $4 \le n \le 6$, when the information available to simultaneously calculate both the activation energy barrier and the prefactor is incomplete, TM reaction's prefactor is taken to be $10^{12} s^{-1}$. Details of occurrence probabilities are given in the Table. 2. More importantly, since desorption of He was not observed in the MD simulations, He clusters never escape to the free surface. Accordingly, the TM reaction at the lowest depth is considered to occur with a probability of 100%, with a zero-activation energy barrier and a prefactor of $10^{14} s^{-1}$ (so that $D_{TM} \gg D_{Diff}$). However, if multiple TMs are possible at the lowest depth (e.g., He_5 cluster at *I = 4*), any of the TM reactions occurs with 100% probability with zero activation barrier, but their prefactors are taken to be such that the TM reaction rates are larger than the diffusion rate and satisfy the probability of occurrence, as shown in Table 2. Calculated activation energy barriers and prefactor following the similar procedure described in the previous sections are shown in Tables III, IV, and V. Note that for He_5 and He_6 clusters the TM reaction at the depth of *I = 6* is ignored.

Table 2. Probabilities of TM reactions for the He_4 He_5 and He_6 cluster at various depths (*I*) at 1200 K

	He_4 →			**He_5 →**				**He_6 →**		
	He_4V	He_4V	He_4V	He_5V	He_5V	He_5V	He_5V_2	He_6V	He_6V	He_6V
Depth (I)	5	4	3	6	5	4	3,4	6	5	3,4
Probability (%)	17.6	77.5	4.9	0.9	38.4	44.3	5.4	3.2	65.3	31.5

Table 3. Energy barriers and prefactors for the TM reactions of the He_4 cluster

He_4 →	***I***	**D_0(s^{-1})**	**E_a (eV)**
He_4V	5	10^{12}	0.34
He_4V	4	3.26×10^{13}	0.25
He_4V	3	10^{14}	0.00

Table 4. Energy barriers and prefactors for the TM reactions of the He_5 cluster

He_5 →	***I***	**D_0(s^{-1})**	**E_a (eV)**
He_5V	6	–*	–*
He_5V	5	10^{12}	0.36
He_5V	4	10^{14}	0.00
He_5V_2	4	10^{13}	0.00

*TM reaction at I =6 is ignored

Table 5. Energy barriers and prefactors for the TM reactions of the He_6 cluster

He_6 →	***I***	**D_0(s^{-1})**	**E_a (eV)**
He_6V	6	–×	–×
He_6V	5	10^{12}	0.26
He_6V	4	10^{14}	0.00

×TM reaction at I =6 is ignored

He_7 Clusters

In KMC simulations, the He_7 cluster is considered as an immobile cluster. As there is (are) no competing process(es) for the TM reactions, it is not possible to extract energetics for the He_7 cluster. Only the energetics of the TM reaction process with the highest probability (see Table 6) can be calculated using the information in Figure S2 from the supplementary information for Ref. [4] as shown in Table 6. However, considering the low activation barrier and the depth at which the most probable TM reaction occurs and He_7 being immobile, in KMC simulations, it will be assumed that the most probable TM reaction will occur with zero barrier at depths $l \leq 9$.

Table 6. Probabilities of TM reactions for the He_7 cluster at various depths (l) at 1200 K

	He_7 →		
	He_7V	He_7V_2	He_7V_2
Depth (l)	6	4, 5	3, 4
Probability (%)	5.3	89.9	4.8
$\boldsymbol{E_{TM}(eV)}$	–	0.06	–
$\boldsymbol{D_0}$ $\boldsymbol{(s^{-1})}$	–	4.5×10^{11}	–

Acknowledgements

The work described in this article was performed at Pacific Northwest National Laboratory, which is operated by Battelle for the United States Department of Energy (US DOE) under Contract DE-AC05-76RL01830. The U.S. Department of Energy, Office of Fusion Energy Sciences (FES) and Office of Advanced Scientific Computing Research (ASCR) has supported this study through the SciDAC-4 program on Plasma-Surface Interactions [10].

References

[1] G. Nandipati, W. Setyawan, H. L. Heinisch, K. J. Roche, R. J. Kurtz, B. D. Wirth, *J. Nucl. Mater.* **462** (2015) 338.
[2] G. Nandipati, W. Setyawan, H. L. Heinisch, K. J. Roche, R. J. Kurtz, B. D. Wirth, *Semiannual Progress Report* DOE/ER-0313/54 (2013) 179.
[3] G. Nandipati, Kinetic Simulations of Microstructural Evolution, [Scientific Software, Ver.: 1.0] (Aug 26, 2020).
[4] L. Hu, K. D. Hammond, B. D. Wirth, and D. Maroudas, *J. Applied Physics* **118**, 163301 (2015).
[5] L. Hu, K. D. Hammond, B. D. Wirth, D. Maroudas, *Surface Science* **626** (2014) 21–25.
[6] G. Nandipati, K. D. Hammond, D. Maroudas, K. J. Roche, R.J. Kurtz, B. D. Wirth, W. Setyawan, *Semiannual Progress Report* DOE/ER–0313/67 (2019) 125.
[7] G. Nandipati, K. D. Hammond, D. Maroudas, K. J. Roche, R.J. Kurtz, B. D. Wirth, W. Setyawan, *Semiannual Progress Report* DOE/ER–0313/69 (2019) 219.
[8] D. Perez, T. Vogel, B. P. Uberuga, *Phys. Rev B* **90** (2014) 014102.
[9] L. Hu, K. D. Hammond, B. D. Wirth, D. Maroudas, *J. Appl. Phys.* **115** (2014) 173512.
[10] D. Maroudas, S. Blondel, L. Hu, K. D. Hammond, B. D. Wirth *J. Phys.: Condens. Matter* **28** (2016) 064004.
[11] Plasma Surface Interactions: Predicting the Performance and Impact of Dynamic PFC Surfaces (https://tinyurl.com/ru8mwqt).

9.3 PREDICTIVE MODELS FOR MECHANICAL PROPERTIES OF OXIDE DISPERSION STRENGTHENED ALLOYS

—B. N. Nguyen, W. Setyawan (Pacific Northwest National Laboratory)

OBJECTIVE

Strengthening an alloy or a matrix material in a composite with the oxide particles that form coherent or semi-coherent interfaces with the baseline material can produce a composite with significantly higher strength and toughness than the unstrengthened material. This research aims at developing mechanical property models to predict the constitutive behavior of oxide dispersion strengthened (ODS) alloys and composites as a function of their constituent mechanical properties, interfaces and temperature.

SUMMARY

Our focus has been on developing computational homogenization models to predict the constitutive behavior of ODS alloys as a function of their constituent mechanical properties, volume fractions and the interfaces between the oxide particles and baseline matrix. The first step of this study involved computation of elastic properties for ODS alloys. The PNNL's Eshelby-Mori-Tanaka Approach (EMTA) tool was used to predict the elastic moduli of 9%Cr steels strengthened by yttria (Y_2O_3) and alumina (Al_2O_3) at selected particle volume fractions. For very small values of oxide particle volume fraction practically used in forming these ODS alloys, EMTA predictions agreed very well with the experimental observations regarding the negligible effects of particle concentration on the homogenized elastic properties of the composite.

PROGRESS AND STATUS

Introduction

Experimental and modeling research on ductile phase toughened tungsten (DPT-W) materials has demonstrated that significant ductility is achieved through plastic deformation of the ductile phase (e.g., copper or nickel-iron) but that the materials lose strength at high temperatures due to reductions in strength of both the matrix and W with increased temperature. Our previous study [1] shows that various toughening and damage mechanisms occurring in the ductile phase are responsible for increased strength and fracture energy for the W composites. However, tailoring the W composite microstructure through adjusting its microstructural features and W-phase arrangement produced only modest improvements in strength for the as-formed or as-conceived composite. Therefore, methods to strengthen the ductile matrix for elevated temperature applications of W-composites are needed. Strengthening a matrix material with nanoparticles to significantly improve its mechanical properties have been explored for many decades in various engineering materials including polymer, ceramic and metallic composites [2-4]. Our research focuses on oxide particles as strengthening materials for the ductile matrix in W-composites considered for fusion energy applications. At this stage, yttria (Y_2O_3) or alumina (Al_2O_3) particles have been considered for our model developments due to their potentials for fusion materials and the available literature data for ODS steels containing these particles [5-9]. Figure 1 gives a schematic picture of a representative volume element (RVE or unit cell) of an ODS alloy that contains a nanoscale oxide particle embedded in a ductile alloy matrix. During forming, the particles may have aligned with the matrix lattice tending to full coherency. However, due to the difference in the lattice constant and due to the fast cooling of the alloy, only semi-coherency may practically remain at the interfaces between the matrix and the oxide particles. This semi-coherency indicates that the shearing of oxide particles by dislocations will be difficult leading to increased hardening observed for the ODS alloys [10]. The particle/matrix interface is responsible for the remarkable increase in strength observed in ODS alloys compared to the baseline unstrengthened materials.

In this work, the interface between the oxide particle and matrix has been modeled as a distinct material (Figure 1). A homogenization scheme for a three-phase composite (i.e., matrix, particle, and interface) based on the incremental Eshelby-Mori-Tanaka approach (EMTA) is being developed to predict the

constitutive stress-strain behavior of the ODS alloy as a function of the particle volume fraction and constitutive properties of the constituent materials including the particle/matrix interface. During the first reporting period of FY 2022, the EMTA for elastic stiffness (summarized in the next section) was used to compute the elastic properties of the 9%Cr ODS steels studied in Refs. [7-8] as a function of temperature and Y_2O_3 and Al_2O_3 volume fractions.

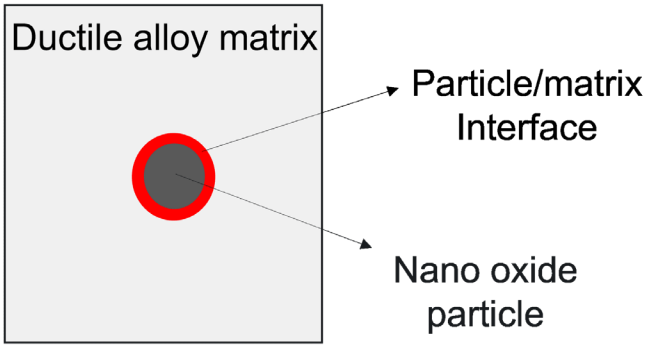

Figure 1. Schematic of a RVE for an alloy strengthened by oxide particles.

Experimental Procedure

The expression of the stiffness tensor for an elastic n_p-aligned-inclusion-phase composite according to the EMTA is [11-13]:

$$\mathbf{C} = \mathbf{C}_\mathrm{m} + \sum_{i=1}^{n_p} f_i(\mathbf{C}_i - \mathbf{C}_\mathrm{m})\mathbf{A}_i \quad (1)$$

where n_p, $\mathbf{C}_i$ and $\mathbf{C}_\mathrm{m}$ are the number of inclusion phases, fourth-order elastic stiffness tensors of inclusion *i* and of the matrix material, respectively. f_i denotes the matrix and inclusion volume fraction, and $\mathbf{A}_i$ is the inclusion strain concentration tensor. In our problem, n_p = 2, and the three phases: matrix phase "m", oxide particle phase "1" and matrix/particle interface phase "2". $\mathbf{A}_i$ is the inclusion strain concentration tensor given by:

$$\mathbf{A}_i = \mathbf{T}_i\left[f_\mathrm{m}\,\mathbf{I} + \sum_{i=1}^{n_\mathrm{p}} f_i\ \mathbf{T}_i\right]^{-1} \quad (2)$$

with $\mathbf{I}$ being the identity tensor, f_m the matrix volume fraction, and $\mathbf{T}_i$ given by

$$\mathbf{T}_i = [\mathbf{I} + \mathbf{S}_i\ \mathbf{C}_\mathrm{m}^{-1}\ (\mathbf{C}_i - \mathbf{C}_\mathrm{m})]^{-1} \quad (3)$$

where $\mathbf{S}_i$ is the Eshelby tensor of inclusion *i* that that depends on the inclusion aspect ratio and the matrix Poisson ratio. Expressions of $\mathbf{S}_i$ for different inclusion shapes are given by Mura [14]. For spherical inclusions considered in this work, the components of the Eshelby tensor are:

$$S_{ijkl} = \frac{5\nu_\mathrm{m}-1}{15(1-\nu_\mathrm{m})}\delta_{ij}\delta_{kl} + \frac{4-5\nu_\mathrm{m}}{15(1-\nu_\mathrm{m})}(\delta_{ik}\delta_{jl} + \delta_{il}\delta_{jk}) \quad (4)$$

where δ_{ij} is the Kronecker delta ($\delta_{ij} = \begin{cases} 0 \text{ if } i \neq j \\ 1 \text{ if } i = j \end{cases}$), and ν_m is the matrix Poisson ratio.

Results

The EMTA was used to compute the elastic properties of the Y_2O_3 and Al_2O_3 strengthened 9%Cr steels studied in Refs [7-8]. The elastic properties of the Y_2O_3 monocrystal and of the 9%Cr steel matrix were taken from Refs. [15] and [16], respectively. The elastic modulus of these materials as a function of temperature can be fitted by the following expressions:

$$E_{Y_2O_3} = -0.0205\,T + 147.87 \text{ GPa for } Y_2O_3, \text{ and}$$
$$E_{9\%Cr} = -20.92\,T + 233.26 \text{ GPa}$$

for the 9%Cr steel where T is the temperature expressed in degrees Centigrade. The temperature-dependent elastic modulus of the Al_2O_3 monocrystal was taken from Ref. [17]. The elastic properties of the particle/matrix interface are not known and were taken to be the average of the values for 9%Cr steel and the oxide particle at a given temperature.

The actual Y_2O_3 and Al_2O_3 particle concentration in 9%Cr steel [7-8] is 0.25 wt% which corresponds to the volume fractions of 3.89E-3 and 4.92E-3 for Y_2O_3 and Al_2O_3 in the composite, respectively. In this study, in addition to 0.25 wt%, we also considered a higher particle concentration up to 2 wt%. Note that significantly higher values than 0.25 wt% may not be realistic to form these ODS steels, but they present an interest for our study to determine the oxide particle effects on the composite elastic modulus. The volume fraction of particle/matrix interface [f_2 in Eqs. (1-2)] is not known. The TEM images have revealed that this interface appears as a thin layer around the particle [10]. As such, its volume fraction is bounded within the [0, f_1] range where f_1 is the actual particle volume fraction. In our parametric study, f_2 was taken to be equal to f_1. Note that if f_2 = 0, the presence of the particle/matrix interface is neglected, and Eq.(1) is reduced to the EMTA solution for a two-phase composite.

Figures 2a and 2b report the predicted elastic modulus for 9%Cr-Y_2O_3 and 9%Cr-Al_2O_3 steels as a function of temperature and at two oxide particle weight fractions: 0.25 wt% and 2 wt%. The results on Figures 2(a-b) show that the presence of either Y_2O_3 or Al_2O_3 at 0.25 wt% has negligible effects on the elastic modulus of the as-formed ODS steels for a wide temperature range from 25 to 1200°C. These predictions agreed very well with the experimental observations at room temperature reported in Ref. [7] that show no effects of these oxide particles at 0.25 wt% on the initial elastic responses of the 9%Cr steels strengthened by either particles. For Al_2O_3 at 2 wt%, EMTA predicted an average increase in alloy's elastic modulus about 2.8 % based on a two-phase solution and about 4.7 % from a three-phase solution. Due to its significantly higher elastic modulus compared to the steel matrix and Y_2O_3, the effect of Al_2O_3 on the alloy elastic modulus is more pronounced at higher Al_2O_3 particle concentrations. However. For practical particle concentrations considered (~0.25 wt%), this effect is too small to be significant.

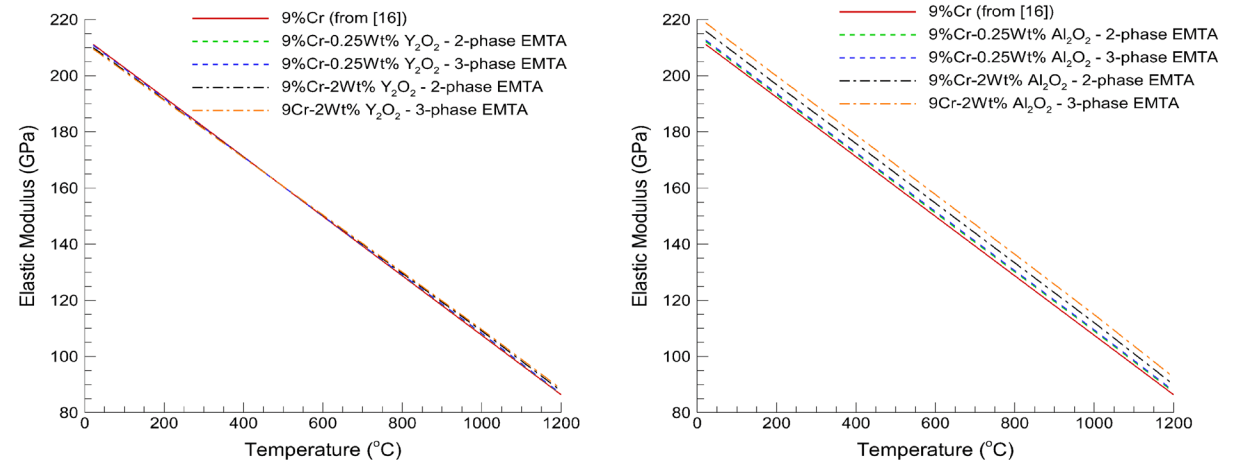

(a) (b)

Figure 2. Predictions of elastic modulus of (a) 9%Cr - Y_2O_3 and (b) 9%Cr - Al_2O_3 steels as a function of temperature and at two oxide particle concentrations: 0.25 wt% and 2 wt%.

Conclusion

The EMTA was shown to successfully predict the elastic moduli of 9%Cr steels strengthened by Y_2O_3 and Al_2O_3 particles. The as-formed steels were modeled as two-phase and three-phase composites. For typically small concentrations of these oxide particles used in alloy forming through powder technology, the effects of the particle concentration on the composite elastic properties are negligible. In this case, the EMTA two-phase and three-phase formulations produced quite similar results that agree with the experimental observations. Although a two-phase solution appears sufficient to compute the composite elastic properties, the EMTA three-phase solution will be needed in our next steps to predict the composite stress-strain response because the particle/matrix interface plastic behavior is responsible for the remarkable increase in hardening and strength observed in the experiments on ODS alloys.

Acknowledgement

This research was supported by the Office of Fusion Energy Sciences, U.S. Department of Energy and performed at PNNL under Contract DE-AC05-76RL01830.

References

[1] BN Nguyen, CH Henager Jr., J Wang, W Setyawan. *Journal of Nuclear Materials* 540 (2020) 152382.
[2] T Mahrholz, J Stängle, M Sinapius. *Composites: Part A* 40 (2009) 235-243.
[3] M Mazaheri, D Mari, R Schaller, G Bonnefont, G Fantozzi. *Journal of the European Ceramic Society* 31 (2011) 2691–2698.
[4] R Casati, M Vedani. *Metals* 4 (2014) 65-83.
[5] L-M Luo, Z-H Zhao, G Yao, Y-C Wu. *Journal of Nuclear Materials* 548 (2021) 152857.
[6] A Ramar, P Spätig, R Schäublin. *Journal of Nuclear Materials* 382 (2008) 210–216.
[7] H Hadraba, R Husak, L Stratil, F Siska, Z Chlup,V Puchy, J Michalicka. *Fusion Engineering and Design* 124 (2017) 1028–1032.
[8] F Siska, L Stratil et al. *Materials Science & Engineering A* 732 (2018) 112-119.
[9] S Ganesh, P Sai Karthik, M Ramakrishna, AV Reddy, SB Chandrasekhar, R Vijay. *Materials Science & Engineering* A 814 (2021) 141192.
[10] A Ramar, N Baluc, R Schäublin. *Journal of Nuclear Materials* 386-388 (2009) 515–519.
[11] JD Eshelby. *Proceedings of the Royal Society of London A: Mathematical, Physical and Engineering Sciences* 252 (1959) 561-569.
[12] T Mori T, K Tanaka. *Acta Metallurgica* 21 (173) 571–574.
[13] BN Nguyen, Z Hou, DH Bacon, MD White. *Greenhouse Gas Science and Technology* 7 (2017) 106-127.
[14] T Mura, “Micromechanics of Defects in Solids,” Boston, MA: Kluwer Academic Publishers; 1987.
[15] JW Palkoa, WM Kriven, SV Sinogeikin, JD Bass, A Sayir. *Journal of Applied Physics* 89 (2001) 7791-7796.
[16] JH Kim, TS Byun, DT Hoelzer. *Journal of Nuclear Materials* 425 (2012) 147–155.
[17] JA Salem, Z Li, RC Bradt. “Thermal Expansion and Elastic Anisotropy in Single Crystal Al_2O_3 and SiC Reinforcements.” NASA Technical Memorandum 106516; ASME Symposium on Advances in Composite Materials and Structures, Anaheim, CA, December, 10-12, 1986.

9.4 PREDICTIVE MODELING OF HE BUBBLE ACCUMULATION IN NANOSTRUCTURED FERRITIC ALLOYS—K. C. Pitike, W. Setyawan (Pacific Northwest National Laboratory)

OBJECTIVE

The overall objective is to develop a predictive model of helium bubble accumulation and distribution in irradiated nanostructured ferritic alloys under relevant fusion environments.

SUMMARY

Density functional theory calculations have been performed to calculate the binding energies between He and alloying solutes, transmutation products, and impurities for neutron-irradiated 14YWT. A manuscript has been submitted reporting the results. To extend the binding energy database to include He clusters, He bubbles, and Fe vacancy and self-interstitial defect clusters, an accurate potential is needed. An effort has been started to develop a machine learning interatomic potential to describe the He-H-Fe interactions. A plan for generating training data is presented.

PROGRESS AND STATUS

Helium interaction with solutes and impurities in neutron-irradiated nanostructured ferritic alloys: A first principles study

The first part of this report is an extended abstract for the manuscript: Pitike, Huibin, Edwards, and Setyawan, “Helium interaction with solutes and impurities in neutron-irradiated nanostructured ferritic alloys: A first principles study”, submitted to Journal of Nuclear Materials, ICFRM special edition.

Nanostructured ferritic alloys (NFAs) are being developed to improve high-temperature thermal creep strength and void swelling of reduced activation ferritic/martensitic (RAFM) steels. Due to the lack of fusion irradiation facilities with a sufficiently high flux, neutron irradiation studies of NFAs have been done in fission reactors. Hence, the irradiation effects of NFAs under fusion environments are largely unknown. Predictive models are crucial to understand the radiation effects in NFAs. To develop damage accumulation models that can account for neutron spectrum effects, interaction data of He with various alloying solutes, transmutation products, and impurities is needed. Such data is largely unavailable.

In this manuscript, we present such interaction data (binding energies), calculated with density functional theory (DFT), for the state-of-the-art NFA, 14YWT. List of possible transmutation products is informed by electron spectroscopy data of neutron-irradiated 14YWT in HFIR reactor up to 22 dpa. Figure 1 summarizes the binding energy of He with these solutes, where positive (red shades) and negative (blue shades) value indicates attraction and repulsion, respectively. Elements that exhibit significant binding (attraction) with an interstitial He are Y (binding energy = 0.46 eV), Mg (0.32), O (0.33), Ti (0.16), and C (0.15). Those that provide significant binding to a substitutional He are O (1.44), Y (1.24), N (0.73), H (0.56), Mg (0.52), Ti (0.34), Si (0.34), C (0.33), Al (0.32), Ni (0.26), Ta (0.23), and Mn (0.16). The presence of these elements in Fe matrix could reduce the transport of He towards oxide particles, dislocations, and internal boundaries, and could promote He bubble nucleation in the matrix.

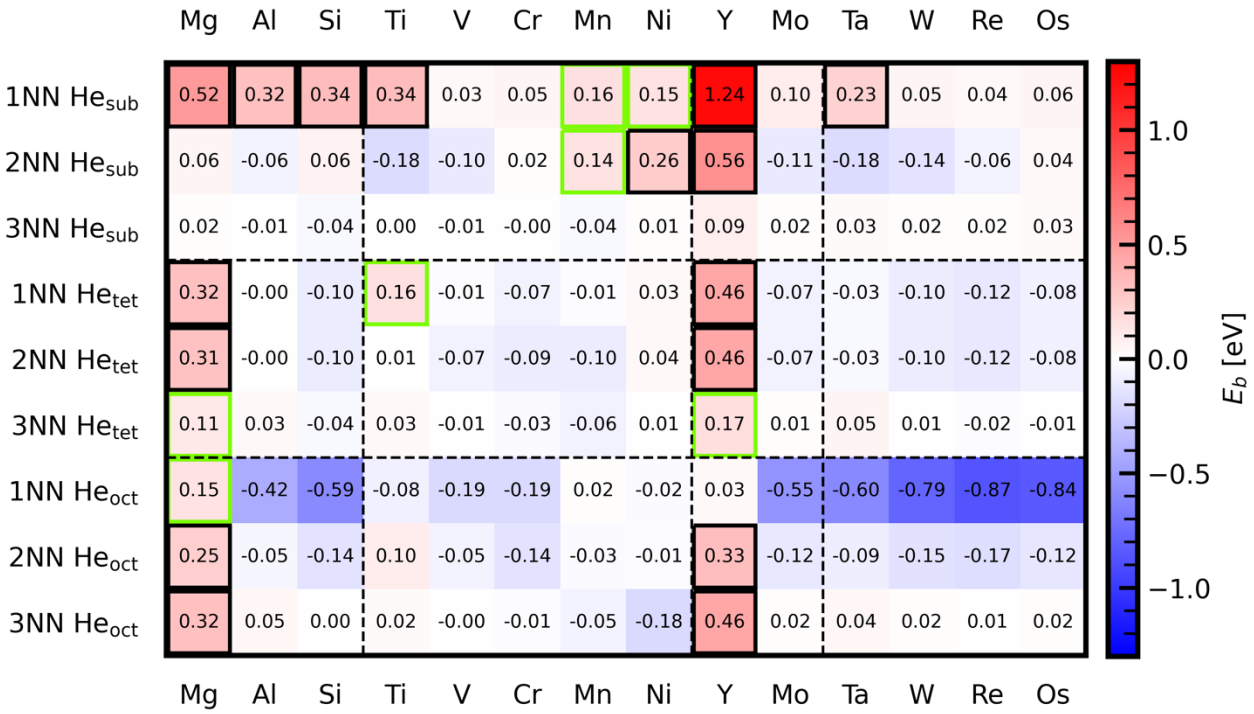

Figure 1. Binding energy heatmap for $[Solute + He]$ interactions. Red and blue shades in the heatmap represent attractive and repulsive interactions, respectively. Interactions with He_{sub}, He_{tet} and He_{oct} are plotted in 1-3, 4-6 and 7-9 rows (separated by horizontal dashed lines), respectively. Vertical dashed lines separate the elements of the same period (row of periodic table). Strong ($E_b \geq 0.31$ eV) and moderate ($0.31 > E_b \geq 0.15$ eV) attractive binding interactions are highlighted with individual black and green borders, respectively.

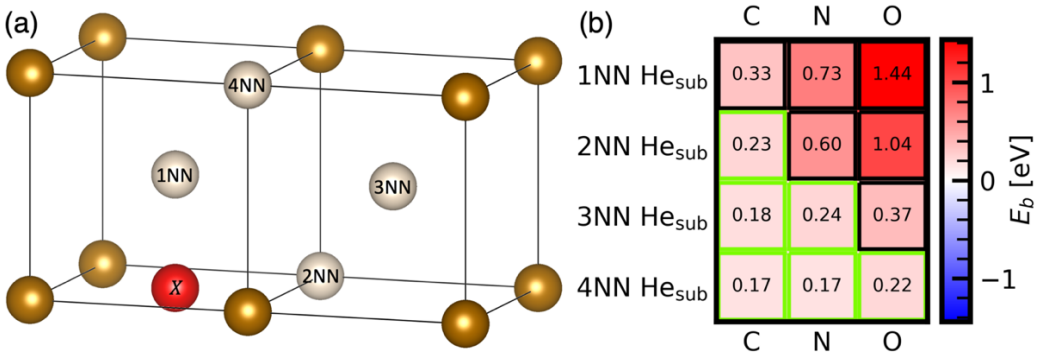

Figure 2. (a) Crystal structure showing impurity (C, N, O), and He_{sub} interactions. (Red: impurity; White: He; Gold: Fe). (b) Binding energy heatmap for $[impurity + He_{sub}]$ interactions. Red and blue shades in the heatmap represent attractive and repulsive interactions, respectively. The interactions beyond 4NN are negligible.

<u>Developing machine learned interatomic potential for studying He bubble accumulation in nanostructured ferritic alloys</u>

Here we report preliminary work and future steps on developing machine learned potential (MLP) for studying He bubble accumulation in nanostructured ferritic alloys.

Modelling the He bubble accumulation in NFAs such as 14YWT is crucial to advance the fundamental understanding of radiation damage in these materials, which could further lead to design principles to improve NFAs. Mesoscale simulations are required to quantitatively study the He bubble accumulation in BCC-Fe and near the Y-Ti-O oxide nanoparticles, spanning between 10s of nm to 100s of μm. First principles calculations at this length scale tend to become prohibitive due to their computational costs. Furthermore, modelling of NFAs at this length scale remains an elusive task due to the unavailability of energy descriptions that can capture the chemical and structural complexity of NFAs. For example, even though classical interatomic potentials are available to describe the Fe-He and Fe-H interactions in BCC-Fe, interatomic potentials to describe the Fe-(Y-Ti-O) interface and the gaseous transmutation products (He and H) interactions at this interface are not yet available.

In this project, we are in the process of developing MLP to study He/H bubbles in NFAs from first principles based DFT calculations. Some of the main advantage of MLPs are that (i) they are highly adaptable to wide range of complex chemical environments, (ii) accurate in describing the energy landscape and (iii) low computational cost. When these MLPs are trained using the energies obtained from DFT calculations, the MLPs can estimate the energies with near-DFT accuracy, for a fraction of computational cost. Furthermore, MLPs are an appropriate choice in this case, because of the complex interactions between Fe-He-H-(Y-Ti-O) in NFAs. At the first step, we sample a wide range of configurations (microstates), that describe the relevant interactions in NFAs, using DFT calculations. At the second step, the MLP is trained on the structural and energy data gathered from DFT calculations. At the third step, the trained MLP potential is rigorously tested to check if the MLP estimates the relevant physical properties with reasonable accuracy compared with DFT data. Steps 1 to 3 are iteratively repeated until desired accuracy is reached.

Figure 3 presents the results from preliminary DFT calculations. Figure 3(a) plots the energy landscape of bcc Fe as a function of applied strain for tensile, shear and volumetric strains. The elastic stiffness constants, $c_{11} = 255$ GPa, $c_{12} = 156$, and $c_{44} = 117$ obtained from the quadratic fits (shown as solid lines) are in good agreement with experimental values ($c_{11} = 243$ GPa, $c_{12} = 138$, and $c_{44} = 122$) [1]. Figure 3(b) presents the density of configurations as a function of energy obtained from DFT calculations with reference to its ground state structure. The 4000 configurations of 3x3x3 super cell (blue line) were sampled by first principles molecular dynamics (NVT) simulations, where temperature was varied between 300K to 1000K. The 1x1x1 unit cell configurations were sampled to exhaustively explore the strain states. Future DFT calculations will include He and H interactions with vacancies, self-interstitial atoms, Y-Ti-O, etc.

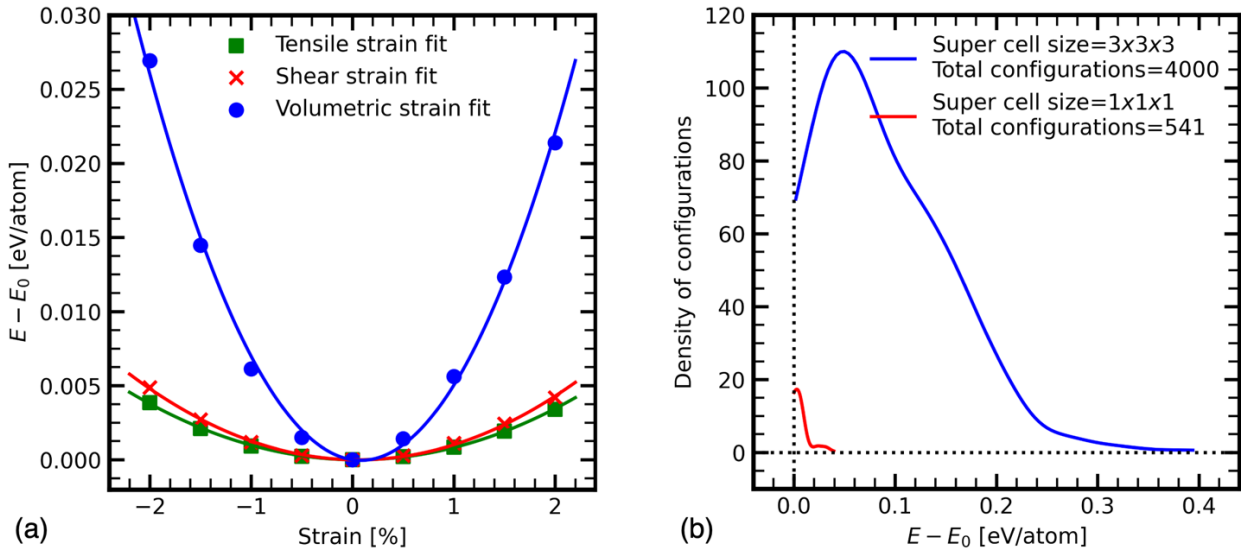

Figure 3. (a) The energies of the configurations sampling volumetric, tensile and shear strain of BCC-Fe plotted against the applied strain. (b) The density of states of configurations sampled.

Acknowledgments

This research was supported by the U.S. Department of Energy, Office of Science, Office of Fusion Energy Sciences, through Contract No. AT2030110-13784 and was performed at the Pacific Northwest National Laboratory, which is operated by Battelle for the U.S. Department of Energy under Contract No. DE-AC05-76RL0-1830. The research was performed using resources available through Research Computing at PNNL.

References

[1] J. A. Raynk, B. S. Chandrasekhar, Elastic Constants of Iron from 4.2 to 300 K, Phys. Rev. 122 (1961), 1714.

9.5 CASCADE SIMULATIONS IN DUCTILE-PHASE TOUGHENED TUNGSTEN—W. Setyawan (Pacific Northwest National Laboratory)

OBJECTIVE

To understand irradiation effects in W-Ni-Fe heavy alloys as a plasma-facing component material in a fusion reactor.

SUMMARY

Atomic displacement cascades are simulated using molecular dynamics to obtain primary defects in the ductile phase of W-Ni-Fe heavy alloys. The ductile phase is modelled as a Ni7Fe3 fcc solid solution. The simulations are performed at 700 °C. Electronic stopping is considered in the simulations. Simulations have been completed for a range of primary-knock-on atom energies of 0.5-100 keV. Primary defects have been analyzed. The number of Frenkel pairs and detailed counting of defect clusters are presented. Analysis of Burgers vectors of interstitial defect clusters is underway.

PROGRESS AND STATUS

Tungsten Heavy Alloys (WHAs) made of W, Ni, and Fe are promising as a structural material for fusion reactor divertors, exhibiting higher fracture toughness (69-107 MPa/√m compared to 5-8 MPa/√m of pure W) and improved ductility compared to pure tungsten [1-4]. A recently published neutron activation study of WHAs [5], if used in the divertor dome of the US ARIES-ACT2 reactor design concept [6, 7] for 10 years, shows the feasibility of using up to ~4.5 wt.% Ni in the WHAs to qualify for the Class C low-level-waste (LLW) classification based on the NRC's specific activity limits for terrestrial waste disposal, and up to ~9.5 wt.% Ni based on the Fetter's activity limits. While the neutron activation analysis is encouraging, the irradiation effects of these WHAs remain largely unknown.

To enable modeling of irradiation damage accumulation in WHAs, in this FY, displacement cascades are simulated to obtain primary defects in the ductile phase. The ductile phase is modeled as a Ni7Fe3 fcc solid solution (i.e., 30 at% of Fe). The simulations are performed at 700 °C, corresponding to the lower limit of the expected operating temperature of He-cooled tungsten-based divertors [8]. Historically, this lower limit is based on tungsten ductile-to-brittle transition temperature. The use of WHAs in place of pure tungsten would extend the limit to a much lower temperature than 700 °C. Empirical potentials *FeNiCr_Bonny_2013_ptDef.eam.alloy* [9] are employed to describe atomic interactions. Cascades with primary-knock-on atom energy (E_{PKA}) from 0.5 to 100 keV have been simulated. Nickel and Fe PKAs are explored to study differences in defect production. Electronic stopping is considered during cascade simulations, and it is modelled as a friction force. The magnitude of the friction force is equal to the electronic stopping power (S_{el}). A table of S_{el} is calculated separately using SRIM-13 code prior to cascade simulations. During cascades, energy loss due to electronic stopping is recorded. For cascades with Ni PKAs, the electronic energy loss is 5% of E_{PKA} at E_{PKA} = 0.5 keV, which increases to 14% at 100 keV. While in cascades with Fe PKAs, the electronic energy loss increases from 6% to 15%.

Table 1 summarizes the size of simulation box for a given E_{PKA} and the number of simulations performed with Ni and Fe PKAs. Figure 1 shows the number of Frenkel pair as a function of E_{PKA} for cascades with Ni and Fe PKAs. Interstitial defects and vacancies are recognized based on Voronoi cell occupation. The energy-dependence of the defect production on a log-log scale reveals two regimes of cascade morphology, as indicated by two characteristic slopes, below and above ~10 keV. The high-energy regime > 10 keV exhibits a steeper slope, associated with formation of large defect clusters. Comparing the results between Ni and Fe PKA, it is evident that the defect production obtained with Ni and Fe PKAs is similar.

Table 1. Supercell size of simulation box given in lattice unit (*a* = 3.59424 Å at 700 °C) and number of simulations with Ni and Fe PKAs as a function of PKA energy

E_{PKA} (keV)	Supercell (*a*)	# Ni PKAs	# Fe PKAs
0.5	16x16x16	14	10
0.7	16x16x16	14	10
1	19x19x19	14	10
2	22x22x22	14	10
3	25x25x25	14	10
5	28x28x28	14	10
7	31x31x31	14	10
10	37x37x37	11	12
20*	55x55x55	10	11
30	70x70x70	11	11
50*	100x90x90	10	11
70	130x115x115	11	12
100	172x152x152	10	10

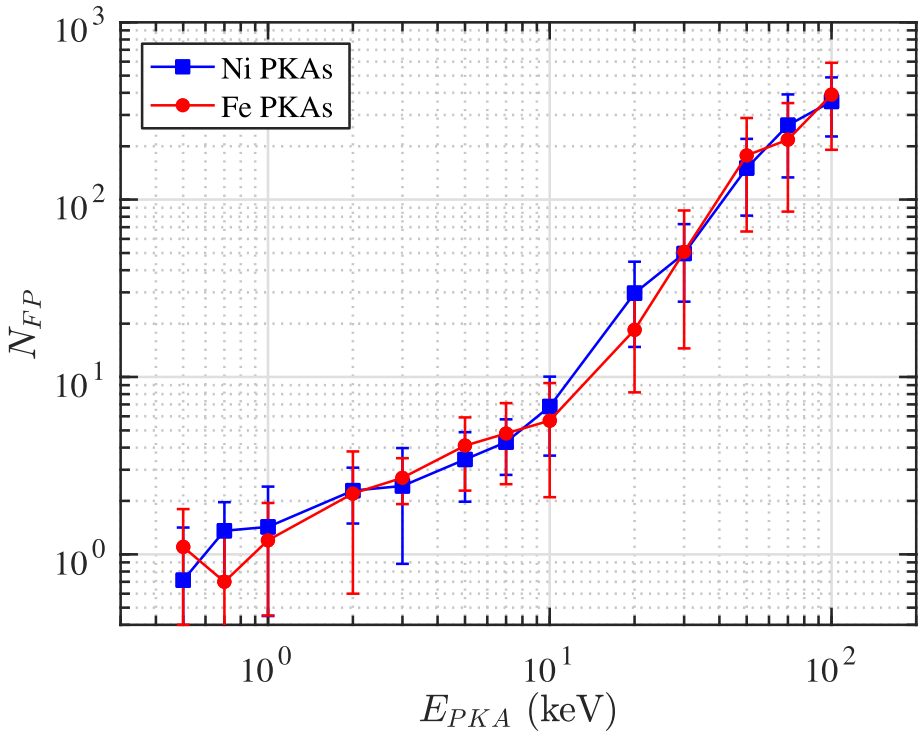

Figure 1. Average number of Frenkel pairs (N_{FP}) in Ni7Fe3 cascades, plotted with the standard deviations.

Defect clustering is analyzed based on a cutoff distance midway between the first and second nearest-neighbor distances in an fcc lattice. Clustered defects are here defined as those with more than one defect in the cluster. The energy-dependence of defect clustering is as follows. In the low-energy regime < 10 keV, only 20% of vacancies are clustered. At 20 keV, the fraction increases sharply to 50%, which increases

further to 0.75 at 100 keV. A similar energy-dependence is observed for the fraction of clustered interstitial defects; however, it is always larger than the fraction of clustered vacancies. For instance, the fraction of clustered interstitials is 85% at 20 keV and 93% at 100 keV. Tables 2 and 3 show the complete counting of interstitial and vacancy clusters from all the simulations. Analysis of Burgers vector of the interstitial clusters is underway. The results will be published in a journal article.

Table 2. Size (S_j) and count (C_j) of interstitial clusters. For $S_j < 21$, C_j are listed in order, starting from S_j = 1, 2, 3, …. For $S_j > 20$, only the sizes are listed with the count given in parentheses only if $C_j > 1$. E_{PKA} in keV is given in the first column.

0.5	17 2
0.7	20 3
1	24 2
2	33 3 2 1 1
3	29 10 2 0 0 1
5	46 6 6 2 1
7	56 10 4 2 0 2
10	47 9 2 2 0 2 2 1 2 0 0 1
20	58 10 4 6 2 2 2 1 1 0 0 2 1 1 2 1 0 0 0 0 — 22 24 26 27 30 33 34 40
30	98 15 11 2 2 2 2 1 0 2 1 1 1 0 2 2 1 0 0 2 — 24 27 29 31 32 34 36 41(2) 45 48 52 79 80 117
50	151 16 15 6 5 3 3 2 2 0 2 5 0 1 2 0 0 2 0 0 — 22 26 27 28 29 30 32 34 35 41 42 43 44 46 47 48 49 55 60 65 69 71(2) 78 84 86 87 88 114 121(2) 122 124 163(2) 174 199 209
70	381 63 27 9 4 4 1 6 2 2 1 5 2 1 2 2 2 1 1 0 — 21 22 23(2) 24(2) 25 26(2) 27 28 29(2) 30 31 34 36 37 40(2) 42 43 47(2) 50 51 53 56 60 61 63 66 67 69(2) 70 75 77 79 83 86 93 95 100 103 106 109 110 111 114 123 131 149 165 182 198 225 242 257
100	603 78 34 13 9 13 5 1 3 3 3 2 1 2 3 2 3 1 2 0 — 21(2) 22 23(3) 24(2) 27 28 29 30 31 35 36 38 39(2) 40 43(2) 46 48 49 51 52(2) 53 54 55 60 61 62 63(2) 68 73 74 89 92 95 98 100 101 105 107 111 112 117 120 122 132(2) 133 138 151 166 173 189 190 201 218 224 227 257 266 281

Table 3. Size (S_j) and count (C_j) of vacancy clusters. For $S_j < 21$, C_j are listed in order, starting from S_j = 1, 2, 3, …. For $S_j > 20$, only the sizes are listed with the count given in parentheses only if $C_j > 1$. E_{PKA} in keV is given in the first column.

0.5	15 3
0.7	17 3 1
1	24 2 0 1
2	41 5 1
3	54 2 1
5	70 4 2 0 1
7	857 1 0 0 1
10	119 4 2 1 0 1
20	226 15 2 1 6 1 1 0 2 0 1 1 1 0 1 0 0 0 0 1 — 29 35 38
30	376 24 7 6 4 2 2 2 1 1 2 1 0 0 0 0 1 0 0 0 — 21 27 29 32 56 62 63 86 127
50	689 52 16 11 5 4 4 3 3 3 1 1 2 1 2 0 0 1 0 1 — 22 24(2) 27(2) 28 31 32 39(2) 41 43 46 49 54 60 61 64 65 67 87 94 105 109 114 148 174 178 187 246
70	1090 137 41 15 15 8 4 8 6 5 6 5 3 3 6 0 0 2 1 2 — 21 22(2) 23(2) 24(3) 25(3) 27 29 32 34 36(2) 37 38(2) 39(3) 40 42 45(2) 47 49 51 52 54 56 60 76 78 80 92 102 108 117 118 120 123 126 130 137 144 193 282
100	1543 198 71 52 34 30 12 14 16 8 6 5 3 4 3 1 2 1 3 5 — 21(2) 22 25 26(2) 28 30(3) 31(3) 32 35(4) 36(2) 37(2) 38(3) 39 40 42 44(3) 45 46 49 52(2) 53 57 68 72 78(2) 83 86 87 97 101 103 114 124 140 146 153 156 157 167 218 248

Acknowledgements

This research has been supported by the U.S. Department of Energy, Office of Science, Office of Fusion Energy Sciences and performed at the Pacific Northwest National Laboratory under contract number DE-AC05-76RL01830.

References

[1.] C.H. Henager, W. Setyawan, T.J. Roosendaal, N.R. Overman, B.A. Borlaug, E.L. Stevens, K.B. Wagner, R.J. Kurtz, G.R. Odette, B.N. Nguyen, K. Cunningham, Ductile-Phase Toughened Tungsten for Plasma-Facing Materials in Fusion Reactors, International Journal of Powder Metallurgy, 53 (2017) 53-69.

[2.] M.E. Alam, G.R. Odette, On the remarkable fracture toughness of 90 to 97W-NiFe alloys revealing powerful new ductile phase toughening mechanisms, Acta Materialia, 186 (2020) 324-340.

[3.] J.V. Haag, D.J. Edwards, C.H. Henager, W. Setyawan, J. Wang, M. Murayama, Characterization of ductile phase toughening mechanisms in a hot-rolled tungsten heavy alloy, Acta Materialia, 204 (2021) 116523.

[4.] M.E. Alam, J. Wang, C.H. Henager, W. Setyawan, G.R. Odette, The effect of hot rolling on the strength and fracture toughness of 90W–7Ni3Fe tungsten heavy metal alloys, Materials Science and Engineering: A, DOI https://doi.org/10.1016/j.msea.2021.141738 (2021) 141738.

[5.] L. El-Guebaly, W. Setyawan, C. H. Henager Jr., R. J. Kurts, G. R. Odette, Neutron Activation Assessment for W-Ni-Fe Tungsten Heavy Alloys with Variable Ni Content, Nuclear Materials and Energy **29**, 101092 (2021), https://doi.org/10.1016/j.nme.2021.101092.

[6.] L. El-Guebaly, L. Mynsberge, A. Davis, C. D'Angelo, A. Rowcliffe, B. Pint, Design and Evaluation of Nuclear System for ARIES-ACT2 Power Plant with DCLL Blanket, Fusion Science and Technology, 72 (2017) 17-40.

[7.] The ARIES Project, http://qedfusion.org/bib.shtml, http://aries.ucsd.edu/ARIES/.

[8.] P. Norajitra, L. V. Boccaccini, E. Diegele, V. Filatov, A. Gervash, et al., Development of a helium-cooled divertor concept: design-related requirements on materials and fabrication technology, Journal of Nuclear Materials, 329 (2004) 1594.

[9.] G. Bonny, N. Castin, D. Terentyev, MSMSE 21, 085004 (2013).

10. IRRADIATION & TESTING ANALYSIS, METHODS, EXPERIMENTS, AND SCHEDULES

10.1 FUSION 2021 FRONTIER TASK 1 IRRADIATION CAPSULE DESIGN—N. Russell, A.M. Schrell, P. Champlin (Oak Ridge National Laboratory)

OBJECTIVE

The Fusion 2021 Frontier Task 1 irradiation program plans to irradiate 13 capsules, seven of the 3 mm disk specimen design and six of the fracture toughness specimen design. These irradiation capsules are designed to reach temperatures 300 °C, 500 °C, and 800 °C for one and three HFIR cycles. Loading will include tungsten, tungsten alloys, and tungsten laminated composite materials.

SUMMARY

The Fusion 2021 Frontier Task 1 irradiation program has two different capsule designs to accommodate 3 mm disk specimens and fracture toughness specimens. Each of these capsule designs reach target temperatures by optimizing the size of the insulating gas gap between the specimen holders and capsule housing. Images of the thermal analyses for the two capsule formats are shown in Figure 1. In addition to the fracture toughness specimens, this design allows for a tungsten fiber irradiation option. This option permits a line of three specimens be replaced by a tungsten container with a bundle of tungsten fibers. These two designs both allow for copper containing specimens, however for the 800 °C capsules, the copper content is limited due to potential for melting in HFIR safety scenarios.

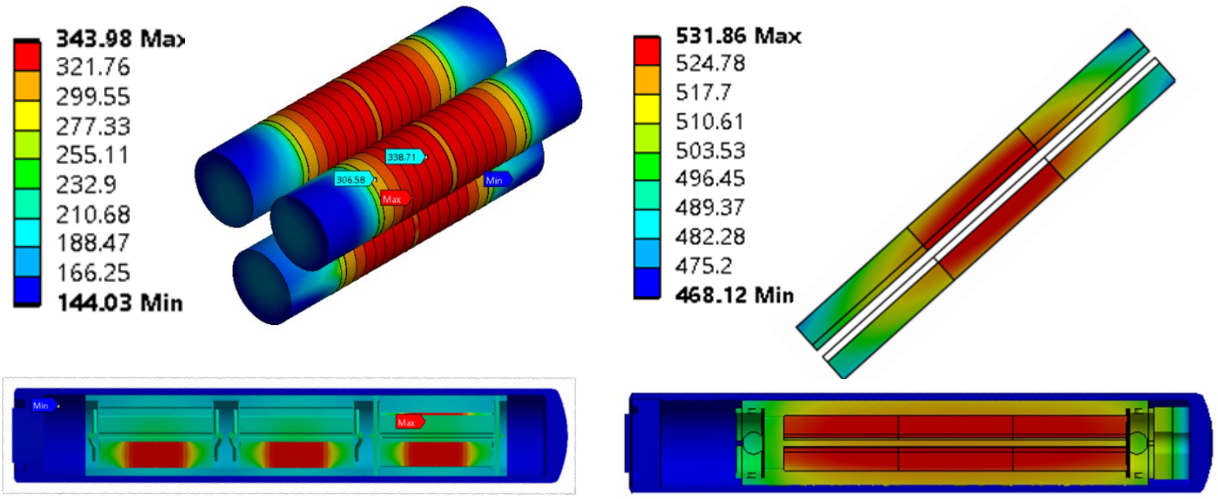

Figure 1. Representative thermal analysis of Frontier Task 1 tungsten irradiation capsules with 3 mm disk design (left) and fracture toughness design (right) for irradiation in HFIR.

PROGRESS AND STATUS

The three-cycle fracture toughness capsules have been built and will be ready for insertion in HFIR cycle 497. The part layout is shown in Figure 2, and a closer view of the specimens is shown in Figure 3. Two more of the 3mm targets are being assembled currently and will be inserted in cycle 498. Assembly parts for this capsule are given in Figure 4 as well as a zoomed in photo of specimens in Figure 5.

Figure 2. FR41 tungsten fracture toughness capsule build, with fiber option.

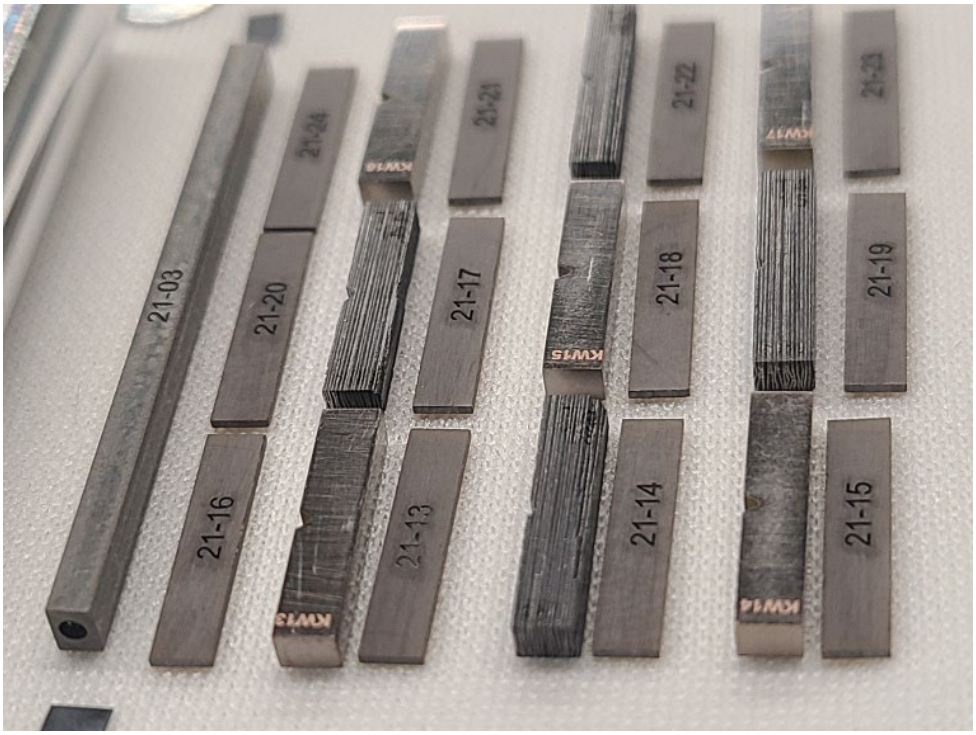

Figure 3. Tungsten fiber container, W/Cu laminate specimens, W/SiC laminate specimens.

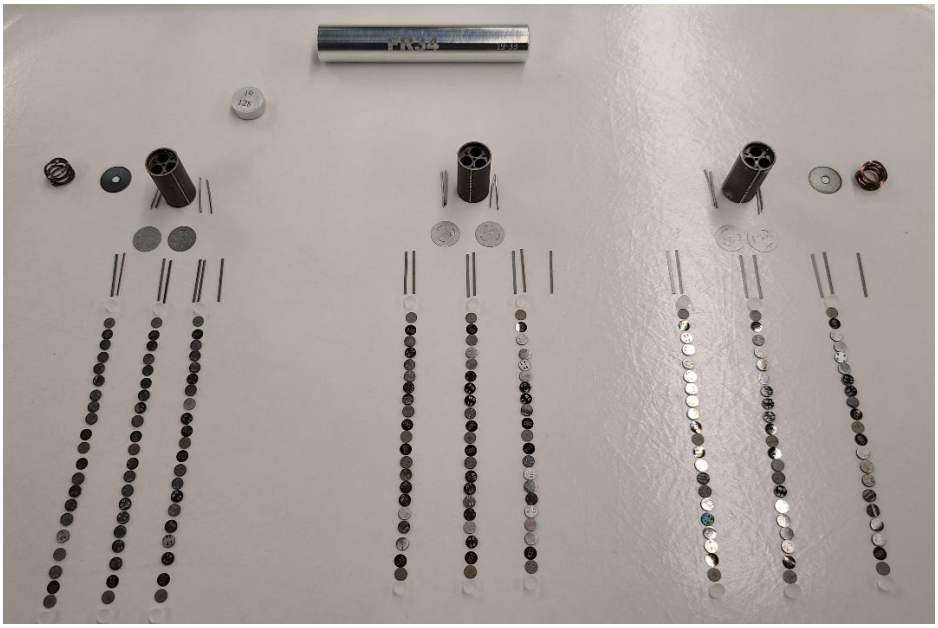

Figure 4. FR34 – 3mm capsule parts beginning assembly.

Figure 5. FR34 assorted specimens.

10.2 FUSION 2021 FRONTIER TASK 3 IRRADIATION CAPSULE DESIGN—N. Russell (Oak Ridge National Laboratory)

OBJECTIVE

The Fusion 2021 Frontier Task 3 irradiation program plans to irradiate 5 capsules with a design temperature of 400°C. Loading will include FeCrAl tensile specimens and Sn shot designed to melt and interact with the specimens.

SUMMARY

The Fusion 2021 Frontier Task 3 irradiation program plans to irradiate FeCrAl tensile specimens submerged in molten Sn to determine corrosion effects during irradiation. The design uses a sealed molybdenum holder to provide a secondary containment within the aluminum housing. The design has a target average specimen temperature of 400°C for one HFIR cycle. Images of the thermal analysis for the molten Sn corrosion design are shown in Figure 1.

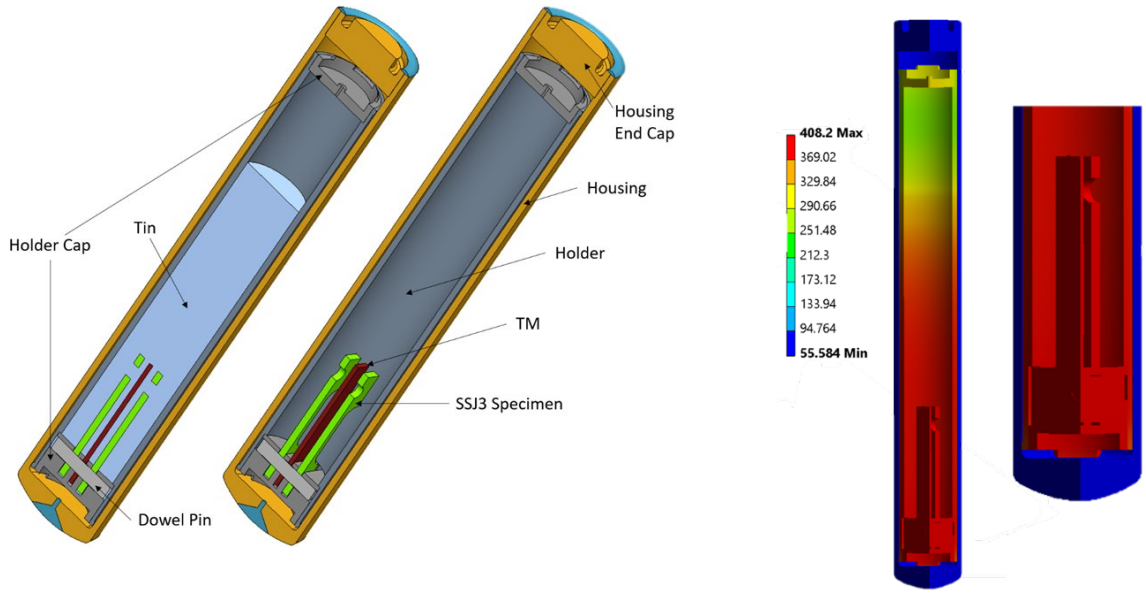

Figure 1. CAD representation (left) with Sn hidden for ease of viewing and representative thermal analysis (right) of Frontier Task 3 molten Sn corrosion irradiation capsules.

PROGRESS AND STATUS

Parts and specimens for these capsules have been delivered and inspected. A few extra sets of parts were ordered to do destructive out-of-pile testing to confirm reliability of the experiment as well as allowing the hot cells an opportunity to test disassembly prior to insertion. A draft of the thermal safety calculation is underway. Internal parts for these capsules are shown in Figure 2 and Figure 3.

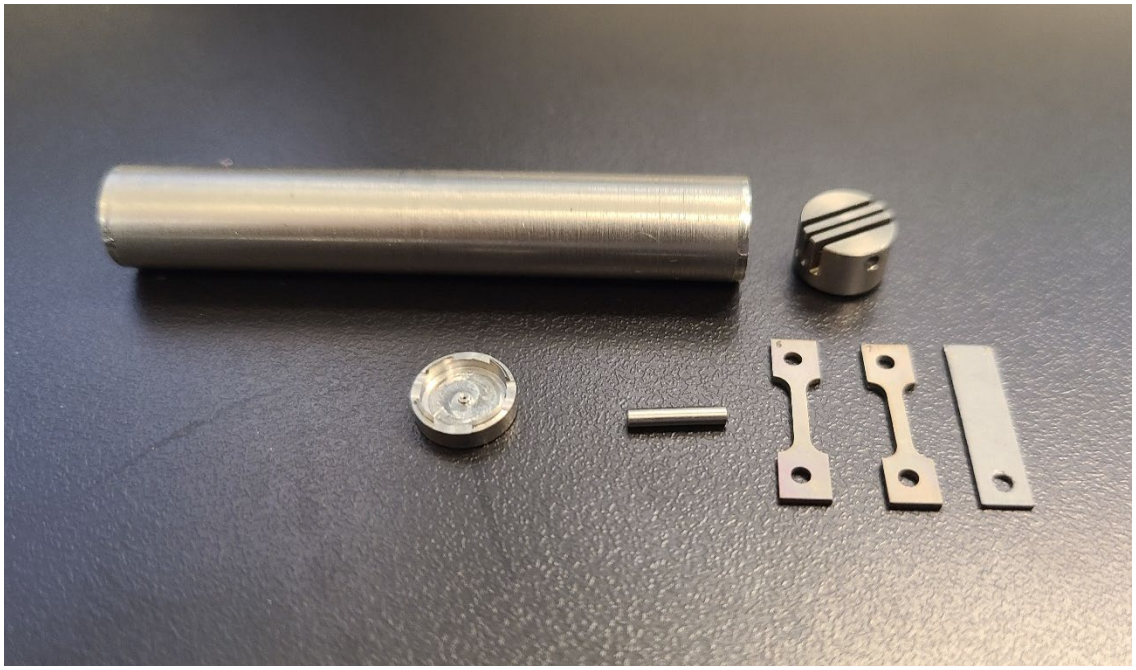

Figure 2. Frontier task 3 molten tin rabbit capsule internal parts.

Figure 3. Frontier task 3 molten tin rabbit capsule specimen region assembly.

10.3 IRRADIATION OF QST F82H TENSILE AND BEND BAR SPECIMENS IN HFIR—N. Russell, C. On, X. Chen, J. Geringer (Oak Ridge National Laboratory)

OBJECTIVE

The objective of this task is the implementation of the general tensile (GENTEN) and general bend bar (GENBEN) designs for irradiation of QST F82H specimens in HFIR. There is a total of 21 irradiation capsules within this campaign consisting of three low dose (5 dpa) capsules and 18 high dose (50 and 80 dpa, 9 of each). There are three different average specimen irradiation temperatures of 300°C, 400°C, and 500°C for these capsules.

SUMMARY

The temperature performance within an irradiation capsule is controlled by optimizing the specimen holder outer diameter (OD), holder material, and fill gas to create an insulating gas gap between the hot inner holder assembly and the cold capsule housing in direct contact with HFIR coolant. Much care and consideration was taken to apply the existing GENTEN and GENBEN designs. These designs developed a surface response model that allows the user to quickly and accurately determine a combination of holder OD, holder material, and fill gas to achieve an average specimen goal temperature. These two capsule designs can be seen below in Figure 1 and Figure 2.

The QST requested hold points be introduced to our standard irradiation capsule build procedure. The first hold point form was for holder design approval. This allowed the ORNL PI and QST PI to be involved choosing appropriate holder ODs and the math behind the neutron induced swelling. All the first hold point forms for the QST irradiation capsules have been reviewed and signed by the capsule designer, ONRL PI, and QST PI. The second hold point was introduced between assembly of the capsule parts and before welding. This hold point form for the capsules show pictures of every step in the assembly process so that QST could review the process and confirm specimen orientation. This hold form is approved for all the low dose and 80 dpa capsules.

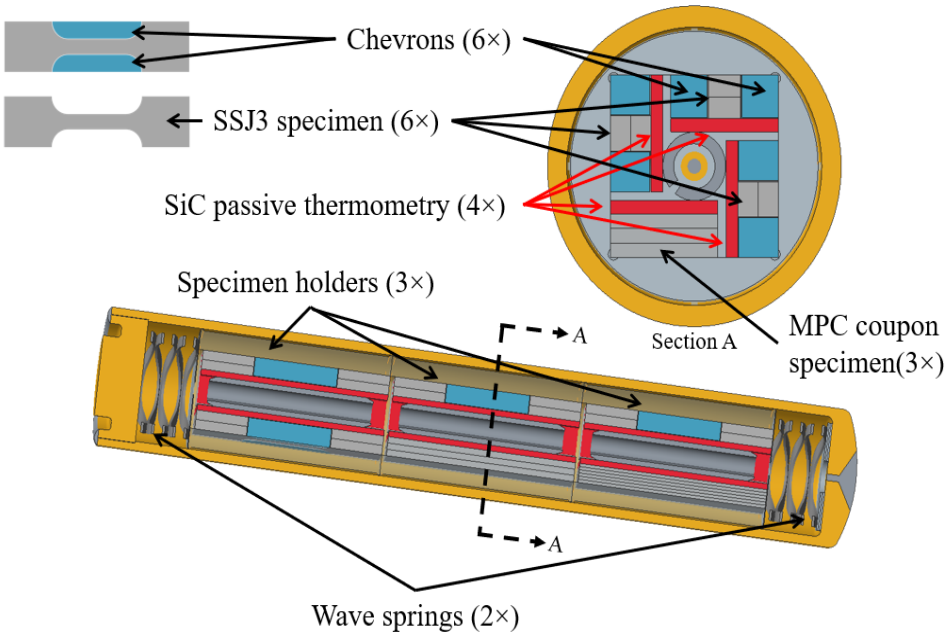

Figure 1. GENTEN irradiation capsule design.

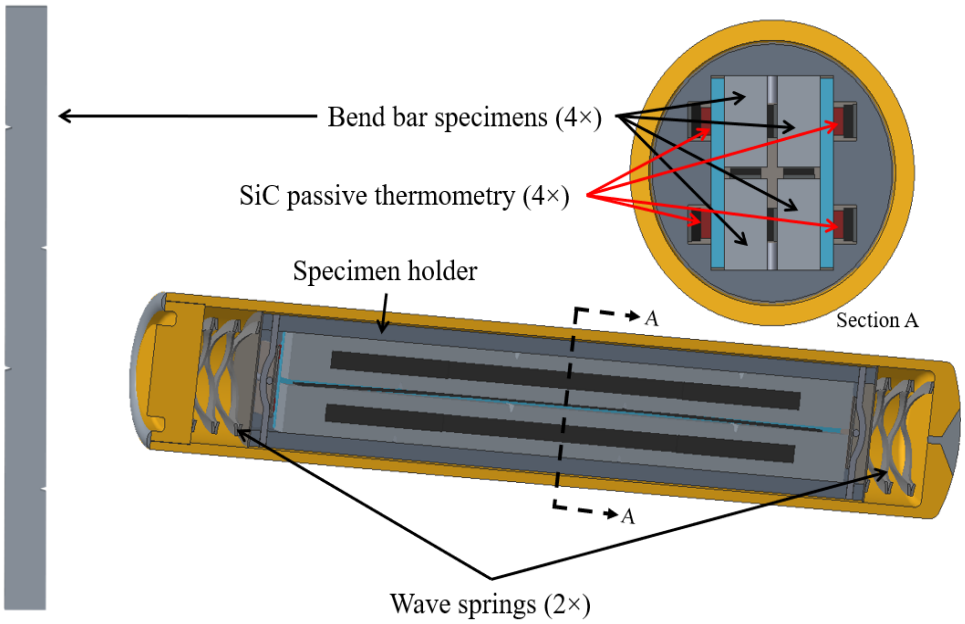

Figure 2. GENBEN irradiation capsule design.

PROGRESS AND STATUS

Moving forward, all the low dose capsules have completed irradiation in HFIR. The 80 dpa irradiation capsules began irradiation in HFIR cycle 496. All the hold point forms for the capsules have been approved and are included with the fabrication package. The 50 dpa high dose capsule designs have been approved by the ORNL PI and QST PI. The 50 dpa capsules are waiting instruction to begin building with estimated insertion into HFIR in FY22.

10.4 HFIR IRRADIATION EXPERIMENTS—C. On, J. W. Geringer, J. L. McDuffee (Oak Ridge National Laboratory)

OBJECTIVE

The goal of this report is to describe the progress of the neutron irradiation experiments that were performed in the High Flux Isotope Reactor (HFIR) and the operating status.

SUMMARY

During the six-month period starting from July 1st to December 31st, 2021 a total of twenty-two rabbit capsules continued their irradiation. There were five new capsules inserted and nine removed from HFIR during this period. Additionally, fourteen new capsules were assembled and shall begin irradiation in cycle 496, which will start on January 4, 2022. The cycles 493-495 were completed during this period.

PROGRESS AND STATUS

Neutron irradiation experiments were performed in support of the research and development of fusion reactor materials using various materials irradiation facilities in the HFIR. The reactor operating history for the period from July 1-December 31, 2021 is detailed in Table 1.

Table 1. HFIR operating record for the semiannual FY2021

Cycle Number	Cycle End Date	Power (MWD)
493	July 25	2184.03
494	September 4	2195.21
495	October 17	2202.82

All the fusion materials program irradiation experiments performed during the first half of the FY2021 used the nominally two-inch rabbit capsules, with no full-length target rod nor instrumented reflector position capsules within that period. Twenty-two target zone rabbit capsules remain in the reactor to complete the scheduled irradiations. Table 2 lists the experiments that were loaded into HFIR in cycle 495. While Table 3 lists the capsules that were removed at the end of each of the cycles. The capsules listed in Table 4 were inserted either during or before FY2021 and will continue in FY2022 and beyond. Tables 2-4 give condensed information on the material, specimen type, temperature, fluence, and period of irradiation.

Table 2. New irradiation capsules that started irradiation in cycle 495

Experiment Designation	Primary Materials	Specimen Types	Irradiation Temperature (°C)	Max Exposure (dpa)	Number of Reactor Cycles	HFIR Cycles Start – End
FR01	Joint W Alloy	Disk	300	1.6	1	495 - 495
FR04	Joint W Alloy	Disk	500	1.6	1	495 - 495
FR07	Joint W Alloy	Disk	800	1.6	1	495 - 495
FR11	Joint W Alloy	Disk	300	5	3	495 - 497
FR13	Joint W Alloy	Disk	500	5	3	495 - 497

Table 3. The rabbit capsules that completed irradiation at the end of FY2021

Experiment Designation	Primary Materials	Specimen Types	Irradiation Temperature (°C)	Max Exposure (dpa)	Number of Reactor Cycles	HFIR Cycles Start – End
ES15**	EUROFER 97	Bend bars	325	20	12	479 - 494
ES16**	EUROFER 97	Bend bars	350	20	12	479 - 494
ES17**	EUROFER 97	Bend bars	375	20	12	479 - 494
FH61	F82H-IEA, F82H-BA12	Bend bars	300	5	4	490 - 493
FH62	F82H-IEA, F82H-BA12	Bend bars	300	5	4	490 - 493
FMP16	F82H	Tensile/MPC*	650	20	11	484 - 494
FR01	Joint W Alloy	Disk	300	1.6	1	495 - 495
FR04	Joint W Alloy	Disk	500	1.6	1	495 - 495
FR07	Joint W Alloy	Disk	800	1.6	1	495 - 495

*MPC= Multi-Purpose Coupon
**ES15, ES16, and ES17= These capsules were removed at the end of cycle 483 and put back in cycle 487. The capsules missed 3 cycles

Table 4. The HFIR fusion materials program rabbit capsules to continue irradiation in FY2021

Experiment Designation	Primary Materials	Specimen Types	Irradiation Temperature (°C)	Max Exposure (dpa)	Number of Reactor Cycles	HFIR Cycles Start – End
FMP07	F82H	Tensile	300	20	11	487 - 497
FMP08	F82H	Tensile	300	80	45	487 - 531
FMP11	F82H	Tensile	385	20	11	488 - 498
FMP12	F82H	Tensile	385	80	45	488 - 532
FMP14	F82H	Tensile	525	20	21	484 - 504
FMP17	F82H	Tensile/MPC*	650	80	45	484 - 528
FMP22	F82H	Bend Bars	300	20	11	488 - 498
FMP23	F82H	Bend Bars	300	80	45	488 - 532
FR11	Joint W Alloy	Disk	300	5	3	495 - 497
FR13	Joint W Alloy	Disk	500	5	3	495 - 497
F13B4	FeCrAlY Steel	Tensile	300	50	29	451 - 497
JCR11-03	SiC/SiC	Mini bend bars	950	200	100	487 - 586
JCR11-05	SiC/SiC	Mini bend bars	950	200	115	444 - 568
JCR11-08	SiC/SiC	Mini bend bars	950	200	115	444 - 560
JCR11-11	SiC/SiC	Mini bend bars	950	100	55	448 - 524
L03067	Hi-Nicalon Type S	Bend Bars	800	200	100	405 - 506
L03069	Hi-Nicalon Type S	Bend Bars	800	200	100	405 - 506
SCF4	SiC/SiC	Miniature flexure bar	250	100	90	457 - 547
SCF5	SiC/SiC	Miniature flexure bar	250	200	45	457 - 511
SCF8	SiC/SiC	Miniature flexure bar	600	100	45	457 - 502
SCF9	SiC/SiC	Miniature flexure bar	600	200	90	457 - 548
SCF11	SiC/SiC	Miniature flexure bar	950	100	57	458 - 517

*MPC= Multi-Purpose Coupon

10.5 CLUSTER ANALYSIS OF COMBINED EDS AND EBSD DATA TO SOLVE AMBIGUOUS PHASE IDENTIFICATIONS—C. M. Parish (Oak Ridge National Laboratory)

Abstract of a manuscript in Microscopy and Microanalysis (In Press, DOI pending)

A common problem in analytical scanning electron microscopy (SEM) using electron backscatter diffraction (EBSD) is the differentiation of phases with distinct chemistry but the same or very similar crystal structure. X-ray energy dispersive spectroscopy (EDS) is useful to help differentiate these phases of similar crystal structure but different elemental makeup. However, open, automated, and unbiased methods of differentiating phases of similar EBSD response based on their EDS response are lacking. This paper describes a simple data analytics-based method, using a combination of singular value decomposition (SVD) and cluster analysis, to merge simultaneously acquired EDS+EBSD information and automatically determine phases from both their crystal and elemental data. I use hexagonal TiB2 ceramic contaminated with multiple crystallographically ambiguous but chemically distinct cubic phases to illustrate the method. Code, in the form of a Python 3 Jupyter Notebook, and the necessary data to replicate the analysis, are provided as supplemental information.

10.6 HIGH ENERGY SMALL-ANGLE X-RAY SCATTERING CAPABILITY DEVELOPMENT AT THE NSLS-II FOR FUSION ENERGY MATERIALS RESEARCH—D.J. Sprouster, J.R. Trelewicz, L.L. Snead (Stony Brook University), D. Olds, A.M.M. Abeykoon (Brookhaven National Laboratory)

OBJECTIVE

In this report, we discuss our recent efforts and progress towards commissioning the high-energy Small Angle X-ray Scattering (SAXS) capabilities at the Pair Distribution Function beamline of the National Synchrotron light Source-II. Baseline capability testing, and preliminary sample measurements on representative standards, and previously characterized specimens has been completed. Benchmark experiments with scattering standards (Silver Behenate and glassy Carbon) indicate that the initial set up is robust, and the procedures to collect calibrated SAXS data, both scattering vector, *Q,* and scattering intensity *I(Q),* are straight forward. The SAXS results from representative samples were also in agreement with previously published results. This capability compliments the high energy diffraction capability that exists at the PDF beamline and could be leveraged in the future to characterize fusion energy materials with nm-scale secondary precipitates either through fabrication or from irradiation (transmutation).

PROGRESS AND STATUS

The development of fusion as a clean, sustainable energy source requires materials that are inherently resistant to demanding operating conditions [1]. Such extreme environments include, but are not limited to, mixed radiation fluxes (neutrons, plasma, electromagnetic), high stresses, high temperatures, high thermal flux, and generation of substantial gaseous (H and He) and solid transmutation products [2, 3]. To address these harsh conditions, new engineered materials to withstand such harsh operating environments are under development [1, 4, 5]. The complicated microstructural response of fusion materials is inherently a multiscale problem [6], necessitating utilization of a range of characterization techniques in unison with computational modeling to predict and understand the complex processes from the atomic and nanometer length scales up through continuum-level material responses. X-ray techniques have very-low size limitations compared to direct imaging methods and effectively bridge the length scale gaps between conventional characterization techniques. Synchrotron based X-ray scattering techniques, including SAXS, can be used to characterize nm and sub-nm scale defects difficult to characterize in conventional TEM. High-energy X-rays offer the opportunity to characterize dense, high-Z materials, intrinsic to the structural materials anticipated in fusion energy devices. It is worth highlighting that high-energy X-ray characterization methods, with large penetration depths, provide structural insights with high statistical precision by averaging over much larger sampling populations compared to their electron-based counterparts [7].

In this report, we describe SBU's recent capability developments at the PDF beamline of the NSLS-II, to test and commission the high energy SAXS capability. As series of SAXS standards and previously characterized specimens were measured at PDF to benchmark and determine performance.

Experimental Procedure

All SAXS measurements were performed in transmission mode with an amorphous Silicon-based flat panel detector (Perken-Elmer). The sample-to-detector distance and tilts of the detector relative to the beam were refined using a Silver Behenate powder standard. The wavelength of the incident X-rays was 0.1665 Å (74.46 keV). The sample-to-detector distance was calculated to be 3291.00 mm. Fifty individual patterns with detector exposures of 0.1s were collected for each specimen. All raw two-dimensional patterns were background corrected by subtracting a dark current image, and the air and Kapton scattering background. The scattering intensity *I(Q)*, where *Q* is the scattering vector defined by $Q=(4\pi/\lambda) \times Sin\ \vartheta$, λ is the wavelength of the incident X-rays and ϑ is half the scattering angle. Noticeable artefact regions of the detector (like the beam stop, dead pixels) were masked. The corrected and masked two-dimensional

detector images were then radially integrated to obtain one-dimensional SAXS patterns. The SAXS measurements at the PDF beamline were made possible by installing equipment to improve the signal-to-noise ratio and to optimize the Q-range, including an evacuated flight tube and small beamstop (2-mm diameter). The primary goal of the flight tube is to reduce the parasitic air-scatter, and the beamstop is to protect the 2D detector from the direct beam. The SAXS standard materials, including Silver Behenate, glassy Carbon, and Kapton background were measured to determine the performance.

Results

Figure 1 shows the scattering signal collected for (a) Silver Behenate and (b) Glassy Carbon scattering standards at PDF beamline, and from LIX (a dedicated SAXS/WAXS beamline) of the NSLS-II. The similarity of the scattering intensity (and positions) of the scattering peaks for Silver Behenate, and decay of the scattering intensity with scattering vector (glassy carbon) indicate the quality of the high energy SAXS at PDF. After calibration of the Q-range and removal of beamstop, the operable Q-range was determined to be 0.008-1.5 $Å^{-1}$. This Q-range corresponds to feature sizes of ~78–0.4 nm. This range is directly in line with nm-scale features in transmutation-rich neutron irradiated W, carbide features in advanced steels, and Helium bubbles in neutron irradiated structural components [7].

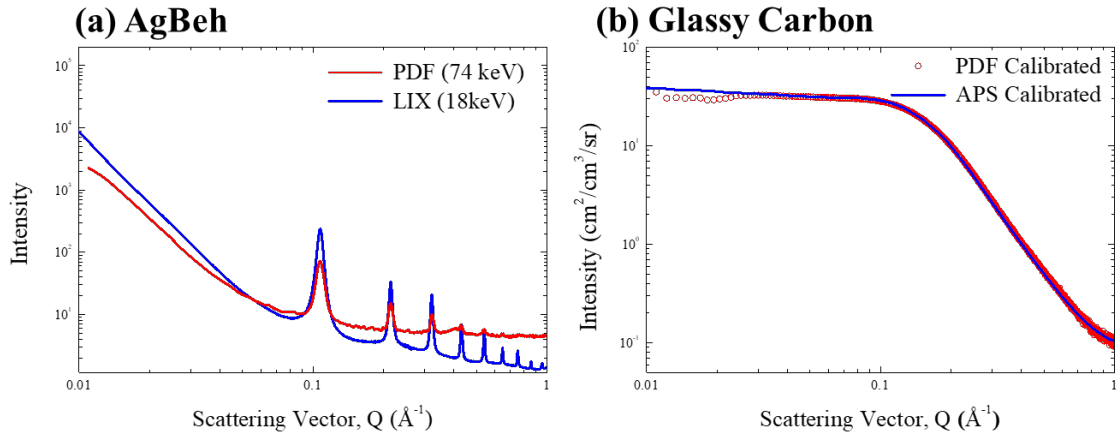

Figure 1. SAXS patterns for (a) Silver Behenate (AgBeh) scattering vector calibration standard, and (b) Glassy Carbon intensity calibration standard collected at PDF and at LIX beamlines.

Figure 2 shows SAXS patterns for two Nickel ion implanted Silica thin films (2μm), annealed to promote precipitation of the implanted Ni. The size distributions determined from the analysis agree with the sizes reported in Ref [8]. Figure 2 (b) shows representative SAXS patterns for ZnO powder X-ray scattering standards, where the power-law decay of the scattering intensity (-3) contain information on the particle shape and surface structure (rough, smooth). The large intensity range (y-axis of Figure 2 (b)) at PDF should be mentioned, with five decades of scattering intensity quantified for the ZnO specimens. Such a large range will enable quantification of very minor concentrations of embedded precipitates and bubbles. The ability to quantify the power law decay at PDF opens the possibility to characterize the shape and nanostructure of powders and monolithic materials.

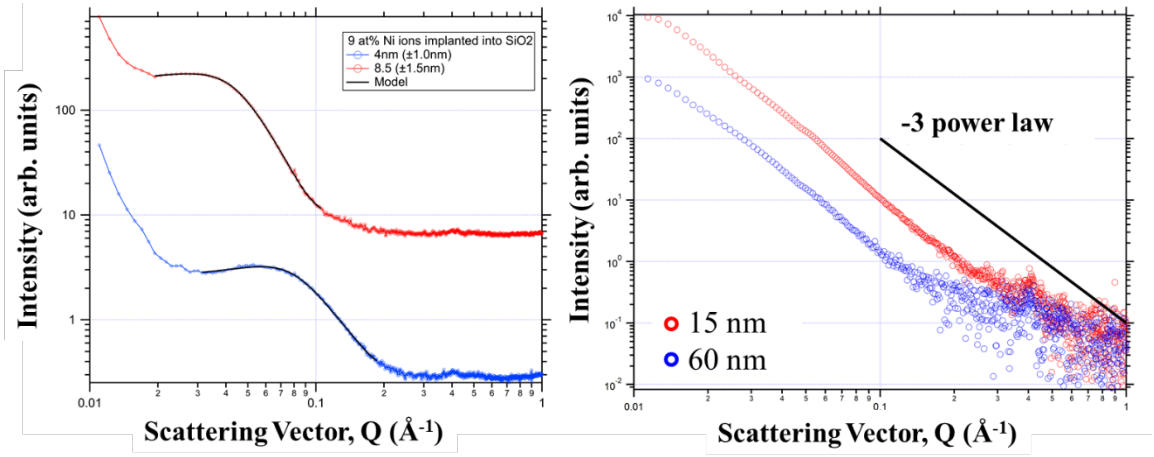

Figure 2. (a) Background-subtracted SAXS intensities (fitted region shown in black with patterns offset for comparison) for Ni implanted Silica. (b) background corrected SAXS patterns for ZnO nanopowder standards (15nm and 60nm Average particle size).

SUMMARY

In previous semi-annual reports, we have presented the high-energy x-ray diffraction capabilities at the NSLS-II, as applied to materials of interest to the FES research portfolio. As a direct development on this past work, we have extended the capabilities at the PDF beamline to now include the small-angle x-ray scattering technique. Through the commissioning tasks, and collection of SAXS patterns from standard specimens, the capability has been effectively achieved and compared/benchmarked to other SAXS beamlines. Potential improvements could include a smaller beamstop to increase the low-Q scattering range.

Acknowledgements

These experiments and analysis were supported by the DOE Office of Fusion Energy Sciences under contract DE-SC0018322 with the Research Foundation for the State University of New York at Stony Brook. This research used the Pair Distribution Function Beamline at the National Synchrotron Light Source-II, a U.S. Department of Energy, Office of Science User Facility, Contract No. DESC0012704 operated for the Department of Energy Office of Science by Brookhaven National Laboratory under Contract No. DESC0012704. This work was supported by the Department of Energy, Basic Energy Sciences, under contract DE-SC0021060.

References

[1] S.J. Zinkle, L.L. Snead, Annu Rev Mater Res 44 (2014) 241-267.
[2] T. Allen, J. Busby, M. Meyer, D. Petti, Mater Today 13(12) (2010) 14-23.
[3] S.J. Zinkle, J.T. Busby, Mater Today 12(11) (2009) 12- 19.
[4] Y. Katoh, L.L. Snead, I. Szlufarska, W.J. Weber, Curr Opin Solid St M 16(3) (2012) 143-152.
[5] S.J. Zinkle, G.S. Was, Acta Mater 61(3) (2013) 735-758.
[6] B.D. Wirth, K. Nordlund, D.G. Whyte, D. Xu, Mrs Bull 36(3) (2011) 216-222.
[7] D.J. Sprouster, J.R. Trelewicz, L.L. Snead, X. Hu, D. Morrall, T. Koyanagi, C.M. Parish, L. Tan, Y. Katoh, B.D. Wirth J. Nucl. Mater., 543, 152574 (2021).
[8] D. J. Sprouster, R. Giulian, L. L. Araujo, P. Kluth, B. Johannessen, N. Kirby, and M. C. Ridgway, J. Appl. Phys. 109, 113517 (2011).